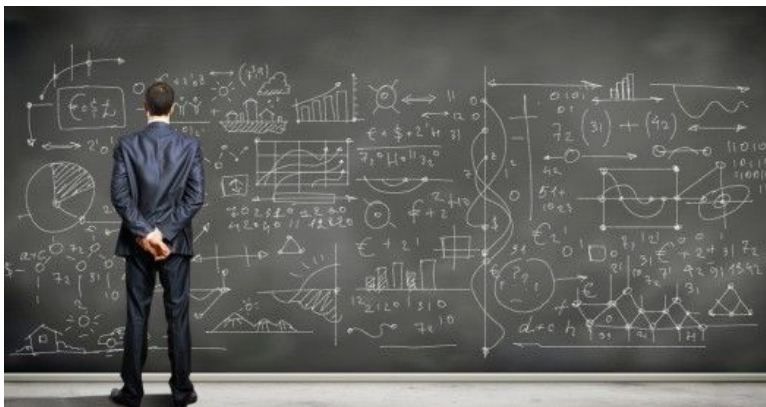


COMPUTATIONAL SCIENCES INTERNATIONAL

# THE HYDRA TOOLKIT

# COMPUTATIONAL FLUID DYNAMICS THEORY MANUAL



CSI-2015-1 REV. A, MAY 2017

COMPUTATIONAL SCIENCES INTERNATIONAL

Copyright © 2015 – 2017 Computational Sciences International

PUBLISHED BY COMPUTATIONAL SCIENCES INTERNATIONAL

All rights reserved. No claim to copyright is made for original U.S. Government Works.

*First printing, December 2015*

# Contents

<b>Contents</b>	<b>5</b>
<b>List of Figures</b>	<b>9</b>
<b>List of Tables</b>	<b>11</b>
<b>I Theoretical Development</b>	<b>17</b>
<b>1 Governing Equations</b>	<b>19</b>
1.1 Navier-Stokes Equations . . . . .	19
1.2 Constitutive Relations . . . . .	23
<b>2 Low-Mach Flows</b>	<b>29</b>
2.1 Low-Mach Equations . . . . .	29
<b>3 Incompressible Flows</b>	<b>31</b>
3.1 Conservation Equations – Indicial Form . . . . .	31
3.2 Conservation Equations – Vector Form . . . . .	34
<b>4 Multicomponent Flows</b>	<b>39</b>
4.1 Multispecies Flows . . . . .	39
4.2 Multifluid Flows . . . . .	42
4.3 Multiphase Flows . . . . .	43
<b>5 Arbitrary Lagrangian-Eulerian Formulation</b>	<b>51</b>
5.1 Basics . . . . .	51
5.2 Kinematics . . . . .	52
5.3 Master Balance Equation . . . . .	56
<b>6 Turbulence Models</b>	<b>61</b>
6.1 Turbulent flows . . . . .	62
6.2 Direct Numerical Simulation . . . . .	65
6.3 Reynolds-Averaged equations . . . . .	66
6.4 Large-Eddy Simulation . . . . .	80
6.5 Hybrid RANS/LES . . . . .	84

6.6	Derived Statistics . . . . .	99
<b>II</b>	<b>Numerical Methods</b>	<b>105</b>
<b>7</b>	<b>Unstructured Grid Topology</b>	<b>107</b>
<b>8</b>	<b>Discontinuous Galerkin/Finite Volume Method</b>	<b>111</b>
8.1	Scalar Conservation Law Formulation . . . . .	111
8.2	Flux Functions . . . . .	113
8.3	Element-Centered Gradient Approximation . . . . .	113
8.4	Phase-speed and Artificial Diffusivity . . . . .	118
8.5	Convergence Studies . . . . .	119
<b>9</b>	<b>Gradient Approximation</b>	<b>133</b>
9.1	Background . . . . .	133
9.2	Element-Centered Gradients . . . . .	136
9.3	Edge-Centered Gradients . . . . .	136
<b>10</b>	<b>Wall-Normal Distance Calculation</b>	<b>141</b>
10.1	Numerical Examples . . . . .	142
<b>11</b>	<b>Eulerian Formulation</b>	<b>147</b>
11.1	The Projection Method . . . . .	147
11.2	Semi-Implicit Projection Method . . . . .	150
11.3	Start-up Procedure . . . . .	155
11.4	Porous Media Flow . . . . .	160
11.5	Spalart-Allmaras Model . . . . .	164
11.6	The Smagorinsky Model . . . . .	168
11.7	The WALE Model . . . . .	169
<b>12</b>	<b>Arbitrary Lagrangian-Eulerian Formulation</b>	<b>171</b>
12.1	Second-order Incremental Projection Method . . . . .	171
12.2	Energy Equation . . . . .	182
12.3	Spalart-Allmaras Model . . . . .	184
12.4	RNG $k - \epsilon$ Model . . . . .	188
<b>13</b>	<b>Fluid-Solid Interaction</b>	<b>201</b>
13.1	FSI Literature Survey . . . . .	201
13.2	Stablized FSI Formulation . . . . .	204
<b>III</b>	<b>Appendix A</b>	<b>209</b>
<b>14</b>	<b>Vector Notation</b>	<b>211</b>
<b>15</b>	<b>Low Reynolds Number Functions used in the <math>k - \epsilon</math> Model</b>	<b>213</b>

<b>16 Bibliography</b>	<b>217</b>
<b>17 Index</b>	<b>237</b>



## List of Figures

1.1	Control volume for conservation laws. . . . .	19
1.2	Schematic of boundary surfaces. . . . .	22
3.1	Flow domain for conservation equations. . . . .	33
5.1	Invertible map. . . . .	51
5.2	Maps used in the ALE formulation. . . . .	52
6.1	Visualization of turbulent flow fields: isotropic turbulence (figure courtesy of Tokyo Institute of Technology)	63
7.1	Primal, median dual, and centroidal dual grids. . . . .	108
7.2	Primal and median dual grids. . . . .	108
7.3	CPU time vs. number elements for the edge extraction on a variety of unstructured grids. (UNSVIZ is a stand-alone test-harness for parallel rendering that was originally used to study edge-extraction algorithms using a 200 MHz Pentium-Pro processor as a baseline.)	109
8.1	Cell face locations for reconstructed $+/-$ values used in the numerical flux evaluation. . . . .	113
8.2	Cell face locations for reconstructed $+/-$ values used in the numerical flux evaluation. . . . .	113
8.3	Data used for least-squares reconstruction. . . . .	115
8.4	Phase speed and artificial diffusivity as a function of non-dimensional wave number. . . . .	119
8.5	Mesh configuration for all-triangular meshes. . . . .	121
8.6	$L^1$ errors at $t = 2.5, 5.0,$ and $10.0$ for the all-triangular meshes. . . . .	122
8.7	Rotated mesh configuration for all-triangular meshes. . . . .	123
8.8	$L^1$ errors at $t = 2.5, 5.0,$ and $10.0$ for the rotated all-triangular meshes. . . . .	123
8.9	Mesh configuration for all-quadrilateral meshes. . . . .	124
8.10	$L^1$ errors at $t = 2.5, 5.0,$ and $10.0$ for the all-quadrilateral meshes. . . . .	124

8.11	Mesh configuration for the rotated all-quadrilateral meshes.	125
8.12	Mesh configuration for the case-a tri-quad meshes. . .	126
8.13	$L^1$ errors at $t = 2.5, 5.0,$ and $10.0$ for the case-a tri-quad meshes. . . . .	126
8.14	Mesh configuration for the case-b tri-quad meshes. . .	127
8.15	$L^1$ errors at $t = 2.5, 5.0,$ and $10.0$ for the case-b tri-quad meshes. . . . .	127
8.16	Mesh configuration for the case-c tri-quad meshes. . .	128
8.17	$L^1$ errors at $t = 2.5, 5.0,$ and $10.0$ for the case-c tri-quad meshes. . . . .	128
8.18	Mesh configuration for the quadrilateral meshes. . . .	129
8.19	$L^1$ Error as a function of time for the quadrilateral meshes. . . . .	130
8.20	Mesh configuration for the mixed meshes. . . . .	131
8.21	$L^1$ Error as a function of time for the mixed meshes. .	132
9.1	Data used for the edge-centered least-squares reconstruction. . . . .	137
9.2	Geometry for normal gradient correction. . . . .	140
10.1	Normal distance calculation results for a cylinder in a channel with top and bottom wall: a) Direct calculation; b) Numerical calculation. . . . .	143
10.2	Normal distance calculation results for two cylinders in a channel with top and bottom wall: a) Direct calculation; b) Numerical calculation. . . . .	144
10.3	Normal distance calculation results on corners: a) Direct calculation; b) Numerical calculation. . . . .	144
10.4	Normal distance calculation results on YF17 geometry: a) perspective view; b) side view. . . . .	145
10.5	Normal distance calculation results on three element airfoil geometry, top view numerical calculation, bottom view direct calculation. . . . .	146
11.1	Dual-edge grid for edge projection. . . . .	153
11.2	Edge velocity interpolation. . . . .	154
11.3	Edge velocity extrapolation. . . . .	154
11.4	Overlapping “ghost” elements for parallel calculations.	154
11.5	Edge normal velocities on internal regions. . . . .	154
11.6	Elements with centroid velocity and characteristic dimensions. . . . .	156
11.7	Pressure boundary conditions. . . . .	156
11.8	Dual-edge assembly from elements 1 and 2. . . . .	157



12.1 Schematic of the two-layer model of a near-wall element used in the wall treatment. Here,  $p$  is the centroid of the element, while  $y_v$  and  $y_p$  represent the normal distances of the viscous sublayer and the element centroid from the wall, respectively, and  $y_n$  refers to the maximum of the normal distances of all the vertices of the given wall element. . . . . 193

12.2 Schematic of the assumed two-layer variation of  $\varepsilon$  in the wall layer elements. See Fig. 12.1 for the definitions of the length scales. . . . . 196



## List of Tables

6.1	Spalart-Allmaras model coefficients . . . . .	70
6.2	Standard $k - \varepsilon$ model coefficients . . . . .	72
6.3	RNG $k - \varepsilon$ model coefficients . . . . .	72
6.4	$k - \omega$ SST model coefficients . . . . .	75
6.5	$k - \varepsilon - \tilde{\nu}^2 - f$ model coefficients . . . . .	78
6.6	$k - \varepsilon - \zeta - f$ model coefficients . . . . .	80
6.7	DES model coefficients . . . . .	98
7.1	Topology test for edge extraction algorithm. . . . .	110
8.1	$L^1$ errors and convergence rates for the all-triangular meshes at $t = 2.5$ , $t = 5.0$ , and $t = 10.0$ . . . . .	122
8.2	$L^1$ errors and convergence rates for the rotated all-triangular meshes at $t = 2.5$ , $t = 5.0$ , and $t = 10.0$ . . . . .	124
8.3	$L^1$ errors and convergence rates at $t = 5$ for the all-quadrilateral meshes. . . . .	125
8.4	$L^1$ errors and convergence rates at $t = 5.0$ for the case-a tri-quad meshes. . . . .	126
8.5	$L^1$ errors and convergence rates at $t = 5.0$ for the case-b tri-quad meshes. . . . .	127
8.6	$L^1$ errors and convergence rates at $t = 2.5$ , $t = 5.0$ , and $t = 10.0$ . . . . .	128
8.7	$\mathcal{L}^1$ errors and convergence rates at $t = 5$ , $t = 100$ , and $t = 200$ for the quadrilateral meshes. . . . .	130
8.8	$L^1$ errors and convergence rates at $t = 50$ , $t = 100$ , and $t = 200$ for the mixed meshes. . . . .	131
12.1	Variable definitions for reference and current configurations. . . . .	171
12.2	Operators definition . . . . .	178



*When you come out of the storm, you won't  
be the same person who walked in. That's  
what this storm's all about.*

*Haruki Murakami*



# *Introduction*

The computational fluid dynamics theory manual presents the theoretical background for the single and multiphase flow solvers. Both solvers and multiphase flow solvers use a hybrid finite-volume/finite-element spatial discretization using the Hydra toolkit. The theory manual begins with the basic governing equations for incompressible and low-Mach flow with an outline of the requisite constitutive relations. Attention is then turned to multicomponent flows before addressing the Arbitrary Lagrangian-Eulerian (ALE) formulation used for fluid-solid interaction problems. Due to the flexibility in the virtual abstract physics and transport interfaces, the Hydra Toolkit is very extensible and can accommodate both multi-species and multi-phase formulations. The turbulence models that are either already available in the Hydra Toolkit or under development are outlined in Chapters [6](#), [11](#) and [12](#). An overview of the numerical methods used in the flow solvers are discussed and followed by a presentation of the formulation details for both the Eulerian and ALE reference frames. Finally, the approach used for stable fluid-solid interaction computations that is suitable for a broad range of fluid/solid densities and both linear and non-linear deformations is presented.





## **Part I**

# **Theoretical Development**



# 1 Governing Equations

This chapter introduces the conservation equations that govern the dynamics of fluids. The governing equations are presented first using index notation and then using Gibb's invariant (vector) notation in order to simplify the subsequent development of topics where one notation is preferred over the other. For example, turbulence models are typically presented using index notation, while sections that deal with numerical algorithms can favor vector notation.

## Navier-Stokes Equations

The basic laws that describe fluid motion include the conservation of mass, momentum, and energy. Figure 1.1 shows a prototypical control volume containing a continuous fluid medium.

The conservation equations may be written using index notation as follows [see Batchelor, 1967, Segel, 1965, Vincenti and Kruger, 1965].

Continuity equation

$$\frac{\partial}{\partial t} \int_{\Omega} \rho d\Omega + \oint_{\Gamma} \rho v_j n_j d\Gamma = 0 \quad (1.1)$$

Momentum equation

$$\frac{\partial}{\partial t} \int_{\Omega} \rho v_i d\Omega + \oint_{\Gamma} \rho v_i v_j n_j d\Gamma = \oint_{\Gamma} (-p\delta_{ij} + \tau_{ij}) n_j d\Gamma + \int_{\Omega} f_i d\Omega \quad (1.2)$$

Energy equation

$$\begin{aligned} \frac{\partial}{\partial t} \int_{\Omega} \rho E d\Omega + \oint_{\Gamma} \rho E v_j n_j d\Gamma = & - \oint_{\Gamma} q_j n_j d\Gamma \\ & + \oint_{\Gamma} u_i (-p\delta_{ij} + \tau_{ij}) n_j d\Gamma \\ & + \int_{\Omega} \dot{q}''' d\Omega + \int_{\Omega} f_j v_j d\Omega \end{aligned} \quad (1.3)$$

Here,  $\Omega$  is the arbitrary control volume shown in Fig. 1.1,  $\Gamma = \Gamma_2 \cup \Gamma_1$  is the boundary of  $\Omega$  where  $\Gamma_2$  and  $\Gamma_1$  indicate regions where Neumann and Dirichlet boundary conditions are applied, and  $n_j$  is the

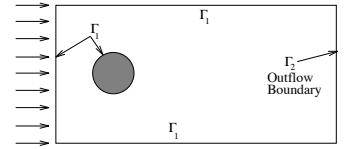


Figure 1.1: Control volume for conservation laws.

unit outward normal vector to the surface  $\Gamma$ . The remaining variables are defined as follows:  $t$  is time,  $x_i$  are the Cartesian coordinates,  $v_i$  is the fluid velocity,  $\rho$  is the fluid density,  $p$  is pressure,  $E = e + 1/2v_i v_i$  is the total energy per unit of mass,  $e$  is the internal energy per unit of mass,  $\tau_{ij}$  is the viscous shear stress tensor,  $q_i$  is the heat flux,  $f_i$  is an external force field,  $q'''$  is the energy source, and  $\delta_{ij}$  is the Kronecker delta. Vector and tensor quantities are understood to be Cartesian where repeated indexes imply a summation, i.e, the Einstein convention.

Applying the divergence theorem, the differential form of the conservation equations may be derived [see [Batchelor, 1967](#)].

Continuity equation

$$\frac{\partial \rho}{\partial t} + \frac{\partial}{\partial x_j} (\rho v_j) = 0 \quad (1.4)$$

Momentum equation

$$\frac{\partial \rho v_i}{\partial t} + \frac{\partial}{\partial x_j} (\rho v_i v_j) = \frac{\partial}{\partial x_j} (-p \delta_{ij} + \tau_{ij}) + f_i \quad (1.5)$$

Energy equation

$$\frac{\partial \rho E}{\partial t} + \frac{\partial}{\partial x_j} (\rho v_j E) = \frac{\partial}{\partial x_j} \left( -q_j + (-p \delta_{ij} + \tau_{ij}) v_i \right) + q''' + f_j v_j \quad (1.6)$$

The energy equation (1.6) can be manipulated to express it in terms of the internal energy ( $e$ ). Using the momentum and continuity equations, Eq.(1.5) is multiplied by  $v_i$ , and with the aid of Eq.(1.4), the equation of mechanical energy may be written as

$$\frac{\partial}{\partial t} (\rho v_i v_i / 2) + \frac{\partial}{\partial x_j} (\rho v_j v_i v_i / 2) = -v_j \frac{\partial p}{\partial x_j} + v_i \frac{\partial \tau_{ij}}{\partial x_j} + f_j v_j \quad (1.7)$$

Subtracting Eq.(1.7) from Eq.(1.6), the energy equation written in terms of internal specific energy is obtained.

$$\frac{\partial \rho e}{\partial t} + \frac{\partial}{\partial x_j} (\rho v_j e) = -\frac{\partial q_j}{\partial x_j} - p \frac{\partial v_j}{\partial x_j} + \tau_{ij} \frac{\partial v_i}{\partial x_j} + q''' \quad (1.8)$$

Substituting the definition of enthalpy  $H = E + p/\rho$  and  $h = e + p/\rho$  in Eqs.(1.6) and (1.8) allows the energy equation to be written in terms of enthalpy.

$$\frac{\partial}{\partial t} (\rho H) + \frac{\partial}{\partial x_j} (\rho v_j H) = \frac{\partial p}{\partial t} - \frac{\partial q_j}{\partial x_j} + \frac{\partial}{\partial x_j} (\tau_{ij} v_i) + q''' + f_j v_j \quad (1.9)$$

$$\frac{\partial \rho h}{\partial t} + \frac{\partial}{\partial x_j} (\rho v_j h) = -\frac{\partial q_j}{\partial x_j} + \tau_{ij} \frac{\partial v_i}{\partial x_j} + \frac{\partial p}{\partial t} + v_j \frac{\partial p}{\partial x_j} + q''' \quad (1.10)$$

### Navier-Stokes Equations in Vector Form

This section presents the Navier-Stokes equation in vector form. The reader may refer to 14 or Gresho and Sani [Gresho and Sani, 1998, pp. 347 – 359] for an overview of notation used for the Navier-Stokes equations.

The conservation equations can be written in a compact vector form as

$$\frac{\partial}{\partial t} \int_{\Omega} \mathbf{U} d\Omega + \oint_{\Gamma} \mathbf{F} \cdot d\Gamma = \int_{\Omega} \mathbf{Q} d\Omega \quad (1.11)$$

where the vector of conserved variables is defined as

$$\mathbf{U} = \begin{Bmatrix} \rho \\ \rho \mathbf{v} \\ \rho E \end{Bmatrix} = \begin{Bmatrix} \rho \\ \rho v_x \\ \rho v_y \\ \rho v_z \\ \rho E \end{Bmatrix} \quad (1.12)$$

The total flux  $\mathbf{F}$  is divided into Euler ( $\mathbf{F}_E$ ) and viscous fluxes ( $\mathbf{F}_V$ )

$$\mathbf{F} = \mathbf{F}_E - \mathbf{F}_V \quad (1.13)$$

where

$$\mathbf{F}_E = \begin{Bmatrix} \rho \mathbf{v} \\ \rho \mathbf{v} \mathbf{v} + \mathbf{I} p \\ \rho \mathbf{v} (E + p/\rho) \end{Bmatrix} = \mathbf{v} \mathbf{U} + \begin{Bmatrix} 0 \\ \mathbf{I} \\ \mathbf{v} \end{Bmatrix} p \quad (1.14)$$

$\mathbf{I}$  is the identity tensor, and

$$\mathbf{F}_V = \begin{Bmatrix} 0 \\ \boldsymbol{\tau} \\ \boldsymbol{\tau} \cdot \mathbf{v} - \mathbf{q} \end{Bmatrix} \quad (1.15)$$

The source vector is defined as

$$\mathbf{Q} = \begin{Bmatrix} 0 \\ \mathbf{f} \\ q''' + \mathbf{f} \cdot \mathbf{v} \end{Bmatrix} \quad (1.16)$$

Here,  $\mathbf{v}$  is the fluid velocity,  $\rho$  is the fluid density,  $p$  is pressure,  $E = e + 1/2 \mathbf{v} \cdot \mathbf{v}$  is the total energy per unit of mass,  $e$  is the internal energy per unit of mass,  $\boldsymbol{\tau}$  is the viscous shear stress tensor,  $\mathbf{q}$  is the heat flux,  $\mathbf{f}$  represents applied forces,  $q'''$  is the energy source. Alternatively, these equations can be written in flux-divergence form

$$\frac{\partial \mathbf{U}}{\partial t} + \nabla \cdot \mathbf{F} = \mathbf{Q} \quad (1.17)$$

where the divergence operator is applied to each row of the flux vector

$$\frac{\partial}{\partial t} \begin{Bmatrix} \rho \\ \rho \mathbf{v} \\ \rho E \end{Bmatrix} + \begin{Bmatrix} \nabla \cdot (\rho \mathbf{v}) \\ \nabla \cdot (\rho \mathbf{v} \mathbf{v} + \mathbf{I} p - \boldsymbol{\tau}) \\ \nabla \cdot (\rho \mathbf{v} (E + p/\rho) - \boldsymbol{\tau} \cdot \mathbf{v} + \mathbf{q}) \end{Bmatrix} = \mathbf{Q}. \quad (1.18)$$

### Boundary Conditions

In order to obtain solutions to the governing equations appropriate boundary and initial conditions are required. The type of boundary conditions to be specified depends on the characteristics of the problem under consideration. The most common boundary conditions are described below in reference to Fig. 1.2.

1. No-slip/no-penetration condition ( $\Gamma_{wall}$ ): This condition is commonly referred to as the “no-slip” condition. The adherence of fluid molecules to a surface requires that the fluid velocity at the surface be equal to the surface velocity, i.e.,  $v_i = \hat{v}_i$ , where  $v_i$  is the velocity of the fluid and  $\hat{v}_i$  is the prescribed surface velocity. In the particular case when the surface is at rest the no slip condition reduces to the familiar  $v_i = 0$  boundary condition.
2. Slip condition ( $\Gamma_{slip}$ ): A slip condition assumes that the fluid does not adhere to the surface. However, it typically also assumes that the fluid can not penetrate the surface, i.e.,  $v_i n_i = \hat{v}_i n_i$ , where  $n_i$  is the unit outward normal to the surface.
3. Infiltration condition ( $\Gamma_{wall}$ ): Surfaces that allow infiltration are permeable and permit a wall-normal velocity to cross the surface  $\mathbf{v}_n = \hat{\mathbf{v}}_n$ . In order to apply an infiltration boundary condition the infiltration velocity ( $\hat{\mathbf{v}}_n$ ) needs to be different from the wall-normal velocity.
4. Temperature condition ( $\Gamma_{wall}$ ): This boundary condition prescribes the fluid temperature at the surface  $T = \hat{T}$ , where  $\hat{T}$  is the wall temperature.
5. Heat flux condition ( $\Gamma_{wall}$ ): This condition is defined on surfaces where a heat flux is prescribed. An adiabatic condition may also be specified when there is no heat flux from the fluid to the surface, i.e.,  $\mathbf{q}_n = 0$ . If the heat flux is defined using Fourier’s Law this boundary condition is expressed as the normal gradient to the wall of temperature equal to zero, i.e.,  $\partial T / \partial \mathbf{n} = 0$ .
6. Inflow condition ( $\Gamma_{inflow}$ ): Inflow surfaces are those where the fluid enters the domain and where the values of flow variables are prescribed. Typically, these are simple Dirichlet boundary conditions.
7. Outflow condition ( $\Gamma_{outflow}$ ): Outflow surfaces are those surfaces where the flow leaves the domain. In the Hydra Toolkit, the default outflow condition is implemented by applying a homogeneous Neumann condition, i.e., the normal gradient of the variables is zero at the surface  $\partial \phi / \partial \mathbf{n} = 0$ , where  $\phi$  is an arbitrary variable, e.g.,  $\phi = \mathbf{v}, T, h, \text{etc} \dots$

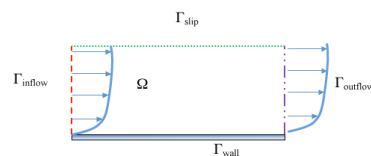


Figure 1.2: Schematic of boundary surfaces.

### *Initial Conditions*

In addition to boundary conditions, the Navier-Stokes equations require that initial conditions for all variables be defined. Although the initial conditions can be selected arbitrarily, incompressible flows require that these conditions be compatible with the boundary conditions in order to define a well-posed problem.

### *Constitutive Relations*

The Navier-Stokes equations, in either integral (1.1)-(1.3) or differential (1.4)-(1.6) form, are statements of conservation of mass, momentum, and energy. These equations, in particular momentum and energy, require the stress tensor and heat flux vector to be expressed as functions of the flow variables in order to have a complete system of equations to solve. It is well-known that the molecular structure of the fluid determines the way the stress tensor and heat flux are defined [White, 1991, Vincenti and Kruger, 1965], e.g., stresses in air and water follow different functional forms than those followed by more complex fluids like blood plasma, latex, molasses, mercury, or glass, precluding a universal model that could be used in all fluids.

### *Newtonian Fluids*

Although there is no single general functional form for the shear stress tensor, in general, the shear stress depends on the strain rate ( $S_{ij}$ ), temperature ( $T$ ), pressure ( $p$ ), and time ( $t$ ) [White, 1991, Vincenti and Kruger, 1965]

$$\tau_{ij} = f(S_{ij}, T, p, t) \quad (1.19)$$

where the strain rate is

$$S_{ij} = \frac{1}{2} \left( \frac{\partial v_i}{\partial x_j} + \frac{\partial v_j}{\partial x_i} \right) \quad (1.20)$$

Newtonian fluids exhibit a linear relationship between shear stress and strain rate expressed as

$$\tau_{ij} = 2\mu \left( S_{ij} - \frac{1}{3} S_{kk} \delta_{ij} \right) \quad (1.21)$$

where  $\mu$  is the fluid viscosity.

Kinetic theory for gases has been used to formally derive equation (1.21) for low density gases [Chapman and Cowling, 1952, Vincenti and Kruger, 1965], however, experimental evidence indicates that this relation is equally valid for liquids [White, 1991].

In many Engineering applications, fluid viscosity depends only on temperature and pressure. Experimental data indicates that there is no universal function that can parameterize the dependency of viscosity on temperature and pressure for all fluids. However, there is enough experimental evidence to state that the viscosity of liquids decrease rapidly with rising temperature, while the viscosity of low-density gases always increase with rising temperature. Additionally, the viscosity always increases with pressure.

Sutherland proposed an equation based on kinetic theory valid for diatomic atoms in a substance composed of a single element

$$\frac{\mu}{\mu_0} = \left( \frac{T}{T_0} \right)^{3/2} \frac{T_0 + S}{T + S} \quad (1.22)$$

where,  $S$  is a constant known as Sutherland constant, and  $T_0$  and  $\mu_0$  are reference temperature and viscosity, respectively. The value of these constants depend on the specific fluid. Another simple approximation is the power law that can be used also for liquids

$$\frac{\mu}{\mu_0} = \left( \frac{T}{T_0} \right)^n \quad (1.23)$$

where  $n$ ,  $\mu_0$ , and  $T_0$  depend on the fluid.

### *Non-Newtonian Fluids*

Depending on the molecular structure of the fluid it is possible to find cases where the shear stress – strain rate relationship is not linear. In general, fluids that do not follow Eq.(1.21) are known as non-Newtonian, and their behavior can be quite complex. For instance, the shear stress at constant strain rate for some substances may increase (rheopectic fluid) or decrease (thixotropic fluid) with time. Additionally, some fluids can support finite stresses without experiencing any deformation. These fluids are known as “yielding” fluids and are part solid and part fluid.

Many models have been proposed to approximate non-Newtonian fluids, the most typical approach prescribes a functional relationship between viscosity, strain-rate and temperature

$$\tau_{ij} = 2\mu(T, S_{ij})S_{ij} \quad (1.24)$$

The following models are representative of this class of non-Newtonian constitutive relationship.

### *Carreau-Yasuda model*

The Carreau-Yasuda model defines the viscosity as

$$\mu = \mu_\infty + (\mu_0 - \mu_\infty) \left( 1 + (\lambda S^a)^{\frac{n-1}{a}} \right) \quad (1.25)$$



where  $\mu_0$  is the low shear-rate Newtonian viscosity,  $\mu_\infty$  is the infinite viscosity (at high strain rates),  $\lambda$  is the “natural” time constant of the fluid, i.e.,  $1/\lambda$  is the critical shear rate at which the fluid changes from Newtonian to power law behavior, and  $n$  is the flow behavior index in the power law regime. The coefficient  $a$  is a material parameter. In the original Carreau model  $a = 2$ .

#### *Cross model*

When it is necessary to describe low-shear rate behavior, the Cross model is useful. This model is defined as

$$\mu = \mu_\infty + \frac{\mu_0 - \mu_\infty}{1 + (\lambda\mathcal{S})^{1-n}} \quad (1.26)$$

where  $\mu_0$  is the Newtonian viscosity,  $\mu_\infty$  is the infinite shear viscosity (usually assumed to be zero for the Cross model),  $\lambda$  is the natural time constant of the fluid ( $1/\lambda$  is the critical shear rate at which the fluid changes from Newtonian to power law behavior), and  $n$  is the flow behavior index in the power law regime.

#### *Ellis-Meter model*

The Ellis-Meter model expresses the viscosity in terms of the effective shear stress  $\mathcal{S}$

$$\mu = \mu_\infty + \frac{\mu_0 - \mu_\infty}{1 + (\mathcal{S}/\mathcal{S}_{1/2})^{(1-n)/n}} \quad (1.27)$$

where  $\mathcal{S}_{1/2}$  is the effective shear stress at which the viscosity is 50% between the Newtonian limit,  $\mu_0$ , and the infinite shear viscosity,  $\mu_\infty$ , and  $n$  represents the flow index in the power law regime.

#### *Herschel-Bulkey model*

The Herschel-Bulkey model can be used to describe the behavior of viscoplastic fluids, such as Bingham plastics, that exhibit a yield response. The viscosity is expressed as

$$\mu = \begin{cases} \mu_0 & \text{if } \tau < \tau_0 \\ \frac{1}{\mathcal{S}}(\tau_0 + k(\mathcal{S}^n - (\tau_0/\mu_0)^n)) & \text{if } \tau \geq \tau_0 \end{cases} \quad (1.28)$$

Here,  $\tau_0$  is the “yield” stress and  $\mu_0$  is a penalty viscosity to model the “rigid-like” behavior in the very low strain rate regime ( $\mathcal{S} \leq \tau_0/\mu_0$ ), when the stress is below the yield stress,  $\tau \leq \tau_0$ . With increasing strain rates, the viscosity transitions into a power law model once the yield threshold is reached,  $\tau \geq \tau_0$ . The parameters  $k$  and  $n$  are the flow consistency and the flow behavior indexes in the power law regime, respectively. Bingham plastics correspond to  $n = 1$ .

*Powell-Eyring model*

The Powell-Eyring model, which is derived from the theory of rate processes, is relevant primarily to molecular fluids but can be used in some cases to describe the viscous behavior of polymer solutions and viscoelastic suspensions over a wide range of shear rates. The viscosity is expressed as

$$\mu = \mu_{\infty} + (\mu_0 - \mu_{\infty}) \frac{\sinh^{-1}(\lambda \mathcal{S})}{\lambda \mathcal{S}} \quad (1.29)$$

where  $\mu_0$  is the Newtonian viscosity,  $\mu_{\infty}$  is the infinite shear viscosity, and  $\lambda$  represents a characteristic time of the measured system.

*Power Law Model*

The power law model defines the viscosity as

$$\mu = k \mathcal{S}^{n-1}; \quad \mu_{min} \leq \mu \leq \mu_{max} \quad (1.30)$$

with

$$\mathcal{S} = \sqrt{\frac{1}{2} S_{ij} S_{ij}} \quad (1.31)$$

where,  $k$  is a consistency coefficient and  $n$  is the flow behavior index. When  $n < 1$  the fluid is shear-thinning (or pseudoplastic), i.e., the apparent viscosity decreases with the strain rate. For  $n > 1$ , the fluid is shear-thickening, i.e., the apparent viscosity increases with the strain rate. Newtonian behavior is recovered for  $n = 1$ .

*Heat Transfer*

Classical thermodynamics indicates that the heat flux vector is a function of the temperature gradient as expressed by Fourier's law

$$q_i = -\kappa \frac{\partial T}{\partial x_i} \quad (1.32)$$

where  $\kappa$  is the coefficient of thermal conductivity. This law has been verified by kinetic theory in one of its most celebrated results [Vincenti and Kruger, 1965]. Similar to the fluid viscosity, the thermal conductivity is a function of temperature and pressure. Note that, contrary to what happens in solids where anisotropic behavior may be observed, in fluids the conductivity is typically represented as a scalar due to the inherent isotropy of fluids.

Analytic relations have been proposed by kinetic theory for the thermal conductivity by Sutherland

$$\frac{\kappa}{\kappa_0} = \left( \frac{T}{T_0} \right)^{3/2} \frac{T_0 + S}{T + S} \quad (1.33)$$

Similar to viscosity, a power law can be used to calculate the thermal conductivity for both gases and liquids

$$\frac{\kappa}{\kappa_0} = \left( \frac{T}{T_0} \right)^n \quad (1.34)$$

Another approach that is frequently used to compute the coefficient of thermal conductivity relies on the use of the Prandtl number

$$Pr = \frac{\mu C_p}{\kappa} \quad (1.35)$$

If the viscosity coefficient, the Prandtl number, and the heat capacity at constant pressure ( $C_p$ ) are known, it is possible to obtain the thermal conductivity coefficient.

### *Equation of State*

Thermodynamics provides the final set of relations required to complete the Navier-Stokes equations. The first law of thermodynamics can be stated in the following form

$$dE = dQ + dW \quad (1.36)$$

where  $dE$  is the change in total energy of the system,  $dQ$  is the heat added to the system, and  $dW$  is the work done on the system. The heat and work can be defined in terms of thermodynamic variables as

$$dW = -pdV \quad (1.37)$$

$$dQ = Tds \quad (1.38)$$

where  $V$  is the volume, and  $S$  is the entropy. Using these definition and expressing the results in terms of a unit mass basis the first law of thermodynamics can be written as

$$de = Tds + \frac{p}{\rho^2}d\rho \quad (1.39)$$

This implies

$$e = e(s, \rho) \quad (1.40)$$

so that only one relationship is required to the define the thermodynamic state of the substance.

Using the fact that

$$de = \frac{\partial e}{\partial s}ds + \frac{\partial e}{\partial \rho}d\rho \quad (1.41)$$

and by comparing Eq.(1.39) and Eq.(1.41), the following relation can be obtained

$$T = \left. \frac{\partial e}{\partial s} \right|_{\rho} \quad p = \rho^2 \left. \frac{\partial e}{\partial \rho} \right|_s \quad (1.42)$$

The enthalpy can be defined as

$$h = e + \frac{p}{\rho} \quad (1.43)$$

which can be used to rewrite the first law in the following way

$$dh = Tds + \frac{1}{\rho} dp \quad (1.44)$$

which similarly defines an equation of state of the following form

$$h = h(s, p) \quad (1.45)$$

from which the other properties can be calculated

$$T = \left. \frac{\partial h}{\partial s} \right|_p, \quad \frac{1}{\rho} = \left. \frac{\partial h}{\partial p} \right|_s \quad (1.46)$$

The specific heats are important thermodynamic properties, and they are defined as

Specific heat at constant pressure

$$C_p = \left. \frac{\partial h}{\partial T} \right|_p \quad (1.47)$$

Specific heat at constant volume

$$C_v = \left. \frac{\partial e}{\partial T} \right|_v \quad (1.48)$$

The ratio of the specific heats is another important thermodynamic relation and is defined as

$$\gamma = \frac{C_p}{C_v} \quad (1.49)$$

When the internal energy and enthalpy depend only on temperature (known as calorically perfect) they can be computed as

$$h = C_p T \quad (1.50)$$

$$e = C_v T. \quad (1.51)$$

relative to a zero temperature reference state.

### *Ideal Gas*

For ideal gases, kinetic theory has shown that the pressure can be computed from a simple equation of state

$$p = (\gamma - 1)\rho e. \quad (1.52)$$

## 2 Low-Mach Flows

In this chapter, the development of the low-Mach acoustically-filtered Navier-Stokes equations is presented. These equations are applicable to flow problems where large density variations are of interest and the energy contained in acoustic waves is negligible relative to the advective waves.

### Low-Mach Equations

The level of compressibility of a flow is usually measured based on its Mach number  $Ma$ , which is defined as the ratio between the flow velocity ( $v$ ) and the speed of sound of the fluid.

$$Ma = \frac{v}{c} \quad (2.1)$$

In the low-Mach number regime, where  $Ma \rightarrow 0$ , both the continuity (1.4) and momentum (1.5) equations are still valid, however, the energy equation (1.10) can be simplified based on dimensional analysis. The following non-dimensional variables are used in the ensuing analysis

$$t = \frac{L}{v_0} t^* \quad (2.2)$$

$$h = C_p T_0 h^* \quad (2.3)$$

$$v_i = v_0 v_i^* \quad (2.4)$$

$$q_i = \frac{\kappa T_0}{L} q_i^* \quad (2.5)$$

$$\tau_{ij} = \frac{\mu v_0}{L} \tau_{ij}^* \quad (2.6)$$

$$p = \rho_0 v_0^2 p^* \quad (2.7)$$

$$\rho = \rho_0 \rho^* \quad (2.8)$$

where  $v_0$ ,  $T_0$ , and  $\rho_0$  are the reference velocity, temperature and density respectively. Then, by substituting the previous definitions in Eq.(1.10), the energy equation can be written as

$$\begin{aligned} \frac{\rho_0 C_p T_0 v_0}{L} \left( \frac{\partial \rho^* h^*}{\partial t^*} + \frac{\partial}{\partial x_j^*} (\rho^* v_j^* h^*) \right) &= - \frac{\kappa T_0}{L^2} \frac{\partial q_j^*}{\partial x_j^*} + \frac{\mu v_0^2}{L^2} \tau_{ij}^* \frac{\partial v_i^*}{\partial x_j^*} \\ &+ \frac{\rho_0 v_0^3}{L} \left( \frac{\partial p^*}{\partial t^*} + v_j^* \frac{\partial p^*}{\partial x_j^*} \right) + q''' \end{aligned} \quad (2.9)$$

Rearranging terms,

$$\begin{aligned} \frac{\partial \rho^* h^*}{\partial t^*} + \frac{\partial}{\partial x_j^*} (\rho^* v_j^* h^*) &= - \frac{1}{Pr Re} \frac{\partial q_j^*}{\partial x_j^*} + \frac{Ma^2 (\gamma - 1)}{Re} \tau_{ij}^* \frac{\partial v_i^*}{\partial x_j^*} \\ &+ Ma^2 (\gamma - 1) \left( \frac{\partial p^*}{\partial t^*} + v_j^* \frac{\partial p^*}{\partial x_j^*} \right) + \frac{L}{\rho_0 C_p T_0 v_0} q''' \end{aligned} \quad (2.10)$$

where  $Pr = C_p \mu / \kappa$  is the Prandtl number and  $Re = \rho v L / \mu$  is the Reynolds number. Therefore, for low-Mach number flows  $Ma \rightarrow 0$  the viscous dissipation and the material derivative of pressure ( $\frac{\partial p}{\partial t} + v_j \frac{\partial p}{\partial x_j}$ ) can be neglected compared to the heat conduction, advection, and rate terms. The source terms may or may not be neglected depending on their definition. Consequently, the energy equation used in low-Mach number flows is

$$\frac{\partial \rho h}{\partial t} + \frac{\partial}{\partial x_j} (\rho v_j h) = - \frac{\partial q_j}{\partial x_j} + q''' \quad (2.11)$$

In terms of temperature for a calorically perfect fluid [White, 1991], the energy equation is

$$\frac{\partial \rho C_p T}{\partial t} + \frac{\partial}{\partial x_j} (\rho v_j C_p T) = - \frac{\partial q_j}{\partial x_j} + q''' \quad (2.12)$$

## 3 Incompressible Flows

This chapter presents the incompressible Navier-Stokes equations in stress-divergence form along with a complete description of initial and boundary conditions. The conservation equations are presented first in indicial notation, and followed by a presentation using vector notation in §3.2.

### *Conservation Equations – Indicial Form*

In the ensuing discussion, the incompressible Navier-Stokes equations with concomitant initial and boundary conditions are presented in indicial notation. The reader may refer to Gresho and Sani [Gresho and Sani, 1998, pp. 357 – 359] for an overview of notation for the Navier-Stokes equations.

#### *Mass Conservation*

The mass conservation principle in divergence form is

$$\frac{\partial \rho}{\partial t} + \frac{\partial(\rho v_j)}{\partial x_j} = 0. \quad (3.1)$$

In the incompressible limit, the velocity field is solenoidal,

$$\frac{\partial v_i}{\partial x_i} = 0 \quad (3.2)$$

which implies a mass density transport equation,

$$\frac{\partial \rho}{\partial t} + v_j \frac{\partial \rho}{\partial x_j} = 0. \quad (3.3)$$

This form of the mass density transport is useful in multi-fluid volume-tracking applications with a solenoidal velocity condition [The Truchas Team, 2003].

For pure incompressible single-fluid flows, the density remains constant both in time and space and Eq. (3.3) is neglected with Eq. (3.2) remaining as a constraint on the velocity field.

### Momentum Conservation

The conservation of linear momentum is

$$\rho \frac{\partial v_i}{\partial t} + \rho v_j \frac{\partial v_i}{\partial x_j} = \frac{\partial \sigma_{ij}}{\partial x_j} + \rho f_i \quad (3.4)$$

where  $v_i$  is the velocity,  $\sigma_{ij}$  is the stress tensor,  $\rho$  is the mass density, and  $f_i$  is the body force. The body force contribution  $\rho f_i$  typically accounts for buoyancy forces with  $f_i$  representing the acceleration due to gravity.

The stress may be written in terms of the fluid pressure and the deviatoric stress tensor as

$$\sigma_{ij} = -p\delta_{ij} + \tau_{ij} \quad (3.5)$$

where  $p$  is the pressure,  $\delta_{ij}$  is the Kronecker delta, and  $\tau_{ij}$  is the deviatoric stress tensor. A constitutive equation relates the deviatoric stress and the strain rate, e.g.,

$$\tau_{ij} = 2\mu S_{ij}. \quad (3.6)$$

The strain-rate tensor is written in terms of the velocity gradients as

$$S_{ij} = \frac{1}{2} \left( \frac{\partial v_i}{\partial x_j} + \frac{\partial v_j}{\partial x_i} \right). \quad (3.7)$$

### Energy Conservation

An analysis of the implication of incompressibility on the energy equation follows the same dimensional analysis performed in the low-Mach formulation discussed in Chapter 2 with the exception that  $Ma = 0$ . Therefore, the viscous dissipation and the material derivative of the pressure are neglected. Consequently equation (2.12) is used also in the development of the incompressible equations and repeated here completeness.

The energy equation may be expressed in terms of temperature,  $T$ , as

$$\frac{\partial \rho C_p T}{\partial t} + \frac{\partial}{\partial x_j} (\rho v_j C_p T) = -\frac{\partial q_j}{\partial x_j} + q''' \quad (3.8)$$

where  $C_p$  is the specific heat at constant pressure,  $q_i$  is the diffusional heat flux rate, and  $q'''$  represents volumetric heat sources and sinks, e.g., due to exothermic/endothermic chemical reactions. Fourier's law relates the heat flux rate to the temperature gradient and thermal conductivity

$$q_i = -\kappa \frac{\partial T}{\partial x_i} \quad (3.9)$$

where  $\kappa_{ij}$  is the thermal conductivity.



### Boundary and Initial Conditions

The prescription of boundary conditions is based on a flow domain with boundaries that are either physical or implied for the purposes of performing a simulation. A simple flow domain is shown in Figure 3.1 where the boundary of the domain is  $\Gamma = \Gamma_1 \cup \Gamma_2$ .

The momentum equations, Eq. (3.4), are subject to boundary conditions that consist of specified velocity on  $\Gamma_1$  as in Eq. (3.10) or traction boundary conditions on  $\Gamma_2$  as in Eq. (3.12).

$$v_i(x_i, t) = \hat{v}_i(x_i, t) \text{ on } \Gamma_1 \quad (3.10)$$

In the case of a no-slip and no-penetration boundary,  $v_i = 0$  is the prescribed velocity boundary condition. The prescribed traction boundary conditions are

$$\sigma_{ij}n_j = \hat{f}_i(x_i, t) \text{ on } \Gamma_2 \quad (3.11)$$

where  $n_j$  is the outward normal for the domain boundary, and  $\hat{f}_i$  are the components of the prescribed traction. In terms of the pressure and strain-rate, the traction boundary conditions are

$$\{-p\delta_{ij} + 2\mu S_{ij}\} n_j = \hat{f}_i(x_i, t) \text{ on } \Gamma_2. \quad (3.12)$$

The traction and velocity boundary conditions can be mixed. In a two-dimensional sense, mixed boundary conditions can consist of a prescribed normal traction and a tangential velocity. For example, at the outflow boundary in Figure 3.1, a homogeneous normal traction and vertical velocity on  $\Gamma_2$  constitute a valid set of mixed boundary conditions. A detailed discussion of boundary conditions for the incompressible Navier-Stokes equations may be found in Gresho and Sani [Gresho and Sani, 1998].

The boundary conditions for the energy equation, Eq. (3.8), consist of a prescribed temperature or heat flux rate. The prescribed temperature is

$$T(x_i, t) = \hat{T}(x_i, t) \quad (3.13)$$

and the prescribed heat flux rate is

$$-\kappa_{ij} \frac{\partial T}{\partial x_j} n_i = \hat{q}(x_i, t) \quad (3.14)$$

where  $\hat{q}$  is the known flux rate through the boundary with normal  $n_i$ . The heat flux rate may also be prescribed in terms of a heat transfer coefficient,

$$-\kappa_{ij} \frac{\partial T}{\partial x_j} n_i = h(T - T_\infty) \quad (3.15)$$

where  $h$  is the heat transfer coefficient and  $T_\infty$  is a reference temperature.

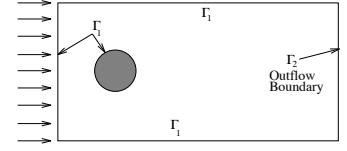


Figure 3.1: Flow domain for conservation equations.

Initial conditions take on the form of prescribed velocity, species, and temperature distributions at  $t = 0$ , i.e.,

$$\begin{aligned} v_i(x_i, 0) &= v_i^0(x_i) \\ T(x_i, 0) &= T^0(x_i). \end{aligned} \quad (3.16)$$

*Remark*

For a well-posed incompressible flow problem, the prescribed initial velocity field in Eq.(3.16) must satisfy Eq.(3.17)-(3.18) (see Gresho and Sani[Gresho and Sani, 1987]). If  $\Gamma_2 = 0$  (the null set, i.e., enclosure flows with  $n_i v_i$  prescribed on all surfaces), then global mass conservation enters as an additional solvability constraint, as shown in Eq.(3.19).

$$\frac{\partial v_i}{\partial x_i} = 0 \quad (3.17)$$

$$n_i v_i(x_i, 0) = n_i v_i^0(x_i) \quad (3.18)$$

$$\int_{\Gamma} n_i v_i^0 d\Gamma = 0 \quad (3.19)$$

*Conservation Equations – Vector Form*

In the ensuing discussion, the invariant bold-face vector notation of Gibbs is used with **boldface** symbols representing vector/tensor quantities. The reader may refer to Gresho and Sani [Gresho and Sani, 1998, pp. 357 – 359] for an overview of notation for the Navier-Stokes equations.

*Mass Conservation*

The mass conservation principle in divergence form is

$$\frac{\partial \rho}{\partial t} + \nabla \cdot (\rho \mathbf{v}) = 0. \quad (3.20)$$

In the incompressible limit, the velocity field is solenoidal,

$$\nabla \cdot \mathbf{v} = 0 \quad (3.21)$$

which implies a mass density transport equation,

$$\frac{\partial \rho}{\partial t} + \mathbf{v} \cdot \nabla \rho = 0. \quad (3.22)$$

For constant density, Eq. (3.22) is neglected with Eq. (3.21) remaining as a constraint on the velocity field.

### Momentum Conservation

To begin, the conservation of linear momentum is

$$\rho \left\{ \frac{\partial \mathbf{v}}{\partial t} + \mathbf{v} \cdot \nabla \mathbf{v} \right\} = \nabla \cdot \boldsymbol{\sigma} + \rho \mathbf{f} \quad (3.23)$$

where  $\mathbf{v} = (v_x, v_y, v_z)$  is the velocity,  $\boldsymbol{\sigma}$  is the stress tensor,  $\rho$  is the mass density, and  $\mathbf{f}$  is the body force. The body force contribution  $\rho \mathbf{f}$  typically accounts for buoyancy forces with  $\mathbf{f}$  representing the acceleration due to gravity.

The stress may be written in terms of the fluid pressure and the deviatoric stress tensor as

$$\boldsymbol{\sigma} = -p\mathbf{I} + \boldsymbol{\tau} \quad (3.24)$$

where  $p$  is the pressure,  $\mathbf{I}$  is the identity tensor, and  $\boldsymbol{\tau}$  is the deviatoric stress tensor. A constitutive equation relates the deviatoric stress and the strain

$$\boldsymbol{\tau} = 2\mu\mathbf{S}. \quad (3.25)$$

The strain-rate tensor is written in terms of the velocity gradients as

$$\mathbf{S} = \frac{1}{2} \left( \nabla \mathbf{v} + (\nabla \mathbf{v})^T \right). \quad (3.26)$$

### Energy Conservation

The conservation of energy is expressed in terms of temperature,  $T$ , as

$$\rho C_p \left\{ \frac{\partial T}{\partial t} + \mathbf{v} \cdot \nabla T \right\} = -\nabla \cdot \mathbf{q} + \dot{q}''' \quad (3.27)$$

where  $C_p$  is the specific heat at constant pressure,  $\mathbf{q}$  is the diffusional heat flux rate, and  $\dot{q}'''$  represents volumetric heat sources and sinks, e.g., due to exothermic/endothermic chemical reactions. Fourier's law relates the heat flux rate to the temperature gradient and thermal conductivity

$$\mathbf{q} = -\kappa \nabla T \quad (3.28)$$

where  $\kappa$  is the thermal conductivity.

### Boundary and Initial Conditions

The prescription of boundary conditions is based on a flow domain with boundaries that are either physical or implied for the purposes of performing a simulation. A simple flow domain is shown in Figure 3.1 where the boundary of the domain is  $\Gamma = \Gamma_1 \cup \Gamma_2$ .

The momentum equations, Eq. (3.23), are subject to boundary conditions that consist of specified velocity on  $\Gamma_1$  as in Eq. (3.29) or traction boundary conditions on  $\Gamma_2$  as in Eq. (3.31).

$$\mathbf{v}(\mathbf{x}, t) = \hat{\mathbf{v}}(\mathbf{x}, t) \text{ on } \Gamma_1 \quad (3.29)$$

In the case of a no-slip and no-penetration boundary,  $\mathbf{v} = 0$  is the prescribed velocity boundary condition.

The prescribed traction boundary conditions are

$$\boldsymbol{\sigma} \cdot \mathbf{n} = \hat{\mathbf{f}}(\mathbf{x}, t) \text{ on } \Gamma_2 \quad (3.30)$$

where  $\mathbf{n}$  is the outward normal for the domain boundary, and  $\hat{\mathbf{f}}$  are the components of the prescribed traction. In terms of the pressure and strain-rate, the traction boundary conditions are

$$\{-p\mathbf{I} + 2\mu\mathbf{S}\} \cdot \mathbf{n} = \hat{\mathbf{f}}(\mathbf{x}, t) \text{ on } \Gamma_2. \quad (3.31)$$

The traction and velocity boundary conditions can be mixed. In a two-dimensional sense, mixed boundary conditions can consist of a prescribed normal traction and a tangential velocity. For example, at the outflow boundary in Figure 3.1, a homogeneous normal traction and vertical velocity on  $\Gamma_2$  constitute a valid set of mixed boundary conditions. A detailed discussion of boundary conditions for the incompressible Navier-Stokes equations may be found in Gresho and Sani [Gresho and Sani, 1998].

The boundary conditions for the energy equation, Eq. (3.8), consist of a prescribed temperature or heat flux rate. The prescribed temperature is

$$T(\mathbf{x}, t) = \hat{T}(\mathbf{x}, t) \quad (3.32)$$

and the prescribed heat flux rate is

$$-\kappa \nabla T \cdot \mathbf{n} = \hat{q}(\mathbf{x}, t) \quad (3.33)$$

where  $\hat{q}$  is the known flux rate through the boundary with normal  $\mathbf{n}$ . The heat flux rate may also be prescribed in terms of a heat transfer coefficient,

$$-\kappa \nabla T \cdot \mathbf{n} = h(T - T_\infty) \quad (3.34)$$

where  $h$  is the heat transfer coefficient, and  $T_\infty$  is a reference temperature.

Initial conditions take on the form of prescribed velocity, species, and temperature distributions at  $t = 0$ , i.e.,

$$\begin{aligned} \mathbf{v}(\mathbf{x}, 0) &= \mathbf{v}^0(\mathbf{x}) \\ T(\mathbf{x}, 0) &= T^0(\mathbf{x}). \end{aligned} \quad (3.35)$$

*Remark*

For a well-posed incompressible flow problem, the prescribed initial velocity field in equation (3.35) must satisfy equations (3.36) and (3.37) (see Gresho and Sani[Gresho and Sani, 1987]). If  $\Gamma_2 = \emptyset$  (the null set, i.e., enclosure flows with  $\mathbf{n} \cdot \mathbf{v}$  prescribed on all surfaces), then global mass conservation enters as an additional solvability constraint as shown in equation (3.38).

$$\nabla \cdot \mathbf{v}^0 = 0 \quad (3.36)$$

$$\mathbf{n} \cdot \mathbf{v}(\mathbf{x}, 0) = \mathbf{n} \cdot \mathbf{v}^0(\mathbf{x}) \quad (3.37)$$

$$\int_{\Gamma} \mathbf{n} \cdot \mathbf{v}^0 d\Gamma = 0 \quad (3.38)$$



## 4 *Multicomponent Flows*

Many industrial flows are not homogeneous and involve multiple constituent fluids that may range from completely miscible to completely immiscible with sharp interfaces. In the following, we adopt the terminology of Drew and Passman [Drew and Passman, 1998] and refer to these as multicomponent flows. Specific examples of multicomponent flows considered here include multispecies flows that are comprised of completely miscible materials. In contrast, multifluid flows typically involve immiscible fluids with a countable number of sharp interfaces where techniques such as interface or volume tracking is a viable computational approach. Finally, multiphase flows may involve a large number of gas bubbles in a continuous liquid, or conversely droplets in a continuous gas. The possibilities for multiphase flows are extremely diverse and encompasses everything from mists to annular, slug and bubbly flows.

### *Multispecies Flows*

#### *Mass Conservation*

The mass conservation principle in divergence form is

$$\frac{\partial \rho}{\partial t} + \frac{\partial(\rho v_j)}{\partial x_j} = 0. \quad (4.1)$$

In the incompressible limit, the velocity field is solenoidal,

$$\frac{\partial v_i}{\partial x_i} = 0 \quad (4.2)$$

which implies a mass density transport equation,

$$\frac{\partial \rho}{\partial t} + v_j \frac{\partial \rho}{\partial x_j} = 0. \quad (4.3)$$

For constant density, Eq. (4.3) is neglected with Eq. (4.2) remaining as a constraint on the velocity field.

In general, species transport is considered in terms of mass concentrations  $Z_1, Z_2, \dots$  for an arbitrary number of species. In order to

simplify the presentation, a single mass fraction is presented representing a binary mixture. Mass conservation applied to one species yields for  $Z_1$

$$\rho \frac{\partial Z_1}{\partial t} + \rho v_i \frac{\partial Z_1}{\partial x_i} = -\frac{\partial J_{1i}}{\partial x_i} + \dot{m}_1 \quad (4.4)$$

where  $J_{1i}$  is the diffusional mass flux rate, and  $\dot{m}_1$  is a volumetric mass source. The mass source may include the injection of mass concentration from a boundary or the source/sink terms from chemical reactions.

The diffusional mass flux rate is based on Fick's law of diffusion,

$$J_{1i} = -\rho \mathcal{D}_{1ij} \frac{\partial Z_1}{\partial x_j} \quad (4.5)$$

where  $\mathcal{D}_{1ij}$  is a tensorial mass diffusivity. Typically, mass diffusivities are only available as scalars so that

$$J_{1i} = -\rho \mathcal{D}_1 \frac{\partial Z_1}{\partial x_i}. \quad (4.6)$$

In the most general form, the species concentration transport equations are

$$\rho \frac{\partial Z_I}{\partial t} + \rho v_i \frac{\partial Z_I}{\partial x_i} = -\frac{\partial J_{Ii}}{\partial x_i} + \dot{m}_I \quad (4.7)$$

where  $I$  indicates the mass concentration, i.e.,  $I = 1, 2, \dots, 10$ .

Turning attention to the species transport equations, boundary conditions for Eq. (4.4) may consist of either a prescribed concentration or a mass flux rate. In the binary mixture example, the prescribed concentration is

$$Z_1(x_i, t) = \hat{Z}_1(x_i, t) \quad (4.8)$$

where  $\hat{Z}_1$  is the known value of concentration for species 1. The prescribed mass flux rate is

$$-\rho \mathcal{D}_{1ij} \frac{\partial Z_1}{\partial x_j} n_i = \hat{f}_1(x_i, t) \quad (4.9)$$

where  $\hat{f}_1(x_i, t)$  is the known mass flux rate through the boundary with normal  $n_i$ . The prescribed flux rate may also be specified in terms of a mass transfer coefficient as

$$-\rho \mathcal{D}_{1ij} \frac{\partial Z_1}{\partial x_j} n_i = h_{\mathcal{D}_\infty} (Z_1 - Z_{1\infty}) \quad (4.10)$$

where  $h_{\mathcal{D}_\infty}$  is the mass transfer coefficient and  $Z_{1\infty}$  is a reference species concentration.



*Mass Conservation – Vector Form*

The mass conservation principle in divergence form is

$$\frac{\partial \rho}{\partial t} + \nabla \cdot (\rho \mathbf{v}) = 0. \quad (4.11)$$

In the incompressible limit, the velocity field is solenoidal,

$$\nabla \cdot \mathbf{v} = 0 \quad (4.12)$$

which implies a mass density transport equation,

$$\frac{\partial \rho}{\partial t} + \mathbf{v} \cdot \nabla \rho = 0. \quad (4.13)$$

For constant density, Eq. (4.13) is neglected with Eq. (4.12) remaining as a constraint on the velocity field.

In general, species transport is considered in terms of mass concentrations  $Z_1, Z_2, \dots$  for an arbitrary number of species. In order to account for the change in mass concentration, mass conservation applied to the individual species yields for  $Z_1$

$$\rho \frac{\partial Z_1}{\partial t} + \rho \mathbf{v} \cdot \nabla Z_1 = -\nabla \cdot \mathbf{J}_1 + \dot{m}_1 \quad (4.14)$$

where  $\mathbf{J}_1$  is the diffusional mass flux rate and  $\dot{m}_1$  is a volumetric mass source. The mass source may include the injection of mass concentration from a boundary or the source/sink terms from chemical reactions.

The diffusional mass flux rate is based on Fick's law of diffusion,

$$\mathbf{J}_1 = -\rho \mathbf{D}_1 \nabla Z_1 \quad (4.15)$$

where  $\mathbf{D}_1$  is a tensorial mass diffusivity. Typically, mass diffusivities are only available as scalars so that

$$\mathbf{J}_1 = -\rho \mathcal{D}_1 \nabla Z_1. \quad (4.16)$$

In the most general form, the species concentration transport equations are

$$\rho \frac{\partial Z_I}{\partial t} + \rho \mathbf{v} \cdot \nabla Z_I = -\nabla \cdot \mathbf{J}_I + \dot{m}_I \quad (4.17)$$

where  $I$  indicates the species mass concentration, i.e.,  $I = 1, 2, \dots, 10$ .

Turning attention to the species transport equations, boundary conditions for Eq. (4.4) may consist of either a prescribed concentration or a mass flux rate. In the binary mixture example, the prescribed concentration is

$$Z_1(\mathbf{x}, t) = \hat{Z}_1(\mathbf{x}, t) \quad (4.18)$$

where  $\hat{Z}_1$  is the known value of concentration for species 1. The prescribed mass flux rate is

$$-\rho \mathbf{D}_1 \nabla Z_1 \cdot \mathbf{n} = \hat{J}_1(\mathbf{x}, t) \quad (4.19)$$

where  $\hat{f}_1(\mathbf{x}, t)$  is the known mass flux rate through the boundary with normal  $\mathbf{n}$ . The prescribed flux rate may also be specified in terms of a mass transfer coefficient as

$$-\rho \mathbf{D}_1 \nabla Z_1 \cdot \mathbf{n} = h_{\mathcal{D}_\infty} (Z_1 - Z_{1_\infty}) \quad (4.20)$$

where  $h_{\mathcal{D}_\infty}$  is the mass transfer coefficient and  $Z_{1_\infty}$  is a reference species concentration.

### *Multifluid Flows*

Following the formulation presented in [Schofield et al., 2010, Schofield and Christon, 2010] (see also [The Truchas Team, 2003]), the governing equations for variable-density incompressible viscous flow are

$$\rho \left( \frac{\partial \mathbf{u}}{\partial t} + \mathbf{u} \cdot \nabla \mathbf{u} \right) = -\nabla p + \nabla \cdot (\mu \nabla \mathbf{u}) + \rho \mathbf{g}, \quad (4.21)$$

$$\nabla \cdot \mathbf{u} = 0, \quad (4.22)$$

where  $\mathbf{u}$  is the velocity,  $\rho$  the density,  $\mu$  is the viscosity,  $p$  is the pressure, and  $\mathbf{g}$  the gravitational force. Here  $\rho$  and  $\mu$  vary in space and time. To close the system of equations (4.21) - (4.22), evolution or state equations are required for  $\rho$  and  $\mu$ . These may be advection equations or relationships between  $\rho$  and  $\mu$  and chemical concentrations.

In the case of volume-of-fluid methods (aka, volume-tracking methods), the volume fraction of each fluid in a computational cell is tracked rather than tracking the density (or viscosity) directly. The volume fraction is defined as the ratio of the volume of a material relative to the cell volume. That is, in a computational cell,  $\mathcal{C}_i$  with volume  $\Omega_i$ , the volume fraction,  $\mathcal{F}_k$ , of material  $k$  with volume,  $V_k$  is defined as

$$\mathcal{F}_k(\Omega_i) = \frac{V_k}{\Omega_i}. \quad (4.23)$$

By construction, in any computational cell

$$\sum_{k=1}^{N_m} \mathcal{F}_k(V_i) = 1, \quad (4.24)$$

where  $N_m$  is the number of materials in the simulation.

In the finite element discretization, each element is used as a control volume. The density in an element is given as

$$\bar{\rho} = \sum_{k=1}^{N_m} \mathcal{F}_k \rho_k \quad (4.25)$$

where  $\mathcal{F}_k$  and  $\rho_k$  are respectively the volume fraction and density of material  $k$ . Following [Ferziger, 2003], the element average viscosity is

computed as

$$\bar{\mu} = \left( \sum_{k=1}^{N_m} \frac{\mathcal{F}_k}{\mu_k} \right)^{-1} \quad (4.26)$$

The volume fractions evolve according to the set of advection equations,

$$\frac{\partial \mathcal{F}_k}{\partial t} + \mathbf{u} \cdot \nabla \mathcal{F}_k = 0 \quad k = 1, \dots, N_m. \quad (4.27)$$

Numerical methods for the solution of Eq. (4.21)-(4.22) with continuous density evolved by an advection equation have been presented by a number of authors [Almgren et al., 1998, Bell and Marcus, 2002, Calgareo et al., 2008, Fraigneau et al., 2001, Guermond and Quartapelle, 2000, Liu and Walkington, 2007, Pyo and Shen, 2007] and a theoretical treatment of the equations is presented by Danchin [Danchin, 2003]. Additional methods and results have been presented for simulations utilizing level sets [Li and Abdou, 2003] and volume tracking [Rudman, 1998, Puckett et al., 1997].

The numerical method used here for the simulation of Eq. (4.21)-(4.22) is a projection method similar to the method of Christon and Patil [Christon and Patil, 2005] and used by Schofield, et al. [Schofield et al., 2010, Schofield and Christon, 2010]

### *Multiphase Flows*

Multiphase flows span a broad range of regimes that vary from mists to annular, slug and bubbly flows and may be laminar or turbulent. Before proceeding with a discussion of the conservation equations, averaging and concomitant closure models, a historical review of some relevant work is presented.

Sha and Soo (1979) [Shaw and Soo, 1979] present a brief summary of the effects of including the forces due to the interaction of the static pressure  $p$  and the volume fraction  $\alpha_k$ . Known as the  $p\nabla\alpha_k$  term, different investigators have disagreed on the effects of including this term in the momentum equations. Most recently, Chang and Liou (2007) [Chang and Liou, 2007] have pointed out the importance of this term in the limiting case of a constant pressure-velocity steady-flow flow. In the work by Sha and Soo [Shaw and Soo, 1979], they suggest including a parameterized variant of the pressure gradient term

$$\nabla p \alpha_k = \alpha_k \nabla p + (1 - B_k) p \nabla \alpha_k \quad (4.28)$$

where  $B_k$  depends on particle size, fluid properties, flow characteristics, etc. They present evidence supporting the need for a full range of  $0 \leq B_k \leq 1$ .

The issue of ill-posed multiphase formulations, where each fluid is inviscid, was first identified in the work by Stewart and Wendroff

(1984) [Stewart and Wendroff, 1984]. This work considered the so-called 6-equation model and showed that it is ill-posed, i.e., the flux Jacobian possesses imaginary eigenvalues. In the presence of interfacial drag, they show that under certain conditions, the discrete system may be unstable. In contrast, they suggest that, in the presence of damping terms, i.e., interfacial drag, viscosity, etc., that there is a range of parameters where the solution will remain stable. That is when the spatial resolution is not too small relative to the physical damping mechanisms.

Besnard and Harlow (1988) [Besnard and Harlow, 1988] presents a two-field turbulence model that considers the turbulence in both fields present. The damping due to the presence of particles is considered, and the work includes a theoretical derivation of the turbulent kinetic energy due to particle drag.

Bestion (1990) [Bestion, 1990] presents the physical closure models used in the CATHARE code. CATHARE is a two-dimensional thermal-hydraulic code for simulating the flow conditions present in primary and secondary circuits of pressurized water reactors. Although CATHARE is a two-dimensional code, the closure models are essentially one-dimensional in nature and of limited use for development of a three-dimensional simulation capability.

Kashiwa, et al. (1993) [Kashiwa et al., 1993] discuss the implicit continuous-fluid Eulerian (ICE) method for multiphase flows. ICE relies on a Lagrangian-remap formalism and results in unconditional stability in terms of the material sound speed. The ICE algorithm is a pressure-based solution method, and suggests the possibility of using projection methods in a pure Eulerian solution method.

In a subsequent report, Kashiwa and Rauenzahn (1994) [Kashiwa and Rauenzahn, 1994] present an multimaterial formalism that encompasses many of the ideas present in the so-called “four-field, two-phase” formulations. Here, the exact ensemble averaged conservation equations are derived, and the resulting equations are shown to be well-posed for a forward in time numerical solution method. In this work, a single pressure model is assumed for the particle-fluid systems considered, and justified in the limit of a solenoidal velocity field  $\nabla \cdot \mathbf{v}$ . The resulting conservation equations are presented summarized in tabular form and shown to be comparable to many of the current multifield formulations, e.g., Lahey [R. T. Lahey, 2009].

A second-order accurate solution method based on high-resolution methods is presented by Tiselj and Petelin (1997) [Tiselj and Petelin, 1997]. Here, the two-fluid model is based on the RELAP5 code which is a six equation one-dimensional model. A splitting technique is used to treat source terms with second-order accuracy, and the final method is applied to a two-phase shock tube.

The question of well-posedness for the two-fluid multiphase flows was considered by Song and Ishii (2000) [Song and Ishii, 2000]. Here, a characteristic analysis for the governing equations for a one-dimensional two-fluid model was considered. They show that the two-fluid model is stable for relatively broad range of momentum flux parameters that render the one-dimensional model strictly hyperbolic, albeit for one-dimensional problems. In subsequent work, Song (2003) [Song, 2003] demonstrates the application of the momentum flux parameters for two-phase channel flow. Here, the momentum flux parameters are based on the void function, wave number, drag coefficient and relative velocity between phases.

The FLICA-4 code is presented by Toumi, et al. (2000) [Toumi et al., 2000]. The solution procedure is based on an extension of Roe's approximate Riemann solver and use of Newton's method for the solution of the coupled non-linear system of equations. A full-core simulation for a pressurized water reactor is presented.

The work by Černe, Petelin and Tiselj (2001) [Černe et al., 2001] presents a hybrid volume-tracking/two-fluid model for two-phase flow. In regions where the grid resolution is sufficient to reconstruct sharp interfaces, the two-phase problem is handled with the volume-of-fluid method. In regions where there is insufficient resolution to represent the interface, a two-fluid model is used. Of particular interest is the development of the criteria for transition from volume-tracking model to a dispersed two-phase representation.

Lahey and Drew (2001) [R. T. Lahey and Drew, 2001] develop a multidimensional four-field, two-fluid model and apply it to a series of problems where experimental data is available. The four-field model is considered desirable because it naturally handles continuous vapor, continuous liquid, dispersed vapor, and dispersed liquid. The test cases presented in this work are suitable for the development and validation of a two-phase flow implementation.

Andrianov's Ph.D. thesis (2003) [Andrianov, 2003] uses a modified Roe flux to solve the fully compressible multiphase system of equations. Here, the application is deflagration-to-detonation. The formulation and solution methods appear to be better suited to reactor accident scenarios.

In 2003, Yadigaroglu [Yadigaroglu, 2003] proposed the term "CMFD" for computational multiphase fluid dynamics in a letter to the editor of the International Journal of Multiphase Flow. To date, the CFD community has not embraced this terminology – for obvious reasons. Related to Yadigaroglu's letter, the paper by Balachandar and Properetti (2005) [Balachandar and Properetti, 2005] presents a brief summary of the computational approaches to disperse multiphase flow.

Staedtke, et al. (2005) [Staedtke et al., 2005] summarize the status

of the ASTAR project. A detailed presentation of the conservation equations and associated closure models is presented. In this work, a number of representative test problems are presented. The focus is primarily on compressible solution techniques, i.e., density-based methods, that include residual distribution and AUSM.

Chang and Liou (2007) [Chang and Liou, 2007] present a single-pressure formulation with the AUSM<sup>+</sup> scheme for multiphase stratified flows. Of particular interest here is the treatment of the pressure gradient in the momentum equations where a consistent treatment is required for correct constant velocity-pressure flows.

Guelfi, et al. (2007) [Guelfi et al., 2007] present an overview of the the NEPTUNE software for thermal-hydraulic computations.

Lahey (2009) [R. T. Lahey, 2009] presents an assessment of closure models in the context of a four-field, two-fluid formulation. Model assessment is conducted using NPHASE [InterPhase Dynamics, 2008a,b, 2010]. This paper also presents an argument for use of the PHASTA code for the so-called DNS of multifluid problems where sharp interfaces are represented by level-sets.

Podowski (2009) [Podowski, 2009] presents an overview of various closure models for multiphase flows with an emphasis on the so-called “mechanistic” modeling. Here, the process of decomposing the momentum source terms into various component forces by superposition is outlined. In addition, a multigroup formulation for representing bubble breakup and coalescence is presented.

In the work by Bestion, et al. (2009) [Bestion et al., 2009], a review of validation data for multiphase CFD codes is presented. The review is presented in the context of the NURESIM integrated project that is focused on developing a standard software platform for nuclear reactor simulations. Here, a number of canonical reactor problems are presented that include departure from nucleate boiling, dry out, etc.

Berry (2010) [Berry, 2010] presents requirements for multiphase flow simulation of light water reactors for the Consortium for Advanced Simulation of Light water reactors (CASL).

The topics of boiling and condensation are presented by Shaver, et al. (2011) [Shaver et al., 2011]. In a related paper, Shaver, et al. (2011) [Shaver et al.] present a validation study using NPHASE and comparing to experimental data for bubbly flow in a cylindrical pipe. Here, the drag, lift, virtual mass and turbulent dispersion forces are defined.

Štrubelj and Tiselj (2011) [Štrubelj and Tiselj, 2011] present a simplified two-phase model that assumes each component velocity is solenoidal, i.e.,  $\nabla \cdot \mathbf{v}_k = 0$ . In this work, a project-like solution algorithm is outlined where the momentum equations are solved in an iterative fashion. Although the algorithm is referred to as a SIMPLE method, the

formulation is presented so that it appears to be a second-order incremental projection method.

### Conservation Equations

This section summarizes the ensemble averaging and resulting conservation equations for multiphase flow. The ensemble averaging and nomenclature follows that used by Drew and Passman [Drew and Passman, 1998].

### Ensemble Average Variables

For multiphase flow, the average is defined in terms of a component indicator

$$X_k(\mathbf{x}, t; \mu) = \begin{cases} 1 & \text{if } \mathbf{x} \in k \text{ in realization } \mu \\ 0 & \text{otherwise} \end{cases} \quad (4.29)$$

with an ensemble average is defined as

$$\bar{\Phi}(\mathbf{x}, t) = \int_{\mathcal{E}} \Phi(\mathbf{x}, t; \mu) dm(\mu) \quad (4.30)$$

where  $dm(\cdot)$  is the density for the measure (probability) on the set of all processes  $\mathcal{E}$ . Reynolds rules of linearity and commutativity apply the ensemble average, and are used to develop the averaged fluid equations of motion.

Here, a short list of some relevant ensemble averaged variables is presented before the phasic conservation equations are discussed.

Volume Fraction:

$$\bar{\alpha}_k = \bar{X}_k \quad (4.31)$$

The ensemble averaged indicator function,  $X_k$  is colloquially referred to as the volume fraction, and represents the volume of phase-k in the total volume. Technically, this is the expected value of a volume of phase-k in a unit volume where  $X_k$  is the indicator function for phase-k.

Interfacial Area Density:

$$\bar{A}_k = -\overline{\mathbf{n}_k \cdot \nabla X_k} \left[ \frac{1}{L} \right] \quad (4.32)$$

Phase Density:

$$\bar{\rho}_k^X = \frac{\bar{X}_k \rho}{\alpha_k} \left[ \frac{M}{L^3} \right] \quad (4.33)$$

Here, the superscript  $X$  indicates that the ensemble average is weighted by the indicator function  $X_k$ .

Mass Source:

$$\overline{\dot{m}}_k = \frac{\overline{\dot{m}_k X_k}}{\alpha_k} \left[ \frac{M}{TL^3} \right] \quad (4.34)$$

Phase Velocity:

$$\overline{\mathbf{v}}_k^X = \frac{\overline{X_k \rho \mathbf{v}_k}}{\alpha_k \overline{\rho_k^X}} \left[ \frac{L}{T} \right] \quad (4.35)$$

Internal Energy:

$$\overline{e}_k^{X\rho} = \frac{\overline{X_k \rho e_k}}{\alpha_k \overline{\rho_k^X}} \left[ \frac{E}{M} \right] \quad (4.36)$$

Here, the superscript  $X\rho$  indicates that the ensemble average is weighted by the indicator function  $X_k$ , and density  $\rho_k$ .

Entropy:

$$\overline{s}_k^{X\rho} = \frac{\overline{X_k \rho s_k}}{\alpha_k \overline{\rho_k^X}} \left[ \frac{E}{M\theta} \right] \quad (4.37)$$

Stress:

$$\overline{\mathbf{T}}_k^{X\rho} = \frac{\overline{X_k \mathbf{T}_k}}{\alpha_k} \left[ \frac{F}{L^2} \right] \quad (4.38)$$

Heat Flux:

$$\overline{\mathbf{q}}_k^{X\rho} = \frac{\overline{X_k \mathbf{q}_k}}{\alpha_k} \left[ \frac{E}{TL^2} \right] \quad (4.39)$$

Here, the averaged heat flux is written in terms of the molecular heat flux  $\mathbf{q}_k$  is

Body Force:

$$\overline{\mathbf{f}}_k^{X\rho} = \frac{\overline{X_k \mathbf{f}_k}}{\alpha_k} \left[ \frac{F}{M} \right] \quad (4.40)$$

Volumetric Energy Source:

$$\overline{Q}_k^{X\rho} = \frac{\overline{X_k Q_k}}{\alpha_k} \left[ \frac{E}{TL^3} \right] \quad (4.41)$$

Interfacial Mass Source:

$$\Gamma_k = \overline{\rho_k e_k (\mathbf{v}_k - \mathbf{v}_{k_i}) \cdot \nabla X_k} \left[ \frac{M}{T \cdot L^3} \right] \quad (4.42)$$

Interfacial Momentum Source:

$$\overline{M}_k^X = -\overline{\mathbf{T}_k \cdot \nabla X_k} \left[ \frac{F}{L^3} \right] \quad (4.43)$$

Interfacial Heat Source:

$$\overline{E}_k^X = \overline{\mathbf{q}_k \cdot \nabla X_k} \left[ \frac{E}{L^3} \right] \quad (4.44)$$



Interfacial Energy Source:

$$\overline{e_{k_i}}\Gamma_k = \overline{\rho_k e_k (\mathbf{v}_k - \mathbf{v}_{k_i}) \cdot \nabla X_k} \left[ \frac{E}{T \cdot L^3} \right] \quad (4.45)$$

Interfacial Work:

$$\overline{W_k^X} = -\overline{\mathbf{T}_k \cdot \mathbf{v}_k \cdot \nabla X_k} \left[ \frac{E}{TL^3} \right] \quad (4.46)$$

### *Ensemble Averaged Conservation Equations*

Dropping the overline, and understanding that the terms correspond to the averaged variables defined above, the averaged continuity equation for phase-k is

$$\frac{\partial \alpha_k \rho_k}{\partial t} + \nabla \cdot (\alpha_k \rho_k \mathbf{v}_k) = \Gamma_k + \alpha_k \dot{m}_k \quad (4.47)$$

where

$$\Gamma_k = \overline{\rho_k (\mathbf{v}_k - \mathbf{v}_{k_i}) \cdot \nabla X_k} \quad (4.48)$$

and  $\mathbf{v}_{k_i}$  is the interfacial velocity for phase-k.

The averaged momentum equation can be written as

$$\frac{\partial \alpha_k \rho_k \mathbf{v}_k}{\partial t} + \nabla \cdot (\alpha_k \rho_k \mathbf{v}_k \mathbf{v}_k) = -\alpha_k \nabla p + \nabla \cdot \left\{ \alpha_k \mu_k (\nabla \mathbf{v}_k + \nabla^T \mathbf{v}_k) \right\} + \mathbf{M}_k + \alpha_k \rho_k \mathbf{f} \quad (4.49)$$

where  $\mathbf{M}_k$  denotes various inter-phase momentum exchange terms, e.g., drag, lift, turbulent dispersion, virtual mass, lubrication, etc., see also [Yeoh and Tu, 2009].

The averaged internal energy equation is

$$\frac{\partial \alpha_k \rho_k e_k}{\partial t} + \nabla \cdot (\alpha_k \rho_k \mathbf{v}_k e_k) = -\nabla \cdot (\alpha_k \mathbf{q}_k) + \alpha_k Q_k + \alpha_k \mathbf{T}_k : \nabla \cdot \mathbf{v}_k + E_k + e_k \Gamma_k \quad (4.50)$$

### *Interfacial Mass Transfer*

From the work by Yeoh and Tu [Yeoh and Tu, 2009], the mass transfer rate per unit volume is

$$\Gamma_k = \frac{h A_I (T_k - T_{k_{liq}})}{h_{fg}} \quad (4.51)$$

### *Interfacial Momentum Transfer*

#### *Drag force*

The interfacial drag force,  $\mathbf{F}_d^D$ , acting on a particle in steady-state condition can be given in terms of the drag coefficient,  $C_D$ , based on the

relative velocity as

$$\mathbf{F}_d^D = -\frac{1}{2}C_D \frac{\alpha_d}{B_d} \rho_c A_d |\mathbf{v}_r| \mathbf{v}_r \quad (4.52)$$

where  $A_d$  is the projected area of a typical particle,  $\alpha_d/B_d$  denotes the particle volume fraction to volume ratio, and  $\mathbf{v}_r = \mathbf{v}_d - \mathbf{v}_c$  is the relative velocity between the disperse (bubbly) and continuous phases, denoted by subscripts  $c$  and  $d$ , respectively. Requiring an equal and opposite force acting on the continuous phase,  $\mathbf{F}_d^D = -\mathbf{F}_c^D$ , ensures that Newton's third law and, consequently, the momentum conservation law hold. Assuming spherical bubbles for the disperse phase, with surface  $A_d = r_d^2 \pi$ , and volume  $B_d = 4r_d^3 \pi / 3$ , equation (4.52) becomes

$$\mathbf{F}_d^D = -\frac{3}{8r_d} C_D \alpha_d \rho_c |\mathbf{v}_r| \mathbf{v}_r \quad (4.53)$$

Various drag models exist and are available, including a simple constant-coefficient ( $C_D = \text{const.}$ ), the Ishii-Zuber [Ishii and Zuber, 1979], the Tomiyama [TOMIYAMA et al., 1998], and the Bozzano-Dente [Bozzano and Dente, 2001] models.

### *Lift force*

Lift is another force that exchanges momentum between fields in the ensemble-averaged formulation for multiphase flows. A common way to implement the lift force acting on the disperse phase is given by [Auton et al., 1988]

$$\mathbf{F}_d^L = -C_L \alpha_d \rho_c \mathbf{v}_r \times (\nabla \times \mathbf{v}_c) \quad (4.54)$$

where  $C_L$  is the lift coefficient,  $\alpha_d$  is the disperse-phase volume fraction,  $\rho_c$  is the density of the continuous phase, and  $\mathbf{v}_r = \mathbf{v}_d - \mathbf{v}_c$  is the relative velocity between the disperse (bubbly) and continuous phases, denoted by subscripts  $c$  and  $d$ , respectively. Similar to the drag force, the lift force is also required to be anti-symmetric:  $\mathbf{F}_d^L = -\mathbf{F}_c^L$ . Various lift models exist and are available, including the simplest, constant-coefficient ( $C_L = \text{const.}$ ) model.

## 5 Arbitrary Lagrangian-Eulerian Formulation

This chapter presents the Arbitrary Lagrangian-Eulerian (ALE) formulation used in flow solver. The discussion begins with background on the required vector calculus and ends with the master balance equations used to develop the solution methods discussed in subsequent chapters of this document. The notes presented here were based, in part, on the work by Scovazzi and Hughes [Scovazzi and Hughes, 2007], Donea [Donea, 1983], Gurtin [Gurtin, 2003], Drumheller [Drumheller, 1998], Förster, Wall and Ramm [C. Forster and Ramm, 2007], Hron and Turek [Hron and Turek, 2006]. The reader may consult these references for additional details.

### Basics

This section outlines some of the fundamentals of vector calculus required for the ALE formulation.

### Invertible map

Let  $\psi$  be a smooth, invertible map from  $\Omega_{\mathbf{X}}$  to  $\Omega_{\mathbf{x}}$ , as shown in Figure 5.1, such that

$$\Omega_{\mathbf{X}} = \psi(\Omega_{\mathbf{x}}) \quad (5.1)$$

and

$$\mathbf{X} = \psi(\mathbf{x}) \quad (5.2)$$

### Jacobian of the map

$$\mathbf{F}_\psi = \frac{\partial \mathbf{x}}{\partial \mathbf{X}} \quad \text{or} \quad F_{\psi_{ij}} = \frac{\partial x_i}{\partial X_j}. \quad (5.3)$$

The map is one-to-one and invertible, so

$$\det(\mathbf{F}_\psi) > 0 \quad (5.4)$$

or

$$J = \det(\mathbf{F}_\psi); \quad J > 0 \quad (5.5)$$

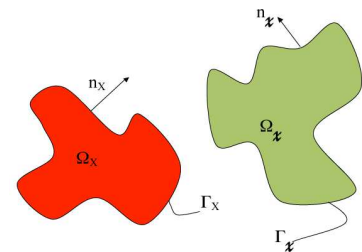


Figure 5.1: Invertible map.

Differential quantities transform as

$$d\mathbf{x} = \mathbf{F}_\psi d\mathbf{X} \tag{5.6}$$

or

$$\begin{pmatrix} dx \\ dy \\ dz \end{pmatrix} = \begin{bmatrix} \frac{\partial x}{\partial X} & \frac{\partial x}{\partial Y} & \frac{\partial x}{\partial Z} \\ \frac{\partial y}{\partial X} & \frac{\partial y}{\partial Y} & \frac{\partial y}{\partial Z} \\ \frac{\partial z}{\partial X} & \frac{\partial z}{\partial Y} & \frac{\partial z}{\partial Z} \end{bmatrix} \begin{pmatrix} dX \\ dY \\ dZ \end{pmatrix} \tag{5.7}$$

*Volume relationships*

The differential volume transforms as

$$d\Omega_{\mathbf{x}} = J d\Omega_{\mathbf{X}} \tag{5.8}$$

and

$$\text{cof}(\mathbf{F}_\psi) = \det(\mathbf{F}_\psi) \mathbf{F}_\psi^{-1} \tag{5.9}$$

since  $J > 0$ , i.e.,  $\det(\mathbf{F}_\psi) > 0$ .

*Nanson's formula*

Nanson's formula for the normal is

$$\mathbf{n}_{\mathbf{x}} d\Gamma_{\mathbf{x}} = \text{cof}(\mathbf{F}_\psi) \mathbf{n}_{\mathbf{X}} d\Gamma_{\mathbf{X}} \tag{5.10}$$

or

$$\mathbf{n}_{\mathbf{x}} d\Gamma_{\mathbf{x}} = J \mathbf{F}_\psi^{-1} \mathbf{n}_{\mathbf{X}} d\Gamma_{\mathbf{X}}. \tag{5.11}$$

*Kinematics*

The starting point for the kinematics are the three frames:

- Material or Lagrangian ( $\mathbf{X} - \Omega_{\mathbf{X}}$ )
- Current or Eulerian ( $\mathbf{x} - \Omega_{\mathbf{x}}$ )
- Referential (ALE) ( $\zeta - \Omega_{\zeta}$ )

*Lagrangian-to-Eulerian Map*

$\mathbf{X}$  - Current position of material point  $\mathbf{X}$

$\phi$  - Map from  $\mathbf{X}$  to  $\mathbf{x}$  at each time  $t$

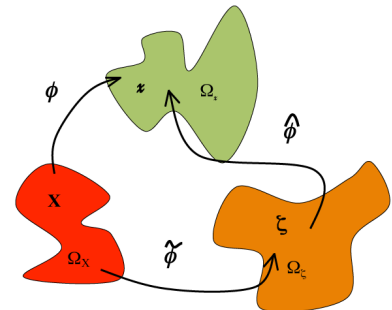


Figure 5.2: Maps used in the ALE formulation.

$$\begin{aligned}\Omega_{\mathbf{x}} &= \phi(\Omega_{\mathbf{X}}, t), \quad \forall t \geq 0, \\ \mathbf{x} &= \phi(\mathbf{X}, t), \quad \forall \mathbf{X} \in \Omega_{\mathbf{X}}.\end{aligned}\tag{5.12}$$

At  $t = 0$ ,  $\Omega_{\mathbf{X}}$  and  $\Omega_{\mathbf{x}}$  coincide thus

$$\phi(\cdot, 0) = I_d(\cdot)\tag{5.13}$$

where  $I_d$  is the identity map.  $\mathbf{X}$  identifies a point at time  $t$  identified in the Eulerian reference at  $\mathbf{x}$ .  $\mathbf{X} = \phi^{-1}(\mathbf{x}, t)$  since,  $\phi(\mathbf{X}, t)$  is invertible.

*Displacement*

$$\begin{aligned}\mathbf{u} &= \phi(\mathbf{X}, t) - \phi(\mathbf{X}, 0) \\ \mathbf{u} &= \phi(\mathbf{X}, t) - \mathbf{X} \\ \mathbf{u} &= \mathbf{x}(t) - \mathbf{X}\end{aligned}\tag{5.14}$$

*Material velocity*

$$\begin{aligned}\mathbf{v} &= \left. \frac{\partial \phi}{\partial t} \right|_{\mathbf{X}} = \dot{\phi} \\ \mathbf{v} &= \left. \frac{\partial \mathbf{u}}{\partial t} \right|_{\mathbf{X}} = \dot{\mathbf{u}}\end{aligned}\tag{5.15}$$

*Deformation gradient*

$$\mathbf{F} = \nabla_{\mathbf{X}} \phi = \nabla_{\mathbf{X}} \mathbf{x}\tag{5.16}$$

$$F_{ij} = \frac{\partial x_i}{\partial X_j}\tag{5.17}$$

$$\mathbf{F} = \begin{bmatrix} \frac{\partial x}{\partial X} & \frac{\partial x}{\partial Y} & \frac{\partial x}{\partial Z} \\ \frac{\partial y}{\partial X} & \frac{\partial y}{\partial Y} & \frac{\partial y}{\partial Z} \\ \frac{\partial z}{\partial X} & \frac{\partial z}{\partial Y} & \frac{\partial z}{\partial Z} \end{bmatrix}\tag{5.18}$$

$$J = \det(\mathbf{F})\tag{5.19}$$

*Time derivative (Lagrangian)*

$$\begin{aligned}\dot{\alpha}(\mathbf{x}, t) &= \left. \frac{\partial \alpha(\mathbf{x}, t)}{\partial t} \right|_{\mathbf{X}} \\ &= \left. \frac{\partial \alpha(\phi(\mathbf{x}, t), t)}{\partial t} \right|_{\mathbf{X}}\end{aligned}\tag{5.20}$$

applying chain rule

$$\begin{aligned}\dot{\alpha}(\mathbf{x}, t) &= \left. \frac{\partial \alpha}{\partial t} \right|_{\mathbf{x}} + \nabla_x \alpha \cdot \left. \frac{\partial \phi}{\partial t} \right|_{\mathbf{X}} \\ &= \left. \frac{\partial \alpha}{\partial t} \right|_{\mathbf{x}} + \nabla_x \alpha \cdot \mathbf{v}\end{aligned}\quad (5.21)$$

where  $\mathbf{v} = \left. \frac{\partial \mathbf{X}}{\partial t} \right|_{\mathbf{X}} \equiv$  “velocity.”

*Inverse mapping*

$$\mathbf{F}^{-1} = \nabla_{\mathbf{X}} \mathbf{X} \quad \text{or} \quad F_{ij}^{-1} = \frac{\partial X_i}{\partial x_j} \quad (5.22)$$

$$\mathbf{F}^{-1} = \begin{bmatrix} \frac{\partial X}{\partial x} & \frac{\partial X}{\partial y} & \frac{\partial X}{\partial z} \\ \frac{\partial Y}{\partial x} & \frac{\partial Y}{\partial y} & \frac{\partial Y}{\partial z} \\ \frac{\partial Z}{\partial x} & \frac{\partial Z}{\partial y} & \frac{\partial Z}{\partial z} \end{bmatrix} \quad (5.23)$$

*Time Derivative of the Jacobian*

$$\dot{J} = J \nabla_x \cdot \mathbf{v} \quad (5.24)$$

*Lagrangian-to-Referential (ALE) map*

This transformation tracks the motion of the referential frame as observed from the Lagrangian frame.

$$\begin{aligned}\Omega_{\tilde{\zeta}} &= \tilde{\phi}(\Omega_X, t), \quad \forall t \geq 0, \\ \mathbf{,} &= \tilde{\phi}(\mathbf{X}, t), \quad \forall \mathbf{X} \in \Omega_X.\end{aligned}\quad (5.25)$$

Assuming that  $\Omega_X$  and  $\Omega_{\tilde{\zeta}}$  coincide at  $t = 0$ , we reproduce an identity map  $\tilde{\phi}(\cdot, 0) = I_d(\cdot)$ .

The displacement of the “referential” domain as observed from the Lagrangian reference frame is defined as  $\tilde{\mathbf{u}}$ .

*Displacement*

$$\begin{aligned}\tilde{\mathbf{u}} &= \tilde{\phi}(\mathbf{X}, t) - \tilde{\phi}(\mathbf{X}, 0) \\ &= \tilde{\phi}(\mathbf{X}, t) - \mathbf{X} \\ &= \mathbf{,}(t) - \mathbf{X}\end{aligned}\quad (5.26)$$

*Velocity*

The velocity of the referential frame observed from the Lagrangian frame for a discrete setting is defined as

$$\tilde{\mathbf{v}} = \left. \frac{\partial \tilde{\phi}}{\partial t} \right|_{\mathbf{X}} = \left. \frac{\partial \tilde{u}}{\partial t} \right|_{\mathbf{X}} \quad (5.27)$$

This velocity is the “mesh velocity” in a discrete sense and is analogous to the material velocity.

*Deformation gradient*

$$\tilde{\mathbf{F}} = \nabla_{\mathbf{X}} \tilde{\phi} = \nabla_{\mathbf{X}} \mathbf{x} \quad (5.28)$$

$$\tilde{F}_{ij} = \frac{\partial \xi_i}{\partial X_j} \quad (5.29)$$

where  $\mathbf{x} = (\xi, \eta, \zeta)$ .

$$\tilde{\mathbf{F}} = \begin{bmatrix} \frac{\partial \xi}{\partial X} & \frac{\partial \xi}{\partial Y} & \frac{\partial \xi}{\partial Z} \\ \frac{\partial \eta}{\partial X} & \frac{\partial \eta}{\partial Y} & \frac{\partial \eta}{\partial Z} \\ \frac{\partial \zeta}{\partial X} & \frac{\partial \zeta}{\partial Y} & \frac{\partial \zeta}{\partial Z} \end{bmatrix} \quad (5.30)$$

$$\tilde{J} = \det(\tilde{\mathbf{F}}) \quad (5.31)$$

*Time derivative*

$$\dot{\alpha}(\mathbf{x}, t) = \left. \frac{\partial \alpha}{\partial t} \right|_{\mathbf{x}} + \tilde{\mathbf{v}} \cdot \nabla_{\xi} \alpha \quad (5.32)$$

where,  $\nabla_{\mathbf{x}}(\cdot)$  means, with respect to  $\mathbf{x}$ .

*Time derivative of the Jacobian  $\tilde{J}$* 

The time derivative of the Jacobian reads:

$$\dot{\tilde{J}} = \tilde{J} \nabla_{\mathbf{x}} \cdot \tilde{\mathbf{v}} \quad (5.33)$$

Where, for solenoidal mesh velocities,  $\nabla_{\mathbf{x}} \cdot \tilde{\mathbf{v}} = 0$ , the time derivative of the Jacobian is  $\dot{\tilde{J}} = 0$ .

### Reynolds Transport Theorem

In order to define the Reynolds transport theorem, several definitions are required.

$\Omega_{\mathbf{x}}$  a domain that deforms according to  $\phi$  with velocity  $\mathbf{v}_m = \frac{\partial \phi}{\partial t} \Big|_{\mathbf{X}}$  and  $\Omega_{\mathbf{x}} = \phi(\Omega_{\mathbf{X}})$ .

$\Gamma_x$  the boundary of the deforming domain with  $\mathbf{n}_x$  outward normal vector.

Using the previous definitions, the Reynolds transport theorem is

$$\frac{d}{dt} \int_{\Omega_{\mathbf{x}}} \alpha = \int_{\Omega_{\mathbf{x}}} \frac{\partial \alpha}{\partial t} \Big|_{\mathbf{x}} + \oint_{\Gamma_{\mathbf{x}}} \alpha \mathbf{v}_m \cdot \mathbf{n}_{\mathbf{x}} \quad (5.34)$$

or

$$\frac{d}{dt} \int_{\Omega_{\mathbf{x}}} \alpha = \int_{\Omega_{\mathbf{x}}} \left[ \frac{\partial \alpha}{\partial t} \Big|_{\mathbf{x}} + \nabla_{\mathbf{x}} \cdot (\alpha \mathbf{v}_m) \right] \quad (5.35)$$

### Master Balance Equation

Master balance equations are used here as a way to generically express the conservation laws in the ALE framework.

### Generic Forms

Following Scovazzi and Hughes [Scovazzi and Hughes, 2007], the scalar form for a material domain is

$$\frac{d}{dt} \int_{\Omega_x = \phi(\Omega_X)} \alpha = - \oint_{\Gamma_x} \mathbf{f}(\alpha) \cdot \mathbf{n}_x + \int_{\Omega_x} S \quad (5.36)$$

where  $\mathbf{f}(\alpha)$  is the flux vector and  $S$  is a volumetric source, and  $\phi(\Omega_X)$  is a smooth, invertible map, such that we can write

$$\frac{d}{dt} \int_{\Omega_x} \alpha = \int_{\Omega} \frac{\partial \alpha}{\partial t} \Big|_x = - \oint_{\Gamma_x} \mathbf{f}(\alpha) \cdot \mathbf{n}_x + \int_{\Omega_x} S \quad (5.37)$$

Rearranging, and using the divergence theorem

$$\int_{\Omega_x} \left\{ \frac{\partial \alpha}{\partial t} \Big|_x + \nabla \cdot \mathbf{f}(\alpha) - S \right\} = 0 \quad (5.38)$$

This is true for any  $\Omega_x$ , so

$$\frac{\partial \alpha}{\partial t} \Big|_x + \nabla \cdot \mathbf{f}(\alpha) = S. \quad (5.39)$$

Using the Reynolds transport theorem Eq. (5.35) and Eq. (5.37)

$$\int_{\Omega_x} \frac{\partial \alpha}{\partial t} \Big|_x = \frac{d}{dt} \int_{\Omega_x} \alpha - \oint_{\Gamma_x} \alpha \frac{\partial \phi}{\partial t} \Big|_x \cdot \mathbf{n} \quad (5.40)$$



where

$$\left. \frac{\partial \phi}{\partial t} \right|_x = \mathbf{v}_m \quad (5.41)$$

Here,  $\mathbf{v}_m$  is the velocity measured from the point of view of  $X$  and is the mesh velocity in a discrete sense. Using this velocity in Eq.(5.37) yields

$$\frac{d}{dt} \int_{\Omega_x} \alpha - \oint_{\Gamma_x} \alpha \mathbf{v}_m \cdot \mathbf{n}_x = - \oint_{\Gamma_x} \mathbf{f}(\alpha) \cdot \mathbf{n}_x + \int_{\Omega_x} S \quad (5.42)$$

or

$$\frac{d}{dt} \int_{\Omega_x} \alpha + \oint_{\Gamma_x} \{ \mathbf{f}(\alpha) - \alpha \mathbf{v}_m \} \cdot \mathbf{n}_x - \int_{\Omega_x} S = 0. \quad (5.43)$$

Recalling that  $\phi(\Omega_X)$  is smooth and using the divergence theorem

$$\int_{\Omega_x} \left\{ \frac{\partial \alpha}{\partial t} + \nabla \cdot (\mathbf{f}(\alpha) - \alpha \mathbf{v}_m) - S \right\} = 0, \quad (5.44)$$

and in strong form

$$\frac{\partial \alpha}{\partial t} + \nabla \cdot (\mathbf{f}(\alpha) - \alpha \mathbf{v}_m) - S = 0 \quad (5.45)$$

which is form-equivalent to Eq. (105) in [AVL, 2004] and Eq. (13) in [C. Forster and Ramm, 2007].

### Vector Form

The vector form of the master balance equation reads

$$\frac{d}{dt} \int_{\Omega_x = \phi(\Omega_X)} \mathbf{ff} = - \oint_{\Gamma_x} \mathbf{F}(\mathbf{ff}) \cdot \mathbf{n}_x + \int_{\Omega_x} \mathbf{S} \quad (5.46)$$

where  $\mathbf{F}$  is a flux vector that, for instance, could include advective, viscous, and pressure-gradient terms.

Following the scalar form,

$$\int_{\Omega_x} \left\{ \left. \frac{\partial \mathbf{ff}}{\partial t} \right|_x + \nabla \cdot \mathbf{F}(\alpha) - \mathbf{S} \right\} = 0 \quad (5.47)$$

using the Reynolds transport theorem,

$$\int_{\Omega_x} \left. \frac{\partial \mathbf{ff}}{\partial t} \right|_x = \frac{d}{dt} \int_{\Omega_x} \mathbf{ff} - \oint_{\Gamma_x} (\mathbf{ff} \mathbf{v}_m) \cdot \mathbf{n}_x \quad (5.48)$$

Thus, the vector form becomes

$$\frac{d}{dt} \int_{\Omega_x} \mathbf{ff} + \oint_{\Gamma_x} \mathbf{F}(\mathbf{ff}) \cdot \mathbf{n}_x - \oint_{\Gamma_x} (\mathbf{ff} \mathbf{v}_m) \cdot \mathbf{n}_x = \int_{\Omega_x} \mathbf{S} \quad (5.49)$$

and finally

$$\frac{d}{dt} \int_{\Omega_x} \mathbf{ff} + \oint_{\Gamma_x} (\mathbf{F}(\mathbf{ff}) - \mathbf{ff} \mathbf{v}_m) \cdot \mathbf{n}_x = \int_{\Omega_x} \mathbf{S} \quad (5.50)$$

where  $\mathbf{ff} \mathbf{v}_m = \mathbf{ff}_i \mathbf{v}_{m_j}$ .

### Navier-Stokes Equations

In this section, the conservation equations are derived using the master balance equation.

#### Continuity equation

For the continuity equation, define

$$f(\alpha) = \rho \mathbf{v}, \quad \alpha = \rho, \quad \text{and} \quad S = 0. \quad (5.51)$$

This yields

$$\frac{\partial \rho}{\partial t} + \nabla \cdot (\rho \mathbf{v} - \rho \mathbf{v}_m) = 0 \quad (5.52)$$

which is the continuity equation. The integral form reads

$$\frac{d}{dt} \int_{\Omega_x} \rho + \oint_{\Gamma_x} \rho (\mathbf{v} - \mathbf{v}_n) \cdot \mathbf{n}_x = 0 \quad (5.53)$$

#### Energy equation

The energy equation is obtained by using Eq.(5.43) and after applying a series of manipulations and simplifying assumptions, the energy equation, in terms of temperature, reads

$$\alpha = \rho C_p T, \quad \mathbf{f}(\alpha) = \rho C_p T \mathbf{v} + \mathbf{q}, \quad \mathbf{q} = -\kappa \nabla_x T \quad (5.54)$$

$$\frac{d}{dt} \int_{\Omega_x} \rho C_p T + \oint_{\Gamma_x} \rho C_p T (\mathbf{v} - \mathbf{v}_m) \cdot \mathbf{n}_x = \oint_{\Gamma_x} \kappa \nabla_x T \cdot \mathbf{n}_x + \int_{\Omega_x} q''' \quad (5.55)$$

where  $q'''$  is the volumetric heat source and  $\kappa$  is the thermal conductivity. Following similar steps as in the continuity equation, the strong form is

$$\rho C_p \frac{\partial T}{\partial t} + \nabla_x \cdot \{ \rho C_p T (\mathbf{v} - \mathbf{v}_m) \} = \nabla_x \cdot (\kappa \nabla_x T) + q''' \quad (5.56)$$

In terms of enthalpy, the energy equation reads

$$\frac{d}{dt} \int_{\Omega_x} \rho h + \oint_{\Gamma_x} \rho h (\mathbf{v} - \mathbf{v}_m) \cdot \mathbf{n}_x = \oint_{\Gamma_x} \kappa \nabla_x T \cdot \mathbf{n}_x + \int_{\Omega_x} q''' \quad (5.57)$$

and in strong form is

$$\frac{\partial \rho h}{\partial t} + \nabla_x \cdot \{ \rho h (\mathbf{v} - \mathbf{v}_m) \} = \nabla_x \cdot (\kappa \nabla_x T) + q''' \quad (5.58)$$

*Momentum equation*

In order to derive the momentum equation the following variables are introduced

$$\alpha = \rho \mathbf{v} \quad (5.59)$$

$$\mathbf{F}(\alpha) = \rho \mathbf{v} \mathbf{v} - \boldsymbol{\alpha} \quad (5.60)$$

$$\mathbf{S} = \mathbf{f} \quad (5.61)$$

$$\boldsymbol{\alpha} = -p\mathbf{I} + \mu \left( \nabla \mathbf{v} + (\nabla \mathbf{v})^T \right) \quad (5.62)$$

Using Eq. (5.50) the momentum equation can be written as:

$$\frac{d}{dt} \int_{\Omega_x} \rho \mathbf{v} + \oint_{\Gamma_x} (\rho \mathbf{v} \mathbf{v} - \rho \mathbf{v} \mathbf{v}_m - \boldsymbol{\alpha}) \mathbf{n}_x = \int_{\Omega_x} \mathbf{f} \quad (5.63)$$

Rearranging and defining

$$\boldsymbol{\sigma} = \mu \left( \nabla \mathbf{v} + (\nabla \mathbf{v})^T \right) \quad (5.64)$$

$$\boldsymbol{\alpha} = -p\mathbf{I} + \boldsymbol{\sigma} \quad (5.65)$$

Therefore, the integral form of the momentum equations can be written as

$$\frac{d}{dt} \int_{\Omega_x} \rho \mathbf{v} + \oint_{\Gamma_x} \rho \mathbf{v} (\mathbf{v} - \mathbf{v}_m) \cdot \mathbf{n}_x = - \int_{\Omega_x} \nabla_x p + \oint_{\Gamma_x} \boldsymbol{\sigma} \cdot \mathbf{n}_x + \int_{\Omega_x} \mathbf{f} \quad (5.66)$$

The strong form of momentum conservation is

$$\frac{\partial \rho \mathbf{v}}{\partial t} + \nabla \cdot \{ \rho \mathbf{v} (\mathbf{v} - \mathbf{v}_m) \} = -\nabla p + \nabla \cdot \boldsymbol{\sigma} + \mathbf{f} \quad (5.67)$$

See Eq. (13) in Förster, Wall and Ramm [C. Förster and Ramm, 2007] for comparison.



## 6 *Turbulence Models*

This chapter introduces the turbulence models that are either already implemented, or being implemented in the Hydra Toolkit. A brief review of turbulence and modeling techniques is presented to set the theoretical foundation for readers unfamiliar with this topic.

The flow solvers in the Hydra Toolkit are designed to incorporate both well-established and state-of-the-art turbulence models, ranging from traditional Reynolds-averaged Navier-Stokes (RANS) through large-eddy simulation (LES) to hybrid RANS-LES models.

- RANS models
  - Spalart-Allmaras model §6.3
  - Re-normalized group (RNG)  $k - \varepsilon$  model §6.3
  - Shear stress transport (SST)  $k - \omega$  model 6.3
  - $k - \varepsilon - v^2 - f$  model §6.3
  - $k - \varepsilon - \zeta - f$  model §6.3
- LES models
  - MILES or ILES: This family of models is obtained using a monotonicity preserving advection treatment (MILES) and is also referred to as implicit LES (ILES).
  - Smagorinsky model §6.4
  - Wall-adapted large eddy (WALE) model §6.4
  - $k_{sgs}$  model
  - Localized dynamic kinetic energy (LDKM)  $k_{sgs}$  model §6.4
  - Variational multi-scale model
- Hybrid RANS/LES models
  - Detached-Eddy Simulation (DES) §6.5
  - Delayed DES (DDES) model

In the following, a very brief overview of turbulence theory is given in §6.1 followed by the basics of direct numerical simulation (DNS) in §6.2. Then the individual turbulence models (listed above) are described in more detail in §6.3–6.5. Finally, §6.6 describes the statistics that can be extracted from the turbulent fields.

### *Turbulent flows*

The equations for conservation of mass, momentum, and energy, i.e., Eqs. (1.1)–(1.3) and (1.4)–(1.6), are believed to contain all the physics required to describe a turbulent flow. However, the extreme complexity of the Navier-Stokes equations precludes the derivation of analytical solutions in all but exceptionally simplified cases. Therefore, in general, numerical methods are applied to obtain solutions for most flow problems. In addition to the complexity of the governing equations, obtaining a solution becomes more demanding if the flow is in the turbulent regime.

Presenting a single unambiguous mathematical definition of turbulence is difficult. We give a *description* of turbulence rather than a formal definition. Turbulence is a flow property, independent of the fluid, with the following characteristics [Tennekes and Lumley, 1997, Pope, 2000]:

*Irregularity:* The Navier-Stokes equations present chaotic behavior in the turbulent regime. This implies that the evolution of the equations is sensitive to small perturbations in initial and boundary conditions. Therefore, the exact reproduction of a turbulent flow realization requires exactly matching all initial and boundary conditions, which cannot be satisfied in reality. This sensitivity and chaotic behavior are only triggered at high Reynolds number, explaining why the evolution of laminar flows is completely deterministic and can always be exactly reproduced.

*Enhanced diffusivity:* The transfer of mass, momentum, and energy is significantly enhanced by turbulence.

*Large Reynolds Number:* At large Reynolds number – when the inertial forces in the fluid are much larger than the viscous forces – the Navier-Stokes equations exhibit a chaotic motion that induces a stochastic behavior of the flow variables.

*Three-dimensional:* Turbulence is characterized by the presence of vorticity fluctuations. These effects are present even when the mean flow is two-dimensional. In fact, vortex stretching, which only occurs in three dimensions, is an important process responsible for the generation of turbulent kinetic energy.

*Dissipative:* Turbulence is a dissipative process, where the turbulent kinetic energy generated in the fluid flow, is converted into internal energy by viscous effects. A constant supply of energy is required to maintain a turbulent flow; if that energy is absent, the turbulent fluctuations decay.

*Multi-Scale:* Turbulence is characteristic of nonlinear flow interactions on a broad range of spatial scales. The larger the Reynolds number the larger the range of scales in the flow, presenting a challenge for numerical calculations.

*Continuous:* Turbulent flow is governed by the Navier-Stokes equations. Regardless of how small the scales of turbulence become, they will always be bigger than molecular scales, satisfying the conditions of continuous media embodied in the derivation of the Navier-Stokes equations [Segel, 1965, Vincenti and Kruger, 1965].

Predicting the instantaneous state of high-Reynolds-number turbulence is virtually impossible and from the practical point of view unnecessary. From the practical viewpoint, the only sensible way to gain physical insight into turbulence is through statistical analysis [Monin and Yaglom, 1979].

While in laminar flows, it makes sense to ask questions such as “*what is the velocity or pressure at a given point in space and time?*”, in turbulent flows the aim of the inquiry must be different. In turbulent flows the variables are random, therefore their (instantaneous) values are inherently unpredictable. A theory (or method) can, however, predict the *probability of events*. Thus the sensible question in turbulent flow becomes “*what is the probability that the velocity or pressure will be less (or more) than a given value at a space-time point?*” In other words, a statistical description aims at determining probabilities (i.e. joint probability density functions of the flow variables) and their derived statistics, such as means, variances, correlations, etc.

One important characteristic of turbulent flows is the presence of multiple time and length scales. These scales can be characterized as large structures that cascade into smaller structures, as shown in Fig. 6.1. In the turbulence literature these scales are known as *eddies*<sup>1</sup>, which are loosely defined as coherent regions in the flow, see Fig. 6.1.

Early turbulence research noted that eddies tend to decay into smaller structures until they reach a point where they cannot reduce further in size. This behavior is reported artistically in the original paper by Lewis F. Richardson [Richardson, 1922]

*Big whorls have little whorls  
That feed on their velocity,  
And little whorls have lesser whorls  
And so on to viscosity.*

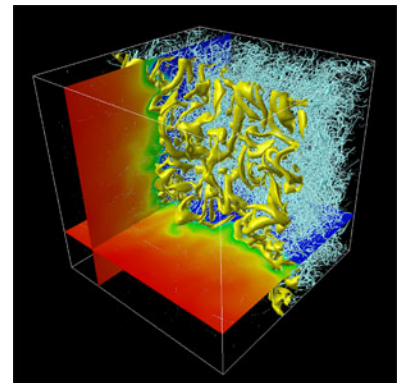


Figure 6.1: Visualization of turbulent flow fields: isotropic turbulence (figure courtesy of Tokyo Institute of Technology)

<sup>1</sup> For a formal spectral definition of eddies see Tennekes and Lumley [Tennekes and Lumley, 1997].

Most of turbulence theory is developed for constant-density, single-component flows in a statistically stationary and equilibrium state. Andrey Kolmogorov helped to establish the foundations of this theory [Tennekes and Lumley, 1997, Pope, 2000, Monin and Yaglom, 1979], when he postulated two influential hypotheses for turbulence [Kolmogorov, 1991]. These hypotheses serve as cornerstones to most approaches in turbulence modeling.

*Kolmogorov's hypothesis of local isotropy.* For very high Reynolds number flows, the small scales of turbulent motion are *locally* isotropic (i.e. no spatial direction is preferred, see Fig. 6.1 and are uniquely determined by the kinematic viscosity,  $\nu = \mu/\rho$ , and the kinetic energy dissipation rate,

$$\varepsilon = 2\nu \overline{s_{ij}s_{ij}} \quad (6.1)$$

where

$$s_{ij} = \frac{1}{2} \left( \frac{\partial v'_i}{\partial x_j} + \frac{\partial v'_j}{\partial x_i} \right) \quad (6.2)$$

is the strain rate of the velocity fluctuations,  $v'_i = v_i - \bar{v}_i$ , about the mean velocity,  $\bar{v}_i$ .

This hypothesis does not imply that the turbulence fluctuations are in general isotropic, but states that as the large anisotropic eddies of the flow, see Fig. 6.1, break into smaller ones, the anisotropy of the flow, characterized by the integral length,  $L$ , and velocity,  $v$ , scales, is progressively lost as the eddies break down to scales so small that the turbulence becomes isotropic, see Fig. 6.1. At those scales, known as Kolmogorov micro-scales of length,  $\eta$ , and time,  $\tau$ , all the anisotropic information of the flow is lost and are characterized by only  $\nu$  and  $\varepsilon$ :

$$\eta = \left( \frac{\nu^3}{\varepsilon} \right)^{1/4} \quad (6.3)$$

$$\tau = \left( \frac{\nu}{\varepsilon} \right)^{1/2} \quad (6.4)$$

*Kolmogorov's similarity hypothesis.* At very high Reynolds numbers at scales much larger than the micro scale but much smaller than the integral scale,  $\eta \ll r \ll L$ , the statistics are determined by  $\varepsilon$  independent of  $\nu$ .

This hypothesis implies that in the range of scales  $1/L \ll \kappa \ll 1/\eta$  (expressed in terms of wave numbers) the kinetic energy spectrum is universally determined by the local length scale,  $\kappa = 2\pi/r$ , and  $\varepsilon$ .

$$E(\kappa) = C\varepsilon^{2/3}\kappa^{-5/3} \quad (6.5)$$



where  $E(\kappa)$  is the power density spectrum of the turbulent kinetic energy,  $\overline{v_i'v_i'}/2$ , and  $C$  is an universal constant. This range of scales is known as the inertial range, and it is expected that constant-density, single-component turbulence in equilibrium states for any sufficiently high Reynolds number flow will follow Eq. (6.5).

Kolmogorov's hypotheses are almost always assumed in the development of turbulence models. However, it is important to appreciate their strict range of applicability: single-component, constant-density, shear-driven, equilibrium flows in a statistically stationary state.

### *Direct Numerical Simulation*

The modern analysis of fluid dynamics relies on numerical algorithms to obtain solutions for the Navier-Stokes equations in general cases. Today obtaining solutions for low  $Re$ , i.e. laminar, flows is a common practice. However, when the flow is turbulent its *multi-scale nature*, *three-dimensional*, and *dissipative* characteristics pose great computational challenges.

In turbulence the range of length and time scales in a flow field is proportional to  $\eta/l \sim Re^{-3/4}$  and  $\tau u/l \sim Re^{-1/2}$ , respectively, see e.g. [Tennekes and Lumley, 1997]. Here,  $\eta$  and  $\tau$  are the Kolmogorov length and time scales, respectively, while  $u$  and  $l$  are the inertial-range velocity and length scales, respectively. Since turbulence is a dissipative phenomenon, its prediction requires resolving all scales present in the flow, which is always three-dimensional.

Direct Numerical Simulation (DNS) is a numerical technique where all scales of a turbulent flow are resolved. DNS is intended to study canonical flow problems where the objective is to gain insight in the physics of turbulence [Moin and Mahesh, 1998]. Very accurate numerical schemes are required in space and time. These schemes are usually in the form of pseudo-spectral methods or compact finite difference schemes that unfortunately, due to their complexity, can only be implemented in simple geometries discretized with structured meshes and periodic boundary conditions. Practitioners of DNS take great care in *demonstrating* the actual scales their numerical algorithms resolve (with well-quantified numerical errors) for a given flow and Reynolds number. This is essential, as the statistics may be influenced by numerical artifacts, such as dissipative numerical discretization and inadequate grid resolution.

Estimates of the total number of grid points,  $N$ , and total number of time steps,  $M$ , required to resolve all relevant scales in homogeneous isotropic forced turbulence by DNS predict a scaling of  $N^3 \sim Re_\lambda^{9/2}$  and  $M \sim Re_\lambda^{3/2}$  based on the Taylor-scale Reynolds number,  $Re_\lambda$ ,

[Pope, 2000]. This means that the total cost of a simulation is proportional to  $N^3 M \sim Re_\lambda^6$ . From these estimates, it is clear that resolving all relevant scales with today's computers is only possible at low and moderate Reynolds numbers. Another interesting consequence of the above estimate is that the *relative* computational effort spent on resolving the smallest (dissipative) scales compared to that of the energy-containing and inertial subrange combined also increases exponentially with the Reynolds number [Pope, 2000]. Consequently, even if more and more powerful computers are available in the future for all-scale-resolving turbulence simulations, more and more effort will be proportionally spent on computing the smallest scales which are the least interesting from the practical viewpoint. Therefore, for engineering purposes statistical methods are preferred which require approximations.

### *Reynolds-Averaged equations*

The use of Reynolds averaging provides a systematic framework for computing finite statistical moments of turbulent flow variables. In this approach any variable,  $\phi$ , is decomposed into a mean,  $\bar{\phi}$ , and a fluctuating part,  $\phi'$ , as

$$\phi = \bar{\phi} + \phi' \quad (6.6)$$

An alternative decomposition, favored in variable-density flows, is the Favre or density-weighted decomposition,

$$\phi = \tilde{\phi} + \phi'' \quad \text{with} \quad \tilde{\phi} = \frac{\overline{\rho\phi}}{\bar{\rho}} \quad (6.7)$$

Although other definitions can also be used [Wilcox, 1998], we define Reynolds averaging as a statistical ensemble average

$$\bar{\phi}(\mathbf{X}, t) = \lim_{N \rightarrow \infty} \frac{1}{N} \sum_{k=1}^N \phi^{(k)}(\mathbf{X}, t) \quad (6.8)$$

which is a discrete analogue of the mathematical expectation, defined as an integral over a probability density function (PDF),

$$\langle \phi(\mathbf{X}, t) \rangle = \int_{-\infty}^{\infty} \psi f(\psi; \mathbf{X}, t) d\psi \quad (6.9)$$

Here  $\phi^{(k)}$  is a single flow realization/experiment,  $N$  is the number of realizations/experiments conducted, while  $\psi$  is the sample space variable of the PDF,  $f$ , see e.g. [Pope, 2000]. We take  $\langle \cdot \rangle \equiv \overline{(\cdot)}$ . It is straightforward to verify that the following rules apply [Monin and

Yaglom, 1979, Sagaut, 2005]:

$$\overline{\phi + \psi} = \bar{\phi} + \bar{\psi}, \quad (6.10a)$$

$$\bar{\alpha} = \alpha, \quad (6.10b)$$

$$\overline{\alpha\phi} = \alpha\bar{\phi}, \quad (6.10c)$$

$$\overline{\phi\psi} = \bar{\phi}\bar{\psi}, \quad (6.10d)$$

$$\overline{\bar{\phi}} = \bar{\phi}, \quad \widetilde{\bar{\phi}} = \bar{\phi}, \quad (6.10e)$$

$$\overline{\phi'} = 0, \quad \overline{\phi''} \neq 0, \quad (6.10f)$$

$$\overline{\rho\phi'} \neq 0, \quad \overline{\rho\phi''} = 0. \quad (6.10g)$$

Here,  $\psi$  and  $\alpha$  are a dummy variable and a constant, respectively.

Variable-density flows are traditionally investigated in the Favre-averaged framework, in which the moment equations take a simpler form than in the Reynolds-averaged framework, at the price of concealing some effects of the density fluctuations. Since through Favre averaging the equations for constant-, and variable-density flows appear the same, most models developed for constant-density turbulence are routinely applied to variable-density flows without modification. However, it is important to emphasize that this practice can only be justified if the flow remains predominantly shear-driven and the density fluctuations are small,  $\rho' \ll \bar{\rho}$ . This is easily seen through

$$\widetilde{\bar{\phi}} = \frac{\overline{\rho\phi}}{\bar{\rho}} = \frac{\rho\bar{\phi}}{\rho} = \bar{\phi} \quad (6.11)$$

which shows that for  $\rho = \text{const.}$ , Favre averaging reduces to Reynolds averaging.

Applying Eq. (6.7) to the conservation equations yields [Chassaing, 2002],

- Continuity equation

$$\frac{\partial \bar{\rho}}{\partial t} + \frac{\partial}{\partial x_j} (\bar{\rho} \bar{v}_j) = 0 \quad (6.12)$$

- Momentum equation

$$\frac{\partial \bar{\rho} \bar{v}_i}{\partial t} + \frac{\partial}{\partial x_j} (\bar{\rho} \bar{v}_i \bar{v}_j) = \frac{\partial}{\partial x_j} \left( -\bar{p} \delta_{ij} + \bar{\tau}_{ij} - \overline{\rho v_i' v_j'} \right) \quad (6.13)$$

- Energy equation

$$\frac{\partial \bar{\rho} \bar{E}}{\partial t} + \frac{\partial}{\partial x_j} (\bar{\rho} \bar{E} \bar{v}_j) = \frac{\partial}{\partial x_j} \left( -\bar{q} - \overline{\rho E' v_j'} + \bar{v}_i \bar{\tau}_{ij} - \overline{p v_j} \right) \quad (6.14)$$

Equations (6.12)-(6.14) only solve for the “average” behavior of the flow. Compared to DNS, which solves for the instantaneous variables, the

burden on the computational requirements is now eliminated. On the other hand, all statistical information that is not contained in the mean variables now need to be accounted for separately as the mean equations are unclosed: the terms representing the effects of the fluctuations on the means have to be approximated based on some physical insight. These are in the form of correlations, such as the Favre Reynolds stress,  $\widetilde{v_i''v_j''}$ , and the turbulent energy flux,  $\widetilde{E''v_j''}$ .

The simplest way to approximate these correlations is through the turbulent viscosity and gradient diffusion hypotheses, see e.g. [Pope, 2000]. According to the turbulent viscosity hypothesis, the effect of turbulent dissipation is simply an added viscosity whose behavior is directly analogous to the viscosity in a Newtonian fluid, i.e. the deviatoric part of the stress tensor is proportional to the deviatoric rate of strain:

$$-(\tau_{ij} + p\delta_{ij})/\rho = -\nu \left( \frac{\partial v_i}{\partial x_j} + \frac{\partial v_j}{\partial x_i} - \frac{1}{3} \frac{\partial v_k}{\partial x_k} \delta_{ij} \right) \quad (6.15)$$

Analogously, the Reynolds stress is then approximated as

$$\widetilde{v_i''v_j''} - \frac{1}{3} \widetilde{v_k''v_k''} \delta_{ij} \approx -\nu_T \left( \frac{\partial \tilde{v}_i}{\partial x_j} + \frac{\partial \tilde{v}_j}{\partial x_i} - \frac{1}{3} \frac{\partial \tilde{v}_k}{\partial x_k} \delta_{ij} \right) \quad (6.16)$$

where  $\nu_T$  is the turbulent viscosity. Related to the turbulent viscosity hypothesis is the gradient diffusion hypothesis, that approximates the turbulent energy flux as

$$\widetilde{E''v_j''} \approx -\Gamma_T \frac{\partial \tilde{E}}{\partial x_j} \quad (6.17)$$

where  $\Gamma_T$  is the turbulent heat conductivity. According to Eq. (6.17) the energy flux  $\widetilde{E''v_j''}$  is aligned with the mean energy gradient.

It is important to grasp the underlying assumptions of the turbulent viscosity and gradient diffusion hypotheses: (1) the correlations among the velocity fluctuations and velocity-energy can be expressed as functions of the mean velocity and energy gradients, respectively, and (2) the proportionality is through a single scalar ( $\nu_T$  and  $\Gamma_T$ , respectively), i.e. the mean shear and mean energy gradient are aligned with the velocity covariance matrix and energy flux, respectively.

An advantage of Eqs. (6.16–6.17) is that no modification is required in a viscous laminar flow solver as these equations merely represent increased viscous and diffusion terms in the momentum and energy equations, respectively. The disadvantage is that the underlying assumptions do not even hold in some of the simplest flows [Pope, 2000]. One example is a turbulent pipe flow with increasing (or decreasing) cross-section, which subjects the flow to rapid distortion and as a result the mean shear rate tensor quickly becomes misaligned

with the Reynolds stress. Another example is variable-density (e.g. multi-component) flows, where the above assumptions only account for the fraction of the turbulent kinetic energy that is generated by mean shear; density-driven turbulence is not accounted for [Livescu et al., 2009].

In the literature a vast diversity of turbulence models can be found spanning the spectrum from simple algebraic relations to  $n$ -equation closure models. However, it has to be born in mind, that every RANS model is calibrated using specific benchmark cases. Therefore, it is unrealistic to expect that a single RANS model can be successfully applied in every turbulent flow problem without some model calibration. Consequently, selecting a RANS model is completely determined by the problem to be solved.

### *Spalart-Allmaras Model*

This model was developed by Spalart and Allmaras [Spalart and Allmaras, 1994], and it consists of one transport equation for the turbulent viscosity ( $\tilde{\nu}$ ). The model is geometry dependent, since it requires the normal distance from the wall ( $d$ ) used in the damping functions needed to control the turbulent viscosity in the near-wall region. Nevertheless, the model boundary conditions are straightforward and easy to implement.

It is important to include this model since besides its reliability in complex flows [Spalart, June 2000, 2000], the most popular hybrid RANS/LES model (DES) is built around this model. (The Hybrid RANS/LES model will be discussed later in this chapter.) It is important to mention that DES has gained significant attention due to its potential for predicting complex unsteady turbulent flows at low computational cost [Spalart, 2009].

For compressible flow, slightly different versions of the Spalart-Allmaras (S-A) model have been proposed – see Deck et al. [Deck et al., 2002] and Simon et al. [Simon et al., 2006]. Here for the sake of generality the model is presented using the compressible formulation found in Simon et al. [Simon et al., 2006]. However, the incompressible formulation can easily be recovered from the compressible form.

The turbulent viscosity transport equation is

$$\frac{\partial \bar{\rho} \tilde{\nu}}{\partial t} + \frac{\partial}{\partial x_j} (\bar{\rho} \tilde{\nu}_j \tilde{\nu}) = \bar{\rho} c_{b1} \tilde{S}_a \tilde{\nu} - \bar{\rho} c_{w1} f_w \left( \frac{\tilde{\nu}}{d} \right)^2 + \frac{\partial}{\partial x_j} \left( \frac{\bar{\rho}}{\sigma} (\nu + \tilde{\nu}) \frac{\partial \tilde{\nu}}{\partial x_j} \right) + \frac{\bar{\rho} c_{b2}}{\sigma} \frac{\partial \tilde{\nu}}{\partial x_j} \frac{\partial \tilde{\nu}}{\partial x_j} \quad (6.18)$$

where the damping functions and the rest of the coefficients are de-

defined as

$$f_w = g \left[ \frac{1 + c_{w3}^6}{g^6 + c_{w3}^6} \right]^{1/6}, \quad f_{v1} = \frac{\chi^3}{\chi^3 + c_{v1}^3}, \quad f_{v2} = 1 - \frac{\chi}{1 + \chi f_{v1}} \quad (6.19)$$

$$\chi = \frac{\tilde{v}}{\nu}, \quad g = r + c_{w2}(r^6 - r), \quad r = \frac{\tilde{v}}{\tilde{S}_a \kappa^2 d^2} \quad (6.20)$$

$$\tilde{S}_a = S_r + \frac{\tilde{v}}{\kappa^2 d^2} f_{v2}, \quad S_r = \sqrt{2 \tilde{R}_{ij} \tilde{R}_{ij}}, \quad \tilde{R}_{ij} = \frac{1}{2} \left( \frac{\partial \tilde{v}_i}{\partial x_j} - \frac{\partial \tilde{v}_j}{\partial x_i} \right) \quad (6.21)$$

Here,  $d$  is the normal distance from the wall and the effective turbulent eddy viscosity is defined as

$$\nu_t = \tilde{v} f_{v1}. \quad (6.22)$$

Model Coefficient	Value
$c_{b1}$	0.1355
$c_{b2}$	0.622
$c_{v1}$	7.1
$\sigma$	2/3
$c_{w1}$	$\frac{c_{b1}}{\kappa^2} + \frac{1+c_{b2}}{\sigma}$
$c_{w2}$	0.3
$c_{w3}$	2
$\kappa$	0.41
$c_{v2}$	5

Table 6.1: Spalart-Allmaras model coefficients

The model coefficients are defined in Table 6.1. Modifications to the model proposed by Spalart have been included to improve the convergence of the model in case of separating/reattaching flows [Deck et al., 2002]. Here, the  $\tilde{S}$  term is computed using the following modified relations

$$\tilde{S}_a = S_r \tilde{f}_{v3} + \frac{\tilde{v}}{\kappa^2 d^2} \tilde{f}_{v2} \quad (6.23a)$$

$$\tilde{f}_{v2} = \left( 1 + \frac{\chi}{c_{v2}} \right)^{-3} \quad (6.23b)$$

$$\tilde{f}_{v3} = \frac{(1 + \chi f_{v1})(1 - \tilde{f}_{v2})}{\chi} \quad (6.23c)$$

The boundary conditions for  $\tilde{v}$  at for solid surfaces and outflow boundaries are

$$\tilde{v}_{\Gamma_{Dwall}} = 0, \quad \tilde{v}_{\Gamma_{Din}} \sim (3 - 5)\nu_\infty, \quad \tilde{v}_{\Gamma_{Nout}} = \frac{\partial \tilde{v}}{\partial x_j} \hat{n}_j = 0 \quad (6.24)$$

where  $\nu_\infty$  is the kinematic viscosity at the free stream.

The source terms are computed at the element center, and require the following data

- Velocity gradient
- Turbulent variable  $\tilde{v}$
- Normal distance from the wall  $d$

The diffusion terms are computed at the cell faces, here the flow, turbulence variables, derivatives of the variables, and distance from the wall are required at the faces.

### *k-ε Model*

The “standard”  $k - \epsilon$  model was first presented by Jones and Launder [Jones and Launder, 1972] and Launder and Spalding [Launder and Spalding, 1974]. It consists of model equations for the most natural turbulence quantities, the turbulent kinetic energy ( $k$ ) and the energy dissipation rate ( $\epsilon$ ).

Turbulent kinetic energy

$$\frac{\partial \bar{\rho} k}{\partial t} + \frac{\partial}{\partial x_j} (\bar{\rho} \tilde{v}_j k) = \frac{\partial}{\partial x_j} \left( (\bar{\mu} + \mu_t / \sigma_k) \frac{\partial k}{\partial x_j} \right) + \bar{\tau} (v_i, v_j) \tilde{S}_{ij} - \bar{\rho} \epsilon \quad (6.25)$$

Energy dissipation rate

$$\begin{aligned} \frac{\partial \bar{\rho} \epsilon}{\partial t} + \frac{\partial}{\partial x_j} (\bar{\rho} \tilde{v}_j \epsilon) &= \frac{\partial}{\partial x_j} \left( (\bar{\mu} + \mu_t / \sigma_\epsilon) \frac{\partial \epsilon}{\partial x_j} \right) + C_{\epsilon 1} \frac{\epsilon}{k} \bar{\tau} (v_i, v_j) \tilde{S}_{ij} \\ &\quad - C_{\epsilon 2} \bar{\rho} \frac{\epsilon^2}{k} - \frac{2}{3} (2 - C_{\epsilon 1}) \bar{\rho} \epsilon \frac{\partial \tilde{v}_j}{\partial x_j} \end{aligned} \quad (6.26)$$

where,

$$\tilde{S}_{ij} = \frac{\partial \tilde{v}_i}{\partial x_j} + \frac{\partial \tilde{v}_j}{\partial x_i} \quad (6.27)$$

$$\bar{\tau} = 2\mu_t \tilde{S}_{ij} \quad (6.28)$$

and the turbulent viscosity is defined as

$$\mu_t = \rho C_\mu k^2 / \epsilon \quad (6.29)$$

The coefficients for the “standard” model are summarized in Table 6.2

A more developed version of the model implementing Renormalization Group theory was developed by Yakhot et al. [Yakhot et al., 1992]. In this model, the coefficients are computed theoretically from first principles providing strong foundations to the approach. The form of

Model Coefficient	Value
$C_{\varepsilon 1}$	1.44
$C_{\varepsilon 2}$	1.92
$C_{\mu}$	0.09
$\sigma_k$	1.0
$\sigma_{\varepsilon}$	1.3

Table 6.2: Standard  $k - \varepsilon$  model coefficients

the equations remains the same as that of the standard  $k - \varepsilon$  model as given by Eqs.(6.25) and (6.26) but with modified definition and values of the coefficients. The governing equations for the transport of  $k$  and  $\varepsilon$  are repeated here for clarity.

$$\frac{\partial \bar{\rho} k}{\partial t} + \frac{\partial}{\partial x_j} (\bar{\rho} \tilde{v}_j k) = \frac{\partial}{\partial x_j} \left( (\bar{\mu} + \frac{\mu_t}{\sigma_k}) \frac{\partial k}{\partial x_j} \right) + \bar{\tau} (v_i, v_j) \tilde{S}_{ij} - \bar{\rho} \varepsilon \quad (6.30)$$

$$\begin{aligned} \frac{\partial \bar{\rho} \varepsilon}{\partial t} + \frac{\partial}{\partial x_j} (\bar{\rho} \tilde{v}_j \varepsilon) &= \frac{\partial}{\partial x_j} \left( (\bar{\mu} + \frac{\mu_t}{\sigma_{\varepsilon}}) \frac{\partial \varepsilon}{\partial x_j} \right) + C_{\varepsilon 1} \frac{\varepsilon}{k} \bar{\tau} (v_i, v_j) \tilde{S}_{ij} \\ &\quad - C_{\varepsilon 2} \bar{\rho} \frac{\varepsilon^2}{k} - \frac{2}{3} (2 - C_{\varepsilon 1}) \bar{\rho} \varepsilon \frac{\partial \tilde{v}_j}{\partial x_j} \end{aligned} \quad (6.31)$$

where

$$C_{\varepsilon 2} = \tilde{C}_{\varepsilon 2} + \frac{C_{\mu} \eta^3 (1 - \eta / \eta_0)}{1 + \beta \eta^3} \quad (6.32)$$

and

$$\eta = \frac{k}{\varepsilon} \sqrt{2 \tilde{S}_{ij} \tilde{S}_{ij}} \quad (6.33)$$

while the rest of the coefficients derived from RNG theory assume constant values and are summarized in Table 6.3.

Model Constant	Value
$C_{\varepsilon 1}$	1.42
$\tilde{C}_{\varepsilon 2}$	1.68
$C_{\varepsilon 2}$	Eq.(6.32)
$C_{\mu}$	0.085
$\sigma_k$	0.72
$\sigma_{\varepsilon}$	0.72
$\beta$	0.012
$\eta_0$	4.38

Table 6.3: RNG  $k - \varepsilon$  model coefficients

It is well known that the  $k - \varepsilon$  model has many limitations, especially for wall-bounded flows where high values of eddy viscosity in the near-wall region are produced. For high Reynolds number flows



often encountered in many industrial applications, a full resolution using a fine mesh of the thin viscous sublayer that occurs near a wall may not be economical. Consequently, a near-wall modeling approach is usually employed to improve the accuracy of the predictions by incorporating the effects of the viscous sub-layer on the transport processes through the use of semi-empirical “wall functions”. For the current implementation, the “law-of-the-wall” approach is used to provide near-wall modeling avoiding the need for highly resolved boundary layer meshes. This approach relies on known results (law-of-the-wall) to obtain the wall shear stress. Wall functions are thus used to bridge the viscosity-dominated thin near-wall region with that of the fully turbulent regime under the assumption that this can be done with only a small deterioration of results compared to a fully resolved flow.

The law-of-the-wall is a universal velocity profile that wall-bounded flows (in the absence of pressure gradients) develop when the proper viscous scales are used to normalize the velocity and length scales. This law can be stated as follows.

$$U^+ = \begin{cases} y^+, & \text{for } y^+ \leq 11.225 \\ \frac{1}{\kappa} \ln(Ey^+), & \text{for } y^+ > 11.225 \end{cases} \quad (6.34)$$

where

$$U^+ = \frac{U}{u_\tau} \quad (6.35)$$

$$y^+ = \frac{yu_\tau}{\nu} \quad (6.35)$$

$$u_\tau = \sqrt{\frac{\tau_{wall}}{\rho}} \quad (6.36)$$

Here,  $U$  is the wall-tangent velocity,  $\nu$  is the kinematic viscosity,  $\rho$  is density,  $\tau_{wall}$  is the shear stress at the wall, and  $\kappa = 0.41$ , and  $E = 9.8$  are constants.

The standard law-of-the-wall profile is limited in its usage. For example, in recirculating flows, the turbulent kinetic energy  $k$  becomes zero at separation and reattachment points where  $\tau_{wall} = 0$ , since, by definition,  $u_\tau$  is zero. This singular behavior causes the predicted results to be erroneous. In order to overcome this, the standard law-of-the-wall is modified based on a new scale for the friction velocity following the method proposed by Launder and Spalding [Launder and Spalding, 1974]. The modified friction velocity is given by

$$u^* = C_\mu^{1/4} \sqrt{k}, \quad (6.37)$$

which does not suffer from a singular behavior at flow reattachment, separation, and at points of flow impingement. Correspondingly, the

wall distances are re-scaled as follows.

$$y^* = \frac{yu^*}{\nu} = \frac{yC_\mu^{1/4}\sqrt{k}}{\nu} \quad (6.38)$$

The modified law-of-the-wall reduces to the standard law-of-the-wall under the conditions of uniform wall shear stress and when the generation and dissipation of turbulent kinetic energy are in balance (i.e. when the turbulence structure is in equilibrium). Under such conditions,  $u^* \approx u^+$  and thus,  $y^* \approx y^+$ .

The wall shear stress for the modified law-of-the-wall is then given by (Craft et al. [Craft et al., 2002], Albets-Chico et al. [Albets-Chico et al., 2008])

$$\tau_{wall} = \begin{cases} \mu \frac{U_p}{y_p} & \text{for } y^* \leq 11.225 \\ \frac{\kappa\rho U_p u^*}{\ln(Ey_p^*)} & \text{for } y^* > 11.225 \end{cases} \quad (6.39)$$

where the subscript  $p$  denotes the wall element center at which all the quantities of interest are evaluated.

For free-stream boundary conditions, the following relations are usually implemented

$$k_{\Gamma_{Din}} = \frac{3}{2} \left[ V_\infty \left( \frac{v'}{V_\infty} \right) \right]^2 \quad (6.40a)$$

$$\varepsilon_{\Gamma_{Din}} = C_\mu^{3/4} \frac{k^{3/2}}{l} \quad (6.40b)$$

$$\varepsilon_{\Gamma_{Din}} = C_\mu \bar{\rho} \frac{k^2}{\mu} \left( \frac{\mu_T}{\mu} \right) \quad (6.40c)$$

Here,  $V_\infty$  is the free-stream velocity,  $v'$  is the intensity of the velocity fluctuations,  $l$  is the turbulent integral scale, and  $\mu_T$  is the turbulent viscosity.

The turbulent transport terms require the evaluation of the distance from the wall, the primary flow and turbulent variables, and their gradients.

### *Shear stress transport (SST) $k$ - $\omega$ model*

Due to the many pathological problems that the different families of the  $k - \varepsilon$  model exhibit, especially in wall-bounded flows with adverse pressure-gradients and flow separation, a new set of two-equation model was proposed by Wilcox [Wilcox, 1988]. The new model involves transport equations for  $k$  and  $\omega$ , here  $\omega$  loosely represents the time scale at which the turbulent kinetic energy ( $k$ ) is dissipated.

One of the main advantages of the  $k - \omega$  over the  $k - \epsilon$  model is that it does not require wall functions or low- $Re$  treatment to allow its integration to the wall, removing the additional empiricism that wall functions induce in the modeling strategy. However, it has been recognized that the predictions of the original  $k - \omega$  model suffered from an anomalous dependency on the  $\omega$  free-stream boundary condition [Menter, 1992]. The anomalous behavior was soon corrected by Menter [Menter, 1994] and Wilcox [Wilcox, 1998] among others. However, the version of Menter has been shown more robust removing the free-stream sensitivity while maintaining the advantages of the original  $k - \omega$  [Wilcox, 1998].

The strategy followed by Menter is to blend the original  $k - \omega$  and  $k - \epsilon$  ( $\epsilon$  is written in terms of  $\omega$ ) models to remove their mutual deficiencies. The  $k - \omega$  model is used in regions close to the wall where it does not require wall functions, while the  $k - \epsilon$  model is used away from the wall where it does not significantly suffer the free-stream boundary condition dependency.

The combination of the models is conducted using blending functions that depend on flow and turbulent variables. Overall, Menter's SST model has been shown to be reliable predicting external flows on adverse and favorable pressure-gradient conditions [Hutton and Ashworth, 2005, Menter, 1994]. The original compressible formulation [Menter, 1994] is reproduced here.

The turbulent transport equations for  $k$  and  $\omega$  follow

$$\frac{\partial \bar{\rho} k}{\partial t} + \frac{\partial}{\partial x_j} (\bar{\rho} \tilde{v}_j k) = \frac{\partial}{\partial x_j} \left( \bar{\rho} (\bar{v} + \sigma_k \nu_t) \frac{\partial k}{\partial x_j} \right) + \bar{\tau} (v_i, v_j) \frac{\partial \tilde{v}_i}{\partial x_j} - \beta^* \bar{\rho} k \omega \quad (6.41)$$

$$\begin{aligned} \frac{\partial}{\partial t} (\bar{\rho} \omega) + \frac{\partial}{\partial x_j} (\bar{\rho} \tilde{v}_j \omega) = & \frac{\partial}{\partial x_j} \left( \bar{\rho} (\bar{v} + \sigma_\omega \nu_t) \frac{\partial \omega}{\partial x_j} \right) - \frac{\gamma}{\nu_t} \bar{\tau} (v_i, v_j) \frac{\partial \tilde{v}_i}{\partial x_j} - \beta \bar{\rho} \omega^2 \\ & + 2(1 - F_1) \bar{\rho} \sigma_\omega \omega^2 \frac{1}{\omega} \frac{\partial k}{\partial x_j} \frac{\partial \omega}{\partial x_j} \end{aligned} \quad (6.42)$$

 Table 6.4:  $k - \omega$  SST model coefficients

$\sigma_k$	$\sigma_\omega$	$\beta$	$\gamma$	$a_1$	$\beta^*$	$\kappa$
$g(\sigma_{k1}, \sigma_{k2})$	$g(\sigma_{\omega1}, \sigma_{\omega2})$	$g(\beta_1, \beta_2)$	$g(\gamma_1, \gamma_2)$	0.31	0.09	0.41
$\sigma_{k2}$	$\sigma_{\omega2}$	$\beta_2$	$\gamma_2$			
1.0	0.856	0.0828	$\beta_2 / \beta^* - \sigma_{\omega2} \kappa^2 / \sqrt{\beta^*}$			
$\sigma_{k1}$	$\sigma_{\omega1}$	$\beta_1$	$\gamma_1$			
0.85	0.5	0.075	$\beta_1 / \beta^* - \sigma_{\omega1} \kappa^2 / \sqrt{\beta^*}$			

The blending functions are defined as follows

$$F_1 = \tanh(\chi^4), \quad \chi = \min \left( \max \left( \frac{\sqrt{k}}{0.09\omega y}; \frac{500\bar{v}}{y^2\omega} \right); \frac{4\bar{\rho}\sigma_\omega 2k}{CDy^2} \right) \quad (6.43a)$$

$$CD = \max \left( 2\bar{\rho}\sigma_\omega 2 \frac{1}{\omega} \frac{\partial k}{\partial x_j} \frac{\partial \omega}{\partial x_j}; 10^{-20} \right) \quad (6.43b)$$

and

$$F_2 = \tanh(\eta^2), \quad \eta = \max \left( 2 \frac{\sqrt{k}}{0.09\omega y}; \frac{500\bar{v}}{y^2\omega} \right). \quad (6.44)$$

The turbulent viscosity is defined as

$$\nu_t = \frac{a_1 k}{\max(a_1 \omega; \Omega F_2)} \quad (6.45)$$

Here  $\Omega$ ,  $F_1$ , and  $y$  are the vorticity magnitude, a blending function, and the wall-normal distance, respectively. The constants for the  $k - \omega$  SST model, Table 6.4, are computed by linearly combining,  $g(a, b) = F_1 a + (1 - F_1) b$ , the set of constants of the  $k - \omega$  and  $k - \varepsilon$  models. The free stream boundary conditions [Menter, 1994] can be easily implemented as follows

$$\omega_{\Gamma_{Din}} = (1 \rightarrow 10) \frac{V_\infty}{L}, \quad \nu_{\Gamma_{Din}} = 10^{-(2 \rightarrow 5)} \nu_\infty, \quad k_{\Gamma_{Din}} = \nu_{t\infty} \omega_\infty \quad (6.46)$$

Here,  $L$  is approximately the length of the domain. The wall-boundary conditions can be implemented by approximating the asymptotic  $\omega$  solution [Wilcox, 1988] at the wall with the following relation [Menter, 1994]

$$\omega_{\Gamma_{Dwall}} = 10 \frac{6\nu}{\beta_1 \Delta y_1^2}, \quad k_{\Gamma_{Dwall}} = 0 \quad (6.47)$$

It is important to mention that roughness effects can be included in the model through  $\omega$  wall-boundary conditions [Wilcox, 1988]. Thus, if we define the the average height of sand-grain roughness elements as  $k_s$ , the following boundary conditions must be implemented as long as  $k_s^+ < 400$

$$\omega = \begin{cases} 2, 500 \nu_w / k_s^2, & \text{if } k_s^2 < 25 \\ 10, 000 \nu_w / k_s^2, & \text{if } k_s^2 \geq 25 \end{cases}, \quad \text{at } y = 0 \quad (6.48)$$

Additionally, it is possible to account for non-permeable boundary conditions [Wilcox, 1988], i.e., infiltration through suction or blowing. This is accomplished through  $\omega$  boundary condition as follows

$$\omega = \frac{v_\tau^2}{\nu} \frac{25}{v_w^+ (1 + 5v_w^+)} \quad (6.49)$$

The sources have to be computed at the cell center and require the following variables:

- Gradients of the velocity and turbulent variables
- Flow and turbulent variables
- Normal distance from the wall

For the turbulent diffusion terms, the same variables are required at the faces.

### *k-ε-v<sup>2</sup>-f Model*

One of the factors that leads to inaccurate predictions in wall-bounded flow simulations using the  $k - \varepsilon$  model is that very close to the wall the velocity scale controlling the turbulent transport is  $\tilde{v}^2$  and not  $k$  [Durbin, 1991].

The so-called  $\tilde{v}^2 - f$  model was introduced in an attempt to correct the near-wall problems of the  $k - \varepsilon$  model without introducing empirical wall functions [Durbin, 1995, Parneix et al., 1998, Behnia and Parneix, 1998, Behnia et al., 1999, Lien and Kalitzin, 2001, Kalitzin et al., 2005]. This model modifies the original  $k - \varepsilon$  model and includes two additional equations. The most representative is a transport equation for the wall-normal stress  $\tilde{v}^2$ . The model has been improved over the years, and the most recent version [Kalitzin et al., 2005] is presented here

Modified  $k - \varepsilon$  model

$$\frac{\partial \bar{\rho} k}{\partial t} + \frac{\partial}{\partial x_j} (\bar{\rho} \tilde{v}_j k) = \frac{\partial}{\partial x_j} \left( \bar{\rho} (\bar{v} + \nu_t / \sigma_k) \frac{\partial k}{\partial x_j} \right) + \bar{\tau}(v_i, v_j) \frac{\partial \tilde{v}_i}{\partial x_j} - \bar{\rho} \varepsilon \quad (6.50)$$

$$\begin{aligned} \frac{\partial \bar{\rho} \varepsilon}{\partial t} + \frac{\partial}{\partial x_j} (\bar{\rho} \tilde{v}_j \varepsilon) &= \frac{\partial}{\partial x_j} \left( \bar{\rho} (\bar{v} + \nu_t / \sigma_\varepsilon) \frac{\partial \varepsilon}{\partial x_j} \right) \\ &+ \frac{1}{T} \left( c_{\varepsilon 1}^* \bar{\tau}(v_i, v_j) \frac{\partial \tilde{v}_i}{\partial x_j} - c_{\varepsilon 2} \bar{\rho} \varepsilon \right) \\ &- \frac{2}{3} (2 - c_{\varepsilon 1}^*) \bar{\rho} \varepsilon \frac{\partial \tilde{v}_j}{\partial x_j} \end{aligned} \quad (6.51)$$

Transport equation for the wall-normal  $\tilde{v}^2$  scale

$$\frac{\partial \bar{\rho} \tilde{v}^2}{\partial t} + \frac{\partial}{\partial x_j} (\bar{\rho} \tilde{v}_j \tilde{v}^2) = \frac{\partial}{\partial x_j} \left( \bar{\rho} (\bar{v} + \nu_t / \sigma_k) \frac{\partial \tilde{v}^2}{\partial x_j} \right) + \bar{\rho} k f - N \bar{\rho} \frac{\tilde{v}^2}{k} \varepsilon \quad (6.52)$$

Production equation for  $\tilde{v}^2$

$$f - L^2 \frac{\partial^2 f}{\partial x_j \partial x_j} = (c_{f1} - 1) \frac{2/3 - \tilde{v}^2/k}{T} - \frac{c_{f2}}{\bar{\rho} k} \bar{\tau}(v_i, v_j) \frac{\partial \tilde{v}_i}{\partial x_j} + (N - 1) \frac{\tilde{v}^2}{k T} \quad (6.53)$$

Here, the turbulent length scale  $L$  is defined as

$$L = C_L \max \left[ \min \left[ \frac{k^{3/2}}{\varepsilon}, \frac{k^{3/2}}{\sqrt{3\tilde{v}^2 c_\mu S}} \right], c_\eta \left( \frac{v^3}{\varepsilon} \right)^{1/4} \right] \quad (6.54)$$

The turbulent viscosity is computed as follows

$$\nu_t = c_\mu \tilde{v}^2 T \quad (6.55)$$

with the time scale  $T$  defined as

$$T = \min \left[ \max \left[ \frac{k}{\varepsilon}, 6\sqrt{\frac{v}{\varepsilon}} \right], \frac{\alpha k}{\sqrt{3\tilde{v}^2 c_\mu S}} \right] \quad (6.56)$$

$$S = \sqrt{2\tilde{S}_{ij}\tilde{S}_{ij}}, \quad \tilde{S}_{ij} = \left( \frac{\partial \tilde{v}_i}{\partial x_j} + \frac{\partial \tilde{v}_j}{\partial x_i} \right) \quad (6.57)$$

The wall no-slip boundary conditions are the following [Kalitzin et al., 2005]

$$k_{\Gamma_{Dwall}} = 0, \quad \tilde{v}^2_{\Gamma_{Dwall}} = 0, \quad \varepsilon_{\Gamma_{Dwall}} \rightarrow \frac{2\nu k}{y^2}, \quad f_{\Gamma_{Dwall}} \rightarrow \frac{4(6-N)v^2\tilde{v}^2}{\varepsilon y^4} \quad (6.58)$$

The current model coefficients impose a  $f_{\Gamma_{Dwall}} = 0$  boundary condition at the wall for the production of  $\tilde{v}^2$ , which promotes the stability of the model [Kalitzin et al., 2005]. The asymptotic relations for “ $\varepsilon$ ” can be directly implemented in grid cells located at the viscous sublayer  $y^+ < 5$ , similar to the asymptotic relation in the  $k - \omega$  model [Wilcox, 1988]. Additionally, the value of “ $\varepsilon$ ” can be estimated at the wall by one order of magnitude of the asymptotic relation value, as suggested in the  $k - \omega$  model [Menter, 1994].

$$\varepsilon_{\Gamma_{Dwall}} = 10 \frac{2\nu k}{\Delta y_1^2} \quad (6.59)$$

Here,  $\Delta y_1$  is the first grid-cell away from the wall.

$c_\mu$	$c_{\varepsilon 1}^*$	$c_{\varepsilon 2}$	$c_{f1}$	$c_{f2}$	$C_L$	$c_\eta$	$N$	$\alpha$
0.22	$1.4(1 + 0.05\sqrt{k/\tilde{v}^2})$	1.9	1.4	0.3	0.23	70	6	0.6

Table 6.5:  $k - \varepsilon - \tilde{v}^2 - f$  model coefficients

### $k - \varepsilon - \zeta - f$ Model

This model was proposed to enhance the stability of the  $k - \varepsilon - \tilde{v}^2 - f$  model by replacing the  $\tilde{v}^2$  equation with a transport equation for the velocity scale ratio  $\zeta = \tilde{v}^2/k$ , which improves the reliability of the original  $\tilde{v}^2 - f$  model [Hanjalic et al., 2004].

Modified  $k - \varepsilon$  model <sup>2</sup>

<sup>2</sup> These equations have not been modified from the original  $\tilde{v}^2 - f$  model, however they are repeated here for the sake of completeness.

$$\frac{\partial \bar{\rho}k}{\partial t} + \frac{\partial}{\partial x_j} (\bar{\rho} \tilde{v}_j k) = \frac{\partial}{\partial x_j} \left( \bar{\rho} (\bar{v} + v_t / \sigma_k) \frac{\partial k}{\partial x_j} \right) + \bar{\tau}(v_i, v_j) \frac{\partial \tilde{v}_i}{\partial x_j} - \bar{\rho} \varepsilon \quad (6.60)$$

$$\begin{aligned} \frac{\partial \bar{\rho} \varepsilon}{\partial t} + \frac{\partial}{\partial x_j} (\bar{\rho} \tilde{v}_j \varepsilon) &= \frac{\partial}{\partial x_j} \left( \bar{\rho} (\bar{v} + v_t / \sigma_\varepsilon) \frac{\partial \varepsilon}{\partial x_j} \right) \\ &+ \frac{1}{T} \left( -c_{\varepsilon 1}^* \bar{\tau}(v_i, v_j) \frac{\partial \tilde{v}_i}{\partial x_j} - c_{\varepsilon 2} \bar{\rho} \varepsilon \right) \\ &- \frac{2}{3} (2 - c_{\varepsilon 1}^*) \bar{\rho} \varepsilon \frac{\partial \tilde{v}_j}{\partial x_j} \end{aligned} \quad (6.61)$$

Transport equation for the ratio of the velocity scale  $\zeta$

$$\frac{\partial \bar{\rho} \zeta}{\partial t} + \frac{\partial}{\partial x_j} (\bar{\rho} \tilde{v}_j \zeta) = \frac{\partial}{\partial x_j} \left( \bar{\rho} (\bar{v} + v_t / \sigma_\zeta) \frac{\partial \zeta}{\partial x_j} \right) + \bar{\rho} f + \frac{\zeta}{k} \bar{\tau}(v_i, v_j) \frac{\partial \tilde{v}_i}{\partial x_j} \quad (6.62)$$

Production equation of  $\zeta$

$$L^2 \frac{\partial^2 f}{\partial x_j \partial x_j} - f = \frac{1}{T} \left( c_1 - \frac{c_2'}{\bar{\rho} \varepsilon} \bar{\tau}(v_i, v_j) \frac{\partial \tilde{v}_i}{\partial x_j} \right) \left( \zeta - \frac{2}{3} \right) \quad (6.63)$$

Here, the turbulent length scale  $L$  is defined as

$$L = C_L \max \left[ \min \left[ \frac{k^{3/2}}{\varepsilon}, \frac{k^{1/2}}{\sqrt{6\zeta c_\mu S}} \right], c_\eta \left( \frac{v^3}{\varepsilon} \right)^{1/4} \right] \quad (6.64)$$

The turbulent viscosity is computed as follows

$$v_t = c_\mu \zeta k T \quad (6.65)$$

with the time scale  $T$  defined as

$$T = \max \left[ \min \left[ \frac{k}{\varepsilon}, \frac{a}{\sqrt{6c_\mu \zeta S}} \right], c_\tau \left( \frac{v}{\varepsilon} \right)^{1/2} \right] \quad (6.66)$$

It is important to note that the  $\zeta$  equation does not include  $\varepsilon$ , instead it includes the production of  $k$  in the dissipation part. This enhances the stability of the model since the problems of  $\varepsilon$  in the near-wall regions are not present in this equation. The boundary conditions for  $k$  and  $\varepsilon$  are implemented in the same way as in the  $v^2 - f$  model. The wall boundary conditions for  $f$  and  $\zeta$  are specified as follows

$$\zeta_{\Gamma_{Dwall}} = 0, \quad f_{\Gamma_{Dwall}} \rightarrow \frac{-2v\zeta}{y^2}, \quad \text{for } y \rightarrow 0 \quad (6.67)$$

It is important to implement the  $v^2 - f$  and  $\zeta - f$  models due to their potential to fix the anomalies of the  $k - \varepsilon$  model without introducing empirical wall-functions. Additionally, these models do not need the distance from the wall, which is a significant advantage.

Model Coefficient	Value
$c_\mu$	0.22
$c_{\varepsilon 1}^*$	$1.4(1 + 0.012/\zeta)$
$c_{\varepsilon 2}$	1.9
$c_1$	0.4
$c_2'$	0.65
$\sigma_k$	1
$\sigma_\varepsilon$	1.3
$\sigma_\zeta$	1.2
$c_\tau$	6
$C_L$	0.36
$c_\eta$	85

Table 6.6:  $k - \varepsilon - \zeta - f$  model coefficients

### *Large-Eddy Simulation*

The accuracy of RANS models depends on the ability of the specific model to represent the effects of turbulent kinetic energy production, transport, and dissipation. In all RANS models, some of which are discussed in §6.3, all scales are modeled: the flow behavior must be captured at the largest scales, the inertial subrange, as well as in the dissipation range. This is a considerable difficulty as very different physics (important at the different ranges of scales) must be captured within the same model equations.

In large eddy simulation (LES) a different approach is taken. The large scales are exactly represented, while only the dissipative scales are modeled (approximated) [Sagaut, 2005]. Thus from the spectral viewpoint of the kinetic energy LES aims to resolve the energy contained in the lower wave numbers, while the energy at high wave-numbers is modeled.

In Kolmogorov's view of turbulence, see §6.1, the anisotropy of the velocity fluctuations (generated at the large scales) is gradually lost in the inertial subrange as kinetic energy cascades to smaller and smaller scales. At the smallest dissipative scales the fluctuations are assumed to be isotropic. The justification of the LES procedure relies heavily on this phenomenological picture, whose accuracy has been repeatedly validated by both experiments and DNS since Kolmogorov first proposed his hypotheses in 1941. In LES the large scales are explicitly resolved (i.e. without modeling or approximation), while a simple model, required only for the dissipative scales, are thought to suffice for most practical purposes. The hope is that the filtered equations accurately represent the important turbulence production mechanisms, and the overall prediction of the flow is then less sensitive to the model, which only acts on the small scales, whose sole purpose is dissipation



of turbulent kinetic energy.

The price-tag of LES is significantly higher than RANS models due to the increase in resolution requirements to represent a sufficiently large portion of the kinetic energy. If LES can be afforded for a problem, it is almost certainly regarded as superior to any RANS model. However, it is important to appreciate the range of applicability of LES, where the rate-controlling mechanism can be well-resolved by the computational grid [Pope, 2004]. Consequently, LES is expected to perform well in situations where the turbulence is shear-driven (i.e. mechanically-driven). On the other hand, it is easy to think of situations where LES is expected to perform poorly. Two examples are: (1) turbulent combustion, where the rate controlling mechanism, molecular-mixing-induced chemical reactions, is always at the sub-grid scale in LES [Pope, 2004]; and (2) variable-density (e.g. multi-component) turbulence, where a large fraction of the turbulent kinetic energy may be produced by density-fluctuations (as opposed to shear and vortex stretching), the flow is non-equilibrium and anisotropic at both large *and* small scales, [Livescu et al., 2009]. In these situations Kolmogorov's phenomenological picture is not justified and there is no reason to assume that LES is superior to RANS, unless special care is taken to accurately resolve all rate-controlling mechanisms.

### LES Governing Equations

In LES the flow variables are filtered with a kernel function,  $G$ ,

$$\bar{\phi}(X, t) = \int_{-\infty}^{+\infty} G(X - r, \Delta) \phi(r, t) dr \quad (6.68)$$

where  $\Delta$  is the filter width. Filtering results in an additive decomposition

$$\phi = \bar{\phi} + \phi' \quad (6.69)$$

The above filtering can be weighted with the fluid density, resulting in Favre filtering, in analogy with Favre averaging. Applying Favre filtering to the instantaneous conservation equations results in a set of Favre *filtered* equations, which formally look like the ensemble-averaged equations (6.12–6.14). These equations govern the filtered flow quantities, which represent the *resolved* scales. The equations are unclosed: the effects of the *unresolved* scales must be accounted for based on some physical insight.

There are different approaches to LES filtering. Filters can be explicit or implicit. Explicit filtering explicitly performs Eq. (6.68) on the computed fluctuating flow field. Depending on the filter function,  $G$ , the decomposition in Eq. (6.69) yields different fields. Implicit filtering relies on the numerical grid to perform the filtering; the resulting de-

composition will be different on different grids and different parts of the computational domain.

The representation of the unresolved scales can also be explicit or implicit. Explicit models explicitly add model terms to the filtered continuum equations. An example is to employ the turbulent viscosity hypothesis with the turbulent viscosity computed via Smagorinsky's model, discussed in §6.4, which is analogous to Prandtl's mixing length model in the Reynolds averaged context. Implicit models rely on the dissipative properties of the applied numerical method, resulting in implicit large eddy simulation (ILES), or, if the numerical treatment ensures monotonicity, monotonically integrated implicit LES (MILES) [Grinstein et al., 2007].

Though the filtered equations formally look like the Reynolds averaged equations, there is an important difference: Statistical averaging results in well-defined deterministic quantities (whose rigorous definitions are based on probability theory), while the filtered fields in LES are random with a fundamental dependence on the artificial (i.e. non-physical) parameter  $\Delta$ , the mesh spacing, and the numerical method. Consequently, LES and its practice raise non-trivial conceptual and numerical questions [Pope, 2004].

### *The Smagorinsky Model*

The Smagorinsky model serves as a baseline for comparison to other models. One of the earliest LES models was proposed by Smagorinsky [Smagorinsky, 1963], which accounts for the unresolved scales via the turbulent viscosity hypothesis and computing the turbulent viscosity by a simple dimensional model

$$\mu_{sgs} = \rho(C_s \Delta)^2 S \quad (6.70)$$

where  $\Delta$  is the length scale and is also assumed to be the filter width. Practical LES formulations rarely implement explicit filters and only rely on the mesh as the filter, i.e., the scales filtered are those that the grid cannot resolve and thus are understood as being filtered. Since it is virtually impossible to provide a mathematical relation for the grid filter and thus the filter width, different techniques have been proposed to compute this length scale. The most common approach is to relate this scale to the mesh cube root of the mesh volume since the largest eddies not resolved are in the order of the mesh size. For more elaborate formulas to compute this length scale on anisotropic grids see Scotti et al. [Scotti et al., 1997].

$$\Delta = (\Delta x \Delta y \Delta z)^{1/3} \quad (6.71)$$

The time scale of the model is then obtained from the magnitude of the strain rate

$$S = \sqrt{2\tilde{S}_{ij}\tilde{S}_{ij}} \quad (6.72)$$

The dimensional approximation is made an equality through the Smagorinsky constant  $C_s$ , whose value is calibrated in isotropic turbulence and is found to be  $0.1 \leq C_s \leq 0.2$ .

### *The Wall-Adapted Large Eddy Model*

The wall-adapted large eddy (WALE) model [Nicoud and Ducros, 1999] computes the unresolved-scale dissipation by employing the turbulent viscosity hypothesis (similar to the Smagorinsky model), but the turbulent viscosity is determined based on both the filtered-scale shear,  $\bar{S}_{ij}$ , and the square of filtered-scale velocity gradient,  $\bar{g}_{ij}$ ,

$$\nu_T = (C_W \Delta)^2 \frac{(S_{ij}^d S_{ij}^d)^{3/2}}{(\bar{S}_{ij} \bar{S}_{ij})^{5/2} + (S_{ij}^d S_{ij}^d)^{5/4}} \quad (6.73)$$

where  $C_W = 0.5$ ,  $\Delta = V^{1/3}$ ,

$$S_{ij}^d = \frac{1}{2} (\bar{g}_{ij}^2 + \bar{g}_{ji}^2) - \frac{1}{3} \bar{g}_{kk}^2 \delta_{ij} \quad \text{with} \quad \bar{g}_{ij} = \frac{\partial \bar{v}_i}{\partial x_j} \quad (6.74)$$

$$\bar{S}_{ij} = \frac{1}{2} \left( \frac{\partial \bar{v}_i}{\partial x_j} + \frac{\partial \bar{v}_j}{\partial x_i} \right) \quad (6.75)$$

According to Nicoud & Ducros [Nicoud and Ducros, 1999], compared to the Smagorinsky model, the WALE model has the following advantages:

- It accounts for both local strain and rotation, which has the potential to capture the full production of turbulent kinetic energy in shear-driven flows.
- The turbulent viscosity approaches zero at the wall, consequently no adjustment of the model constant or damping function is necessary in the vicinity of the wall. Only local information is required to compute the turbulent viscosity. As a consequence, the model is well-suited for complex flow geometries.
- The model is invariant to coordinate translation and rotation.
- The turbulent viscosity cannot be negative or infinite.

### *The Localized Dynamic $k_{sgs}$ -Equation Model*

In the localized dynamic  $k_{sgs}$ -equation model the unresolved-scale viscosity,  $\nu_{sgs}$ , and unresolved (or subgrid) kinetic energy,  $k_{sgs}$ , are modeled using the localized dynamic  $k$ -equation model (LDKM), due to

its success predicting complex and fundamental turbulent flows [Kim and Menon, 1999, Menon and Patel, 2006]

$$\frac{\partial \bar{\rho} k_{sgs}}{\partial t} + \frac{\partial}{\partial x_j} (\bar{\rho} \tilde{v}_j k_{sgs}) = \frac{\partial}{\partial x_j} \left( \bar{\rho} (\bar{v}/Pr + \nu_{sgs}) \frac{\partial k_{sgs}}{\partial x_j} \right) - \bar{\tau}(v_i, v_j) \frac{\partial \tilde{v}_i}{\partial x_j} - C_\epsilon \bar{\rho} \frac{k_{sgs}^{3/2}}{\Delta}. \quad (6.76)$$

$$\nu_{sgs} = C_\nu \Delta \sqrt{k_{sgs}} \quad (6.77)$$

Here,  $C_\nu$  and  $C_\epsilon$  are LES coefficients that are obtained dynamically as a part of the solution using a scale similarity approach. Further details on the dynamic evaluation can be found in the original references [Kim and Menon, 1999, Menon and Patel, 2006].

### *Hybrid RANS/LES*

The properties of additive filters, constructed by blending two or more independent operators in the framework of computational fluid dynamics, were formally described by Germano [Germano, 2004] and Sánchez-Rocha and Menon [Sánchez-Rocha and Menon, 2009]. In particular, they defined a hybrid RANS/LES filter by blending the RANS statistical operator and the LES filter operator and went on to derive the hybrid incompressible Navier-Stokes equations. The resulting differential equations depend explicitly on the hybrid variables, on the statistical operator, and on the filtered quantities, increasing the number of independent variables. To close the equations, Germano introduced a simple reconstruction procedure, which in theory allows the calculation of the statistical and the filtered fields from the hybrid variables. Germano did not conduct any numerical simulation to support the the new formulation. His work has been continued by extending the hybrid formulation to compressible flows and conducting numerical calculations to prove the importance of the exact formulation.

### *Hybrid RANS/LES Operators*

Having defined the RANS and the LES operators, a hybrid additive operator and its Favre representation can be constructed by combining Eq. (6.8) and (6.68) with a blending function

$$\bar{\phi}(X, t) = \mathcal{F} \dot{\bar{\phi}}(X, t) + (1 - \mathcal{F}) \ddot{\bar{\phi}}(X, t) \quad (6.78)$$

$$\tilde{\phi}(X, t) = \frac{\bar{\rho} \phi}{\bar{\rho}}. \quad (6.79)$$

In order to present the hybrid formulation without ambiguity, a slight change in notation is required. The RANS operators are identified us-

ing an over dot,  $(\dot{\phi})$  and  $(\check{\phi})$ , whereas the LES operators are identified using two over dots  $(\ddot{\phi})$  and  $(\overset{\circ}{\phi})$ .

Here,  $\mathcal{F}$  is a normalized function that in general, depends on time and space. It is defined as  $\mathcal{F} : \{ (\| X \|, t) \in [0, \infty) \rightarrow \mathcal{F}(X, t) \in [0, 1] \}$ . Furthermore, it must have continuous derivatives to at least second order in space and first order in time, i.e.,  $\mathcal{F}(X, t)$  is a  $C^2(x_i)$  and  $C^1(t)$  function (this will be evident when the hybrid equations are derived). Under this hybrid definition, Eq. (6.78) recovers RANS and LES variables when  $\mathcal{F} = 1$  and  $\mathcal{F} = 0$ , respectively. Similar to RANS and LES, the unsteady variable ( $\phi$ ) can be constructed using the hybrid variables with the standard decomposition

$$\phi = \bar{\phi} + \phi', \quad \phi = \tilde{\phi} + \phi''. \quad (6.80)$$

Here, the hybrid fluctuations can be easily shown to be related to the RANS and LES fluctuations as

$$\phi' = \mathcal{F}\dot{\phi}' + (1 - \mathcal{F})\dot{\phi}'' \quad (6.81)$$

and

$$\phi'' = \mathcal{F}\frac{\dot{\rho}}{\rho}\dot{\phi}'' + (1 - \mathcal{F})\frac{\ddot{\rho}}{\rho}\dot{\phi}'''. \quad (6.82)$$

It can also be shown that, in general, the hybrid filter Eq. (6.78) does not commute with differentiation and does not satisfy all the Reynolds rules of averaging regardless of the properties of the constitutive operators. Thus,

$$\overline{\frac{\partial \phi}{\partial x_i}} = \frac{\partial \bar{\phi}}{\partial x_i} + \frac{\partial \mathcal{F}}{\partial x_i}(\ddot{\phi} - \dot{\phi}) \quad (6.83a)$$

$$\overline{\frac{\partial \phi}{\partial t}} = \frac{\partial \bar{\phi}}{\partial t} + \frac{\partial \mathcal{F}}{\partial t}(\ddot{\phi} - \dot{\phi}) \quad (6.83b)$$

$$\overline{\phi + \psi} = \bar{\phi} + \bar{\psi}, \quad (6.84a)$$

$$\bar{\alpha} = \alpha, \quad (6.84b)$$

$$\overline{\alpha \phi} = \alpha \bar{\phi}, \quad (6.84c)$$

$$\overline{\phi \psi} \neq \bar{\phi} \bar{\psi}, \quad (6.84d)$$

$$\bar{\phi} \neq \dot{\phi}, \quad \tilde{\phi} \neq \check{\phi}, \quad (6.84e)$$

$$\bar{\phi}' \neq 0, \quad \bar{\phi}'' \neq 0, \quad (6.84f)$$

$$\overline{\rho \phi'} \neq 0, \quad \overline{\rho \phi''} \neq 0, \quad (6.84g)$$

since

$$\bar{\phi} = (2 - \mathcal{F})\mathcal{F}\dot{\phi} + (1 - \mathcal{F})^2\dot{\phi}'''. \quad (6.85)$$

Here,  $\alpha$  and  $\psi$  are a constant and an unsteady function similar to  $\phi$ , respectively. Equations (6.83) and (6.85) indicate that the hybrid filter does not commute with differentiation, and the application of the hybrid operator on the hybrid variable does not recover the same hybrid variable, i.e.,  $\overline{\overline{\phi}} \neq \overline{\phi}$ . These are general properties of this hybrid operator and do not depend on the constitutive operators.

The last relevant property of the hybrid operator is related to its ability to reconstruct the RANS and the LES variables if the hybrid field is known. Germano [Germano, 2004] showed that by applying Eq. (6.8) in Eq. (6.78), the RANS variable can be calculated directly from the hybrid variable as

$$\dot{\overline{\phi}} = \overline{\dot{\phi}}. \quad (6.86)$$

Once the RANS field is known, the LES variable can be obtained by substituting Eq. (6.86) in Eq. (6.78)

$$\ddot{\overline{\phi}} = \frac{\overline{\phi} - \mathcal{F}\dot{\overline{\phi}}}{1 - \mathcal{F}}. \quad (6.87)$$

To extend Germano's original incompressible formulation to compressible flow, the governing equations have to be derived using the generalized second-order central moments [Germano, 1992]. This gives a better representation of the unclosed terms that appears when the operator is applied in the non linear terms. This way, the final equations are invariant with respect to the operators employed. For the compressible formulation, the generalized second-order central moments are defined as

$$\overline{\tau}(a, b) = \overline{\rho}(\widetilde{a\tilde{b}} - \widetilde{a}\widetilde{b}), \quad \overline{\chi}(a, b) = \overline{a\tilde{b}} - \widetilde{a}\widetilde{b}, \quad \overline{\zeta}(a, b) = \overline{a\tilde{b}} - \widetilde{a}\widetilde{b} \quad (6.88)$$

Here,  $a$  and  $b$  are dummy variables, and  $\tau$ ,  $\chi$ , and  $\zeta$  represent, the compressible operators required by the RANS, the LES, and the hybrid formulations respectively. It is important to highlight that  $\tau$  and  $\zeta$  are symmetric operators while  $\chi$  is not. Additionally, both  $\chi$  and  $\zeta$  operators are required to account for the additional nonlinear terms present in the energy equation, and therefore they do not appear in Germano's [Germano, 2004] incompressible formulation. By substituting Eqs. (6.78) and (6.79) in Eq. (6.88), the dependency of the hybrid central moments on the RANS and LES variables can be shown to be

$$\begin{aligned} \overline{\tau}(a, b) = & \mathcal{F}\overline{\tau}(a, b) + (1 - \mathcal{F})\overline{\tau}(a, b) \\ & + \overline{\rho} \left[ \mathcal{F} \left( 1 - \mathcal{F} \frac{\overline{\rho}}{\rho} \right) \frac{\overline{\rho}}{\rho} \widetilde{a\tilde{b}} - \mathcal{F} (1 - \mathcal{F}) \frac{\overline{\rho}}{\rho^2} \widetilde{a\tilde{b}} \right] \\ & + \overline{\rho} \left[ (1 - \mathcal{F}) \left( 1 - (1 - \mathcal{F}) \frac{\overline{\rho}}{\rho} \right) \frac{\overline{\rho}}{\rho} \widetilde{a\tilde{b}} - \mathcal{F} (1 - \mathcal{F}) \frac{\overline{\rho}}{\rho^2} \widetilde{a\tilde{b}} \right] \end{aligned} \quad (6.89)$$

$$\begin{aligned}
\bar{\chi}(a, b) &= \mathcal{F}\dot{\bar{\chi}}(a, b) + (1 - \mathcal{F})\ddot{\bar{\chi}}(a, b) \\
&+ \left[ \mathcal{F} \left( 1 - \mathcal{F} \frac{\dot{\bar{\rho}}}{\bar{\rho}} \right) \dot{\bar{a}}\dot{\bar{b}} - \mathcal{F}(1 - \mathcal{F}) \frac{\dot{\bar{\rho}}}{\bar{\rho}} \dot{\bar{a}}\dot{\bar{b}} \right] \\
&+ \left[ (1 - \mathcal{F}) \left( 1 - (1 - \mathcal{F}) \frac{\ddot{\bar{\rho}}}{\bar{\rho}} \right) \ddot{\bar{a}}\ddot{\bar{b}} - \mathcal{F}(1 - \mathcal{F}) \frac{\ddot{\bar{\rho}}}{\bar{\rho}} \ddot{\bar{a}}\ddot{\bar{b}} \right]
\end{aligned} \tag{6.90}$$

$$\begin{aligned}
\bar{\zeta}(a, b) &= \mathcal{F}\dot{\bar{\zeta}}(a, b) + (1 - \mathcal{F})\ddot{\bar{\zeta}}(a, b) \\
&+ \left[ \mathcal{F} \left( 1 - \mathcal{F} \frac{\dot{\bar{\rho}}^2}{\bar{\rho}^2} \right) \dot{\bar{a}}\dot{\bar{b}} - \mathcal{F}(1 - \mathcal{F}) \frac{\dot{\bar{\rho}}}{\bar{\rho}^2} \dot{\bar{a}}\dot{\bar{b}} \right] \\
&+ \left[ (1 - \mathcal{F}) \left( 1 - (1 - \mathcal{F}) \frac{\ddot{\bar{\rho}}^2}{\bar{\rho}^2} \right) \ddot{\bar{a}}\ddot{\bar{b}} - \mathcal{F}(1 - \mathcal{F}) \frac{\ddot{\bar{\rho}}}{\bar{\rho}^2} \ddot{\bar{a}}\ddot{\bar{b}} \right]
\end{aligned} \tag{6.91}$$

It is trivial to show that these equations recover RANS and LES central moments when  $\mathcal{F} = 1$  and  $\mathcal{F} = 0$ , respectively. Using the above operator, the hybrid Reynolds stress tensor is constructed by operating Eq. (6.89) on  $v_i$  and  $v_j$

$$\begin{aligned}
\bar{\tau}(v_i, v_j) &= \mathcal{F}\dot{\bar{\rho}}(\dot{\bar{v}}_i\dot{\bar{v}}_j - \dot{\bar{v}}_i\dot{\bar{v}}_j) + (1 - \mathcal{F})\ddot{\bar{\rho}}(\ddot{\bar{v}}_i\ddot{\bar{v}}_j - \ddot{\bar{v}}_i\ddot{\bar{v}}_j) \\
&+ \bar{\rho} \left[ \mathcal{F} \left( 1 - \mathcal{F} \frac{\dot{\bar{\rho}}}{\bar{\rho}} \right) \frac{\dot{\bar{\rho}}}{\bar{\rho}} \dot{\bar{v}}_i\dot{\bar{v}}_j - \mathcal{F}(1 - \mathcal{F}) \frac{\dot{\bar{\rho}}}{\bar{\rho}^2} \dot{\bar{v}}_i\dot{\bar{v}}_j \right] \\
&+ \bar{\rho} \left[ (1 - \mathcal{F}) \left( 1 - (1 - \mathcal{F}) \frac{\ddot{\bar{\rho}}}{\bar{\rho}} \right) \frac{\ddot{\bar{\rho}}}{\bar{\rho}} \ddot{\bar{v}}_i\ddot{\bar{v}}_j - \mathcal{F}(1 - \mathcal{F}) \frac{\ddot{\bar{\rho}}}{\bar{\rho}^2} \ddot{\bar{v}}_i\ddot{\bar{v}}_j \right].
\end{aligned} \tag{6.92}$$

It is clear that the compressible generic central moments in their explicit form include density ratios induced by the Favre formulation that do not appear in the incompressible formulation of Germano [Germano, 2004]. However, it is easy to show, and it will be shown, that for incompressible flow, Eq. (6.92) reduces to the incompressible hybrid Reynolds stress tensor derived by Germano.

### Compressible Hybrid RANS/LES Navier-Stokes Equations

Having established the required hybrid operators, Eqs. (6.78)-(6.91), they are applied to the compressible Navier-Stokes equations Eqs. (1.4)-(1.6).

$$\frac{\partial \bar{\rho}}{\partial t} + \frac{\partial}{\partial x_j} (\bar{\rho} \tilde{v}_j) = \frac{\partial \mathcal{F}}{\partial x_j} [\dot{\bar{\rho}} \dot{\tilde{v}}_j - \ddot{\bar{\rho}} \ddot{\tilde{v}}_j] + \frac{\partial \mathcal{F}}{\partial t} [\dot{\bar{\rho}} - \ddot{\bar{\rho}}] \tag{6.93}$$

$$\begin{aligned}
\frac{\partial \bar{\rho} \tilde{v}_i}{\partial t} + \frac{\partial}{\partial x_j} (\bar{\rho} \tilde{v}_i \tilde{v}_j + \bar{p} \delta_{ij} - \tilde{\tau}_{ij} + \bar{\tau}(v_i, v_j)) = \\
\frac{\partial \mathcal{F}}{\partial x_j} \left[ \dot{\rho} \dot{\tilde{v}}_i \dot{\tilde{v}}_j - \ddot{\rho} \ddot{\tilde{v}}_i \ddot{\tilde{v}}_j + \dot{\bar{\tau}}(v_i, v_j) - \ddot{\bar{\tau}}(v_i, v_j) \right. \\
\left. + (\dot{\bar{p}} - \ddot{\bar{p}}) \delta_{ij} - (\dot{\tilde{\tau}}_{ij} - \ddot{\tilde{\tau}}_{ij}) \right] \\
- \frac{\partial}{\partial x_j} \left\{ \frac{\partial \mathcal{F}}{\partial x_j} (\dot{\mu} \dot{\tilde{v}}_i - \ddot{\mu} \ddot{\tilde{v}}_i) + \frac{\partial \mathcal{F}}{\partial x_i} (\dot{\mu} \dot{\tilde{v}}_j - \ddot{\mu} \ddot{\tilde{v}}_j) \right. \\
\left. - \frac{2}{3} \frac{\partial \mathcal{F}}{\partial x_k} (\dot{\mu} \dot{\tilde{v}}_k - \ddot{\mu} \ddot{\tilde{v}}_k) \delta_{ij} \right\} + \frac{\partial \mathcal{F}}{\partial t} [\dot{\rho} \dot{\tilde{v}}_i - \ddot{\rho} \ddot{\tilde{v}}_i]
\end{aligned} \tag{6.94}$$

$$\begin{aligned}
\frac{\partial \bar{\rho} \tilde{E}}{\partial t} + \frac{\partial}{\partial x_j} \left( \bar{\rho} \tilde{E} \tilde{v}_j + \bar{p} \tilde{v}_j - \bar{\kappa} \frac{\partial \tilde{T}}{\partial x_j} - \tilde{\tau}_{ij} \tilde{v}_i + \bar{\tau}(E, v_j) \right. \\
\left. + \bar{\chi}(v_j, p) - \bar{\chi} \left( \frac{\partial T}{\partial x_j}, \kappa \right) - \bar{\zeta}(\tau_{ij}, v_i) \right) = \\
\frac{\partial \mathcal{F}}{\partial x_j} \left\{ \dot{\rho} \dot{\tilde{v}}_i \dot{\tilde{E}} - \ddot{\rho} \ddot{\tilde{v}}_i \ddot{\tilde{E}} + \dot{\bar{\tau}}(E, v_j) - \ddot{\bar{\tau}}(E, v_j) \right. \\
\left. + \dot{\tilde{v}}_j \dot{\bar{p}} - \ddot{\tilde{v}}_j \ddot{\bar{p}} + \dot{\bar{\chi}}(v_j, p) - \ddot{\bar{\chi}}(v_j, p) \right. \\
\left. - \left( \dot{\bar{\kappa}} \frac{\partial \tilde{T}}{\partial x_j} - \ddot{\bar{\kappa}} \frac{\partial \tilde{T}}{\partial x_j} + \dot{\bar{\chi}} \left( \frac{\partial T}{\partial x_j}, \kappa \right) - \ddot{\bar{\chi}} \left( \frac{\partial T}{\partial x_j}, \kappa \right) \right) \right. \\
\left. - \left( \dot{\tilde{\tau}}_{ij} \dot{\tilde{v}}_i - \ddot{\tilde{\tau}}_{ij} \ddot{\tilde{v}}_i + \dot{\bar{\zeta}}(\tau_{ij}, v_i) - \ddot{\bar{\zeta}}(\tau_{ij}, v_i) \right) \right\} \\
+ \frac{\partial \mathcal{F}}{\partial t} [\dot{\rho} \dot{\tilde{E}} - \ddot{\rho} \ddot{\tilde{E}}]
\end{aligned} \tag{6.95}$$

with the pressure, shear stress tensor, and total energy defined as

$$\bar{p} = \bar{\rho} R \tilde{T} \tag{6.96}$$

$$\tilde{\tau}_{ij} = 2\bar{\mu} \left( \tilde{S}_{ij} - \frac{1}{3} \tilde{S}_{kk} \delta_{ij} \right), \quad \tilde{S}_{ij} = \frac{1}{2} \left( \frac{\partial \tilde{v}_i}{\partial x_j} + \frac{\partial \tilde{v}_j}{\partial x_i} \right), \tag{6.97a}$$

$$\dot{\tilde{\tau}}_{ij} = 2\dot{\bar{\mu}} \left( \dot{\tilde{S}}_{ij} - \frac{1}{3} \dot{\tilde{S}}_{kk} \delta_{ij} \right), \quad \dot{\tilde{S}}_{ij} = \frac{1}{2} \left( \frac{\partial \dot{\tilde{v}}_i}{\partial x_j} + \frac{\partial \dot{\tilde{v}}_j}{\partial x_i} \right), \tag{6.97b}$$

$$\ddot{\tilde{\tau}}_{ij} = 2\ddot{\bar{\mu}} \left( \ddot{\tilde{S}}_{ij} - \frac{1}{3} \ddot{\tilde{S}}_{kk} \delta_{ij} \right), \quad \ddot{\tilde{S}}_{ij} = \frac{1}{2} \left( \frac{\partial \ddot{\tilde{v}}_i}{\partial x_j} + \frac{\partial \ddot{\tilde{v}}_j}{\partial x_i} \right) \tag{6.97c}$$

$$\bar{\rho} \tilde{E} = \bar{\rho} C_v \tilde{T} + \frac{\bar{\rho}}{2} \tilde{v}_i \tilde{v}_i + \frac{1}{2} \bar{\tau}(v_i, v_i) \tag{6.98a}$$

$$\dot{\bar{\rho}} \dot{\tilde{E}} = \dot{\bar{\rho}} C_v \dot{\tilde{T}} + \frac{\dot{\bar{\rho}}}{2} \dot{\tilde{v}}_i \dot{\tilde{v}}_i + \frac{1}{2} \dot{\bar{\tau}}(v_i, v_i) \tag{6.98b}$$

$$\ddot{\bar{\rho}} \ddot{\tilde{E}} = \ddot{\bar{\rho}} C_v \ddot{\tilde{T}} + \frac{\ddot{\bar{\rho}}}{2} \ddot{\tilde{v}}_i \ddot{\tilde{v}}_i + \frac{1}{2} \ddot{\bar{\tau}}(v_i, v_i) \tag{6.98c}$$



As expected, the application of the hybrid operator to the Navier-Stokes equations results in unclosed terms that need to be modeled. Furthermore, the hybrid operator introduces new terms into the final equations. These terms are

$$\sigma_\rho = \frac{\partial \mathcal{F}}{\partial x_j} [\dot{\rho}\dot{v}_j - \ddot{\rho}\ddot{v}_j] + \frac{\partial \mathcal{F}}{\partial t} [\dot{\rho} - \ddot{\rho}] \quad (6.99)$$

$$\begin{aligned} \sigma_{\rho v_i} = & \frac{\partial \mathcal{F}}{\partial x_j} \left[ \dot{\rho}\dot{v}_i\dot{v}_j - \ddot{\rho}\ddot{v}_i\ddot{v}_j + \dot{\tau}(v_i, v_j) - \ddot{\tau}(v_i, v_j) \right. \\ & \left. + (\dot{p} - \ddot{p})\delta_{ij} - (\dot{\tau}_{ij} - \ddot{\tau}_{ij}) \right] \\ & - \frac{\partial}{\partial x_j} \left\{ \frac{\partial \mathcal{F}}{\partial x_j} (\dot{\mu}\dot{v}_i - \ddot{\mu}\ddot{v}_i) + \frac{\partial \mathcal{F}}{\partial x_i} (\dot{\mu}\dot{v}_j - \ddot{\mu}\ddot{v}_j) \right. \\ & \left. - \frac{2}{3} \frac{\partial \mathcal{F}}{\partial x_k} (\dot{\mu}\dot{v}_k - \ddot{\mu}\ddot{v}_k)\delta_{ij} \right\} + \frac{\partial \mathcal{F}}{\partial t} [\dot{\rho}\dot{v}_i - \ddot{\rho}\ddot{v}_i] \end{aligned} \quad (6.100)$$

$$\begin{aligned} \sigma_{\rho E} = & \frac{\partial \mathcal{F}}{\partial x_j} \left\{ \dot{\rho}\dot{v}_j\dot{E} - \ddot{\rho}\ddot{v}_j\ddot{E} + \dot{\tau}(E, v_j) - \ddot{\tau}(E, v_j) \right. \\ & \left. + \dot{v}_j\dot{p} - \ddot{v}_j\ddot{p} + \dot{\chi}(v_j, p) - \ddot{\chi}(v_j, p) \right. \\ & \left. - \left( \dot{\kappa} \frac{\partial \dot{T}}{\partial x_j} - \ddot{\kappa} \frac{\partial \dot{T}}{\partial x_j} + \dot{\chi} \left( \frac{\partial T}{\partial x_j}, \kappa \right) - \ddot{\chi} \left( \frac{\partial T}{\partial x_j}, \kappa \right) \right) \right. \\ & \left. - \left( \dot{\tau}_{ij}\dot{v}_i - \ddot{\tau}_{ij}\ddot{v}_i + \dot{\zeta}(\tau_{ij}, v_i) - \ddot{\zeta}(\tau_{ij}, v_i) \right) \right\} \\ & + \frac{\partial \mathcal{F}}{\partial t} [\dot{\rho}\dot{E} - \ddot{\rho}\ddot{E}] \end{aligned} \quad (6.101)$$

and

$$\begin{aligned} \sigma_{\dot{\tau}(a,b)} = & \dot{\rho} \left[ \mathcal{F} \left( 1 - \mathcal{F} \frac{\dot{\rho}}{\rho} \right) \frac{\dot{\rho}}{\rho} \dot{a}\dot{b} - \mathcal{F} \left( 1 - \mathcal{F} \right) \frac{\dot{\rho}}{\rho^2} \dot{a}\dot{b} \right] \\ & + \dot{\rho} \left[ \left( 1 - \mathcal{F} \right) \left( 1 - \left( 1 - \mathcal{F} \right) \frac{\dot{\rho}}{\rho} \right) \frac{\dot{\rho}}{\rho} \dot{a}\dot{b} - \mathcal{F} \left( 1 - \mathcal{F} \right) \frac{\dot{\rho}}{\rho^2} \dot{a}\dot{b} \right] \end{aligned} \quad (6.102)$$

$$\begin{aligned} \sigma_{\dot{\chi}(a,b)} = & \left[ \mathcal{F} \left( 1 - \mathcal{F} \frac{\dot{\rho}}{\rho} \right) \dot{a}\dot{b} - \mathcal{F} \left( 1 - \mathcal{F} \right) \frac{\dot{\rho}}{\rho} \dot{a}\dot{b} \right] \\ & + \left[ \left( 1 - \mathcal{F} \right) \left( 1 - \left( 1 - \mathcal{F} \right) \frac{\dot{\rho}}{\rho} \right) \dot{a}\dot{b} - \mathcal{F} \left( 1 - \mathcal{F} \right) \frac{\dot{\rho}}{\rho} \dot{a}\dot{b} \right] \end{aligned} \quad (6.103)$$

$$\begin{aligned} \sigma_{\dot{\zeta}(a,b)} = & \left[ \mathcal{F} \left( 1 - \mathcal{F} \frac{\dot{\rho}^2}{\rho^2} \right) \dot{a}\dot{b} - \mathcal{F} \left( 1 - \mathcal{F} \right) \frac{\dot{\rho}}{\rho^2} \dot{a}\dot{b} \right] \\ & + \left[ \left( 1 - \mathcal{F} \right) \left( 1 - \left( 1 - \mathcal{F} \right) \frac{\dot{\rho}^2}{\rho^2} \right) \dot{a}\dot{b} - \mathcal{F} \left( 1 - \mathcal{F} \right) \frac{\dot{\rho}}{\rho^2} \dot{a}\dot{b} \right] \end{aligned} \quad (6.104)$$

Equations (6.99)-(6.101) represent turbulent terms that contribute to the governing equations during the RANS to LES transition (RTLTL) zone. They occur due to the lack of commutation between hybrid operator and differentiation. Similarly, the hybrid terms (Eqs. (6.102)-(6.104)) are also only relevant in the RTLTL zone, originate due to the non-linearity of the hybrid central moments, and consist of products between RANS and LES variables. In the following, Eqs. (6.99)-(6.104) will be referred to as “hybrid contributions” or “hybrid terms” indistinctly. Note that these terms become infinite if the blending function implemented in the hybrid operator is discontinuous. Therefore, a well defined hybrid formulation requires at least a  $C^2(x_i)$  and  $C^1(t)$  “ $\mathcal{F}$ ” function.

The hybrid contributions provide the mechanism that keeps the balance between modeled and resolved scales in the RTLTL zone, where neither RANS nor LES completely models nor resolves the turbulence of the flow. In order to demonstrate this point, let us further analyze the hybrid contributions. To simplify the analysis, Eqs. (6.88) are substituted in Eqs. (6.99)-(6.101), and additionally it is assumed that the turbulence is only weakly affected by compressibility effects, which is a valid assumption provided that the fluctuating Mach number is  $Ma' < 0.3$  [Spina et al., 1994]. Therefore, all density ratios appearing in Eqs. (6.102)-(6.104) can be assumed as unity for this discussion. It is also assumed that the blending function  $\mathcal{F}$  is continuous and a function of space only, with bounded first and second order derivatives. Under these conditions Eqs. (6.99)-(6.104) reduce to

$$\sigma_\rho = \frac{\partial \mathcal{F}}{\partial x_j} [\dot{\rho}\dot{v}_j - \ddot{\rho}\ddot{v}_j] \quad (6.105)$$

$$\begin{aligned} \sigma_{\rho v_i} = & \frac{\partial \mathcal{F}}{\partial x_j} [\dot{\rho}\dot{v}_i\dot{v}_j - \ddot{\rho}\ddot{v}_i\ddot{v}_j + (\dot{p} - \ddot{p})\delta_{ij} - (\dot{\tau}_{ij} - \ddot{\tau}_{ij})] \\ & - \frac{\partial}{\partial x_j} \left\{ \frac{\partial \mathcal{F}}{\partial x_j} (\dot{\mu}\dot{v}_i - \ddot{\mu}\ddot{v}_i) + \frac{\partial \mathcal{F}}{\partial x_i} (\dot{\mu}\dot{v}_j - \ddot{\mu}\ddot{v}_j) - \frac{2}{3} \frac{\partial \mathcal{F}}{\partial x_k} (\dot{\mu}\dot{v}_k - \ddot{\mu}\ddot{v}_k) \delta_{ij} \right\} \end{aligned} \quad (6.106)$$

$$\sigma_{\rho E} = \frac{\partial \mathcal{F}}{\partial x_j} \left\{ \dot{\rho}\dot{v}_j E - \ddot{\rho}\ddot{v}_j E + \dot{v}_j \dot{p} - \ddot{v}_j \ddot{p} - \left( \kappa \frac{\partial T}{\partial x_j} - \ddot{\kappa} \frac{\partial T}{\partial x_j} \right) - \left( \dot{\tau}_{ij}\dot{v}_i - \ddot{\tau}_{ij}\ddot{v}_i \right) \right\} \quad (6.107)$$

$$\sigma_{\overline{\tau}(a,b)} = \frac{\mathcal{F}(1-\mathcal{F})}{\bar{\rho}} (\dot{\rho}\dot{a} - \ddot{\rho}\ddot{a}) (\dot{\rho}\dot{b} - \ddot{\rho}\ddot{b}) \quad (6.108)$$

$$\sigma_{\overline{\chi}(a,b)} = \frac{\mathcal{F}(1-\mathcal{F})}{\bar{\rho}} (\dot{\rho}\dot{a} - \ddot{\rho}\ddot{a}) (\dot{b} - \ddot{b}) \quad (6.109)$$

$$\sigma_{\zeta(a,b)} = \frac{\mathcal{F}(1-\mathcal{F})}{\bar{\rho}^2} (\bar{\rho}a - \bar{\rho}\bar{a}) (\bar{\rho}b - \bar{\rho}\bar{b}) \quad (6.110)$$

Equations (6.105)-(6.110) indicate that the hybrid contributions are directly proportional to differences between RANS and LES variables. In order to extract additional information, the RANS and the LES differences can be approximated with the instantaneous turbulent fluctuation  $\phi^{\dot{\cdot}} = \phi - \bar{\phi} = \mathcal{C}(\bar{\bar{\phi}} - \bar{\phi})$ , since  $\bar{\bar{\phi}} \rightarrow \phi$  for  $\Delta \rightarrow 0$  and  $\bar{\phi}^{\dot{\cdot}} = \mathcal{C}(\bar{\bar{\phi}} - \bar{\phi}) = 0$ . Here,  $\phi$  is the instantaneous variable and  $\mathcal{C}$  is an order one coefficient. Therefore, by substituting  $\phi^{\dot{\cdot}} = \mathcal{C}(\bar{\bar{\phi}} - \bar{\phi})$  in Eqs. (6.105)-(6.110), and assuming  $\mathcal{C} = 1$  the hybrid contributions can be expressed as

$$\sigma_{\rho} = -\frac{\partial \mathcal{F}}{\partial x_j} (\rho v_j)^{\dot{\cdot}} \quad (6.111)$$

$$\begin{aligned} \sigma_{\rho v_i} = & -\frac{\partial \mathcal{F}}{\partial x_j} \left[ (\rho v_i v_j)^{\dot{\cdot}} + p^{\dot{\cdot}} \delta_{ij} - \tau_{ij}^{\dot{\cdot}} \right] \\ & + \frac{\partial}{\partial x_j} \left\{ \frac{\partial \mathcal{F}}{\partial x_j} (\mu v_i)^{\dot{\cdot}} + \frac{\partial \mathcal{F}}{\partial x_i} (\mu v_j)^{\dot{\cdot}} - \frac{2}{3} \frac{\partial \mathcal{F}}{\partial x_k} (\mu v_k)^{\dot{\cdot}} \delta_{ij} \right\} \end{aligned} \quad (6.112)$$

$$\sigma_{\rho E} = -\frac{\partial \mathcal{F}}{\partial x_j} \left\{ (\rho v_j E)^{\dot{\cdot}} + (v_j p)^{\dot{\cdot}} - \left( \kappa \frac{\partial T}{\partial x_j} \right)^{\dot{\cdot}} - (\tau_{ij} v_i)^{\dot{\cdot}} \right\} \quad (6.113)$$

$$\sigma_{\bar{\tau}(a,b)} = \frac{\mathcal{F}(1-\mathcal{F})}{\bar{\rho}} (\rho a)^{\dot{\cdot}} (\rho b)^{\dot{\cdot}} \quad (6.114)$$

$$\sigma_{\bar{\chi}(a,b)} = \frac{\mathcal{F}(1-\mathcal{F})}{\bar{\rho}} (\rho a)^{\dot{\cdot}} (b)^{\dot{\cdot}} \quad (6.115)$$

$$\sigma_{\bar{\zeta}(a,b)} = \frac{\mathcal{F}(1-\mathcal{F})}{\bar{\rho}^2} (\rho a)^{\dot{\cdot}} (\rho b)^{\dot{\cdot}} \quad (6.116)$$

Equations (6.111)-(6.116) demonstrate that the hybrid contributions represent physical turbulent scales that are not directly accounted for by either RANS or LES. Therefore, if Eqs. (6.99)-(6.104) cannot be reconstructed from the hybrid field, they have to be either modeled or prescribed. Here, it is important to stress that Eqs. (6.111)-(6.116) are just an approximation of the hybrid terms and their only purpose is to illustrate the physical meaning of the hybrid terms. Therefore, Eqs. (6.111)-(6.116) should not be used to compute or model the hybrid terms. Here Eqs. (6.99)-(6.104) have to be used instead. It will be shown that the hybrid contribution plays an important role preserving equilibrium in the transition from RANS to LES, and in compensating for the turbulence that RANS does not model and LES does not resolve.

Here, it is important to mention, that current hybrid RANS/LES approach assumes that the transition from RANS to LES is only obtained through the turbulent model equations. However, some of the existing hybrid RANS/LES models can be obtained by simplifying Eqs. (6.89)-(6.91) and (6.93)-(6.95).

*Speziale VLES model:* This approach scales the Reynolds stress tensor to bridge DNS with RANS  $\tau_{ij}^s = \alpha \tau_{ij}^R$ . Here the scaling function  $\alpha = [1 - \exp(-\beta\Delta/\eta)]^n$  depends on the grid resolution ( $\Delta$ ), the Kolmogorov length scale ( $\eta$ ), and model coefficients  $\beta$  and  $n$  [Speziale, 1998]. This approach can be recovered if the LES operator in Eqs. (6.93)-(6.92) is replaced by the identity operator  $\ddot{\phi} = \phi$  and the HT are neglected. Under these conditions Eq. (6.92) simplifies to  $\bar{\tau}(v_i, v_j) = \mathcal{F}\ddot{\tau}(v_i, v_j)$ , since the central moments for the identity operator are zero  $\ddot{\tau}(a, b) = 0$ . Hence, the blending function can be directly related with the scaling factor  $\mathcal{F} = \alpha$ . Thus, what is left is to provide a closure for  $\alpha$  for which different methods have been proposed [Batten et al., 2004, Liu and Shih, 2006, Delanghe et al., 2005, Girimaji, 2006]. The equations indicate that the model transitions from RANS to DNS. However, it is not clear how this approach could formally fit LES in between, as stated originally by Speziale [Speziale, 1998].

*Zonal RANS/LES approach:* In this approach the RANS and LES governing equations are usually solved in different flow domains with a discontinuous model transition [Piomelli and Balaras, 2002, Georgiadis et al., 2003, Hamba, 2003, Tucker and Davidson, 2004, Schluter et al., 2004, Zhong and Tucker, 2004, Davidson and Dahlström, 2005, Temmerman et al., 2005, Davidson and Billson, 2006, Hamba, 2006]. This approach can be recovered from Eqs. (6.93)-(6.92) by neglecting the HT and implementing a discontinuous function in  $\mathcal{F}$ .

*Blended hybrid RANS/LES approaches:* In this approach the RANS and LES model equations are usually combined using a blending function [Baggett, 1998, Xiao et al., 2003, Baurle et al., 2003, Xiao et al., 2004, Fan et al., 2004, Kawai and Fujii, 2005, Sánchez-Rocha et al., 2006], inducing a RTLT region. This approach is obtained from Eqs. (6.93)-(6.92) by neglecting the hybrid terms and implementing a continuous blending function  $\bar{\tau}(v_i, v_j) = \mathcal{F}\ddot{\tau}(v_i, v_j) + (1 - \mathcal{F})\ddot{\tau}(v_i, v_j)$ . In particular, if the same closure equations are used for both RANS and LES central moments, the hybrid formulation reduces to a blending of turbulence viscosities  $\bar{\tau}(v_i, v_j) - \frac{2}{3}\delta_{ij}\bar{\tau}(v_k, v_k) = 2[\mathcal{F}\mu_{rans} + (1 - \mathcal{F})\mu_{sgs}](\tilde{S}_{ij} - \frac{1}{3}\tilde{S}_{kk})$ , which is one of the most common forms of hybrid models. In fact, the Detached Eddy Simulation approach [Spalart et al., 1997, 2006] can be presented in this form

where  $\mu_{DES} = \mathcal{F}\mu_{rans} + (1 - \mathcal{F})\mu_{sgs}$ , with the transition from RANS to LES built in the model equation of  $\mu_{DES}$ .

### *Time Dependent Hybrid RANS/LES Formulation*

Although it will not be pursued any further numerically in this work, it is worth mentioning the case when the hybridization is conducted over time, i.e.,  $\mathcal{F} = f(t)$ , which is relevant for LES simulations that are conducted from an initial steady RANS field.

$$\frac{\partial \bar{\rho}}{\partial t} + \frac{\partial}{\partial x_j} (\bar{\rho} \tilde{v}_j) = \frac{\partial \mathcal{F}}{\partial t} [\dot{\bar{\rho}} - \ddot{\bar{\rho}}] = -\frac{\partial \mathcal{F}}{\partial t} (\rho) \dot{\quad} \quad (6.117)$$

$$\frac{\partial \bar{\rho} \tilde{v}_i}{\partial t} + \frac{\partial}{\partial x_j} (\bar{\rho} \tilde{v}_i \tilde{v}_j + \bar{p} \delta_{ij} - \tilde{\tau}_{ij} + \bar{\tau}(v_i, v_j)) = \frac{\partial \mathcal{F}}{\partial t} [\dot{\bar{\rho}} \tilde{v}_i - \ddot{\bar{\rho}} \tilde{v}_i] = -\frac{\partial \mathcal{F}}{\partial t} (\rho v_i) \dot{\quad} \quad (6.118)$$

$$\begin{aligned} \frac{\partial \bar{\rho} \tilde{E}}{\partial t} + \frac{\partial}{\partial x_j} \left( \bar{\rho} \tilde{E} \tilde{v}_j + \bar{p} \tilde{v}_j - \bar{\kappa} \frac{\partial \tilde{T}}{\partial x_j} - \tilde{\tau}_{ij} \tilde{v}_i + \bar{\tau}(E, v_j) \right. \\ \left. + \bar{\chi}(v_j, p) - \bar{\chi} \left( \frac{\partial T}{\partial x_j}, \kappa \right) - \bar{\zeta}(\tau_{ij}, v_i) \right) = \frac{\partial \mathcal{F}}{\partial t} [\dot{\bar{\rho}} \tilde{E} - \ddot{\bar{\rho}} \tilde{E}] = -\frac{\partial \mathcal{F}}{\partial t} (\rho E) \dot{\quad} \quad (6.119) \end{aligned}$$

Equations (6.117)-(6.119) indicate that the transition from a steady RANS to an unsteady LES simulation is promoted by unsteady sources that help to trigger instabilities in the flow that will develop into resolved turbulence. Here, it is only speculated that the inclusion of these terms would help to reduce the time it takes for a steady field (used for initialization or used for forced studies) to develop realistic unsteady turbulence.

Note that for time-dependent blending functions, Eq. (6.86) will not be valid if the RANS operator represents a time-averaged operator, since in this case the blending function will not commute with the time-averaging operator  $\overline{\mathcal{F}\phi} \neq \mathcal{F}\bar{\phi}$ . Nevertheless, even in this case, Eqs. (6.117)-(6.119) are still valid.

### *Incompressible Hybrid Navier-Stokes Equations*

Although the incompressible hybrid RANS/LES Navier-Stokes equations for an additive hybrid operator were first presented by Germano [Germano, 2004], these equations are repeated and expanded here to highlight the hybrid contributions and to establish our new notation. The incompressible formulation is derived from the compressible hybrid approach by assuming incompressibility and by eliminating the energy and the state equations.

$$\frac{\partial \bar{v}_j}{\partial x_j} = \frac{\partial \mathcal{F}}{\partial x_j} [\dot{\bar{v}}_j - \ddot{\bar{v}}_j] \quad (6.120)$$

$$\begin{aligned}
\frac{\partial \bar{v}_i}{\partial t} + \bar{v}_j \frac{\partial \bar{v}_i}{\partial x_j} + \frac{\partial}{\partial x_j} (\bar{p}/\rho \delta_{ij} - \bar{\tau}_{ij}/\rho + \bar{\tau}(v_i, v_j)/\rho) = \\
\frac{\partial \mathcal{F}}{\partial x_j} \left[ \dot{\bar{v}}_i \dot{\bar{v}}_j - \ddot{\bar{v}}_i \ddot{\bar{v}}_j + \dot{\bar{\tau}}(v_i, v_j)/\rho - \ddot{\bar{\tau}}(v_i, v_j)/\rho \right. \\
\left. + (\dot{\bar{p}} - \ddot{\bar{p}})/\rho \delta_{ij} - (\dot{\bar{\tau}}_{ij} - \ddot{\bar{\tau}}_{ij})/\rho \right] \\
- \nu \frac{\partial}{\partial x_j} \left\{ \frac{\partial \mathcal{F}}{\partial x_j} (\dot{\bar{v}}_i - \ddot{\bar{v}}_i) + \frac{\partial \mathcal{F}}{\partial x_i} (\dot{\bar{v}}_j - \ddot{\bar{v}}_j) \right\} \\
+ \frac{\partial \mathcal{F}}{\partial t} [\dot{\bar{v}}_i - \ddot{\bar{v}}_i]
\end{aligned} \tag{6.121}$$

$$\bar{\tau}_{ij} = \mu \left( \frac{\partial \bar{v}_i}{\partial x_j} + \frac{\partial \bar{v}_j}{\partial x_i} \right), \quad \dot{\bar{\tau}}_{ij} = \mu \left( \frac{\partial \dot{\bar{v}}_i}{\partial x_j} + \frac{\partial \dot{\bar{v}}_j}{\partial x_i} \right), \quad \ddot{\bar{\tau}}_{ij} = \mu \left( \frac{\partial \ddot{\bar{v}}_i}{\partial x_j} + \frac{\partial \ddot{\bar{v}}_j}{\partial x_i} \right). \tag{6.122}$$

$$\dot{\bar{\tau}}(a, b) = \rho (\dot{\bar{a}}\bar{b} - \bar{a}\dot{\bar{b}}) \tag{6.123}$$

$$\ddot{\bar{\tau}}(a, b) = \rho (\ddot{\bar{a}}\bar{b} - \bar{a}\ddot{\bar{b}}) \tag{6.124}$$

$$\bar{\tau}(a, b) = \rho (\bar{a}\bar{b} - \bar{a}\bar{b}) \tag{6.125}$$

Equations (6.120), (6.121), and (6.125) represent the incompressible hybrid Navier-Stokes equations and the hybrid second order central moment. The explicit expression for the hybrid central moment is obtained by substituting Eq. (6.78) in Eq. (6.125)

$$\bar{\tau}(a, b) = \mathcal{F} \dot{\bar{\tau}}(a, b) + (1 - \mathcal{F}) \ddot{\bar{\tau}}(a, b) + \rho \mathcal{F} (1 - \mathcal{F}) (\dot{\bar{a}} - \ddot{\bar{a}}) (\dot{\bar{b}} - \ddot{\bar{b}}) \tag{6.126}$$

and by operating Eq. (6.126) in  $v_i$  and  $v_j$ , the hybrid Reynolds stress tensor is directly obtained as

$$\begin{aligned}
\bar{\tau}(v_i, v_j) = \rho [\mathcal{F} (\dot{\bar{v}}_i \dot{\bar{v}}_j - \ddot{\bar{v}}_i \ddot{\bar{v}}_j) + (1 - \mathcal{F}) (\bar{v}_i \bar{v}_j - \ddot{\bar{v}}_i \ddot{\bar{v}}_j) \\
+ \mathcal{F} (1 - \mathcal{F}) (\dot{\bar{v}}_i - \ddot{\bar{v}}_i) (\dot{\bar{v}}_j - \ddot{\bar{v}}_j)].
\end{aligned} \tag{6.127}$$

The momentum equation derived here is slightly different from Germano's original derivation since the definition for the viscous stress tensor (6.122) is maintained, while Germano applied continuity to simplify the momentum equation. Nevertheless, it can be shown that both equations are consistent.

Finally, by substituting Eqs. (6.123) and (6.124) in Eq. (6.121), and including the differences between RANS and LES variables with the turbulence fluctuations ( $\dot{\bar{\phi}} = \phi - \bar{\phi} = \mathcal{C}(\bar{\phi} - \dot{\bar{\phi}})$ , with  $\mathcal{C} = 1$ ), it can be shown that the hybrid contributions take the following form

$$\sigma_\rho = - \frac{\partial \mathcal{F}}{\partial x_j} v_j \dot{\bar{\tau}} \tag{6.128}$$

$$\begin{aligned} \sigma_{\rho v_i} = & -\frac{\partial \mathcal{F}}{\partial x_j} \left[ (v_i v_j)^{\dot{}} + p^{\dot{}} / \rho \delta_{ij} - \tau_{ij}^{\dot{}} / \rho \right] \\ & + \nu \frac{\partial}{\partial x_j} \left\{ \frac{\partial \mathcal{F}}{\partial x_j} v_i^{\dot{}} + \frac{\partial \mathcal{F}}{\partial x_i} v_j^{\dot{}} \right\} - \frac{\partial \mathcal{F}}{\partial t} v_i^{\dot{}} \end{aligned} \quad (6.129)$$

$$\sigma_{\bar{\tau}(v_i, v_j)} = \rho \mathcal{F} (1 - \mathcal{F}) v_i^{\dot{}} v_j^{\dot{}} \quad (6.130)$$

Similar to the compressible formulation, the incompressible hybrid contributions represent turbulence scales and need to be included.

### *RANS-SST/LES-LDKM Hybrid Model*

In order to solve the governing equations, the generic hybrid central moments have to be defined using RANS and LES equations. For RANS, the closure model implemented at present uses a standard eddy viscosity and a gradient diffusion assumption.

$$\bar{\tau}(v_k, v_k) = 2\bar{\rho}k \quad (6.131)$$

$$\bar{\tau}(v_i, v_j) = -2\bar{\rho}\nu_t(\tilde{S}_{ij} - \frac{1}{3}\tilde{S}_{kk}\delta_{ij}) + \frac{2}{3}\bar{\rho}k\delta_{ij} \quad (6.132)$$

$$\dot{\chi}\left(\frac{\partial T}{\partial x_j}, \kappa\right) + \dot{\zeta}(\tau_{ij}, v_i) - \dot{\tau}(E, v_j) - \dot{\chi}(v_j, p) = \frac{\bar{\rho}C_p\nu_t}{Pr_T} \frac{\partial \tilde{T}}{\partial x_j} \quad (6.133)$$

$$+ \bar{\rho}(\bar{\nu} + \nu_t\sigma^*) \frac{\partial k}{\partial x_j} - \dot{\tau}(v_i, v_j)\tilde{v}_i. \quad (6.134)$$

Here,  $k$  is the turbulent kinetic energy (TKE),  $\nu$  is the kinematic viscosity,  $\nu_t$  is the turbulent eddy viscosity,  $C_p$  is the heat capacity at constant pressure, and  $\sigma^*$  and  $Pr_T$  are constants set to 1/2 and 1, respectively [Wilcox, 1988]. Similarly, the same assumptions are used to construct the LES closures defined as

$$\ddot{\tau}(v_k, v_k) = 2\bar{\rho}k^{sgs} \quad (6.135)$$

$$\ddot{\tau}(v_i, v_j) = -2\bar{\rho}\nu_{sgs}(\tilde{S}_{ij} - \frac{1}{3}\tilde{S}_{kk}\delta_{ij}) + \frac{2}{3}\bar{\rho}k^{sgs}\delta_{ij} \quad (6.136)$$

$$\ddot{\chi}\left(\frac{\partial T}{\partial x_j}, \kappa\right) + \ddot{\zeta}(\tau_{ij}, v_i) - \ddot{\tau}(E, v_j) - \ddot{\chi}(v_j, p) = \frac{\bar{\rho}C_p\nu_{sgs}}{Pr_t} \frac{\partial \tilde{T}}{\partial x_j} + \bar{\rho} \frac{\nu_{sgs}}{Pr_t} \frac{\partial \tilde{E}}{\partial x_j} \quad (6.137)$$

$$+ \frac{\nu_{sgs}}{Pr_t} \frac{\partial \tilde{p}}{\partial x_j} - \ddot{\tau}(v_i, v_j)\tilde{v}_i. \quad (6.138)$$

Here,  $k^{sgs}$  is the subgrid kinetic energy,  $\nu_{sgs}$  is the subgrid eddy viscosity, and  $Pr_t$  is a coefficient assumed unity [Menon and Patel, 2006]. Finally, model equations for  $\nu_t$ ,  $k$ ,  $\nu_{sgs}$ , and  $k^{sgs}$  have to be defined to close the system of equations.

In this work, RANS and LES turbulence models are coupled in the hybrid formulation by blending equivalent RANS and LES models. Here, the two-equation  $k - \omega$  SST model [Menter, 1994] and the one-equation localized dynamic  $k^{sgs}$  (LDKM) LES model [Menon and Patel, 2006] were selected to compute  $\nu_t$ ,  $k$ ,  $\nu_{sgs}$ , and  $k^{sgs}$ , since both methods have transport equations for the kinetic energy of the turbulence ( $k$  for RANS and  $k^{sgs}$  for LES), which are used to design the hybrid model equation. The  $k - \omega$  SST model is selected due to its well documented success predicting complex flows [Hutton and Ashworth, 2005, Menter, 1994, Wilcox, 1998, 1988].

An equation for the hybrid turbulent kinetic energy ( $\mathcal{K} = \mathcal{F}k + (1 - \mathcal{F})k^{sgs}$ ) can be derived formally by merging RANS and LES transport equations following the same procedure used to derive the hybrid Navier-Stokes equations. However, this approach would yield an equation with extra terms that cannot be readily computed, and unlike the hybrid Navier-Stokes equations, it is not possible to demonstrate any physical significance for all the additional terms derived in the hybrid *model* equation. The formal combination of two model equations does not guarantee that the physics of the flow is modeled any better. Here, a model equation that identically recovers the RANS  $k$  and LES  $k^{sgs}$  equations is proposed in such a way that its structure resembles Eqs. (6.93)-(6.95) without the hybrid contributions. This model equation is

$$\frac{\partial \bar{\rho} \mathcal{K}}{\partial t} + \frac{\partial}{\partial x_j} (\bar{\rho} \tilde{v}_j \mathcal{K} - KT_j) = KS \quad (6.139)$$

where

$$KT_j = \mathcal{F} \left( \bar{\rho} (\bar{v} + \sigma_k \nu_t) \frac{\partial \mathcal{K}}{\partial x_j} \right) + (1 - \mathcal{F}) \left( \bar{\rho} \left( \frac{\bar{v}}{Pr} + \nu_{sgs} \right) \frac{\partial \mathcal{K}}{\partial x_j} \right) \quad (6.140a)$$

$$KS = \mathcal{F} \left( -\tilde{\tau}(v_i, v_j) \frac{\partial \tilde{v}_i}{\partial x_j} - \beta^* \bar{\rho} \mathcal{K} \omega \right) + (1 - \mathcal{F}) \left( -\tilde{\tau}(v_i, v_j) \frac{\partial \tilde{v}_i}{\partial x_j} - C_\epsilon \bar{\rho} \frac{\mathcal{K}^{3/2}}{\Delta} \right). \quad (6.140b)$$

Equation (6.139) is the model equation for the hybrid turbulent kinetic energy ( $\mathcal{K}$ ). The model equation is constructed by directly blending the source and the transport terms of the  $k - \omega$  SST “ $k$ ” and the LES “ $k^{sgs}$ ” equations. An additional modification is required in Eqs. (6.132) and (6.136) to eliminate their explicit dependence on  $k$  and  $k^{sgs}$ .



Both turbulence variables are substituted by  $\mathcal{K}$  so that

$$\dot{\tilde{\tau}}(v_i, v_j) = -2\bar{\rho}v_t(\tilde{S}_{ij} - \frac{1}{3}\tilde{S}_{kk}\delta_{ij}) + \frac{2}{3}\bar{\rho}\mathcal{K}\delta_{ij} \quad (6.141)$$

$$\ddot{\tilde{\tau}}(v_i, v_j) = -2\bar{\rho}v_{sgs}(\tilde{S}_{ij} - \frac{1}{3}\tilde{S}_{kk}\delta_{ij}) + \frac{2}{3}\bar{\rho}\mathcal{K}\delta_{ij} \quad (6.142)$$

This additional modification does not alter the original RANS-SST and LES-LDKM equations, which are identically recovered when  $\mathcal{F} = 1$  and  $\mathcal{F} = 0$ , respectively. The RANS-SST model requires an additional equation for the specific energy dissipation rate “ $\omega$ ” defined by

$$\begin{aligned} \frac{\partial}{\partial t}(\bar{\rho}\omega) + \frac{\partial}{\partial x_j}(\bar{\rho}\tilde{v}_j\omega) = & -\frac{\gamma}{v_t}\dot{\tilde{\tau}}(v_i, v_j)\frac{\partial\tilde{v}_i}{\partial x_j} - \beta\bar{\rho}\omega^2 + \frac{\partial}{\partial x_j}\left[\bar{\rho}(\bar{v} + \sigma_\omega v_t)\frac{\partial\omega}{\partial x_j}\right] \\ & + 2(1 - F_1)\bar{\rho}\sigma_\omega^2\frac{1}{\omega}\frac{\partial\mathcal{K}}{\partial x_j}\frac{\partial\omega}{\partial x_j} \end{aligned} \quad (6.143)$$

$$F_1 = \tanh(\chi^4), \quad \chi = \min\left(\max\left(\frac{\sqrt{\mathcal{K}}}{0.09\omega y}, \frac{500\bar{v}}{y^2\omega}\right); \frac{4\bar{\rho}\sigma_\omega^2\mathcal{K}}{CDy^2}\right) \quad (6.144a)$$

$$CD = \max\left(2\bar{\rho}\sigma_\omega^2\frac{1}{\omega}\frac{\partial\mathcal{K}}{\partial x_j}\frac{\partial\omega}{\partial x_j}; 10^{-20}\right) \quad (6.144b)$$

Here,  $\Omega$ ,  $F_1$ , and  $y$  are the vorticity magnitude, a blending function, and the wall-normal distance, respectively. Here, it is stressed that the equation for  $\omega$  is not explicitly hybridized since there is no equivalent equation in the LES model implemented here. The constants for the RANS-SST model, here represented as  $\psi$ , are computed from two sets of constants  $\psi_1$  and  $\psi_2$  as  $\psi = F_1\psi_1 + (1 - F_1)\psi_2$ . Here, the values of these two sets were previously defined. Finally, the RANS and the LES eddy viscosities are defined by

$$v_t = \frac{a_1\mathcal{K}}{\max(a_1\omega; \Omega F_2)} \quad (6.145)$$

and

$$v_{sgs} = C_v\Delta\sqrt{\mathcal{K}} \quad (6.146)$$

where

$$F_2 = \tanh(\eta^2), \quad \eta = \max\left(2\frac{\sqrt{\mathcal{K}}}{0.09\omega y}, \frac{500\bar{v}}{y^2\omega}\right). \quad (6.147)$$

This hybrid RANS/LES turbulent model has been successfully applied to simulate complex unsteady flow separation [Sánchez-Rocha et al., 2006, Lynch and Smith, 2008].

*Detached Eddy Simulation (DES)*

Turbulent viscosity transport equation:

$$\begin{aligned} \frac{\partial \tilde{\rho} \tilde{v}}{\partial t} + \frac{\partial}{\partial x_j} (\tilde{\rho} \tilde{v}_j \tilde{v}) &= \tilde{\rho} c_{b1} \tilde{S}_a \tilde{v} - \tilde{\rho} c_{w1} f_w \left( \frac{\tilde{v}}{\tilde{d}} \right)^2 \\ &+ \frac{\partial}{\partial x_j} \left( \frac{\tilde{\rho}}{\sigma} (v + \tilde{v}) \frac{\partial \tilde{v}}{\partial x_j} \right) + \frac{\tilde{\rho} c_{b2}}{\sigma} \frac{\partial \tilde{v}}{\partial x_j} \frac{\partial \tilde{v}}{\partial x_j} \end{aligned} \quad (6.148)$$

Here, the damping functions and the rest of the coefficients are defined as

$$f_w = g \left[ \frac{1 + c_{w3}^6}{g^6 + c_{w3}^6} \right]^{1/6}, \quad f_{v1} = \frac{\chi^3}{\chi^3 + c_{v1}^3}, \quad f_{v2} = 1 - \frac{\chi}{1 + \chi f_{v1}} \quad (6.149)$$

$$\chi = \frac{\tilde{v}}{v}, \quad g = r + c_{w2}(r^6 - r), \quad r = \frac{\tilde{v}}{\tilde{S}_a \kappa^2 \tilde{d}^2} \quad (6.150)$$

$$\tilde{S}_a = S_r + \frac{\tilde{v}}{\kappa^2 \tilde{d}^2} f_{v2}, \quad S_r = \sqrt{2 \tilde{R}_{ij} \tilde{R}_{ij}}, \quad \tilde{R}_{ij} = \frac{1}{2} \left( \frac{\partial \tilde{v}_i}{\partial x_j} - \frac{\partial \tilde{v}_j}{\partial x_i} \right) \quad (6.151)$$

Here,  $d$  is the distance from the wall and the effective turbulent viscosity is defined as

$$\tilde{d} = \min(d_{RANS}, d_{LES}) \quad (6.152)$$

where

$$d_{LES} = C_{des} \Delta \quad (6.153)$$

$$\Delta = \max(\Delta x, \Delta y, \Delta z) \quad (6.154)$$

and  $d_{RANS} = d$  is the distance from the wall.

The turbulent eddy viscosity is

$$\nu_t = \tilde{v} f_{v1}. \quad (6.155)$$

$c_{b1}$	$c_{b2}$	$c_{v1}$	$\sigma$	$c_{w1}$	$c_{w2}$	$c_{w3}$	$\kappa$	$c_{v2}$	$C_{des}$
0.1355	0.622	7.1	2/3	$\frac{c_{b1}}{\kappa^2} + \frac{1+c_{b2}}{\sigma}$	0.3	2	0.41	5	0.65

Table 6.7: DES model coefficients

The model coefficients are defined in Table 6.7. Modifications to the model proposed by Spalart have been included to improve the convergence of the model in cases of flow reattachment [Deck et al., 2002]. Here, the  $\tilde{S}$  term is computed using the following modified

relations

$$\tilde{S}_a = S_r \tilde{f}_{v3} + \frac{\tilde{v}}{\kappa^2 d^2} \tilde{f}_{v2} \quad (6.156a)$$

$$\tilde{f}_{v2} = \left(1 + \frac{\chi}{c_{v2}}\right)^{-3} \quad (6.156b)$$

$$\tilde{f}_{v3} = \frac{(1 + \chi f_{v1})(1 - \tilde{f}_{v2})}{\chi} \quad (6.156c)$$

### *Derived Statistics*

This section presents some of the tools that are available to analyze turbulent flow data. There are two primary objectives for analyzing data from a large-eddy simulation. The first is to develop an understanding of the flow field in question through the use of these tools. This may lead to Engineering design changes or implementation of flow controls to modify the flow. The second objective is to reveal pathologies caused by the numerical integration of the flow equations and concomitant closure models under realistic conditions. It is hoped that a clear understanding of these pathologies may lead to better simulation models.

In order to probe LES data, statistical analysis tools are needed that allow the distillation of the tremendous volume of data produced from simulation (or experiment) down to a few manageable quantities of interest that may be directly compared to experimental data. The nature of turbulent flows does not allow for a predictive solution in the strict sense of the word. One must therefore be content with the prediction of its statistics.

Some of the most important statistical quantities of interest (and the most physically revealing) correspond to the first moments of the flow variables, i.e., the mean values. Moments of flow variables such as the velocity are routinely measured in experiments and form the basis of the Reynolds Averaged Navier-Stokes (RANS) solution approach for turbulent flows. There are several techniques used to obtain these moments from raw data, e.g., LES data. Before proceeding with an overview of the derived statistics, several definitions are required.

### *Reynolds Averaged Statistics*

Reynolds time averages, ensemble averages, homogeneous spatial averages, and probability densities are four techniques commonly used to determine mean quantities (or moments) of a turbulent flow. Reynolds averaging is used to derive the time invariant mean quantities of a stationary flow as a function of position. Ensemble averaging is suited for transient flows and describes the mean values as a function of both

space and elapsed time. Spatial averaging describes the spatial invariance of mean values in a homogeneous flow that may or may not be stationary.

The fourth and most powerful technique for determining mean values is through the use of probability densities of stationary processes. If the probability density of the flow variables is known for the entire domain of interest, then all of the moments of the flow variables can be obtained from the probability density. In practice, this probability density is difficult to determine and contains more information than is desired, therefore it will not be considered further here. The remainder of this section will concentrate on the definition and use of the Reynolds, spatial, and ensemble averaging.

A stationary flow is one in which mean values are independent of the initial time from which the means are determined. Stationary flows are also referred to as statistically steady. In other words, the mean values do not change with time. Consider the temporally and spatially varying quantity  $\phi(x_i, t)$ , its Reynolds time average is

$$\langle \phi(x_i) \rangle = \lim_{T \rightarrow \infty} \frac{1}{T} \int_{t_0}^{t_0+T} \phi(x_i, t') dt' \quad (6.157)$$

where  $t_0$  denotes an arbitrary starting time for the integration.

An example of a stationary flow is a jet flow issuing from the nozzle on a pipe at high Reynolds number with a fixed mass flow rate that is controlled by a valve. After some time, the flow settles down and a stationary flow is achieved. A probe designed to measure the velocity field placed at some location within the jet would measure a fluctuating velocity that if examined closely would seem to be oscillating randomly about a steady mean.

In contrast, for non-stationary flows, a time-invariant mean cannot be defined, i.e., the mean is time-dependent. For this type of flow, ensemble averaging may be used where flow data is accumulated over a number of trials, i.e., repeating the experiment until the mean values are independent of the number of experiments performed. At this point the mean values are said to have converged to a statistically reliable value. A formal definition of an ensemble average for a generic variable  $\phi(x_i, t)$  is

$$\langle \phi(x_i, \tau) \rangle_E = \lim_{N_E \rightarrow \infty} \frac{1}{N_E} \sum_{n=1}^{N_E} \phi(x_i, t = \tau) \quad (6.158)$$

where  $\tau = t - t_0$  is the elapsed time from the start of the experiment,  $t_0$ , and  $N_E$  is the number of experiments.

An example of a non-stationary flow may be seen in the turbulent flow around a moving body, e.g., a turning submarine. In this situation, the flow can never become stationary. In contrast, the flow

around a stationary bluff body would become stationary after an initial start-up transient.

A homogeneous flow is one in which the statistical properties of the flow do not vary with spatial location. All the mean values are independent of location and can be described by a single value at an instant in time, instead of a value at each spatial location. The mean values of homogeneous flows are determined from a volume integral such as

$$\overline{\phi(t)} = \lim_{V \rightarrow \infty} \frac{1}{V} \int_V \phi(x_i, t) dV \quad (6.159)$$

where  $V$  is the volume of the domain and  $dV = dx_1 dx_2 dx_3$ . If in addition, the flow is isotropic then the properties of the flow do not vary with direction. In other words, the flow is invariant to a rotation in coordinate system. Homogeneous flow is an idealization because boundary conditions such as no-slip/no-penetration surfaces introduce inhomogeneities into the flow.

The best example of homogeneous flow is the flow behind a mesh in a wind tunnel, i.e., so-called “screen” turbulence. In the central region away from the tunnel walls, the flow approaches homogeneous and isotropic conditions. If we assume the flow to be incompressible, then the turbulence is entirely known from the velocity and pressure fields at an instant in time, which we refer to as a realization. If the flow is homogeneous, the mean values can be obtained from a single realization of the flow instead of Reynolds time averaging over many realizations. The two techniques for measuring mean values are expected to be equivalent in a homogeneous flow.

### *Mean and Fluctuating Decomposition*

All of the statistical measures of turbulent flows presented in this section are based upon the Reynolds average for stationary flows. With the definition of the Reynolds average given above, any variable can be decomposed into its mean and fluctuating component,

$$\phi(x_i, t) = \langle \phi(x_i) \rangle + \phi'(x_i, t) \quad (6.160)$$

and will obey the following Reynolds-averaging rules,

$$\langle \phi' \rangle = 0 \quad (6.161)$$

$$\langle \langle \phi \rangle \rangle = \langle \phi \rangle \quad (6.162)$$

$$\langle \phi \psi \rangle = \langle \phi \rangle \langle \psi \rangle + \langle \phi' \psi' \rangle \quad (6.163)$$

$$\langle \phi' \langle \psi \rangle \rangle = \langle \psi' \langle \phi \rangle \rangle = 0. \quad (6.164)$$

The time average is approximated by the discrete summation,

$$\langle \phi(x_i) \rangle = \lim_{N \rightarrow \infty} \frac{\sum_{n=1}^N \phi_n(x_i, t_n) \Delta t_n}{\sum_{n=1}^N \Delta t_n} \quad (6.165)$$

where  $\Delta t_n$  is the time step increment for the  $n$ th time integration step and  $t_n = \sum_{m=1}^n \Delta t_m$  is the accumulated time. Let  $\phi$  represent a scalar quantity and let  $v_i$ , ( $i = 1, 2, 3$ ) represent the  $i$ th Cartesian component of the instantaneous velocity. The variance of a scalar is

$$\sigma^2 = \langle (\phi - \langle \phi \rangle)^2 \rangle = \langle \phi^2 \rangle - \langle \phi \rangle^2 \quad (6.166)$$

where the root mean square (r.m.s.) is  $\sigma$ . Similarly, the Reynolds stress tensor is

$$R_{ij} = \langle v'_i v'_j \rangle = \langle v_i v_j \rangle - \langle v_i \rangle \langle v_j \rangle \quad (6.167)$$

and the turbulent kinetic energy is one half of the trace of the Reynolds stress tensor

$$q' = \frac{1}{2} \langle v'_k v'_k \rangle = \frac{1}{2} (\langle v_k v_k \rangle - \langle v_k \rangle \langle v_k \rangle) \quad (6.168)$$

where repeated indices imply summation. The turbulent scalar flux vector is

$$\langle \phi' v'_i \rangle = \langle \phi v_i \rangle - \langle \phi \rangle \langle v_i \rangle. \quad (6.169)$$

The triple correlation between three independent scalars is defined as

$$\begin{aligned} \langle \phi' \psi' \lambda' \rangle &= \langle \phi \psi \lambda \rangle - \langle \phi \rangle \langle \psi \rangle \langle \lambda \rangle \\ &\quad - (\langle \phi \rangle \langle \psi' \lambda' \rangle + \langle \psi \rangle \langle \phi' \lambda' \rangle + \langle \lambda \rangle \langle \phi' \psi' \rangle). \end{aligned} \quad (6.170)$$

Correlations of this type appear in second order moment closure models such as the Reynolds stress turbulence model. Higher order correlations can be defined in a similar manner.

### Higher Order Statistics

Higher order moments of velocity, velocity differences, and velocity derivatives have been used to analyze isotropic turbulence. The skewness of velocities is defined as

$$S_{0i} = \frac{\langle v_i^3 \rangle}{\langle v_i^2 \rangle^{3/2}} \quad (6.171)$$

and the flatness factor of velocities is

$$F_{0i} = \frac{\langle v_i^4 \rangle}{\langle v_i^2 \rangle^2}. \quad (6.172)$$

The skewness is a measure of the asymmetry of the fluctuations;  $S_{0i} > 0$  are predominately positive, and  $S_{0i} < 0$  are predominately negative. The flatness is a relative measure of remotely occurring, symmetric spiking fluctuations.

The skewness of velocity derivatives is defined as

$$S_{1i} = \frac{\left\langle \left( \frac{\partial v_i}{\partial x_i} \right)^3 \right\rangle}{\left\langle \left( \frac{\partial v_i}{\partial x_i} \right)^2 \right\rangle^{3/2}} \quad (6.173)$$

and the flatness factor of velocity derivatives

$$F_{1i} = \frac{\left\langle \left( \frac{\partial v_i}{\partial x_i} \right)^4 \right\rangle}{\left\langle \left( \frac{\partial v_i}{\partial x_i} \right)^2 \right\rangle^2} \quad (6.174)$$

where there is no summation of indices.

Skewness and flatness of velocity differences have been also measured<sup>3</sup>,

$$S_{\Delta i}(r) = \frac{\langle (\Delta v_i)^3 \rangle}{\langle (\Delta v_i)^2 \rangle^{3/2}} \quad (6.175)$$

<sup>3</sup> G. K. Batchelor. *The Theory of Homogeneous Turbulence*. Cambridge University Press, 1953

and the flatness factor is

$$F_{\Delta i}(r) = \frac{\langle (\Delta v_i)^4 \rangle}{\langle (\Delta v_i)^2 \rangle^2} \quad (6.176)$$

where  $\Delta v_i = v_i(x_i + r_i, t) - v_i(x_i, t)$  and  $r_i = x_i + r$ .

For homogeneous and isotropic turbulence, the velocity fluctuations have a Gaussian probability distribution. Since this distribution is symmetric, all odd moments are zero. The nonzero moment higher than the variance is the flatness that obtains a value of 3.0. The derivative skewness is  $\sim -0.3 - -0.5$  and the derivative flatness is  $\sim 3 - 4$ <sup>4</sup>. Velocity derivative skewness and flatness are dominated by the smaller scales in the flow so these statistics provide a good measure of how well the numerical scheme is resolving the smaller scales of the flow.

<sup>4</sup> G. K. Batchelor. *The Theory of Homogeneous Turbulence*. Cambridge University Press, 1953

### *Anisotropic Stress Tensor*

An intrinsic distinction exists between isotropic and anisotropic Reynolds stresses. The isotropic stress is  $\frac{2}{3}q'\delta_{ij}$ , and the deviatoric anisotropic part is

$$a_{ij} = \langle v'_i v'_j \rangle - \frac{2}{3}q'\delta_{ij}. \quad (6.177)$$

The normalized anisotropy tensor is defined as  $b_{ij} = \frac{a_{ij}}{2q'}$ . It is readily seen that  $a_{kk} = 0$ , and any anisotropy is seen by non-zero values of the off-diagonal terms.





## **Part II**

# **Numerical Methods**



## 7 Unstructured Grid Topology

This chapter outlines some of the principal aspects of the algorithms used to treat unstructured grids in the Hydra toolkit. Central to the compressible and incompressible flow solvers, is the use of so-called “edge-based” algorithms.

The use of edge-based algorithms for advection (both cell-centered and node-centered) rely on topological grid constructs such as vertices, edges, primal and dual-grids. Figure 7.1 illustrates a primal grid and the associated centroidal and median dual grids. In the primal grid, each cell consists of an ordered set of vertices connected by cell edges or faces. Each vertex of the dual grid (both centroidal and median dual grids may be considered here) is associated with a cell of the primal mesh.

Edges, are in general lines that connect a pair of vertices. In the primal grids of interest here, the edges will be straight lines. However, the edges of the dual grids need not be straight lines as shown in Fig. 7.2. Edges of the dual grid intersect primal edges. In general, vertices, edges and faces of both the primal and dual grids are ordered independently. Of course, if a structured mesh is considered, there are certain obvious simplifications to the description of the grid topology that can be exploited.

Most unstructured grid descriptions rely on the identification of elements or cells and the nodal coordinates connected to each cell. As demonstrated in Christon and Spelce [Christon and Spelce, 1992] the computational cost to extract unique edges on an arbitrary unstructured grid scales as  $CN_{el} \log(N_{el})$  where  $N_{el}$  is the number of elements in the mesh.

For our purposes, a carefully designed and implemented edge extraction algorithm is used to construct the edge-based data structures used in the Hydra toolkit. The concepts for the edge extraction algorithm are based on the algorithms developed in QACINA [Christon, 2007], but extended to treat arbitrary topology meshes comprised of multiple element types. These algorithms scale approximately as  $N_{el} \log(N_{el})$ , but with a constant that is bounded and small,  $2.5 \times 10^{-7} \leq C \leq 10^{-6}$  based on timings on a 1.7 GHz Pentium-4 processor. Figure 7.3 shows

Figure 7.1: Primal, median dual, and centroidal dual grids.

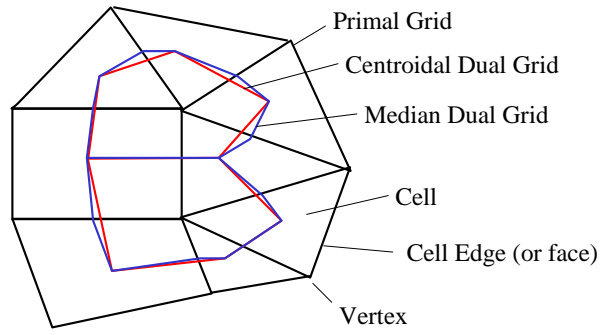
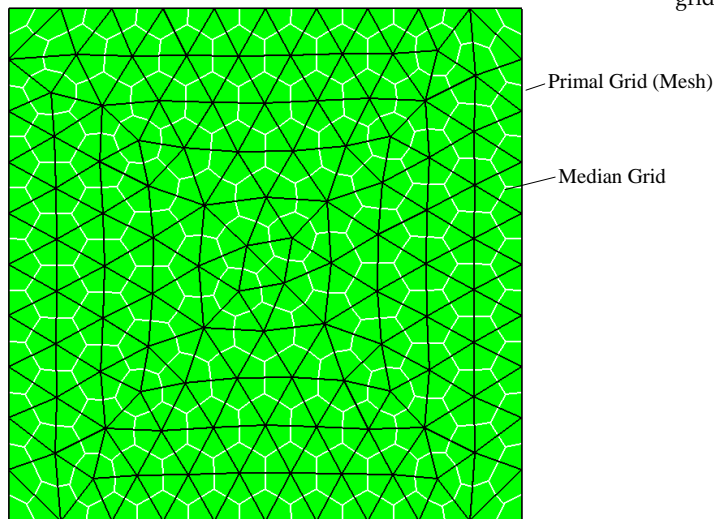


Figure 7.2: Primal and median dual grids.



the CPU time vs. number of elements in the grid for a variety of two and three-dimensional unstructured grids. From this result, it is clear that the topology-based edge extraction easily scales to  $O(10^6)$  elements in serial, i.e., on a per-processor basis. Further, the range of computing hardware shown in Fig. 7.3 serves to indicate the expected performance for the current desktop. The algorithm extensions required for parallel implementation are trivial as the extraction calculation is “embarrassingly parallel”.

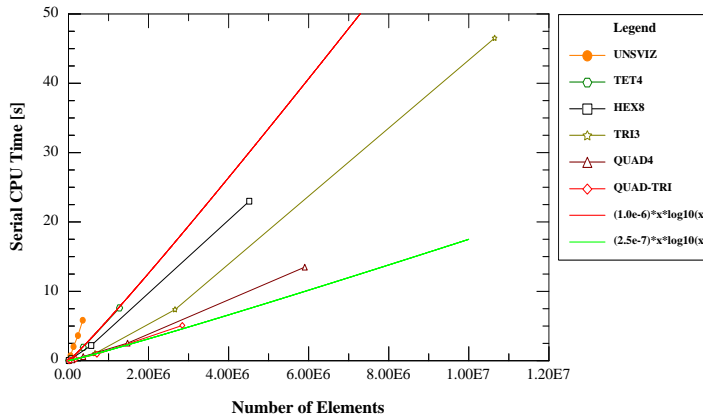


Figure 7.3: CPU time vs. number elements for the edge extraction on a variety of unstructured grids. (UNSVIZ is a stand-alone test-harness for parallel rendering that was originally used to study edge-extraction algorithms using a 200 MHz Pentium-Pro processor as a baseline.)

In order to verify the edge extraction algorithms used in the framework, Euler’s formula was used. For a polygonal surface, the number of edges may be computed directly in terms of the number of nodes  $N_{np}$  and the number of elements  $N_{el}$  in the grid as

$$N_{edge} = N_{el} + N_{np} - 1. \quad (7.1)$$

For a domain that contains holes, the number of edges is computed in terms of the number of nodes, elements and holes  $N_{hole}$  as

$$N_{edge} = N_{el} + N_{np} + N_{hole} - 1. \quad (7.2)$$

The results presented in Table 7.1 verify that the edge extraction algorithm is functioning correctly – at least in two-dimensions.

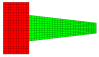
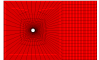




Mesh	$N_{np}$	$N_{el}$	$N_{hole}$	Int. Edges	Ext. Edges	$N_{edge}$
	517	460	0	864	112	976
	2892	2800	1	5508	184	5692
	70306	69636	2	136773	1894	139667
	82	130	2	177	36	213
	368	665	1	962	71	1033
	402	688	1	1010	80	90

Table 7.1: Topology test for edge extraction algorithm.

## 8 Discontinuous Galerkin/Finite Volume Method

This chapter outlines the basic Discontinuous Galerkin/Finite Volume formulation using a simple scalar conservation law as a prototype. The issues associated with gradient estimation are outlined, and a series of convergence results presented to demonstrate the basic behavior of the underlying numerics.

### Scalar Conservation Law Formulation

A prototypical scalar conservation law is chosen to illustrate the Discontinuous Galerkin method,

$$\frac{\partial u}{\partial t} + \nabla \cdot \mathbf{f}(u, \mathbf{c}) = 0 \quad \text{in } \Omega \times (0, T) \quad (8.1)$$

where  $\mathbf{f}(u, \mathbf{c}) = \mathbf{c}u$  is the physical flux,  $\mathbf{c}$  is the advective velocity, and  $u$  is the dependent variable. The model PDE is subject to initial conditions

$$u(\mathbf{x}, 0) = u_0(\mathbf{x}) \quad \forall \mathbf{x} \in \Omega \quad (8.2)$$

and boundary conditions

$$u = \hat{u} \quad \text{on } \Gamma_D \quad (8.3)$$

and

$$(\mathbf{f} \cdot \mathbf{n}) = (\hat{\mathbf{f}} \cdot \mathbf{n}) \quad \text{on } \Gamma_N \quad (8.4)$$

where  $\Gamma = \Gamma_D \cup \Gamma_N$ . Here,  $\hat{u}$  and  $\hat{\mathbf{f}}$  are prescribed values of the conserved variable and the corresponding flux on the boundary.

The discontinuous Galerkin formulation proceeds by first discretizing in space, e.g., with quadrilaterals, triangles, or some combination. At each time  $t \in [0, T]$ , an approximate solution  $u^h$  is sought in the finite element space of *discontinuous* functions  $W^h$ . In order to determine the approximate solution, the weak formulation is required, i.e., on each element

$$\int_{\Omega^e} w^h \left\{ \frac{\partial u^h}{\partial t} + \nabla \cdot \mathbf{f}(u^h, \mathbf{c}) \right\} = 0 \quad \forall w^h \in W^h \quad (8.5)$$

where  $\Omega^e$  is the element volume.

Proceeding with integration-by-parts, i.e., applying the divergence theorem to weaken the spatial derivatives yields

$$\frac{d}{dt} \int_{\Omega^e} w^h u^h + \oint_{\Gamma^e} w^h \mathbf{f}(u^h, \mathbf{c}) \cdot \mathbf{n} - \int_{\Omega^e} \nabla w^h \cdot \mathbf{f}(u^h, \mathbf{c}) \cdot \mathbf{n} = 0 \quad \forall w^h \in W^h \quad (8.6)$$

If the test function,  $w^h$  is chosen to be a piecewise-constant function over each element, then a finite volume formulation is recovered. For our purposes, we chose the piecewise-constant test functions which yields

$$\frac{d}{dt} \int_{\Omega^e} 1 u^h + \oint_{\Gamma^e} 1 \mathbf{f}(u^h, \mathbf{c}) \cdot \mathbf{n} = 0 \quad (8.7)$$

The cell-averaged conserved variable is defined as

$$\bar{u} = \frac{1}{\Omega^e} \int_{\Omega^e} u^h \quad (8.8)$$

Using this definition, the formulation yields a system of ordinary differential equations (ODEs)

$$\frac{d\bar{u}}{dt} + \frac{1}{\Omega^e} \oint_{\Gamma^e} \mathbf{f}(u^h, \mathbf{c}) \cdot \mathbf{n} = 0 \quad (8.9)$$

**Remark 1** *In order to provide compatibility with modern PLIC-based volume-tracking algorithms that are based on a finite volume formalism, we choose piecewise-constant test functions for the compressible and incompressible flow solvers in Hydra. However, it should be noted that this choice does not restrict the current methods or software from being extended to include higher order (higher than linear) reconstruction techniques or the incorporation of higher-order test functions. In addition, this choice makes it very simple to share a common discretization for both the compressible and incompressible flow solvers.*

Integrating Eq. (8.9) over a time-step,

$$\int_t^{t+\Delta t} \frac{d\bar{u}}{dt} + \frac{1}{\Omega^e} \int_t^{t+\Delta t} \oint_{\Gamma^e} \mathbf{f}(u^h, \mathbf{c}) \cdot \mathbf{n} = 0 \quad (8.10)$$

which permits the definition of a time-averaged flux or numerical flux,

$$\mathcal{F} \cdot \mathbf{n} \approx \frac{1}{\Delta t} \int_t^{t+\Delta t} \mathbf{f}(u^h, \mathbf{c}) \cdot \mathbf{n} \quad (8.11)$$

Thus, using the numerical flux, the formulation yields

$$\int_t^{t+\Delta t} \frac{d\bar{u}}{dt} + \frac{1}{\Omega^e} \oint_{\Gamma^e} \mathcal{F}(u^h, \mathbf{c}) \cdot \mathbf{n} = 0 \quad (8.12)$$



## Flux Functions

There are many ways to formulate the numerical approximation to the physical flux. One is to use an approximate Riemann solver. For the current discussion, we use the local Lax-Freidrichs flux which is an approximate, two-point, monotone, Lipschitz flux.

At a given dual-edge (or face of an element),  $i$ , the numerical flux is defined as

$$\mathcal{F}_i \cdot \mathbf{n}_i = \frac{1}{2} \{ (\mathbf{f}_i(u_i^-) + \mathbf{f}_i(u_i^+)) \cdot \mathbf{n}_i - a(u_i^+ - u_i^-) \} \quad (8.13)$$

where  $a$  is the maximal eigenvalue of the flux Jacobian and the (normal) flux Jacobian is

$$\left( \frac{\partial \mathbf{f}_i}{\partial u} \right) \cdot \mathbf{n}_i = \mathbf{c}_i \cdot \mathbf{n}_i \quad (8.14)$$

Thus, for the scalar advection problem,  $a$  is simply the normal velocity at a cell face. In contrast to continuous Galerkin methods, the flux on dual-edges is continuous rather than the conserved variables.

In Figure 8.1 the  $-$  state is always located on the inside of the cell face, and the  $+$  state is based on the adjacent cell and is on the positive normal side of the cell. In terms of dual-edges, Hydra associates the two elements (edge vertices), the ownership of the outward facing normal, the normal, and face area in its dual-edge data structure.

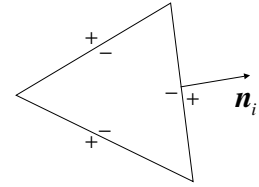


Figure 8.1: Cell face locations for reconstructed  $+/-$  values used in the numerical flux evaluation.

## Element-Centered Gradient Approximation

The numerical flux evaluation relies on multi-dimensional reconstruction of the field variables at the  $\pm$  locations of each cell as shown in Figure 8.1. The polynomial reconstruction at cell faces from cell-averaged values may be categorized as constant, linear, quadratic, etc. Constant reconstruction corresponds to a donor-cell method for advection. While future efforts may rely on higher-order reconstruction, e.g., quadratic. Currently, the Hydra toolkit uses only linear reconstruction.

The reconstruction of the field at face  $i$  of a given cell, is computed using a limited gradient as

$$u_i^- = \bar{u} + \phi \nabla_c \bar{u} \cdot \mathbf{f} \mathbf{f}_i \quad (8.15)$$

with the  $+$  values reconstructed from the adjacent cell and its limited gradient and cell-averaged data. Here,  $\nabla_c(\cdot)$  indicates a spatially centered gradient with  $\phi \in [0, 1]$  the slope limiter. Figure 8.2 shows the reconstruction at a typical cell face.

As pointed out by Barth and Jespersen [Barth and Jespersen, 1989], there are several constraints on the gradient calculation that are required to achieve a desired level of accuracy. The first corresponds to linear consistency and requires that the the gradient calculation  $\nabla_c \bar{u}$  be

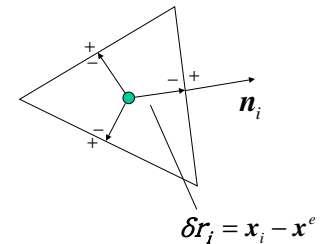


Figure 8.2: Cell face locations for reconstructed  $+/-$  values used in the numerical flux evaluation.

exact when  $\bar{u}$  has a linear variation, i.e., linear consistency. The second constraint requires that  $\nabla_c$  exist for arbitrary mesh configurations.

### *The Green-Gauss Gradient*

The Green-Gauss approximation of the gradient relies on a boundary integral around a closed control volume, i.e.,

$$\nabla_c \bar{u} = \frac{1}{\Omega^e} \int_{\Gamma^e} u^* d\Gamma \quad (8.16)$$

where  $\Omega^e$  is the cell volume and

$$u^* = \frac{1}{2}(u^+ + u^-) \quad (8.17)$$

Alternatively,  $u^*$  may be computed using linear interpolation as

$$u^* = \frac{u^+ \delta r^+ + u^- \delta r^-}{\delta r^+ + \delta r^-} \quad (8.18)$$

where  $\delta r^\pm = \|\mathbf{f}\mathbf{f}\mathbf{r}^\pm\|$ .

In either case, Eq. (8.16) fails to produce an exact gradient when the field is linear, e.g., when  $u(x, y) = a + bx + cy$  (see Barth and Jespersen [Barth and Jespersen, 1989], Marvripilis [Mavripilis, 2003]). Barth and Jespersen [Barth and Jespersen, 1989] suggest an alternative method for computing  $\nabla_c \bar{u}$  that satisfies linear consistency and is suitable for unstructured grids. However, it also requires a somewhat more complicated path integral. This approach was used by Barth and Fredrickson [Barth and Frederickson, 1990] for higher-order reconstruction methods, albeit at the cost of a slightly non-local gradient computation. This approach is not implemented in the Hydra toolkit.

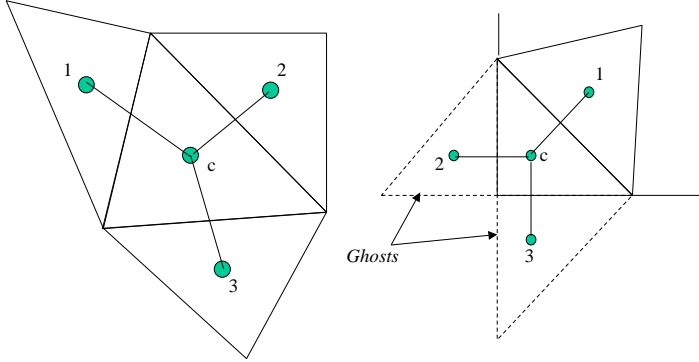
### *The Least-Squares Gradient*

An alternative least-squares gradient estimation procedure that satisfies linear consistency and may be used for both node-centered and cell-centered finite volume methods was proposed by Barth [Barth, 1993] in 1993. The least-squares procedure satisfies linear consistency and is independent of the mesh topology.

The least-squares procedure attempts to find discontinuous reconstruction polynomials that are close to their  $C^0$  counterparts for each vertex of the grid. Figure 8.3 shows the minimum data required for the least-squares reconstruction on a patch of triangles.

The least-squares reconstruction procedure is equivalent to solving the following non-square problem using the vertex data surrounding each cell. Using the convention that  $\Delta x_{ic} = x_i - x_c$  and  $\Delta \bar{u}_{ic} = \bar{u}_i - \bar{u}_c$

Figure 8.3: Data used for least-squares reconstruction.



for each of the surrounding cells, the minimization problem becomes

$$\begin{bmatrix} \Delta x_{1c} & \Delta y_{1c} \\ \Delta x_{2c} & \Delta y_{2c} \\ \Delta x_{3c} & \Delta y_{3c} \end{bmatrix} \left\{ \begin{array}{c} \frac{\partial u}{\partial x} \\ \frac{\partial u}{\partial y} \end{array} \right\} = \left\{ \begin{array}{c} \Delta \bar{u}_{1c} \\ \Delta \bar{u}_{2c} \\ \Delta \bar{u}_{3c} \end{array} \right\}. \quad (8.19)$$

In order to actually solve for the least-squares gradients, the normal equations are formed as follows. First, Eq. (8.19) can be written as

$$\begin{bmatrix} \mathbf{L}_1 & \mathbf{L}_2 \end{bmatrix} \{\nabla_c \bar{u}\} = \{\mathbf{f}\} \quad (8.20)$$

Then, forming the normal equations,

$$\begin{bmatrix} L_{11} & L_{12} \\ L_{21} & L_{22} \end{bmatrix} \left\{ \begin{array}{c} \frac{\partial u}{\partial x} \\ \frac{\partial u}{\partial y} \end{array} \right\} = \left\{ \begin{array}{c} \mathbf{L}_1 \cdot \mathbf{f} \\ \mathbf{L}_2 \cdot \mathbf{f} \end{array} \right\} \quad (8.21)$$

where  $L_{ij} = \mathbf{L}_i \cdot \mathbf{L}_j$  and  $f_i = \mathbf{L}_i \cdot \mathbf{f}$ .

Alternatively, this may be written two dimensions as

$$\begin{bmatrix} \sum \Delta x_{ic}^2 & \sum \Delta x_{ic} \Delta y_{ic} \\ \sum \Delta x_{ic} \Delta y_{ic} & \sum \Delta y_{ic}^2 \end{bmatrix} \left\{ \begin{array}{c} \frac{\partial u}{\partial x} \\ \frac{\partial u}{\partial y} \end{array} \right\} = \left\{ \begin{array}{c} \sum \Delta x_{ic} \Delta u_{ic} \\ \sum \Delta y_{ic} \Delta u_{ic} \end{array} \right\} \quad (8.22)$$

where the sum is over all edges connected to the cell vertex at  $(x_c, y_c)$ . The resulting system of equations  $[L]\{\nabla_c \bar{u}\} = \{\mathbf{f}\}$  may be solved at each vertex independently, i.e., in a “cell-by-cell” or “element-by-element” fashion and requires only local neighbor information. In

three dimensions, the normal equations become

$$\begin{bmatrix} \sum \Delta x_{ic}^2 & \sum \Delta x_{ic} \Delta y_{ic} & \sum \Delta x_{ic} \Delta z_{ic} \\ \sum \Delta x_{ic} \Delta y_{ic} & \sum \Delta y_{ic}^2 & \sum \Delta y_{ic} \Delta z_{ic} \\ \sum \Delta x_{ic} \Delta z_{ic} & \sum \Delta y_{ic} \Delta z_{ic} & \sum \Delta z_{ic}^2 \end{bmatrix} \begin{Bmatrix} \frac{\partial \bar{u}}{\partial x} \\ \frac{\partial \bar{u}}{\partial y} \\ \frac{\partial \bar{u}}{\partial z} \end{Bmatrix} = \begin{Bmatrix} \sum \Delta x_{ic} \Delta u_{ic} \\ \sum \Delta y_{ic} \Delta u_{ic} \\ \sum \Delta z_{ic} \Delta u_{ic} \end{Bmatrix} \quad (8.23)$$

In order to test that this procedure yields gradients that are exact for a linear field, assume that the exact solution, in the form of a grid function, has a form  $\bar{u}(x, y) = a + bx + cy$ . By evaluating the function at grid points, e.g.,  $\bar{u}_c = a + bx_c + y_c$ , and substituting into Eq. (8.22), the following right-hand-result is obtained

$$\begin{Bmatrix} f_1 \\ f_2 \end{Bmatrix} = \begin{Bmatrix} \sum \Delta x_{ic} (\Delta x_{ic} + \Delta y_{ic}) \\ \sum \Delta y_{ic} (\Delta x_{ic} + \Delta y_{ic}) \end{Bmatrix} \quad (8.24)$$

i.e.,  $\Delta \bar{u}_{ic} = \Delta x_{ic} + \Delta y_{ic}$ .

Cramer's rule may used to solve the symmetric  $2 \times 2$  system for  $\nabla_c \bar{u}$ , e.g.,

$$\frac{\partial \bar{u}}{\partial x} = \frac{1}{\det(L)} \begin{vmatrix} f_1 & L_{12} \\ f_2 & L_{22} \end{vmatrix} \quad (8.25)$$

Expanding this result in terms of the vertex differences, the x-gradient becomes

$$\frac{\partial \bar{u}}{\partial x} = \frac{\sum \Delta x_{ic}^2 \sum \Delta y_{ic}^2 - (\sum \Delta x_{ic} \Delta y_{ic})^2}{\sum \Delta x_{ic}^2 \sum \Delta y_{ic}^2 - (\sum \Delta x_{ic} \Delta y_{ic})^2} = 1 \quad (8.26)$$

That is, the computed x-gradient of  $\bar{u}$  is exact when the field is linear. Similar results are obtained for  $\partial \bar{u} / \partial y$ , and for  $\partial \bar{u} / \partial z$  in three dimensions.

In order to compute gradients at boundaries, ghost data as shown in Figure 8.3 is introduced. For the cell-centered data, finite element like homogeneous natural boundary conditions are implemented by default. This corresponds to prescribing  $\partial \bar{u} / \partial n = 0$  at the boundary where  $n$  is the outward-pointing boundary normal. This approach is taken for the compressible, incompressible, and cell-centered heat-conduction solvers in the Hydra toolkit providing the default finite-element homogeneous natural or "do-nothing" conditions.

With the gradient approximation in hand, attention is turned to the limiting procedure. Consideration of monotonicity suggests that the reconstructed field from Eq. (8.15) should not exceed the minimum/maximum of the neighboring vertex values. As a starting point, we follow the limiting procedure introduced by Barth and Jespersion [Barth and Jespersion, 1989]. The limiting procedure proceeds as follows.

1. For a given vertex, compute the local minimum/maximum based

on local neighbors as

$$\begin{aligned}\bar{u}_{min} &= \min(\bar{u}, \bar{u}_i) \quad i = 1, \dots, N_{edge} \\ \bar{u}_{max} &= \max(\bar{u}, \bar{u}_i) \quad i = 1, \dots, N_{edge}\end{aligned}\quad (8.27)$$

2. Calculate the minimum/maximum field differences,

$$\begin{aligned}\delta u_{min} &= \bar{u}_{min} - \bar{u} \\ \delta u_{max} &= \bar{u}_{max} - \bar{u}\end{aligned}\quad (8.28)$$

3. For each local edge, compute the slope limiter,

$$\phi_i = \begin{cases} \min(1, \delta u_{max} / \delta u_i) & \text{if } \delta u_i > 0 \\ \min(1, \delta u_{min} / \delta u_i) & \text{if } \delta u_i < 0 \\ 1 & \text{if } \delta u_i = 0 \end{cases}\quad (8.29)$$

where  $\delta u_i = \mathbf{ffr}_i \cdot \nabla \bar{u}$ .

4. Compute the minimum value for the limiter over all local edges of the current cell.

$$\phi = \min(\phi_i) \quad i = 1, \dots, N_{edge}\quad (8.30)$$

### *The Weighted Least-Squares Gradient*

The unweighted least-squares gradient approximation relies on solving the normal equations for which the determinant corresponds to a difference in quantities that scales as  $O(\Delta x^4)$ . The consequence is ill-conditioning that can result in inaccurate gradients. An alternative is to use a weighting scheme that results in an  $O(1)$  determinant and avoids ill-conditioning of the normal equations. One example of this type of weighted least-squares may be found in Anderson and Bonhaus[Anderson and Bonhaus, 1994]. Mavriplis[Mavriplis, 2003] suggests a simpler version of weighted least squares which we summarize here.

Using Eq. (8.23) as a starting, the weighting suggested by Mavriplis is introduced as

$$\begin{bmatrix} \sum w_{ic}^2 \Delta x_{ic}^2 & \sum w_{ic}^2 \Delta x_{ic} \Delta y_{ic} & \sum w_{ic}^2 \Delta x_{ic} \Delta z_{ic} \\ \sum w_{ic}^2 \Delta x_{ic} \Delta y_{ic} & \sum w_{ic}^2 \Delta y_{ic}^2 & \sum w_{ic}^2 \Delta y_{ic} \Delta z_{ic} \\ \sum w_{ic}^2 \Delta x_{ic} \Delta z_{ic} & \sum w_{ic}^2 \Delta y_{ic} \Delta z_{ic} & \sum w_{ic}^2 \Delta z_{ic}^2 \end{bmatrix} \begin{Bmatrix} \frac{\partial u}{\partial x} \\ \frac{\partial u}{\partial y} \\ \frac{\partial u}{\partial z} \end{Bmatrix} = \begin{Bmatrix} \sum w_{ic}^2 \Delta x_{ic} \Delta u_{ic} \\ \sum w_{ic}^2 \Delta y_{ic} \Delta u_{ic} \\ \sum w_{ic}^2 \Delta z_{ic} \Delta u_{ic} \end{Bmatrix}\quad (8.31)$$

where

$$w_{ic} = \frac{1}{\sqrt{\Delta x_{ic}^2 + \Delta y_{ic}^2 + \Delta z_{ic}^2}}.\quad (8.32)$$

There are a number of other approaches for computing least-squares gradient approximations, see for example the work by Rider and Kothe [Rider and Kothe, 2002] and Kothe, et al. [Kothe et al., 2002]. The inverse-distance weighted least-squares procedure is currently used in the Hydra Toolkit.

### *Phase-speed and Artificial Diffusivity*

The numerical performance of the numerical flux may be understood in terms of the phase error and artificial diffusivity introduced by the underlying discretization. A detailed discussion of the analysis techniques used to assess numerical performance may be found in the work by Christon, et al. [Christon et al., 2004, Voth et al., 2004, Christon et al., 2003].

For the Hydra toolkit, we consider the performance of the semi-discrete method described above. In this context, the numerical phase speed is simply the ratio of the apparent discrete advective speed and the true speed,  $\tilde{c}/c$ . The diffusive behavior is captured in terms of an inverse Peclet number where for a purely non-diffusive method,  $1/Pe^{art} = 0$ .

Figure 8.4 shows the non-dimensional phase speed and artificial diffusivity as functions of the non-dimensional wave number up to the grid Nyquist limit. The values that the associated limiters may achieve based on the input data are shown in the inset. There are four cases that correspond to various forms of data that may be present on the grid.

1.  $\phi_{m-1} = \phi_m = 0$ : This situation corresponds to  $2\Delta x$  signals on the grid where the slope limiters are fully activated. In this case, the phase speed corresponds to that associated with a central-differences discretization with first-order upwinding at the Nyquist grid limit. In other words, the method attempts to completely damp these signals to avoid oscillatory solutions.
2.  $\phi_{m-1} = 0, \phi_m = 1$ : Here, a change in slope occurs, with smooth-data to the right. In this case, the the artificial diffusivity is reduced to 50% of the first-order upwind case, and the phase-speed increased at long wavelengths. This has the effect of controlling oscillations and avoiding signal separation due to dispersive effects.
3.  $\phi_{m-1} = 1, \phi_m = 0$ : Here, a change in slope occurs again, with smooth-data to the right. In this case, the the artificial diffusivity is reduced to 50% of the first-order upwind case, and the phase-speed decreased at long wavelengths. Again, this has the controls oscillations and avoids signal separation due to dispersive effects.
4.  $\phi_{m-1} = 1, \phi_m = 1$ : Here, smooth data is present, and there is no limiting performed. In this case, the artificial diffusivity is zero and corresponds to the limit of pure advection, and the phase-speed is that associated with a second-order central-difference approximation of the gradient. This corresponds to the case when all signals are adequately resolved on the grid.

The advection methods used in the Hydra toolkit are non-linear, monotonicity-preserving, and follow the general behavior described here. For smooth data, the methods are non-dissipative, and deliver second-order spatial convergence. For the limit of oscillatory data at the  $2\Delta x$  Nyquist limit, the methods attempt to damp only the short wavelength data while preserving the resolved long wavelength data on the grid.

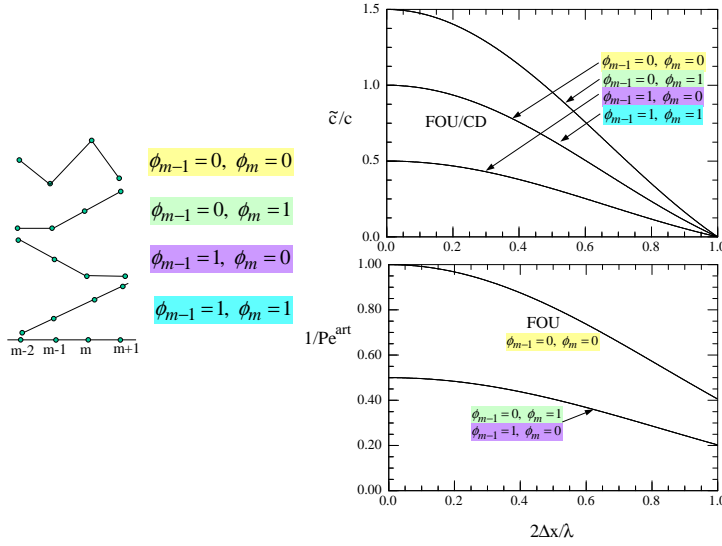


Figure 8.4: Phase speed and artificial diffusivity as a function of non-dimensional wave number.

### Convergence Studies

There are various metrics available that may be used to assess the accuracy of a solution method or, alternatively, to verify its correctness. For our purposes, we are interested in extracting the leading order terms in the discretization error.

The discretization error is comprised of both spatial and temporal errors. It is defined as the difference between the computed and exact solutions,

$$\mathbf{e}_i = \bar{u}_i^e - \bar{u}_i, \quad (8.33)$$

where the exact grid function  $\bar{u}_i^e$  is defined in terms of the exact field solution  $u_i^e$  as

$$\bar{u}_i^e = \frac{1}{\Omega_i} \int_{\Omega_i} u_i^e d\Omega. \quad (8.34)$$

It can be shown that the discretization error is proportional to the truncation error which permits the discretization error to be written

in a one-dimensional form as

$$\mathbf{e}_j = \alpha h^p + \beta \Delta t^q + H.O.T., \quad (8.35)$$

where  $p$  corresponds to the order of the spatial discretization,  $q$  to the order of the temporal discretization, and  $H.O.T.$  indicates higher-order terms.

It is typical to use reconstruction methods that are matched with the time integrator, i.e.,  $p = q$ . In addition, the time step and mesh size are related by the CFL number,

$$\Delta t = \frac{CFL h}{\lambda} \quad (8.36)$$

where  $\lambda$  is the magnitude of the largest eigenvalue of the flux Jacobian. This permits the discretization error to be written as

$$\mathbf{e}_j = \left( \alpha + \beta \frac{CFL}{\lambda} \right) \Delta x^p + H.O.T. \quad (8.37)$$

In terms of a global error metric,

$$\|\mathbf{e}\| = \bar{\alpha} h^p + H.O.T. \quad (8.38)$$

For all of the computations presented below, errors are measured in terms of a discrete  $L^1$  norm,

$$\|\mathbf{e}\| = \frac{\sum_i |\bar{u}_i^e - \bar{u}_i|}{\sum_i |\bar{u}_i^e|} \quad (8.39)$$

or in terms of a discrete  $L^\infty$  norm,

$$\|\mathbf{e}\| = \max_j |\bar{u}_j^e - \bar{u}_j|. \quad (8.40)$$

Using a sequence of two grids, the global error metric may be used to extract the order of accuracy  $p$ , e.g.,

$$\frac{\|\mathbf{e}_1\|}{\|\mathbf{e}_2\|} = \left( \frac{h_1}{h_2} \right)^p, \quad (8.41)$$

where the subscript refers to the grid level. For all calculations presented here,  $h_1/h_2 = 2$ .

For smooth solutions we expect to recover an order of accuracy that is consistent with the formal accuracy of the method, e.g., second-order or  $O(h^2)$  for a formally second-order spatial discretization ( $p = 2$ ). For solutions with non-smooth data, e.g., shocks, we expect to achieve first-order or  $O(h)$  convergence rates measured in the  $L^1$  norm. In addition to the order of accuracy, the magnitude of the measured error is also useful in a multi-methods comparison. In the ensuing discussion, results of convergence studies for a series of smooth and non-smooth initial data and grid configurations are reported.



*Translating Gaussian*

The first problem in our suite of problems used to study the convergence of edge-based advection algorithms consists of a translating Gaussian pulse. The governing equation for this problem is

$$\frac{\partial u}{\partial t} + \nabla \cdot (\mathbf{c}u) = 0, \quad (8.42)$$

The initial conditions are

$$u(x, 0) = \exp \left\{ -\frac{(x - \bar{x})^2}{2\sigma_0^2} \right\}, \quad (8.43)$$

where

$$\bar{x} = x_0 + \int_0^t c(\tau) d\tau, \quad (8.44)$$

and

$$\sigma^2 = \sigma_0^2 + 2\kappa t. \quad (8.45)$$

The exact solution is

$$\hat{u}(x, t) = \frac{\sigma_0}{\sigma} \exp \left\{ -\frac{(x - \bar{x})^2}{2\sigma^2} \right\}. \quad (8.46)$$

For our purposes, a computational domain with  $0 \leq x \leq 15$  is used. The initial conditions are specified with  $\mathbf{c} = (1.0, 0)$  and  $\sigma_0 = 0.25$  with the Gaussian centered at  $x_0 = 2.05$ . In order to compute convergence rates, the solution error is computed as a function of time. The convergence rates are calculated at  $t = 2.5, 5.0, 10.0$  time units for a variety of grids discretized with both triangular and quadrilateral elements.

*Uniform Triangular Elements*

The  $15 \times 1$  computational domain discretized by a regular configuration of triangular elements is shown in Figure 8.5.

The  $L^1$  error and associated convergence rates are tabulated at three times,  $t = 2.5, 5.0, 10.0$  time units, in Table 8.1 and shown graphically in Figure 8.6. The convergence rates are approaching  $h^2$  as the mesh is refined – note that mesh refinement was achieved by a doubling procedure that retains the original nodal coordinates from the original coarse-grid.

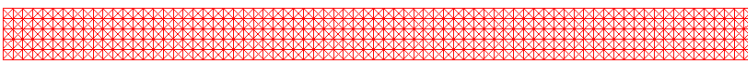


Figure 8.5: Mesh configuration for all-triangular meshes.

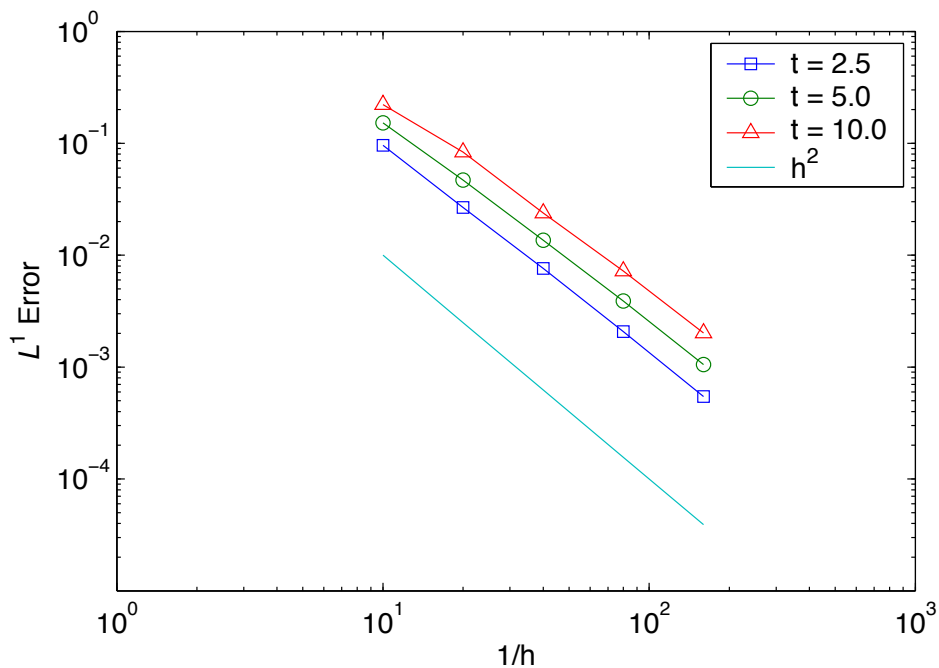


Figure 8.6:  $L^1$  errors at  $t = 2.5$ ,  $5.0$ , and  $10.0$  for the all-triangular meshes.

Table 8.1:  $L^1$  errors and convergence rates for the all-triangular meshes at  $t = 2.5$ ,  $t = 5.0$ , and  $t = 10.0$ .

Mesh Size	$t = 2.5$		$t = 5.0$		$t = 10.0$	
	$L^1$ Error	Rate	$L^1$ Error	Rate	$L^1$ Error	Rate
10	9.592E-02	–	1.520E-01	–	2.219E-01	–
20	2.670E-02	1.8449	4.690E-02	1.6969	8.350E-02	1.4104
40	7.608E-03	1.8113	1.360E-02	1.7859	2.385E-02	1.8076
80	2.074E-03	1.8750	3.895E-03	1.8038	7.207E-03	1.7266
160	5.464E-04	1.9245	1.052E-03	1.8879	2.020E-03	1.8351

*Triangular Elements – Rotated Grid*

The computations reported in §8.5 are repeated here on a series of grids with identical resolution, but which are rotated by  $30^\circ$  from the  $x$ -axis. Although the wave propagation problem remains one-dimensional along the mesh lines, it exercises the multi-dimensional discrete operators of the code and test the natural boundary conditions which specify that  $\partial u / \partial n = 0$ .

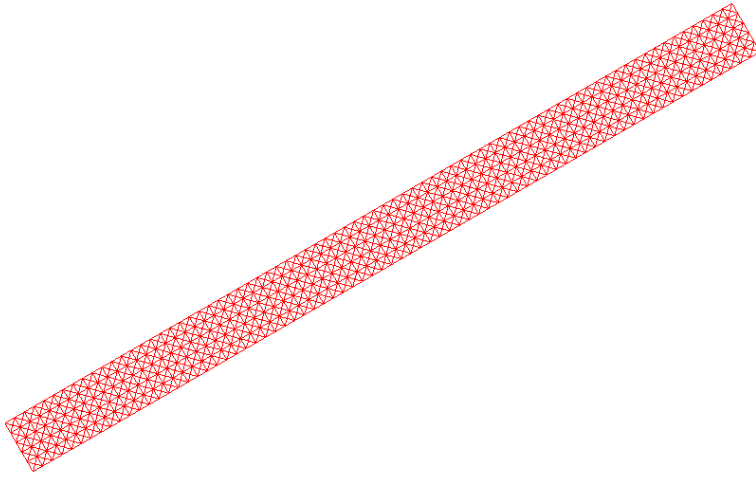


Figure 8.7: Rotated mesh configuration for all-triangular meshes.

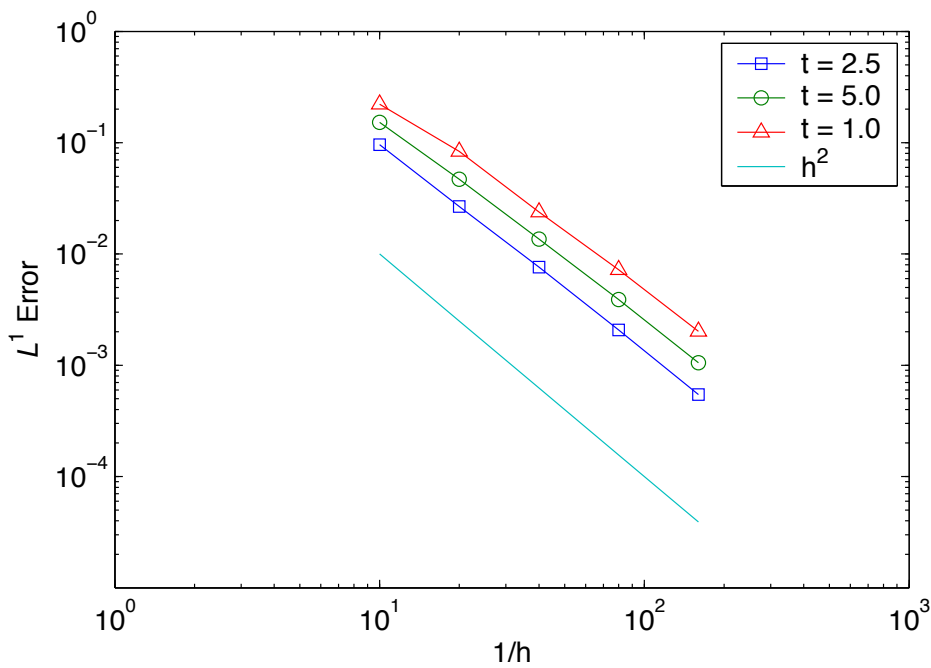


Figure 8.8:  $L^1$  errors at  $t = 2.5, 5.0,$  and  $10.0$  for the rotated all-triangular meshes.

Table 8.2:  $L^1$  errors and convergence rates for the rotated all-triangular meshes at  $t = 2.5$ ,  $t = 5.0$ , and  $t = 10.0$ .

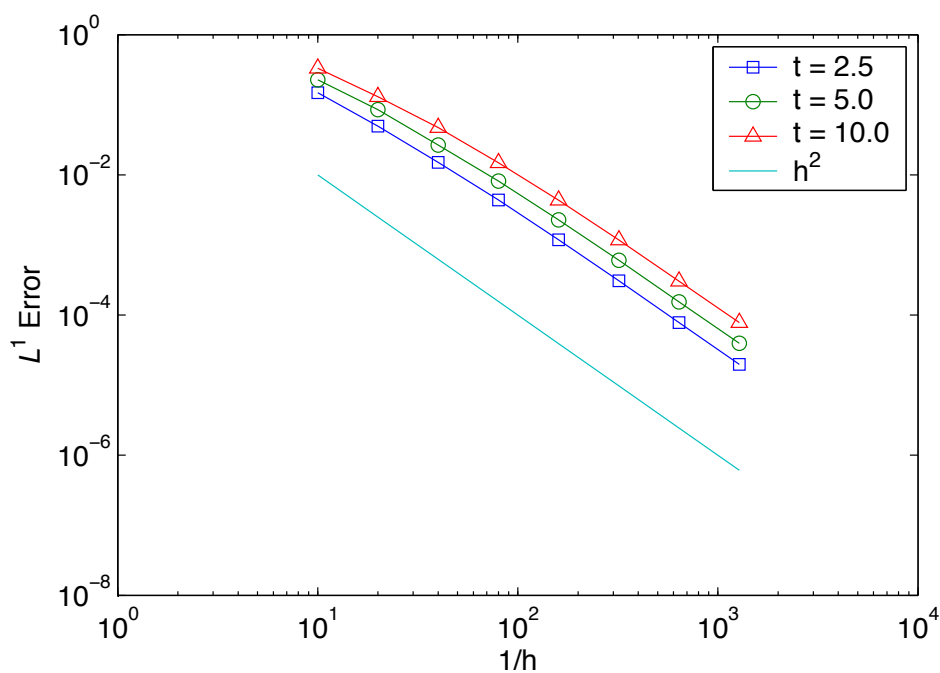
Mesh Size	$t = 2.5$		$t = 5.0$		$t = 10.0$		
	$L/h$	$L^1$ Error	Rate	$L^1$ Error	Rate	$L^1$ Error	Rate
10		9.592e-02		1.520e-01		2.220e-01	
20		2.670e-02	1.8449	4.689e-02	1.6970	8.349e-02	1.4105
40		7.608e-03	1.8114	1.360e-02	1.7858	2.385e-02	1.8077
80		2.074e-03	1.8749	3.895e-03	1.8039	7.207e-03	1.7265
160		5.464e-04	1.9246	1.052e-03	1.8879	2.020e-03	1.8348

### Quadrilateral Elements

In this section, the translating Gaussian test case is performed on a sequence of all quadrilateral grids as shown in Figure 8.9. A convergence plot is shown in Figure 8.10 along with the associated error data in Table 8.3.



Figure 8.9: Mesh configuration for all-quadrilateral meshes.

Figure 8.10:  $L^1$  errors at  $t = 2.5$ ,  $5.0$ , and  $10.0$  for the all-quadrilateral meshes.

### Quadrilateral Elements – Rotated Grid

The computations reported in §8.5 are repeated here on a series of grid with identical resolution, but which are rotated by  $30^\circ$  from the  $x$ -axis.

Table 8.3:  $L^1$  errors and convergence rates at  $t = 5$  for the all-quadrilateral meshes.

Mesh Size	$t = 2.5$		$t = 5.0$		$t = 10.0$	
	$L^1$ Error	Rate	$L^1$ Error	Rate	$L^1$ Error	Rate
$1/h$						
10	1.490E-01	–	2.268E-01	–	3.326E-01	–
20	4.956E-02	1.589	8.545E-02	1.408	1.303E-01	1.352
40	1.506E-02	1.718	2.655E-02	1.686	4.738E-02	1.459
80	4.384E-03	1.781	8.163E-03	1.702	1.485E-02	1.674
160	1.186E-03	1.886	2.280E-03	1.840	4.342E-03	1.774
320	3.069E-04	1.951	6.020E-04	1.921	1.173E-03	1.888
640	7.816E-05	1.974	1.544E-04	1.963	3.043E-04	1.946
1280	1.981E-05	1.980	3.941E-05	1.970	7.819E-04	1.961

Although the wave propagation problem remains one-dimensional along the mesh lines, it exercises the multi-dimensional discrete operators of the code and test the natural boundary conditions which specify that  $\partial u / \partial n = 0$ .

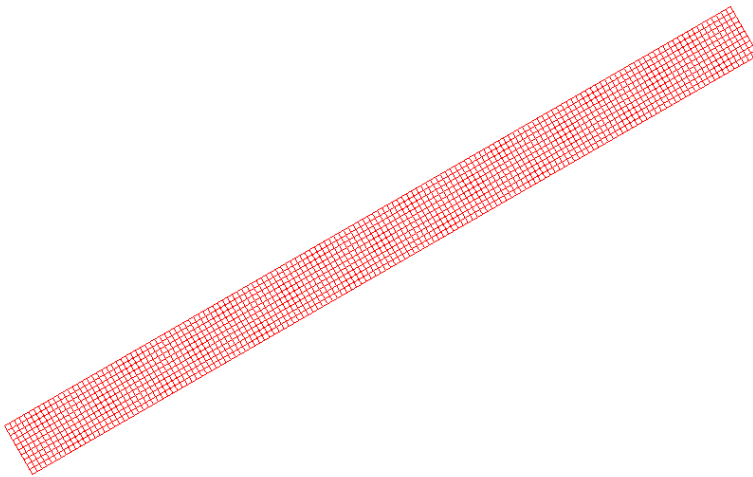


Figure 8.11: Mesh configuration for the rotated all-quadrilateral meshes.

### *Mixed Quad/Tri Meshes*

In this section, a the results of a series of convergence studies performed using mixed triangle/quadrilateral meshes are reported. Three cases were considered: a) a longitudinal split with triangles on the bottom of the domain and quadrilaterals on the top, b) a mixed domain starting with a patch of quadrilaterals, and c) a mixed domain starting with a patch of triangles.

## Case-A: Longitudinal Split

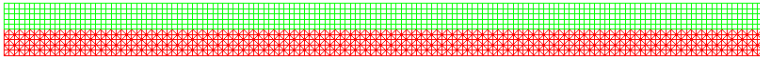
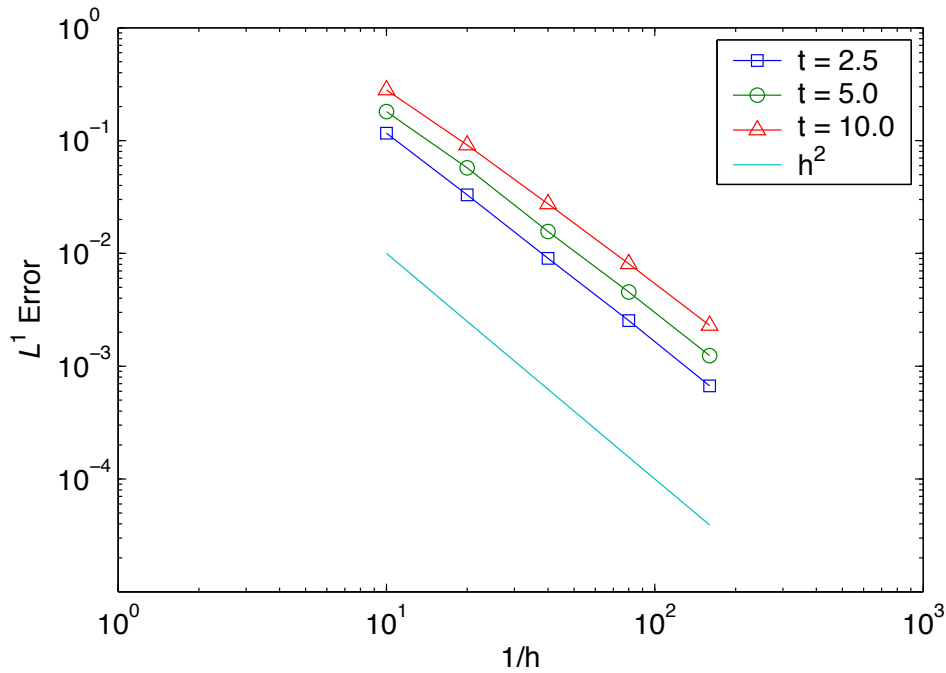


Figure 8.12: Mesh configuration for the case-a tri-quad meshes.

Figure 8.13:  $L^1$  errors at  $t = 2.5, 5.0,$  and  $10.0$  for the case-a tri-quad meshes.Table 8.4:  $L^1$  errors and convergence rates at  $t = 5.0$  for the case-a tri-quad meshes.

Mesh Size $1/h$	$t = 2.5$		$t = 5.0$		$t = 10.0$	
	$L^1$ Error	Rate	$L^1$ Error	Rate	$L^1$ Error	Rate
10	1.165E-01		1.811E-01		2.806E-01	
20	3.300E-02	1.8194	5.724E-02	1.6615	9.133E-02	1.6196
40	9.050E-03	1.8665	1.565E-02	1.8711	2.742E-02	1.7359
80	2.532E-03	1.8374	4.548E-03	1.7829	8.103E-03	1.7586
160	6.683E-04	1.9218	1.239E-03	1.8753	2.299E-03	1.8175

Case-B: Quad/Tri Patches

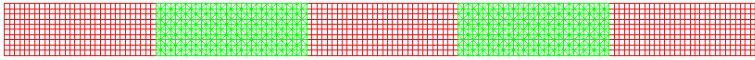


Figure 8.14: Mesh configuration for the case-b tri-quad meshes.

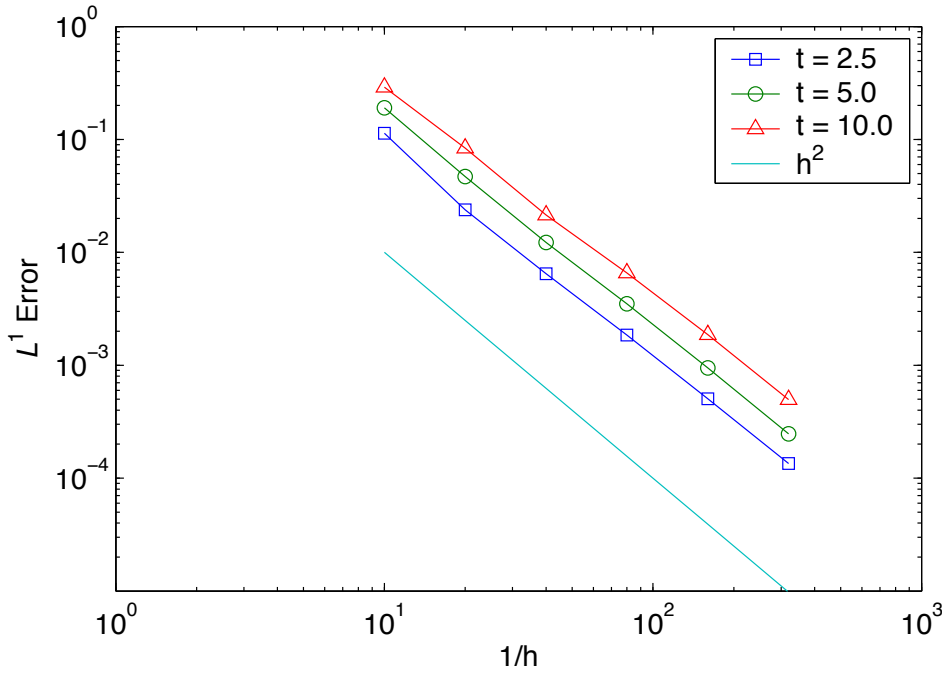


Figure 8.15:  $L^1$  errors at  $t = 2.5, 5.0,$  and  $10.0$  for the case-b tri-quad meshes.

Table 8.5:  $L^1$  errors and convergence rates at  $t = 5.0$  for the case-b tri-quad meshes.

Mesh Size $1/h$	$t = 2.5$		$t = 5.0$		$t = 10.0$	
	$L^1$ Error	Rate	$L^1$ Error	Rate	$L^1$ Error	Rate
10	1.136E-01		1.906E-01		2.901E-01	
20	2.379E-02	2.2560	4.703E-02	2.0191	8.395E-02	1.7888
40	6.455E-03	1.8818	1.225E-02	1.9410	2.139E-02	1.9726
80	1.849E-03	1.8036	3.498E-03	1.8077	6.567E-03	1.7037
160	5.042E-04	1.8745	9.486E-04	1.8828	1.868E-03	1.8134
320	1.347E-04	1.9046	2.471E-04	1.9405	4.972E-04	1.9097

Case-C: Tri/Quad Patches

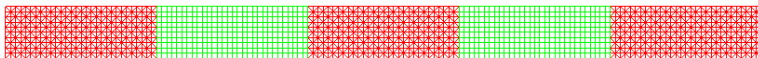


Figure 8.16: Mesh configuration for the case-c tri-quad meshes.

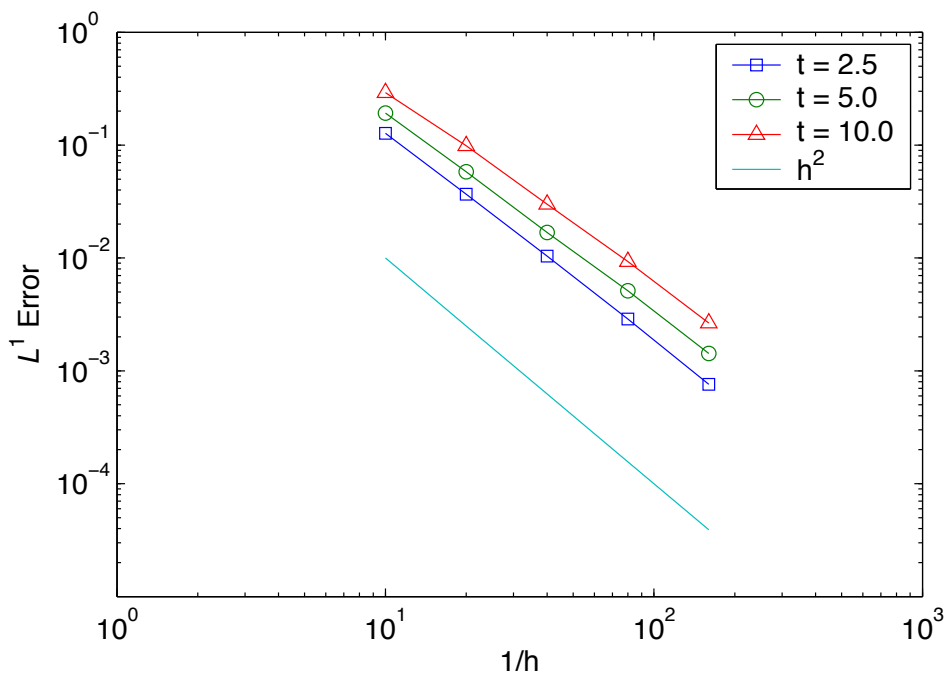


Figure 8.17:  $L^1$  errors at  $t = 2.5, 5.0,$  and  $10.0$  for the case-c tri-quad meshes.

Table 8.6:  $L^1$  errors and convergence rates at  $t = 2.5, t = 5.0,$  and  $t = 10.0$ .

Mesh Size	$t = 2.5$		$t = 5.0$		$t = 10.0$		
	$1/h$	$L^1$ Error	Rate	$L^1$ Error	Rate	$L^1$ Error	Rate
	10	1.273E-01		1.920E-01		2.922E-01	
	20	3.666E-02	1.7957	5.812E-02	1.7242	9.880E-02	1.5644
	40	1.040E-02	1.8183	1.682E-02	1.7893	2.989E-02	1.7250
	80	2.884E-03	1.8501	5.120E-03	1.7156	9.293E-03	1.6853
	160	7.586E-04	1.9265	1.428E-03	1.8423	2.650E-03	1.8103



*Rotating Cone*

The rotating cone problem has been documented in the work by Baptista, et al. [Baptista et al., 1995]. For our purposes, the problem consists of ‘pure’ advection problem, i.e.,

$$\frac{\partial u}{\partial t} + \nabla \cdot (\mathbf{c}u) = 0, \quad (8.47)$$

where  $\mathbf{c} = (c_x, c_y)$ ,  $u = -\omega y$ ,  $v = \omega x$ , and  $\omega = \pi/100$ . The domain is defined  $-100 \leq x \leq 100$ , and  $-100 \leq y \leq 100$ .

The exact solution to this problem is

$$\hat{u}(x, y, t) = \exp \left\{ -\frac{(x - \bar{x})^2}{2\sigma_0^2} - \frac{(y - \bar{y})^2}{2\sigma_0^2} \right\}, \quad (8.48)$$

where

$$\bar{x} = x_0 + \int_0^t c_x(\tau) d\tau, \quad (8.49)$$

and

$$\bar{y} = y_0 + \int_0^t c_y(\tau) d\tau. \quad (8.50)$$

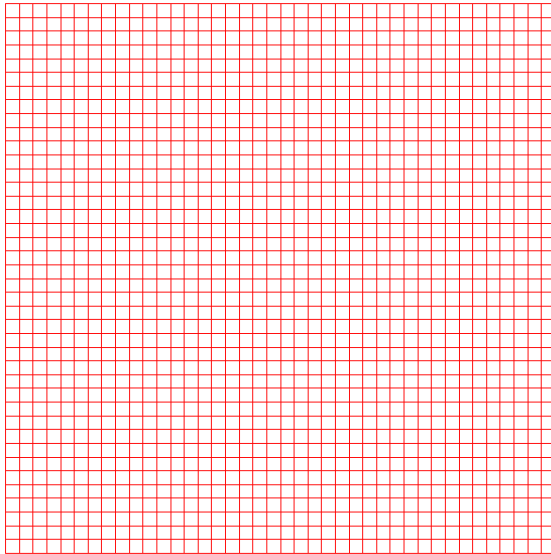
*Quadrilateral Elements*

Figure 8.18: Mesh configuration for the quadrilateral meshes.

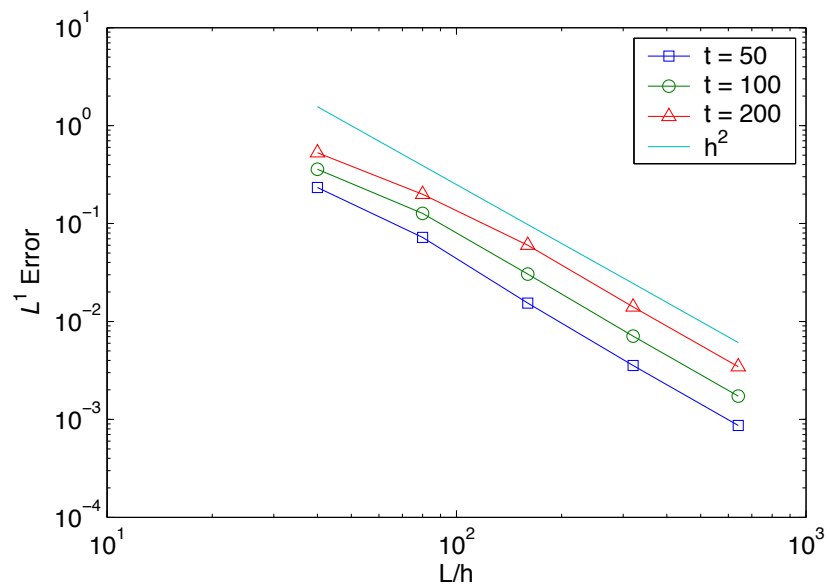


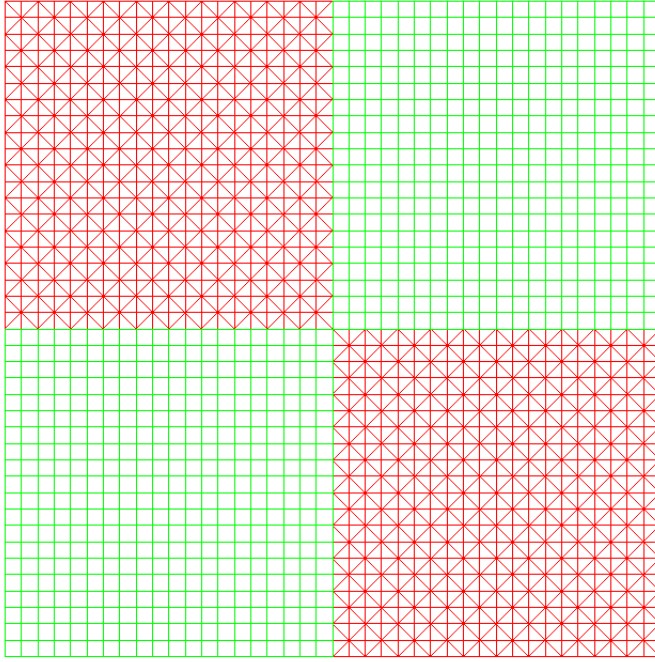
Figure 8.19:  $L^1$  Error as a function of time for the quadrilateral meshes.

Table 8.7:  $\mathcal{L}^1$  errors and convergence rates at  $t = 5$ ,  $t = 100$ , and  $t = 200$  for the quadrilateral meshes.

Mesh Size	$t = 50$		$t = 100$		$t = 200$		
	$L/h$	$L^1$ Error	Rate	$L^1$ Error	Rate	$L^1$ Error	Rate
40		2.335E-01	–	3.585E-01	–	5.290E-01	–
80		7.206E-02	1.6965	1.271E-01	1.4961	1.989E-01	1.4114
160		1.539E-02	2.2271	3.046E-02	2.0607	6.002E-02	1.7284
320		3.552E-03	2.1153	7.078E-03	2.1056	1.409E-02	2.0907
640		8.675E-03	2.0337	1.728E-03	2.0342	3.444E-03	2.0322

*Mixed Quad/Tri Meshes*

Figure 8.20: Mesh configuration for the mixed meshes.

Table 8.8:  $L^1$  errors and convergence rates at  $t = 50$ ,  $t = 100$ , and  $t = 200$  for the mixed meshes.

Mesh Size	$t = 50$		$t = 100$		$t = 200$	
$L/h$	$L^1$ Error	Rate	$L^1$ Error	Rate	$L^1$ Error	Rate
40	1.613E-01	–	3.049E-01	–	4.670E-01	–
80	3.516E-02	2.1981	8.849E-02	1.7847	1.526E-01	1.6136
160	8.298E-03	2.0830	1.857E-02	2.2522	3.633E-02	2.0707
320	2.828E-03	1.5531	4.399E-03	2.0779	8.324E-03	2.1257
640	1.121E-04	1.3342	1.304E-03	1.7541	2.265E-03	1.8777

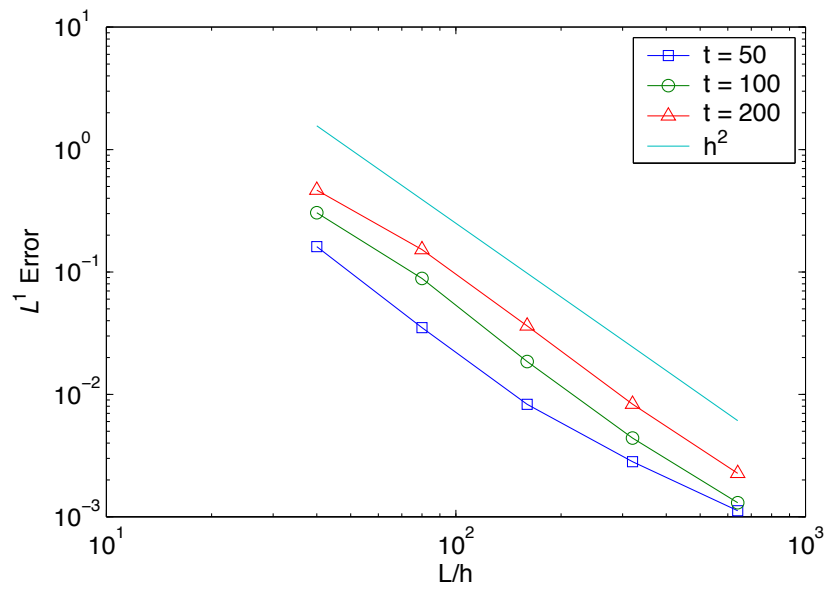


Figure 8.21:  $L^1$  Error as a function of time for the mixed meshes.

## 9 *Gradient Approximation*

The Hydra toolkit provides a general set of tools for implementing multiphysics applications using essentially any unstructured-grid spatial discretization. For finite-volume centric applications where local-conservation is deemed to be important, the gradient approximation becomes central to designing accurate and robust methods. This chapter reviews the cell and edge-centered gradient approximations that have been tested during the development of the Hydra, the associated compressible and incompressible flow solvers, and highlights those methods that perform the best.

### *Background*

The topic of gradient estimation is central to the development of accurate finite-volume methods on unstructured grids. Therefore, the early-development of Hydra focused on the choice of the best gradient approximation. The development of robust and accurate gradient estimators for unstructured grids is still an area of relatively active research as shown by some of the very recent work by Bechten and Straatman [Betchen and Straatman, 2010] and Puigt, et al. [Puigt et al., 2010].

The following criteria were used to develop the gradient estimation techniques implemented in Hydra.

- Deliver linear consistency
- Suitable for unstructured grids with mixed element types
- Second-Order Accuracy
- Computational complexity

In addition, the choice of where the gradient estimation is centered on an unstructured grid is important. We considered primarily face-centered and element-centered gradient estimations as these were of primary interest for the development of the compressible and incompressible flow solvers. During the scoping studies for Hydra devel-

opment, we considered the following possible choices in light of our primary criteria listed above.

*Green-Gauss:* As demonstrated by Barth and co-workers [Barth and Jespersen, 1989, Barth and Frederickson, 1990, Barth, 1993, Barth, Barth and Ohlberger, 2004], the Green-Gauss estimator does reproduce exact gradients for linear fields. (*Rejected*)

*Modified Green-Gauss:* The recent work by Betchen and Straatman [Betchen and Straatman, 2010] uses a modified construction of the gradient with the underlying formulation based on the Green-Gauss gradient. This has not been tested in Hydra. The LST scheme by Chang and Yuan [Chang and Yuan, 2009] and the approach by Svärd and Nordström [Svärd and Nordström, 2004] also remain untested in Hydra. The work by Klinger, et al. [Klinger et al., 2004] suggests a methodology that delivers second-order accuracy on highly non-orthogonal meshes. This was tested and rejected because it did not deliver exact gradients for linear fields. (*Untested/Rejected*)

*Gradient Smoothing:* There are a number of papers that suggest that adequate accuracy can be obtained by applying a local smoothing operation to the Green-Gauss gradient estimate. This type of approach is characterized by the work done by Liu and Xu [Liu and Xu, 2008]. Testing in Hydra showed that this approach does not reproduce exact gradients for linear fields. (*Rejected*)

*Gradient Correction:* There are a number of gradient correction practices touted in the literature as found in the work by Lehnhäuser and Schäfer [Lehnhäuser and Schäfer, 2002], AVL's SWIFT code [AVL, 2004] and Liu and Xu [Liu and Xu, 2008]. These methods are used with primarily with Green-Gauss, and sometimes least-squares gradient estimators, and are applied to the viscous/diffusive terms in an incompressible flow solver. (*Used with edge gradients*)

*Ničeno's Method:* The work by Ničeno [Ničeno, 2006] selects two points that are co-linear with the dual-edge (face) normal, and directly constructs an edge-gradient. The edge-gradient is comprised of a face-gradient oriented in the normal-direction using the fictitious normal-aligned points, and a linear combination of the connected element gradients projected in the normal direction. This approach directly constructs the normal flux required for the diffusive terms and makes use of cell-centered least-squares gradient approximations. The unique aspect of this work is that it suggests an implementation approach that constructs one-sided element-oriented "stiffness" operators that can be assembled to form the global matrix. This approach may be useful for obtaining performance gains in

Hydra. At this time, this approach remains untested in Hydra.  
(*Untested*)

*Coirier's Diamond Path:* This method was developed by Coirier in 1994 and suggested as an accurate scheme for gradient estimation in Vigneron, et al. [Vigneron et al., 2005]. As the method is only presented in 2-D, it was rejected as a suitable method. (*Rejected*)

*Least-Squares:* A large number of researchers have advocated the use of least-squares gradient estimators [Barth and Jespersen, 1989, Barth and Frederickson, 1990, Barth, 1993, Barth, Barth and Ohlberger, 2004, Mavriplis, 2003, Mavriplis, 2007, Anderson and Bonhaus, 1994, Ollivier-Gooch and Altena, 2002, A. and Turner, 2005]. We have adopted the weighted least-squares procedure for both cell and edge-centered gradient estimation. This methodology is the only one we have found that essentially satisfies all of the criteria above. For the incompressible flow solver, the edge-based gradients are modified to deal with extreme mesh distortion in the construction of the diffusive fluxes as explained in the ensuing discussion. (*Used for cell and edge gradients*)

*Modified Least-Squares:* The work on constrained least-squares work by Rider and Kothe [Rider and Kothe, 2002], and Kothe, et al. [Kothe et al., 2002] and by Chenoweth, et al. [Chenoweth et al., 2007] has not been tested in Hydra. (*Untested*)

*FEM Projection:* Another approach that was considered what the use of an  $\mathcal{L}^2$  projection of cell-centered data to the nodes, followed by a gradient calculation using the element shape functions. This was rejected as it can not be used for edge gradients, and would involve increased computational complexity as well as communication in parallel. (*Rejected*)

*Non-conforming Meshes:* The work by Chang and Yuan [Chang and Yuan, 2009] describes the construction of the diffusive fluxes for general non-conforming meshes. This technique makes use of nodal unknowns to construct the flux, but effectively eliminates the nodal variables to cast the discrete operator in terms of element-centered data. The node-centered variables are cast as a projection of the element-centered values with weights based on the local topology of the mesh. In effect, this approach attempts to use an FEM-like projection to construct nodal data used in an integration over the edge-centered dual-grid element. This construction is used with a trapezoidal integration of the values over each cell-face in order to construct a gradient using effectively Coirier's diamond path. This approach requires the storage of an inverse connectivity, but

appears to consistently deliver second-order accuracy on arbitrary grids. Extension to treat meshes with arbitrary combinations of tetrahedron, wedges, pyramids and hexahedra has not been attempted. (*Untested*)

*Compatible/Mimetic Methods:* The work by Lipnikov, et al. [Kuznetsov et al., 2004, Lipnikov et al., 2007] describes the use of the so-called mimetic or compatible discretization method for construction of diffusive fluxes on meshes comprised of arbitrary polyhedra. At the time of this writing, these methods were considered to be excessively computationally intensive for a production-level code. (*Untested*)

We also note the work by Wang [Wang, 1999] on arbitrary polyhedral meshes. If future efforts pursue arbitrary polyhedral meshes, this may be of some value. For node-centered gradient approximations, the work by Smith, et al. [Smith et al., 2007] presents a detailed comparison of gradient estimators.

### *Element-Centered Gradients*

The cell-centered gradient approximations presented in Chapter 8 detail the weighted least-squares method used for cell-centered gradients in Hydra. The Green-Gauss, least-squares and weighted least-squares methods are presented in detail in Chapter 8 as well.

### *Edge-Centered Gradients*

The edge-centered least-squares gradient calculation closely follows the development in §8.3. However, because the gradient is centered at the dual-edge, the field value is unknown requiring the estimation of both the field value and its gradient at the dual-edge.

The least-squares procedure attempts to find discontinuous reconstruction polynomials that are close to their  $C^0$  counterparts. For the edge-centered gradient, cell-centered data is used to construct the least-squares approximation. Figure 9.1 shows the data required for the least-squares reconstruction on a patch of triangles and quadrilaterals.

Using the convention that  $\Delta x_{ic} = x_i - x_c$ , we proceed by expanding for each known data point around point 'c'. For  $N$  points, the expansion is

$$\begin{aligned} u_1 &= u_c + \frac{\partial u}{\partial x} \Delta x_{1c} + \frac{\partial u}{\partial y} \Delta y_{1c} \\ u_2 &= u_c + \frac{\partial u}{\partial x} \Delta x_{2c} + \frac{\partial u}{\partial y} \Delta y_{2c} \\ &\vdots \\ u_N &= u_c + \frac{\partial u}{\partial x} \Delta x_{Nc} + \frac{\partial u}{\partial y} \Delta y_{Nc} \end{aligned} \tag{9.1}$$



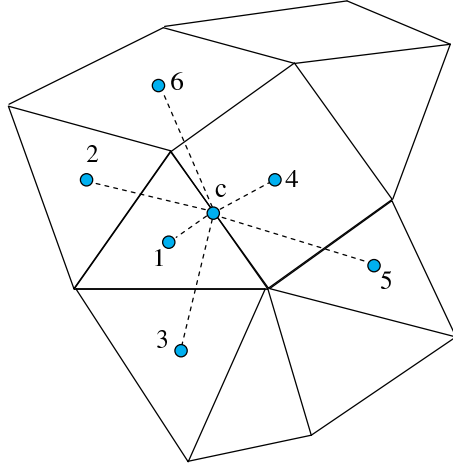


Figure 9.1: Data used for the edge-centered least-squares reconstruction.

For a three-dimensional grid patch with  $N$  data points, this becomes

$$\begin{aligned}
 u_1 &= u_c + \frac{\partial u}{\partial x} \Delta x_{1c} + \frac{\partial u}{\partial y} \Delta y_{1c} + \frac{\partial u}{\partial z} \Delta z_{1c} \\
 u_2 &= u_c + \frac{\partial u}{\partial x} \Delta x_{2c} + \frac{\partial u}{\partial y} \Delta y_{2c} + \frac{\partial u}{\partial z} \Delta z_{2c} \\
 &\vdots \\
 u_N &= u_c + \frac{\partial u}{\partial x} \Delta x_{Nc} + \frac{\partial u}{\partial y} \Delta y_{Nc} + \frac{\partial u}{\partial z} \Delta z_{Nc}
 \end{aligned} \tag{9.2}$$

The edge-centered least-squares reconstruction procedure is equivalent to solving the following non-square problem using the data surrounding each edge. the minimization problem becomes

$$\begin{bmatrix} 1 & \Delta x_{1c} & \Delta y_{1c} & \Delta z_{1c} \\ 1 & \Delta x_{2c} & \Delta y_{2c} & \Delta z_{2c} \\ \vdots & & \vdots & \\ 1 & \Delta x_{Nc} & \Delta y_{Nc} & \Delta z_{Nc} \end{bmatrix} \begin{bmatrix} u_c \\ \frac{\partial u}{\partial x} \\ \frac{\partial u}{\partial y} \\ \frac{\partial u}{\partial z} \end{bmatrix} = \begin{bmatrix} u_1 \\ u_2 \\ \vdots \\ u_N \end{bmatrix} \tag{9.3}$$

Following the cell-centered least-squares procedure, in order to solve for least-squares problem in Eq. (9.3), the normal equations are formed as

$$\begin{bmatrix} \sum 1 & \sum \Delta x_{ic} & \sum \Delta y_{ic} & \sum \Delta z_{ic} \\ \sum \Delta x_{ic} & \sum \Delta x_{ic}^2 & \sum \Delta x_{ic} \Delta y_{ic} & \sum \Delta x_{ic} \Delta z_{ic} \\ \sum \Delta y_{ic} & \sum \Delta x_{ic} \Delta y_{ic} & \sum \Delta y_{ic}^2 & \sum \Delta y_{ic} \Delta z_{ic} \\ \sum \Delta z_{ic} & \sum \Delta x_{ic} \Delta z_{ic} & \sum \Delta y_{ic} \Delta z_{ic} & \sum \Delta z_{ic}^2 \end{bmatrix} \begin{bmatrix} u_c \\ \frac{\partial u}{\partial x} \\ \frac{\partial u}{\partial y} \\ \frac{\partial u}{\partial z} \end{bmatrix} = \begin{bmatrix} \sum u_i \\ \sum u_i \Delta x_{ic} \\ \sum u_i \Delta y_{ic} \\ \sum u_i \Delta z_{ic} \end{bmatrix} \tag{9.4}$$

where the summation is over all data points connected to the edge center 'c' by dual-edge adjacency. Thus, the symmetric  $4 \times 4$  system

is formed one dual-edge at a time in an “edge-by-edge” fashion and requires neighbor information that is accessible by traversing dual-edges.

The implementation in Hydra uses a weighted least-squares approximation with the weighting proposed by Mavriplis [Mavriplis, 2003]. Using Eq. (9.4) as a starting point, the edge-centered weighted least-squares problem is

$$\begin{bmatrix} \sum w_{ic}^2 & \sum w_{ic}^2 \Delta x_{ic} & \sum w_{ic}^2 \Delta y_{ic} & \sum w_{ic}^2 \Delta z_{ic} \\ \sum w_{ic}^2 \Delta x_{ic} & \sum w_{ic}^2 \Delta x_{ic}^2 & \sum w_{ic}^2 \Delta x_{ic} \Delta y_{ic} & \sum w_{ic}^2 \Delta x_{ic} \Delta z_{ic} \\ \sum w_{ic}^2 \Delta y_{ic} & \sum w_{ic}^2 \Delta x_{ic} \Delta y_{ic} & \sum w_{ic}^2 \Delta y_{ic}^2 & \sum w_{ic}^2 \Delta y_{ic} \Delta z_{ic} \\ \sum w_{ic}^2 \Delta z_{ic} & \sum w_{ic}^2 \Delta x_{ic} \Delta z_{ic} & \sum w_{ic}^2 \Delta y_{ic} \Delta z_{ic} & \sum w_{ic}^2 \Delta z_{ic}^2 \end{bmatrix} \begin{Bmatrix} u_c \\ \frac{\partial u}{\partial x} \\ \frac{\partial u}{\partial y} \\ \frac{\partial u}{\partial z} \end{Bmatrix} = \begin{Bmatrix} \sum w_{ic}^2 u_i \\ \sum w_{ic}^2 u_i \Delta x_{ic} \\ \sum w_{ic}^2 u_i \Delta y_{ic} \\ \sum w_{ic}^2 u_i \Delta z_{ic} \end{Bmatrix} \quad (9.5)$$

where

$$w_{ic} = \frac{1}{\sqrt{\Delta x_{ic}^2 + \Delta y_{ic}^2 + \Delta z_{ic}^2}} \quad (9.6)$$

**Remark 2** This scaling results in a determinant of the least-squares matrix that is  $O(1)$  for the element-centered gradient estimate. However, for the full least-squares problem,  $\sum w_{ic}^2$  can become large as  $\Delta x_{ic}, \Delta y_{ic}, \Delta z_{ic}$  become small while the other entries of the matrix are scaled properly. An alternative weighting that more closely approximates a diagonal-scaling, and can be computed edge-by-edge, is desirable and should be explored in in Hydra toolkit.

### Diffusive Fluxes

The diffusive flux terms that arise in the Navier-Stokes equations, the energy equation, and advective-diffusion equations are constructed using the basic gradient estimate described above.

The diffusive flux terms are typically of the form

$$I = \int_{\Gamma} \nabla u \cdot \mathbf{n} d\Gamma \quad (9.7)$$

where  $\mathbf{n}$  is the face normal where the gradient estimate is computed.

In the finite volume community, the diffusive fluxes are frequently constructed using a modified gradient based on the local cell geometry and dual-edge configuration. It is not uncommon to find situations where a dual-edge does not align directly with the face-normal associated with the dual edge. In this situation, it can be desirable to weight the gradient by a one-dimensional gradient associated with the

dual-edge data. Figure 9.2 shows a typical situation where  $a$  and  $b$  represent cell-centers of triangles with their associated field data  $u_a$  and  $u_b$ . The vector between the cell-centers is  $\mathbf{d} = \mathbf{x}_b - \mathbf{x}_a$  with magnitude  $d = \sqrt{\mathbf{d} \cdot \mathbf{d}}$ .

The so-called “directional correction” can be designed in several ways. The base edge-gradient is typically formulated as an average or interpolation of the Green-Gauss cell-centered gradients. Here, we present the directional correction in terms of the least-squares gradient. This choice was made because it is not possible to construct an interpolated/corrected gradient preserves linear consistency from an underlying gradient estimator that does not preserve linear consistency.

The method used in AVL SWIFT [AVL, 2004] replaces the normal part of the face gradient with a gradient computed in the normal direction using the cell-center data  $u_a$  and  $u_b$ .

$$\nabla u = \nabla^{LS} u - (\nabla^{LS} u \cdot \mathbf{d}) \frac{\mathbf{n}}{\mathbf{n} \cdot \mathbf{d}} + (u_b - u_a) \frac{\mathbf{n}}{\mathbf{n} \cdot \mathbf{d}} \quad (9.8)$$

where  $\nabla^{LS} u$  is the least-squares edge-gradient computed using Eq. (9.5).

In comparison, the method advocated by Liu and Xu [Liu and Xu, 2008] and by Puigt, et al. [Puigt et al., 2010] uses a slightly different correction. In this case, the orientation is biased in the direction of the distance vector between adjacent cell-centers.

$$\nabla u = \nabla^{LS} u - (\nabla^{LS} u \cdot \mathbf{d}) \frac{\mathbf{d}}{\sqrt{\mathbf{d} \cdot \mathbf{d}}} + (u_b - u_a) \frac{\mathbf{d}}{\sqrt{\mathbf{d} \cdot \mathbf{d}}} \quad (9.9)$$

An alternative approach is to retain the projection into the normal direction, but scale according to the distance vector.

$$\nabla u = \nabla^{LS} u - (\nabla^{LS} u \cdot \mathbf{d}) \frac{\mathbf{n}}{\sqrt{\mathbf{d} \cdot \mathbf{d}}} + \frac{(u_b - u_a)}{\sqrt{\mathbf{d} \cdot \mathbf{d}}} \frac{\mathbf{n}}{\sqrt{\mathbf{d} \cdot \mathbf{d}}} \quad (9.10)$$

This approach has seen limited testing, but does not appear to provide a significant improvement over the implemented approach in Eq.(9.8).

Yet another similar formulation has been advocated by Mavriplis [Mavriplis, 2007]. However, the stated formulation on pg. 15 in [Mavriplis, 2007] does not appear to be consistent as it appears to fail to give the effective face difference any direction yielding rank inconsistency.

The scaling of the directional corrections is similar, with the AVL correction in Eq. (9.8) leading to a difference between two large numbers in the limit as  $\mathbf{n}$  and  $\mathbf{d}$  become orthogonal and  $\mathbf{n} \cdot \mathbf{d}$  approach zero. Practically speaking, the normal and distance vectors can only be orthogonal on a mesh where the elements have completely collapsed.

In contrast, the more typical gradient fix-up in Eq. (9.9) relies on the the actual cell-center distance for the gradient adjustment and appears to be well-behaved on meshes with extreme distortion. However, this formulation not produce results that are of sufficient accuracy as borne out by testing on the  $15^\circ$  skew lid-driven cavity.

In all three cases, if the input field is considered to be linear in the spatial coordinates, then the gradient-corrections will preserve linear consistency assuming that correction is applied to gradient that delivers linear consistency.

**Remark 3** In Eq. (9.8) and (9.9), we have used  $\nabla^{LS} u$  instead of the typical use of the averaged cell-centered gradients, i.e.,  $1/2(\nabla u_a + \nabla u_b)$  corresponding to dual-edge vertex values of the gradients. Note also, that the AVL flux is reported based on using an interpolation of the cell-centered gradients rather than the average. See §11.2 for details on dual-edge interpolation.

As a point of comparison, discontinuous Galerkin methods also use a constructed diffusive flux that is based on the average of the element-local gradients, jumps in the field variable and the element gradient. One such flux is the Nicens flux. The form of the Nicens flux is

$$h_\sigma^e = \frac{1}{2}(\sigma_a + \sigma_b) - \alpha^e(u_b - u_a) + \beta^e(\sigma_b - \sigma_a) \quad (9.11)$$

where  $h_\sigma^e$  is the flux,  $\sigma$  is proportional to the gradient of  $u$ , and subscripts  $a, b$  indicate opposite sides of an element face, e.g., vertices of the dual-edge. There is an obvious relationship between the average and jump terms to the flux estimates in Eq. (9.8) and (9.9). However, the jump in the gradient terms  $(\sigma_b - \sigma_a)$  does not have an obvious correspondence. In the future, the discontinuous Galerkin fluxes may be implemented directly in the Hydra toolkit.

Currently, the AVL gradient correction is used in the diffusive least-squares operators in Hydra.

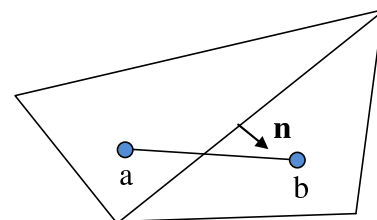


Figure 9.2: Geometry for normal gradient correction.

## 10 Wall-Normal Distance Calculation

Hydra provides a framework for implementing advanced turbulence models in arbitrarily complex geometry that is discretized with unstructured meshes. This requires an ability to estimate the normal distance from a given grid point to the nearest surface in essentially any geometrical configuration. This appears to be a geometrically complex and computationally intensive process for arbitrarily complex geometry if search/intersection methods are used. Instead, Hydra computes a distance function by solving a simple Poisson problem with a distance reconstruction.

The equation that controls the variation of the normal distance to a boundary surface is a special case of the Eikonal equation [Sethian, 1999, Fares and Schroder, 2002]

$$\begin{aligned} \|\nabla\phi(\mathbf{x})\| &= F(\mathbf{x}) \text{ in } \Omega, \quad F(\mathbf{X}) > 0, \\ \phi &= g(\mathbf{x}) \text{ on } \Gamma \end{aligned} \tag{10.1}$$

Here,  $\phi$  is the level set,  $\mathbf{X}$  are the spatial coordinates,  $F(\mathbf{X})$  is a prescribed function,  $\Omega$  is the domain in  $\mathbb{R}^n$  and  $\Gamma$  is the boundary of  $\Omega$ . For the special case where  $F(\mathbf{x}) = 1$ ,

$$\|\nabla\phi\| = 1 \tag{10.2}$$

The level set curves  $\phi(\mathbf{x}) = C$  that satisfy Eq.(10.2) provide the distance  $C$  to the surface  $\phi = g(\mathbf{x})$ . Thus to compute the normal distance to an arbitrary boundary surface Eq. (10.2) has to be resolved. Unfortunately, solving this equations is a challenging task. Specially since the  $\phi$  field may be non-differentiable [Sethian, 1999] .

An alternative approach that has been proposed to address the solution of the Eikonal equation is to include diffusion terms that provides smooth differentiable  $\phi$  solutions and easy the numerical treatment.

$$\|\nabla\phi\| = 1 + \Gamma\nabla^2\phi \tag{10.3}$$

Here  $\Gamma$  is the diffusion coefficient. It is important to note that  $\Gamma$  must have the proper limit  $\Gamma \rightarrow 0$  in order to accurately reproduce the distance from the wall. This is especially true close to the wall, where the

turbulent models require accurate values for these distance in order to yield accurate results.

Although, from a mathematical stand point the problem of computing the wall-normal distance is trivial, obtaining accurate solution with simple numerical algorithms is not a completely solve issue [Sethian, 1999, Tucker, 2003]. A good review of the methods currently available to solve the Eikonal or approximate versions of it can be found in Refs. [Sethian, 1999, Tucker, 2003]. One of the most interesting approaches is to solve Eq.(10.3), however the numerical treatment is not trivial and could potentially increase the cost of the simulation when grid deforming simulations are required [Tucker, 2005].

In order to reduce the significant overload of resolving the Eikonal or one of its approximate equation, a simple approach was proposed that is able to provide accurate results in the region close to the boundary. It is exactly in this region where most modern turbulence models require an accurate representation of this distance. The Poisson equation is more amenable to solve than the previous equations [Tucker, 2003]

$$\nabla^2\phi = -1 \quad (10.4)$$

In this approach  $\phi$  does not directly represent the distance to the surface, therefore an additional relation is required to compute the distance to the surface:

$$d = \pm \sqrt{\sum_{j=1,3} \left(\frac{\partial\phi}{\partial x_j}\right)^2} + \sqrt{\sum_{j=1,3} \left(\frac{\partial\phi}{\partial x_j}\right)^2} + 2\phi \quad (10.5)$$

The numerical complexity of the Poisson method is significantly superior to the other approaches described in the literature [Tucker, 2005]. Additionally, the literature indicates that the Poisson method is able to produce results comparable to methods when the turbulence models are incorporated [Tucker, 2003, Tucker and Davidson, 2004, Tucker, 2005, 2006, 2007]. Therefore Eqs.(10.4) and Eq.(10.5) are adopted to compute the distance to the wall-surfaces.

### *Numerical Examples*

This section presents numerical examples to illustrate the potential of the approach previously described to approximate the wall-normal distance in complex geometries. The examples presented are summarized next

- Cylinder within a channel with walls in the top and bottom sides
- Two cylinder within a channel with walls in the top and bottom sides

- 90° corner
- Three dimensional YF17 geometry
- Three element airfoil geometry

These problem aim to demonstrate the potential of the approach used in Hydra predict the wall-normal distance in complex geometries typically found in complex 3-D geometries of engineering interest.

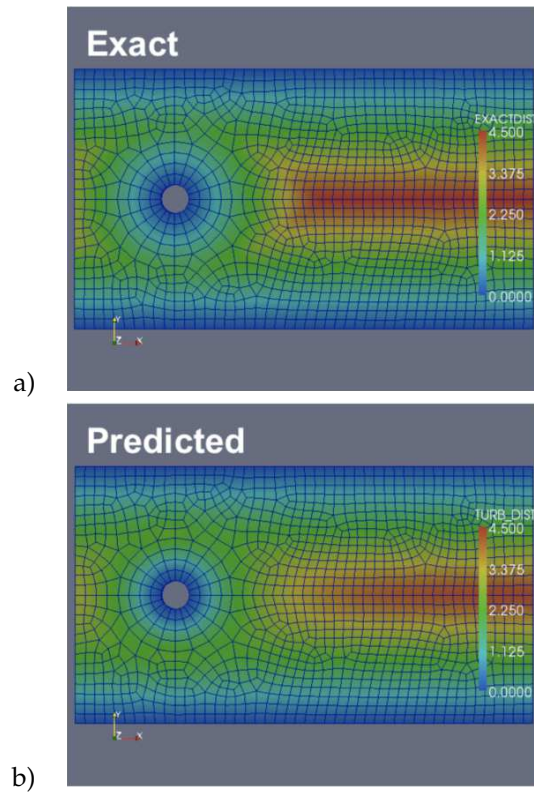


Figure 10.1: Normal distance calculation results for a cylinder in a channel with top and bottom wall: a) Direct calculation; b) Numerical calculation.

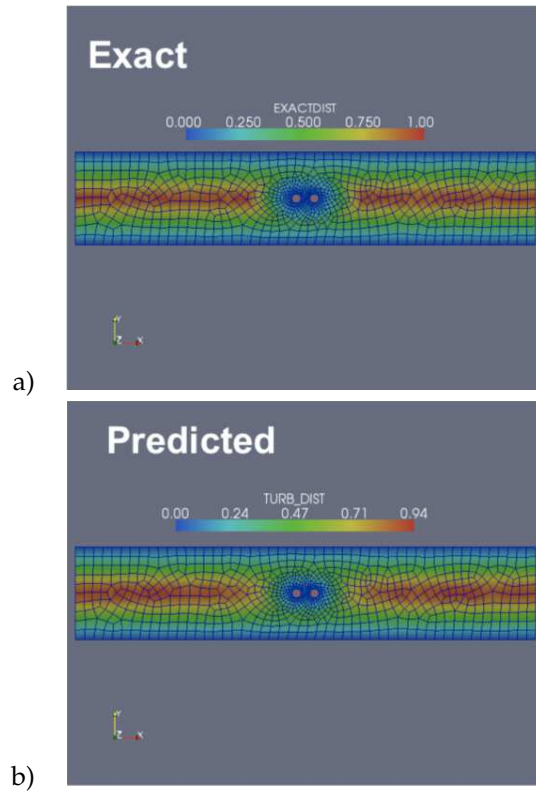


Figure 10.2: Normal distance calculation results for two cylinders in a channel with top and bottom wall: a) Direct calculation; b) Numerical calculation.

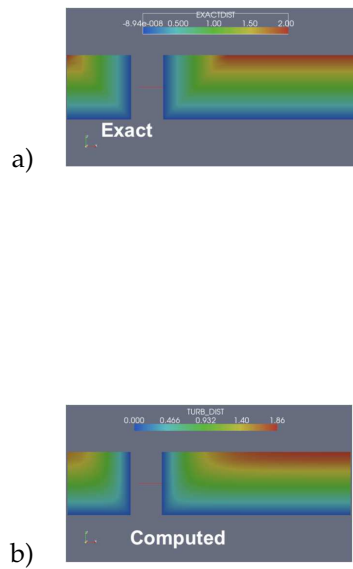


Figure 10.3: Normal distance calculation results on corners: a) Direct calculation; b) Numerical calculation.



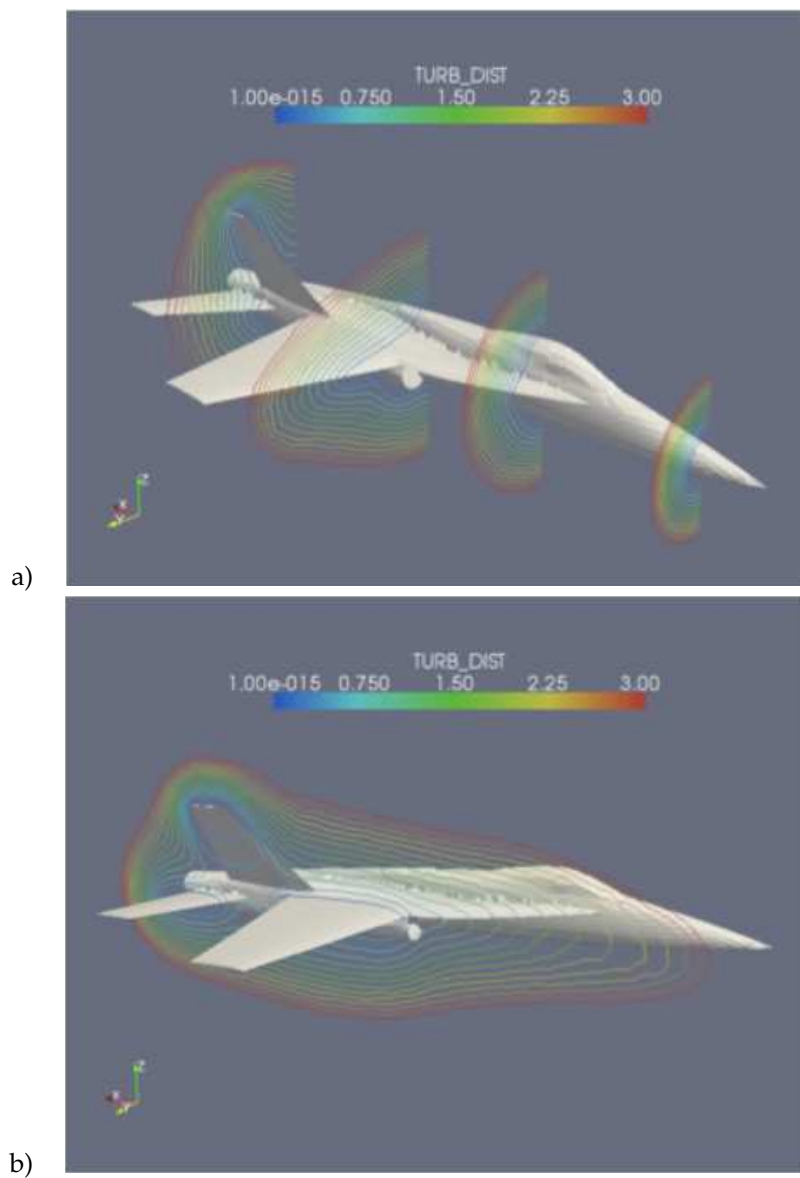


Figure 10.4: Normal distance calculation results on YF17 geometry: a) perspective view; b) side view.

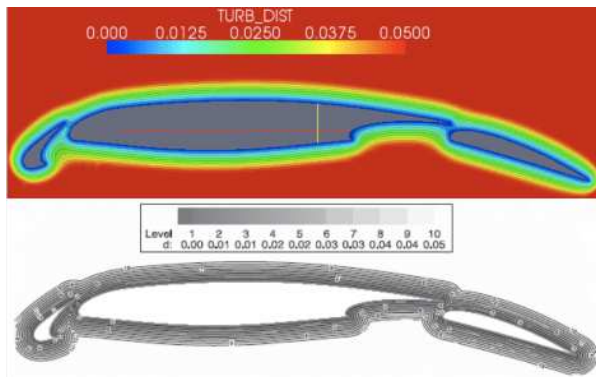


Figure 10.5: Normal distance calculation results on three element airfoil geometry, top view numerical calculation, bottom view direct calculation.

## 11 *Eulerian Formulation*

This chapter presents the basic formulation that the hybrid FVM/FEM flow solver currently uses. The interested reader may pursue the references included in this chapter for details on the incompressible flow solution algorithms and their implementation.

One of the primary targets is coupled multiphysics problems such as fluid-structure interaction (FSI). FSI problems are inherently time-dependent, and even when the structural response is quasi-static, the fluid dynamics may still be transient. For this reason, the initial deployment of the flow solvers in the Hydra Toolkit have focused on projection methods because of their computational efficiency and accuracy for transient flows.

For steady-state problems, the Hydra Toolkit architecture admits virtually any solution method, and it is anticipated that steady-state methods based on inexact Newton-Krylov or Jacobian-free Newton-Krylov (JFNK) strategies will be implemented at some point. Similarly, the SIMPLE family of solution methods can be considered for implementation at some point in the future.

### *The Projection Method*

The solution of the time-dependent incompressible Navier-Stokes equations poses several algorithmic problems due to the div-free constraint, and the concomitant spatial and temporal resolution required to perform time-accurate solutions particularly when complex geometry is involved. Although fully-coupled solution strategies are available, the cost of such methods is generally considered prohibitive for time-dependent simulations where high-resolution grids are required. The application of projection methods provides a computationally efficient alternative to fully-coupled solution methods.

A detailed review of projection methods is beyond the scope of this section, but a partial list of relevant work is provided for the interested reader. Projection methods, also commonly referred to as fractional-step, pressure correction methods, or Chorin's method [Chorin, 1968] have grown in popularity over the past 20 years due to the relative ease

of implementation and computational performance. This is reflected by the volume of work published on the development of second-order accurate projection methods, see for example van Kan [Kan, 1986], Bell, et al. [Bell et al., 1989], Gresho, et al. [Gresho, 1990, Gresho and Chan, 1990, Gresho et al., 1995, Gresho and Chan, 1996], Almgren, et al. [Almgren et al., 1993, 1996, 2000], Rider [Rider, 1994a,b, Rider et al., 1995, Rider, 1995], Minion [Minion, 1996], Guermond and Quartapelle [Guermond and Quartapelle, 1997], Puckett, et al. [Puckett et al., 1997], Sussman, et al. [Sussman et al., 1999], and Knio, et al. [Knio et al., 1999]. The numerical performance of projection methods has been considered by Brown and Minion [Brown and Minion, 1995, Minion and Brown, 1997], Wetton [Wetton, 1998], Guermond [Guermond, 1996, 1997], Guermond and Quartapelle [Guermond and Quartapelle, 1998a,b], and Almgren et al. [Almgren et al., 2000].

As background, a brief review of Chorin's original projection method is presented before proceeding with the finite element form of the projection algorithm. The vector form of the momentum equations may be written as

$$\rho \frac{\partial \mathbf{v}}{\partial t} + \nabla p = \mathcal{F}(\mathbf{v}), \quad (11.1)$$

where for a constant viscosity,

$$\mathcal{F}(\mathbf{v}) = \mathbf{f} + \mu \nabla^2 \mathbf{v} - \rho \mathbf{v} \cdot \nabla \mathbf{v}. \quad (11.2)$$

Now,  $\mathcal{F}(\mathbf{v})$  may be decomposed into a div-free component

$$\nabla \cdot \left\{ \frac{\partial \mathbf{v}}{\partial t} \right\} = 0, \quad (11.3)$$

and a curl-free part

$$\nabla \times \nabla p = 0. \quad (11.4)$$

Discretizing in space and time, the decomposition, neglecting the contribution of the pressure gradient, yields

$$\rho \frac{(\mathbf{v}^{*n+1} - \mathbf{v}^n)}{\Delta t} = \mathcal{F}^h(\mathbf{v}), \quad (11.5)$$

where  $\mathcal{F}^h(\mathbf{v})$  is the spatially discrete analogue of  $\mathcal{F}$  in Eq. (11.2), and  $\mathbf{v}^{*n+1}$  is an approximate discrete velocity field at time  $n + 1$ . Note that the discrete divergence of  $\mathbf{v}^{*n+1}$  is generally not zero, i.e.  $G^T \mathbf{v}^{*n+1} \neq 0$  where  $G^T$  is the discrete divergence operator. The functional dependence of  $\mathcal{F}^h$  upon the discrete velocity,  $\mathbf{v}$ , depends upon whether the algorithm is implicit, explicit, or semi-implicit. However, the dependence on pressure, or rather pressure gradient, is explicit so that

$$\frac{(\mathbf{v}^{*n+1} - \mathbf{v}^n)}{\Delta t} = \frac{(\mathbf{v}^{n+1} - \mathbf{v}^n)}{\Delta t} + \frac{1}{\rho} G p^{n+1}, \quad (11.6)$$

where  $G$  is the discrete gradient operator, and  $G^T$  is the discrete divergence operator. Applying the discrete divergence operator to Eq. (11.6) yields a Poisson equation for the pressure at time level  $n + 1$ ,

$$G^T \frac{1}{\rho} G p^{n+1} = \frac{1}{\Delta t} G^T \mathbf{v}^{*n+1}. \quad (11.7)$$

By eliminating the velocity at time level  $n$ , Eq. (11.6) yields a relationship for the projected div-free velocity field.

$$\mathbf{v}^{n+1} = \mathbf{v}^{*n+1} - \frac{\Delta t}{\rho} G p^{n+1}. \quad (11.8)$$

Chorin's method is considered to be a non-incremental projection method that yields first-order accuracy in time for the velocity. In the ensuing discussion, we will use the more modern second-order incremental projection method that delivers second-order accuracy in time.

### *Projection Properties*

The philosophy behind projection algorithms is to provide a legitimate way to decouple the pressure and velocity fields in the hope of providing an efficient computational method for transient, incompressible flow simulations. In practice, the action of the projection,  $\mathcal{P}$ , is to remove the part of the approximate velocity field that is not div-free, i.e.,  $\mathbf{v} = \mathcal{P}(\mathbf{v}^*)$ . In effect, the projection is achieved by decomposing the velocity field into div-free and curl-free components using a Helmholtz decomposition. The decomposition may be written as

$$\rho \mathbf{v}^* = \rho \mathbf{v} + \nabla \lambda, \quad (11.9)$$

where  $\mathbf{v}^*$  is a non-solenoidal velocity field,  $\mathbf{v}$  is its div-free counterpart, and  $\nabla \lambda$  is the curl-free component, i.e.,  $\nabla \times \nabla \lambda = 0$ .

Thus, given an approximate, non-solenoidal velocity field,  $\mathbf{v}^*$ ,  $\mathcal{F}(\mathbf{v}^*)$  may be projected onto a divergence-free subspace such that

$$\rho \frac{\partial \mathbf{v}}{\partial t} = \mathcal{P}(\mathcal{F}(\mathbf{v}^*)), \quad (11.10)$$

and

$$\nabla p = \mathcal{Q}(\mathcal{F}(\mathbf{v}^*)). \quad (11.11)$$

Here,  $\mathcal{P}$  and  $\mathcal{Q}$  are the projection operators, and they have the following properties.  $\mathcal{P}$  projects a vector into a div-free subspace, and  $\mathcal{Q}$  projects a vector into a curl-free subspace. Both  $\mathcal{P}$  and  $\mathcal{Q}$  are idempotent, i.e.,  $\mathcal{P} = \mathcal{P}^2$  and  $\mathcal{Q} = \mathcal{Q}^2$ . Therefore, repeated application of the projection operators does not continue to modify the projected results. The projection operators are orthogonal, and commute, i.e.,  $\mathcal{P}\mathcal{Q} = \mathcal{Q}\mathcal{P} = 0$ .

The explicit forms of the continuous projection operators are

$$\mathcal{P}(\cdot) = \left\{ I - \nabla(\nabla^2)^{-1}\nabla \cdot \right\} (\cdot), \quad (11.12)$$

and

$$\mathcal{Q}(\cdot) = I - \mathcal{P} = \nabla(\nabla^2)^{-1}\nabla \cdot (\cdot). \quad (11.13)$$

It should be noted that  $\mathcal{P}$ , and  $\mathcal{Q}$  have *built-in* all the appropriate physical boundary conditions. Further, The eigenvalues of  $\mathcal{P}$  and  $\mathcal{Q}$  are either 0 or 1 so that the projections are always norm-reducing.

### *Semi-Implicit Projection Method*

As a starting point for the semi-implicit projection method, we adopted Gresho's second-order "P2" method [Gresho, 1990, Gresho and Chan, 1990]. The desire for local-conservation compelled the use of a discontinuous-Galerkin/Finite Volume framework with all variables cell-centered, i.e., collocated velocity and pressure. The introduction of the PetSC linear algebra packages, and in specific, the use of Sandia's ML preconditioner drove the choice to use node-centered pressures and leave all transported variables located at cell centers. Thus, a hybrid DG/FVM - Galerkin FEM method forms the basis for the incompressible solver.

The use of a hybrid discretization for the implementation of a projection solver is not new. The first use of a predominantly finite volume scheme with a continuous Galerkin pressure-Poisson operator appeared in the work of Bell, et al. [Bell et al., 1989]. More recently, Aliabadi and co-workers have developed a hybrid finite element/volume method [Tu and Aliabadi, 2007, Tu et al., 2009, Wan et al., 2009] that is very similar to the methods presented here.

The governing equations presented in §3 serve as the starting point for the development of the hybrid solution method. Here, we use vector notation and write the stress in terms of fluid pressure and deviatoric stress, i.e.,  $\sigma = -p\mathbf{I} + \tau$ , and the advective terms in divergence form. Following the procedure outlined in Chapter 8.1, we discretize in space, integrate by parts, and apply the divergence theorem. Using piecewise-constant weight functions yields

$$\rho \frac{d}{dt} \int_{\Omega^e} \mathbf{v} d\Omega^e + \oint_{\Gamma^e} \rho \mathbf{v} \cdot \mathbf{n} d\Gamma^e - \oint_{\Gamma^e} \boldsymbol{\sigma} \cdot \mathbf{n} d\Gamma^e + \int_{\Omega^e} \nabla p d\Omega^e - \int_{\Omega^e} \mathbf{f} d\Omega^e = 0 \quad (11.14)$$

Using the definition for the cell-average from Eq. (8.8), the spatially-discrete momentum equations become

$$\rho \Omega^e \frac{d\bar{\mathbf{v}}}{dt} + \oint_{\Gamma^e} \rho \mathbf{v} \cdot \mathbf{n} d\Gamma^e - \oint_{\Gamma^e} \boldsymbol{\sigma} \cdot \mathbf{n} d\Gamma^e + \int_{\Omega^e} \nabla p d\Omega^e - \int_{\Omega^e} \mathbf{f} d\Omega^e = 0 \quad (11.15)$$

where the over-bar ( $\bar{\mathbf{v}}$ ) has been dropped for simplicity. With the divergence constraint, the discrete momentum equations form a system

of differential algebraic equations (DAEs) rather than simple ordinary differential equations (ODEs). For this reason, simple time-marching schemes can not be applied to the div-constrained system of equations.

The projection algorithm can be derived in a number of ways. Here, we choose to first develop the time-integrator, and identify the terms associated with the projection via a Helmholtz decomposition of the velocity. Before proceeding we define the following mass, advective, viscous, gradient and body-force operators.

$$M^e = \rho \Omega^e \quad (11.16)$$

$$A^e(\rho, \mathbf{v})\mathbf{v} = \oint_{\Gamma^e} \rho \mathbf{v}(\mathbf{v} \cdot \mathbf{n}) d\Gamma^e \quad (11.17)$$

$$K^e \mathbf{v} = \oint_{\Gamma^e} \boldsymbol{\sigma} \cdot \mathbf{n} d\Gamma^e \quad (11.18)$$

$$\mathbf{B}^e p \Omega^e = \int_{\Omega^e} \nabla p d\Omega^e \quad (11.19)$$

$$\mathbf{F}^e = \int_{\Omega^e} \mathbf{f} d\Omega^e \quad (11.20)$$

We form the global operators, apply forward-Euler first, then backward-Euler with explicit advection in both cases, and take the sum of the fully-discrete systems results in the following

$$M \frac{\mathbf{v}^{n+1} - \mathbf{v}^n}{\Delta t} - \theta K \mathbf{v}^{n+1} = (1 - \theta) \mathbf{F}^n + \theta \mathbf{F}^{n+1} \\ - A(\rho, \mathbf{v}) \mathbf{v}^n + (1 - \theta) K \mathbf{v}^n - \mathbf{B} p^n - \theta \mathbf{B}(p^{n+1} - p^n) \quad (11.21)$$

where  $0 \leq \theta \leq 1$ ,  $\theta = 0$  corresponds to a forward-Euler,  $\theta = 1/2$  a trapezoidal rule, and  $\theta = 1$  backward-Euler treatment of viscous and body-force terms.

Using the Helmholtz decomposition as

$$\rho \mathbf{v}^* = \rho \mathbf{v}^{n+1} + \nabla \lambda \quad (11.22)$$

we introduce the following definition

$$\lambda = \theta \Delta t (p^{n+1} - p^n) \quad (11.23)$$

Substituting in Eq. (11.21), and recognizing that  $K \nabla \lambda = 0$  in  $\Omega$ , the momentum equation can be solved for the approximate velocity as

$$[M - \theta \Delta t K] \mathbf{v}^* = [M + (1 - \theta) \Delta t K] \mathbf{v}^n \\ - \Delta t A(\rho, \mathbf{v}) \mathbf{v}^n - \Delta t \mathbf{B} p^n + \Delta t \{(1 - \theta) \mathbf{F}^n + \theta \mathbf{F}^{n+1}\} \quad (11.24)$$

Using the Helmholtz decomposition, and requiring  $\nabla \cdot \mathbf{v}^{n+1} = 0$ , yields a pressure-Poisson equation (PPE) that can be solved for the Lagrange multiplier  $\lambda$ .

$$\nabla \cdot \frac{1}{\rho} \nabla \lambda = \nabla \cdot \mathbf{v}^* \quad (11.25)$$

Here,  $\lambda$  is node-centered, and so a typical Galerkin finite element procedure is used to discretize Eq. (11.25). This process is well-known, and only the final weak form is presented

$$\int_{\Omega} \nabla w \cdot \left( \frac{1}{\rho} \nabla \lambda \right) d\Omega = \int_{\Gamma} w \left\{ \frac{1}{\rho} \frac{\partial \lambda}{\partial n} \right\} d\Gamma - \int_{\Gamma} w \mathbf{v}^* \cdot \mathbf{n} d\Gamma + \int_{\Omega} \mathbf{v}^* \cdot \nabla w d\Omega \quad (11.26)$$

The discrete PPE is

$$K_p \lambda = D \quad (11.27)$$

**Remark 4** *An alternative formulation for the PPE problem simply uses the cell-centered divergence of the intermediate velocity for the right-hand-side of the PPE as  $\int_{\Omega} \nabla \cdot \mathbf{v}^*$ . Testing has indicated that this form of the PPE led to smoother pressures, but also resulted in start-up velocity and pressure that were somewhat less accurate than those obtained using Eq. (11.26).*

Given a velocity and pressure at time-level  $n$ , the P2 algorithm proceeds as follows.

**Algorithm 1** *Basic P2 Algorithm*

1. Solve for  $\mathbf{v}^*$

$$[M - \theta \Delta t K] \mathbf{v}^* = [M + (1 - \theta) \Delta t K] \mathbf{v}^n - \Delta t A(\rho, \mathbf{v}) \mathbf{v}^n - \Delta t \mathbf{B} p^n + \Delta t \{ (1 - \theta) \mathbf{F}^n + \theta \mathbf{F}^{n+1} \} \quad (11.28)$$

2. Form the right-hand-side of the PPE, solve for  $\lambda$ ,

$$K_p \lambda = D \quad (11.29)$$

3. Update the pressure

$$p^{n+1} = p^n + \frac{1}{\theta \Delta t} \lambda \quad (11.30)$$

*Note that testing over the last 20 years or so has indicated that using  $\theta = 1/2$  to update the pressure can lead to temporal oscillations in the pressure. For this reason, we use  $\theta = 1$  in the implementation.*

4. Project the cell-centered velocities

$$\mathbf{v}^{n+1} = \mathbf{v}^* - \frac{1}{\rho} \mathbf{B} \lambda \quad (11.31)$$

5. Compute face gradients and project the face-centered velocities

$$v_f = v_f^* - \frac{1}{\rho_f} ((\mathbf{B})\lambda)_f \cdot \mathbf{n} \quad (11.32)$$

6. Repeat steps 1 - 5 until the termination time is reached



### Pressure/Lagrange-Multiplier Gradients

The pressure and Lagrange-multiplier gradients are computed using the uniform-strain B-matrix associated with the element – currently the HEX8, TET4, PYR5 and WEDGE6 elements. The B-matrix is optionally formed and stored at the element-class level. The pressure gradient force contribution to the momentum equations is computed as

$$\mathbf{F}^e = \Delta t \sum_I^{Nnpe} \mathbf{B}_I^e p_I^e \Omega^e \quad (11.33)$$

where  $1 \leq I \leq Nnpe$ .

Given the element-level gradient, face gradients are currently computed using a smoothing operation that spans the elements attached to dual-edges as neighbors. The elements in the neighbor list include those attached by dual-edges to the vertices of a given dual-edge where the gradient is desired. The smoothing process is volume-weighted, i.e.,

$$(\mathbf{B}\lambda)_f = \frac{\sum_i^{Nnbr} (\mathbf{B}^e \lambda \Omega^e)_i \Omega_i}{\sum_i^{Nnbr} \Omega_i} \quad (11.34)$$

### Dual-Edge Interpolation

The calculation of dual-edge quantities arises in a number of places in the hybrid projection algorithm. This process can be viewed as a projection onto a Galerkin basis using a 1-D mesh as shown in Figure 11.1. It has been found that an inverse-distance weighted interpolation procedure provides more accurate face values for general unstructured grids.

The data at points  $a$  and  $b$  are assumed to be known cell-averaged values. An inverse-distance weighted interpolation to calculate the face value at  $f$ . For a generic variable,  $\phi$ , this is written as

$$\phi_f = \frac{\phi_a h_b^e + \phi_b h_a^e}{(h_a^e + h_b^e)} \quad (11.35)$$

Alternatively, this can be written as

$$\phi_f = \zeta_a \phi_a + (1 - \zeta_a) \phi_b \quad (11.36)$$

where

$$\zeta_a = \frac{h^b}{h^a + h^b} \quad (11.37)$$

For convenience, the value of  $\zeta_a$  is stored in the dual-edge data structure *DualEdge* in the Hydra.

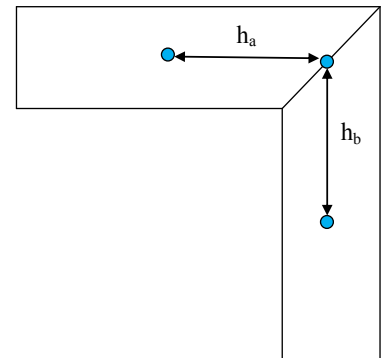


Figure 11.1: Dual-edge grid for edge projection.

### Dual-Edge Velocities and Divergence

The implementation of the P2 algorithm relies on the so-called “co-velocity” approach where dual-edge velocities are made divergence-free and used for advection. This is an extremely important concept as it enables the incompressible flow solver to be easily extended to perform volume-tracking for multi-fluid simulations.

The calculation of the dual-edge velocities proceeds as follows. For physical domain boundaries, the process may be thought of as a symmetric mirror of the velocities in  $\Omega$  followed by the calculation of the edge velocity as

$$\mathbf{v}_f = \frac{1}{2} (\mathbf{v}_1 + \mathbf{v}_g) \tag{11.38}$$

Here, the factor of 1/2 factor is valid since the boundary ghosts receive data from the symmetric mirror at a location that is twice the distance from the element centroid to the boundary. Here,  $g$  identifies the ghost data, and  $d$  is the normal distance from the element centroid to the element boundary.

Alternatively, this can be thought of as extrapolation to the boundary edges as  $\mathbf{v}_f = \mathbf{v}_1$ .

Where Dirichlet velocity boundary conditions are imposed, the ghost data is specified by the prescribed velocity boundary condition.

For domain-based parallelism, it’s necessary to account for data in the sense of the overlapping elements or ghost elements. Edges with a vertex containing ghost data are referred to as REAL\_GHOST. The REAL\_GHOST data is populated in buffers by a swap communication before the external dual-edge velocities are computed. For the edges attached to vertices with REAL\_GHOST data, the edge interpolation outlined in §11.2 is used. As a reminder, the interpolation factors are pre-computed and stored in the dual-edge data structure.

Once all the data attached to external edges has been constructed, the dual-edge velocities are computed as

$$v_f = \mathbf{v}_f \cdot \mathbf{n} \quad \forall \text{ external edges} \tag{11.39}$$

After the external dual-edge velocities have been computed with the prescribed boundary conditions inserted, the dual-edge velocities associated with internal edges are computed using the interpolation outlined in §11.2.

$$\mathbf{v}_f = [\zeta \mathbf{v}_1 + (1 - \zeta) \mathbf{v}_2] \cdot \mathbf{n} \tag{11.40}$$

Note that the unit normal for each dual edge is also conveniently stored in the dual-edge data structure *DualEdge*. All of the dual-edge velocities are stored in the DUALEDGE\_VEL data index.

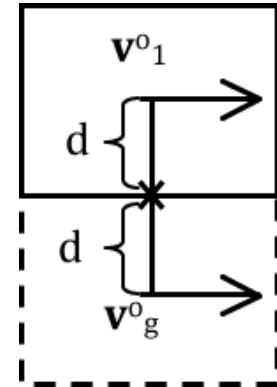


Figure 11.2: Edge velocity interpolation.

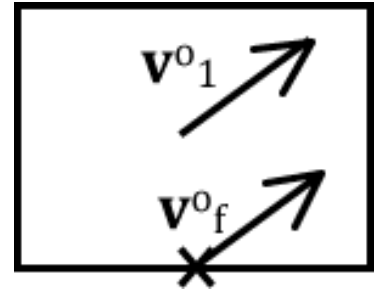


Figure 11.3: Edge velocity extrapolation.

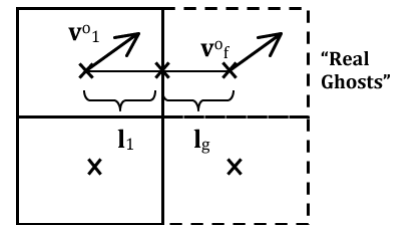


Figure 11.4: Overlapping “ghost” elements for parallel calculations.

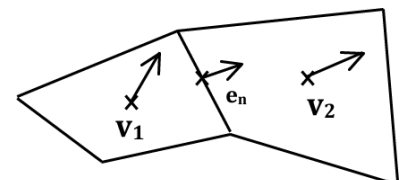


Figure 11.5: Edge normal velocities on internal regions.

The dual-edge velocities can also be used to compute the natural form of the divergence computed as

$$\operatorname{div}(\mathbf{v})^e = \frac{1}{\Omega^e} \sum_i^{Nedge} v_{f_i} \Gamma_i \quad (11.41)$$

where  $Nedge$  is the number of dual-edges connected to a given element.

The dual-edge velocities are also used to compute the source terms for the pressure-Poisson problem in Eq.(11.25).

### *Advection Treatment*

The advection in uses the basic flux function outlined in §8.2. For explicit advection, the treatment is obvious. Several minor modifications to the explicit advection are required for volume-tracking in multi-fluid applications. The explicit advection is conditionally stable.

The implicit advection also uses the flux function outlined in §8.2, but treats the dependent (advected) variables implicitly. For scalar transport equations, this method provided unconditional stability. However, for the momentum equations, a sharp stability is not available. Operational experience indicates that the upper stability range is on the order of  $CF = 20$  to  $CFL = 40$ .

### *Time-Step Estimation*

The time-step estimation makes use of multiple characteristic element dimensions and a centroid velocity that is projected onto the relevant length scales. A minimum over all possible length and velocity scale choices determine the acceptable time-step size.

For the explicit advection algorithm, a  $CFL \leq 1$  is required. For both implicit and explicit advection, a fixed  $CFL$  time-integrator may be used that bounds the  $CFL$  number at an appropriate level.

### *Start-up Procedure*

The incompressible flow solver uses a start-up procedure that guarantees that the solvability conditions discussed in Chapter 3 are met. This guarantees that a well-posed incompressible Navier-Stokes problem is defined regardless of the prescribed initial and boundary conditions. This procedure is also required to insure that the solution to index-1 DAE's via the projection method produce solutions identical to the those for the index-2 DAE's, i.e., the fully-coupled velocity-pressure system.

In addition to the calculation of a suitable initial velocity field that satisfies the boundary conditions, and is divergence-free, an initial

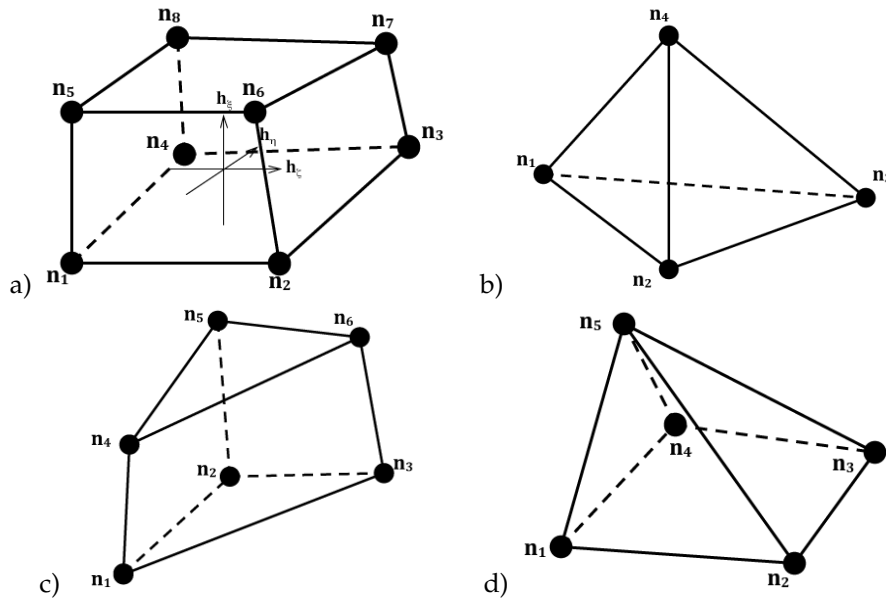


Figure 11.6: Elements with centroid velocity and characteristic dimensions.

pressure is required that is consistent with the initial velocity field and prescribed boundary conditions.

Given a set of initial conditions and prescribed boundary conditions,  $\hat{v}$  on  $\Gamma_{Dv}$ ,  $\hat{p}$  on  $\Gamma_{Dp}$ , and  $\mathbf{v}^0(\mathbf{x})$  in  $\Omega$  as shown in Fig. 11.7.

The start-up procedure follows the steps below.

### 1. Dual-Edge Velocities

To begin, we define the initial edge-normal flux velocities  $v_f^0$ . We setup ghost data, and calculate the edge-normal velocities by interpolation at all domain boundaries following the procedure in §11.2. This yields dual-edge velocities,  $v_f^*$ , that are in general not divergence-free.

### 2. RMS Divergence

Given the dual-edge “fluxing” velocities with BC’s inserted, we compute

$$\int_{\Omega_e} \nabla \cdot \mathbf{v} = \oint_{\Gamma_e} (\mathbf{v}_f \cdot \mathbf{e}_n) d\Gamma \quad (11.42)$$

which is stored and referred to in the code as DIVERGENCE.

**Remark 5** Formally, the volume-averaged divergence is defined as

$$\int_{\Omega_e} \nabla \cdot \mathbf{v} = \frac{1}{\Omega^e} \oint_{\Gamma_e} (\mathbf{v}_f \cdot \mathbf{e}_n) d\Gamma \quad (11.43)$$

For our purposes, Eq. (11.42) is used since it simplifies the computation of the RMS divergence metric, and other internal quantities in the code.

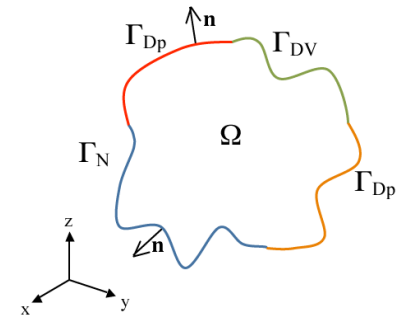


Figure 11.7: Pressure boundary conditions.

Using 1-point quadrature at the dual-edges, i.e., element-faces,

$$\int_{\Omega_e} \nabla \cdot \mathbf{v} \approx \sum_f \mathbf{v}_f \cdot \mathbf{e}_n \Gamma_f = \sum_f v_f \Gamma_f \quad (11.44)$$

the computation proceeds edge-by-edge with an assembly to vertices, a.k.a, elements as shown below. The sign-convention for the assembly follows the convection outlined in Chapter 8.

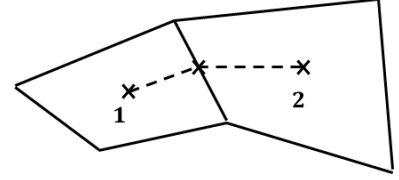


Figure 11.8: Dual-edge assembly from elements 1 and 2.

$$\begin{aligned} (\nabla \cdot \mathbf{v})^1 + &= u_f \Gamma_f \\ (\nabla \cdot \mathbf{v})^2 - &= u_f \Gamma_f \end{aligned} \quad (11.45)$$

The RMS divergence is computed as

$$div_{RMS} = \frac{1}{\Omega} \sqrt{\frac{\sum_{i=1}^{Nel} [(\nabla \cdot \mathbf{v})^i]^2}{Nel}} \quad (11.46)$$

If the RMS divergence is larger than a user prescribed tolerance, then the initial velocity is projected onto a div-free subspace before proceeding.

### 3. Div-Free Projection

Assuming that the initial RMS divergence is too large, then a div-free projection is performed.

We begin with the usual decomposition of the velocity into div-free and curl-free components

$$\mathbf{v}^* = \mathbf{v} + \frac{1}{\rho} \nabla \lambda \quad (11.47)$$

Here,  $\mathbf{v}^0 = \mathbf{v}^*$ , and

$$\nabla \cdot \mathbf{v}^* \neq 0, \quad \nabla \cdot \mathbf{v} = 0 \text{ (by construction)} \quad (11.48)$$

Taking the divergence yields

$$\nabla \cdot \mathbf{v}^* = \nabla \cdot \frac{1}{\rho} \nabla \lambda \quad (11.49)$$

where

$$\lambda = 0 \text{ on } \Gamma_{Dp} \quad (11.50)$$

and

$$\frac{\partial \lambda}{\partial \mathbf{n}} = 0 \quad (11.51)$$

everywhere except on  $\Gamma_{Dp}$ .

Starting with the usual weighted-residual form,

$$\int_{\Omega} w \left\{ \nabla \cdot \frac{1}{\rho} \nabla \lambda \right\} = \int_{\Omega} w \nabla \cdot \mathbf{v}^* \quad (11.52)$$

where  $\nabla \cdot \mathbf{v}^*$  is computed using the dual-edge velocity. Integrating by parts, we obtain

$$\int_{\Gamma} w \left\{ \frac{1}{\rho} \frac{\partial \lambda}{\partial \mathbf{n}} \right\} - \int_{\Omega} \nabla w \cdot \frac{1}{\rho} \nabla \lambda = \int_{\Omega} w \nabla \cdot \mathbf{v}^* \quad (11.53)$$

After applying the divergence theorem, the weak-form becomes

$$\int_{\Omega} \nabla w \cdot \frac{1}{\rho} \nabla \lambda = \int_{\Gamma} w \left\{ \frac{1}{\rho} \frac{\partial \lambda}{\partial \mathbf{n}} \right\} - \int_{\Omega} w \nabla \cdot \mathbf{v}^* \quad (11.54)$$

This is simply a pressure-Poisson equation (PPE) for the Lagrange multiplier.

Alternatively, the PPE problem may be formulated as

$$\begin{aligned} \int_{\Omega} \nabla w \cdot \frac{1}{\rho} \nabla \lambda &= \int_{\Gamma} w \left\{ \frac{1}{\rho} \frac{\partial \lambda}{\partial \mathbf{n}} \right\} - \int_{\Omega} w \nabla \cdot \mathbf{v}^* \\ &= \int_{\Gamma} w \left\{ \frac{1}{\rho} \frac{\partial \lambda}{\partial \mathbf{n}} \right\} - \int_{\Omega} \nabla \cdot (w \mathbf{v}^*) + \int_{\Omega} \mathbf{v}^* \cdot \nabla w \\ &= \int_{\Gamma} w \left\{ \frac{1}{\rho} \frac{\partial \lambda}{\partial \mathbf{n}} \right\} - \int_{\Gamma} w \mathbf{v}_f^* \cdot \mathbf{n}_f + \int_{\Omega} \mathbf{v}^* \cdot \nabla w \end{aligned} \quad (11.55)$$

Here, the dual-edge velocities are used directly on the external boundary integral.

In a discrete form, the PPE problem becomes

$$K\lambda = D(\mathbf{v}) \quad (11.56)$$

After solving the PPE problem for  $\lambda$ , we project both the element and dual-edge velocities. Using the Helmholtz decomposition, and knowing  $v_f^*$  and  $\lambda$ , we can compute the div-free velocity as

$$v_f = v_f^* - \frac{1}{\rho_f} \nabla_f \lambda \cdot \mathbf{n}_f \quad (11.57)$$

In the fully-discrete sense, we have  $\lambda$  at nodes, and need to compute  $(\frac{1}{\rho_f} \nabla_f \lambda)$  at the dual-edges. We follow the procedure outlined in §11.2 to compute the dual-edge gradients, i.e., face-gradients, for the projection. The dual-edge velocities are projected as

$$v_f = v_f^* - \frac{1}{\rho_f} (\mathbf{B}\lambda)_f \cdot \mathbf{n}_f \quad (11.58)$$

where the edge-density used in the projection of the dual-edge velocity is computed as

$$\rho_f = \xi \rho^a + (1 - \xi) \rho^b \quad (11.59)$$

and  $(\mathbf{B}\lambda)_f$  is computed using Eq. (11.34).

**Remark 6** *In the future, the calculation of the dual-edge density may need to be modified for volume-tracking in multi-fluid calculations. In this case, it has been found that using a harmonic average for the density performs well, although there is no single unique density estimate.*

Following the projection of the dual-edge velocities, the prescribed Dirichlet velocities are injected in the dual-edge velocity to insure that the final div-free dual-edge velocities exactly match the prescribed velocities.

Finally, the element-velocity is projected onto the div-free subspace as

$$\mathbf{v} = \mathbf{v}^* - \frac{1}{\rho}(\nabla\lambda)^e \quad (11.60)$$

Currently, a simple average of the dual-edge gradient is used, although other choices should be explored.

$$(\nabla\lambda)^e = \frac{1}{N_{epe}} \sum_{i=1}^{N_{epe}} (\mathbf{B}\lambda)_f^i \quad (11.61)$$

#### 4. Initial Pressure

Once the div-free velocities have been obtained, an initial pressure is computed that is consistent with the initial and boundary conditions. We begin by writing the momentum in terms of acceleration.

$$\rho\mathbf{a} = \mathbf{f} + \nabla \cdot [\mu(\nabla\mathbf{v} + \nabla\mathbf{v}^T)] - \nabla \cdot (\rho\mathbf{v}\mathbf{v}) - \nabla p \quad (11.62)$$

Using the div-free velocity,  $\mathbf{v}^0$ ,

$$\mathbf{a}^0 = \frac{1}{\rho} \left\{ \mathbf{f} + \nabla \cdot [\mu(\nabla\mathbf{v}^0 + (\nabla\mathbf{v}^0)^T)] - \nabla \cdot (\rho\mathbf{v}^0\mathbf{v}^0) - \nabla p^0 \right\} \quad (11.63)$$

Now, since  $\nabla \cdot \mathbf{v}^0 = 0$ , then,  $\nabla \cdot \mathbf{a}^0 = 0$ , and we can form the continuous PPE for  $p^0$ .

$$\nabla \cdot \frac{1}{\rho} \nabla p^0 = \frac{1}{\rho} \nabla \cdot \left\{ \mathbf{f} + \nabla \cdot [\mu(\nabla\mathbf{v}^0 + (\nabla\mathbf{v}^0)^T)] - \nabla \cdot (\rho\mathbf{v}^0\mathbf{v}^0) \right\} \quad (11.64)$$

For convenience, we define a ‘‘partial acceleration’’

$$\tilde{\mathbf{a}} = \frac{1}{\rho} \left\{ \mathbf{f} + \nabla \cdot [\mu(\nabla\mathbf{v}^0 + (\nabla\mathbf{v}^0)^T)] - \nabla \cdot (\rho\mathbf{v}^0\mathbf{v}^0) \right\} \quad (11.65)$$

so that the continuous PPE may be written as

$$\nabla \cdot \frac{1}{\rho} \nabla p^0 = \nabla \cdot \tilde{\mathbf{a}}, \quad (11.66)$$

where  $p^0 = \hat{p}^0$  on  $\Gamma_{Dp}$ , and  $\frac{\partial p}{\partial \mathbf{n}} = 0$  on  $\Gamma_N$ .

Using the DG/FVM formalism, we compute the partial acceleration as

$$\int_{\Omega_e} \rho \tilde{\mathbf{a}} = \int_{\Omega_e} \mathbf{f} + \int_{\Omega_e} \nabla \cdot [\mu(\nabla\mathbf{v}^0 + (\nabla\mathbf{v}^0)^T)] - \int_{\Omega_e} \nabla \cdot (\rho\mathbf{v}^0\mathbf{v}^0) \quad (11.67)$$

For the initial pressure, all that is required is the acceleration, so it is OK to just use the “donor-cell” approximation for the advective terms. However, the dual-edge velocity gradients and viscosity are required.

$$\tilde{\mathbf{a}} = \mathbf{f} + \frac{1}{\rho V} \sum_f \mu (\nabla \mathbf{v}^0 + (\nabla \mathbf{v}^0)^T)_f \cdot \mathbf{n}_f \Gamma_f - \frac{1}{\rho V} \sum_f (\rho \mathbf{v}^0) v_f^0 \Gamma_f \quad (11.68)$$

With the partial acceleration in hand, dual-edge accelerations are computed following the same procedure outlined above for the dual-edge velocities. For boundaries where a time-dependent velocity is prescribed, then we impose  $\tilde{\mathbf{a}}_f = \frac{\partial \mathbf{v}}{\partial t}$  otherwise,  $\tilde{\mathbf{a}}_f = 0$ .

In order to compute the pressure, it's necessary to solve the PPE for the initial pressure. Once again using the finite element method, the weak form becomes

$$\begin{aligned} \int_{\Omega} w \left\{ \nabla \cdot \frac{1}{\rho} \nabla p^0 \right\} &= \int_{\Omega} w (\nabla \cdot \tilde{\mathbf{a}}) \\ \int_{\Omega} \left\{ \nabla w \cdot \frac{1}{\rho} \nabla p^0 \right\} &= \oint_{\Gamma} w \left( \frac{1}{\rho} \frac{\partial p}{\partial \mathbf{n}} \right) - \int_{\Omega} w (\nabla \cdot \tilde{\mathbf{a}}) \end{aligned} \quad (11.69)$$

where  $(\nabla \cdot \tilde{\mathbf{a}})$  is just a source term that is piecewise constant for each element and can be computed in the same way as the divergence above.

Similar to the projection step, we use following formulation for the PPE because it tends to produce sharper pressures.

$$\begin{aligned} \int_{\Omega} \nabla w \cdot \frac{1}{\rho} p^0 \lambda &= \int_{\Gamma} w \left\{ \frac{1}{\rho} \frac{\partial p^0}{\partial \mathbf{n}} \right\} - \int_{\Omega} w \nabla \cdot \tilde{\mathbf{a}} \\ &= \int_{\Gamma} w \left\{ \frac{1}{\rho} \frac{\partial p^0}{\partial \mathbf{n}} \right\} - \int_{\Omega} \nabla \cdot (w \tilde{\mathbf{a}}) + \int_{\Omega} \tilde{\mathbf{a}} \cdot \nabla w \\ &= \int_{\Gamma} w \left\{ \frac{1}{\rho} \frac{\partial p^0}{\partial \mathbf{n}} \right\} - \int_{\Gamma} w \tilde{\mathbf{a}}_f \cdot \mathbf{n}_f + \int_{\Omega} \tilde{\mathbf{a}} \cdot \nabla w \end{aligned} \quad (11.70)$$

This leads to a linear system of equations,  $Kp^0 = D(\tilde{\mathbf{a}})$ . Solving for  $p^0$ , we have the initial pressure and velocities,  $\mathbf{v}^0$ ,  $\mathbf{v}_f^0$ , and are ready to start time-marching.

### *Porous Media Flow*

Porous media flows represent a wide variety of engineering, geological, and biomedical applications. Many of these applications require the knowledge of the flow field within a porous medium in an “averaged” sense. In order to obtain the averaged flow, the Navier-Stokes equation along with any transport equations that are applicable (temperature, species etc.) are spatially smoothed to obtain continuum equations that are valid everywhere. The most common forms of smoothing employ volume-averaging (see,[Whitaker, 1999]) and homogenization techniques. In the present formulation, the volume-averaged equations are used to solve the porous media equations.



### Volume Averaging

Let  $\psi$  denote a generic scalar quantity. Some averages are defined on  $\psi$  as follows that are used in the volume-averaging procedure

- **Superficial phase average:**

$$\langle \psi \rangle = \frac{1}{V} \int_{V_\beta} \psi dV \quad (11.71)$$

- **Intrinsic phase average:**

$$\langle \psi \rangle^\beta = \frac{1}{V_\beta} \int_{V_\beta} \psi dV \quad (11.72)$$

- **Relation between averages:**

$$\langle \psi \rangle = \epsilon \langle \psi \rangle^\beta \quad (11.73)$$

where,

$$\epsilon = \frac{V_\beta}{V}, \quad (11.74)$$

is the porosity of the medium.

### Darcy-Brinkman-Forchheimer Model

Using a volume-averaging approach, the averaged form of the mass and momentum conservation equations for a fluid-saturated “constant” porosity medium that takes into account the presence of solid boundaries (Brinkman correction [Brinkman, 1949]) and inertial effects (Forchheimer correction) are given as follows [Khaled and Vafai, 2003, Nithiarasu et al., 2000].

**Mass conservation:**

$$\nabla \cdot \langle \mathbf{v} \rangle = 0. \quad (11.75)$$

**Momentum conservation:**

$$\frac{\rho}{\epsilon} \left( \frac{\partial \langle \mathbf{v} \rangle}{\partial t} + \frac{1}{\epsilon} \langle \mathbf{v} \rangle \cdot \nabla \langle \mathbf{v} \rangle \right) = -\nabla \langle p \rangle^\beta + \nabla \cdot \mu_\beta \nabla \langle \mathbf{v} \rangle - \frac{\mu}{\mathbf{K}} \langle \mathbf{v} \rangle - \frac{\rho C_F}{\sqrt{\mathbf{K}}} |\langle \mathbf{v} \rangle| \langle \mathbf{v} \rangle \quad (11.76)$$

Here,  $\mu_\beta$  is the Brinkman effective viscosity,  $C_F$  is the Forchheimer coefficient, and  $\mathbf{K}$  is the permeability tensor. The Forchheimer coefficient  $C_F$  is expressed as

$$C_F = \frac{1.75}{\sqrt{150\epsilon^3}}. \quad (11.77)$$

The third and fourth term on the R.H.S. of Eq.11.76 represent the Darcy and Forchheimer drag terms. These terms are treated as momentum “sink” (negative source) terms in the present implementation.

**Remark:** The factor  $\frac{1.75}{\sqrt{150}}$  is calculated internally within the code.

In Eqs. 11.75 and 11.76, the superficial average velocity,  $\langle \mathbf{v} \rangle$ , is considered in the derivation because of its solenoidal characteristic. However, an intrinsic average of pressure,  $\langle p \rangle^\beta$ , is preferred because it more closely resembles the pressure that one could measure or the pressure that one could impose as a boundary condition [Ochoa-Tapia and Whitaker, 1995a].

A formal and rigorous volume averaging procedure (see, [Ochoa-Tapia and Whitaker, 1995a]) yields  $\mu_\beta = \frac{\mu}{\epsilon}$ . Substituting for  $\mu_\beta$  in Eq.11.76, we get the following equation:

$$\frac{\rho}{\epsilon} \left( \frac{\partial \langle \mathbf{v} \rangle}{\partial t} + \frac{1}{\epsilon} \langle \mathbf{v} \rangle \cdot \nabla \langle \mathbf{v} \rangle \right) = -\nabla \langle p \rangle^\beta + \nabla \cdot \frac{\mu}{\epsilon} \nabla \langle \mathbf{v} \rangle - \mu \mathbf{K}^{-1} \langle \mathbf{v} \rangle - \rho C_F \mathbf{K}^{-\frac{1}{2}} |\langle \mathbf{v} \rangle| \langle \mathbf{v} \rangle. \quad (11.78)$$

### Interface boundary conditions

The boundary conditions at the interface between a pure fluid and homogeneous porous medium are provided below [Betchen et al., 2006].

**Continuity of velocity:**

$$\langle \mathbf{v} \rangle|_{\text{Porous}} = \mathbf{v}|_{\text{Fluid}} \quad (11.79)$$

**Continuity of pressure:**

$$\langle p \rangle^\beta|_{\text{Porous}} = p|_{\text{Fluid}} \quad (11.80)$$

**Continuity of normal stress:**

$$(\mathbf{n} \cdot \mathbf{n} \cdot \langle \boldsymbol{\sigma} \rangle)|_{\text{Porous}} = (\mathbf{n} \cdot \mathbf{n} \cdot \boldsymbol{\sigma})|_{\text{Fluid}} \quad (11.81)$$

**Continuity of shear stress:**

$$(\mathbf{n} \cdot \mathbf{t} \cdot \langle \boldsymbol{\sigma} \rangle)|_{\text{Porous}} = (\mathbf{n} \cdot \mathbf{t} \cdot \boldsymbol{\sigma})|_{\text{Fluid}} \quad (11.82)$$

where,

$$\langle \sigma_{ij} \rangle|_{\text{Porous}} = -\langle p \rangle^\beta \delta_{ij} + \mu_\beta \left( \frac{\partial \langle u_i \rangle}{\partial x_j} + \frac{\partial \langle u_j \rangle}{\partial x_i} \right), \quad (11.83)$$

and

$$\sigma_{ij}|_{\text{Fluid}} = -p \delta_{ij} + \mu \left( \frac{\partial u_i}{\partial x_j} + \frac{\partial u_j}{\partial x_i} \right). \quad (11.84)$$

Continuity of pressure and normal stresses as given by Eqs.11.80 and 11.81 together with the definitions of stress tensors given by Eqs.11.83 and 11.84 implies the continuity of viscous normal stresses.

$$\mu \left( \frac{\partial u_i}{\partial x_j} + \frac{\partial u_j}{\partial x_i} \right) = \mu_\beta \left( \frac{\partial \langle u_i \rangle}{\partial x_j} + \frac{\partial \langle u_j \rangle}{\partial x_i} \right). \quad (11.85)$$

**Remark:**

Some justifications and pitfalls of the assumption of dropping  $\epsilon$  in the transport equation and boundary conditions are given below.

1. *Viscous term approximation:* For porous media problems coupled to homogeneous fluid regions, setting  $\mu_\beta = \mu$  causes the flow rate through the pure-fluid domain to be spuriously high due to the overestimation of the interfacial velocity [Tan and Pillai, 2009].
2. *Advective term approximation:* It has been shown [Vafai and Tien, 1981] that for many practical problems, the magnitude of the advective term responsible for boundary layer growth is negligible beyond a very small developing region near the porous-pure fluid interface. Hence, any approximation to this term is considered “higher order”. Inertial contributions are mainly accounted through the Forchheimer correction.
3. *Transient term approximation:* The neglect of porosity in the transient terms is strictly valid only for steady state flows and is not thoroughly justified for highly transient dynamics.
4. *Continuity of interface stresses:* In the porous medium, since the solid phase shares the total stress with the fluid, the fluid stresses may not be continuous across the interface between a “homogeneous-fluid” region and the fluid in the porous medium. Jump boundary conditions may be prescribed across the interface which has been considered theoretically and experimentally in [Ochoa-Tapia and Whitaker, 1995a], [Ochoa-Tapia and Whitaker, 1995b], [Ochoa-Tapia and Whitaker, 1998] and analyzed in [Alazmi and Vafai, 2001]. However, the implementation of interface stress jump conditions have been successful only for highly simplified geometries. Recent numerical works that have utilized such jump boundary conditions include [Tan and Pillai, 2009], [Yu et al., 2009], [Yu et al., 2010] and [Chen et al., 2008].

*Permeability Estimation*

An estimation of the macroscopic permeability tensor of the porous medium,  $\mathbf{K}$ , is critical to solving the averaged equations for fluid flow. Simpler models/correlations that provide a good estimate of the permeability values are often sought. Such models need to consider the dependence of the permeability on the geometry of the porous medium, the orientation of the pores/fibers with respect to the flow, and the porosity  $\epsilon$  of the medium. For many engineering applications, the permeability tensor can be assumed isotropic that is characterized

by a single scalar,  $K$ . A typical correlation that is often used in engineering calculations for estimating the permeability  $K$  is the Carman-Kozeny relation. This relates  $K$  to the porosity  $\epsilon$  and is given by,

$$K = \frac{r_f^2}{4k_{kc}} \frac{\epsilon^3}{(1 - \epsilon)^2}, \quad (11.86)$$

where,  $k_{kc}$  represents the Carman-Kozeny constant and  $r_f$  represents the average radius of the porous particles/fibers.

### *Turbulence and Porous medium*

The current code implementation does not include volume-averaged equations for the turbulent flows within the porous medium. While the turbulence option can be turned on for a porous region, the macroscopic equations applicable only for a pure-fluid region are alone solved. The effects of the presence of solid boundaries in the porous region on the production and destruction of turbulence are not taken into account. Hence, care must be taken while activating a turbulence model within a porous region and also interpreting the obtained results.

### *Spalart-Allmaras Model*

The implementation details of the Spalart-Allmaras model are described in §6.3.

The Reynolds-stress is approximated using the Boussinesq hypothesis as

$$-\overline{v_i v_j} = 2\nu_T S_{ij} \quad (11.87)$$

where,

$$S_{ij} = \frac{1}{2} \left( \frac{\partial v_i}{\partial x_j} + \frac{\partial v_j}{\partial x_i} \right) \quad (11.88)$$

$$S = \sqrt{2S_{ij}S_{ij}} \quad (11.89)$$

$$R_{ij} = \frac{1}{2} \left( \frac{\partial v_i}{\partial x_j} - \frac{\partial v_j}{\partial x_i} \right) \quad (11.90)$$

$$S_r = \sqrt{2R_{ij}R_{ij}} \quad (11.91)$$

and the over-bar indicating that the velocities are Reynolds-averaged has been dropped for convenience.

For our purposes, we write the model as

$$\begin{aligned} \rho \frac{\partial \tilde{v}}{\partial t} + \nabla \cdot (\rho \mathbf{v} \tilde{v}) &= \rho C_{b1} S \tilde{v} - \rho C_{w1} f_w \left( \frac{\tilde{v}}{d} \right)^2 \\ &+ \rho \frac{1 + C_{b2}}{\sigma} \nabla \cdot (\nu + \tilde{v}) \nabla \tilde{v} \\ &- \rho \frac{C_{b2}}{\sigma} (\nu + \tilde{v}) \nabla \cdot \nabla \tilde{v} \end{aligned} \quad (11.92)$$

where,

$$f_w = g \left[ \frac{1 + C_{w3}^6}{g^6 + C_{w3}^6} \right]^{\frac{1}{6}} \quad (11.93)$$

$$g = r + C_{w2}(r^6 - r) \quad (11.94)$$

$$r = \frac{\nu_T}{S \kappa^2 d^2} \quad (11.95)$$

Using the DG/FVM formalism, the model equation is

$$\begin{aligned} \int_{\Omega^e} \left\{ \rho \frac{\partial \tilde{v}}{\partial t} + \nabla \cdot (\rho \mathbf{v} \tilde{v}) \right\} d\Omega &= \int_{\Omega^e} \rho C_{b1} S \tilde{v} d\Omega - \int_{\Omega^e} \rho C_{w1} f_w \left( \frac{\tilde{v}}{d} \right)^2 d\Omega \\ &+ \oint_{\Gamma^e} \frac{1 + C_{b2}}{\sigma} [(\nu + \tilde{v}) \nabla \tilde{v}]|_{\Gamma^e} \cdot \mathbf{n} d\Gamma \\ &- \oint_{\Gamma^e} \frac{C_{b2}}{\sigma} (\nu + \tilde{v})|_{\Omega^e} \nabla \tilde{v} \cdot \mathbf{n} d\Gamma \end{aligned} \quad (11.96)$$

Here, the evaluation of viscosity and Spalart-Allmaras variable in the diffusive terms must be handled carefully to avoid numerical instabilities.

In operator form, the fully-discrete equation using forward-Euler time integration are

$$M \left\{ \frac{\tilde{v}^{n+1} - \tilde{v}^n}{\Delta t} \right\} + A(\rho, \mathbf{v}) \tilde{v}^n = K^n \tilde{v}^n + P^n \tilde{v}^n - D^n \tilde{v}^n \quad (11.97)$$

and with backward-Euler, the equation is

$$M \left\{ \frac{\tilde{v}^{n+1} - \tilde{v}^n}{\Delta t} \right\} + A(\rho, \mathbf{v}) \tilde{v}^n = K \tilde{v}^{n+1} + P^{n+1} \tilde{v}^{n+1} - D^{n+1} \tilde{v}^{n+1} \quad (11.98)$$

where  $M$  is a diagonal  $Nel \times Nel$  matrix where  $M_{ii} = \rho \Omega^e \delta_{ii}$ ,

$$K \tilde{v} = \oint_{\Gamma^e} \frac{1 + C_{b2}}{\sigma} [(\nu + \tilde{v}) \nabla \tilde{v}]|_{\Gamma^e} \cdot \mathbf{n} d\Gamma - \oint_{\Gamma^e} \frac{C_{b2}}{\sigma} (\nu + \tilde{v})|_{\Omega^e} \nabla \tilde{v} \cdot \mathbf{n} d\Gamma \quad (11.99)$$

and the production and dissipation terms written as

$$P \tilde{v} = \rho C_{b1} S \tilde{v} \Omega^e \quad (11.100)$$

$$D\tilde{v} = \rho C_w f_w \left( \frac{\tilde{v}}{d} \right)^2 \Omega^e \quad (11.101)$$

Taking a linear-combination of forward and backward-Euler, i.e., the  $\theta$ -method, becomes

$$\begin{aligned} [M - \theta \Delta t K + \theta \Delta t (D^{n+1} - P^{n+1})] \tilde{v}^{n+1} = \\ [M + (1 - \theta) \Delta t K + (1 - \theta) \Delta t (P^n - D^n)] \tilde{v}^n - \Delta t \mathcal{A}(\rho, \mathbf{v}) \tilde{v}^n \end{aligned} \quad (11.102)$$

Equation (11.102) is non-linear in  $\tilde{v}$ , and requires linearization in order to complete the implementation. We follow the suggestions in the original Spalart-Allmaras paper [Spalart and Allmaras, January 1992], and apply their positivity-preserving algorithm here.

Beginning with the production and dissipation terms, we let

$$P^{n+1} \tilde{v}^{n+1} = P^n \tilde{v}^{n+1} + \tilde{v}^n \frac{\partial P^n}{\partial \tilde{v}} \Delta \tilde{v} \quad (11.103)$$

and

$$D^{n+1} \tilde{v}^{n+1} = D^n \tilde{v}^{n+1} + \tilde{v}^n \frac{\partial D^n}{\partial \tilde{v}} \Delta \tilde{v} \quad (11.104)$$

where  $\Delta \tilde{v} = (\tilde{v}^{n+1} - \tilde{v}^n)$ .

The production/dissipation operators and their derivatives are

$$P^n = \rho C_{b1} \tilde{S}^n \Omega^e \quad (11.105)$$

$$D^n = \rho C_{w1} f_w \frac{\tilde{v}^n}{d^2} \Omega^e \quad (11.106)$$

$$\frac{\partial P^n}{\partial \tilde{v}} = \rho C_{b1} \frac{\partial \tilde{S}^n}{\partial \tilde{v}} \Omega^e \quad (11.107)$$

$$\frac{\partial D^n}{\partial \tilde{v}} = \left[ \rho C_{w1} \frac{\partial f_w}{\partial \tilde{v}} \frac{\tilde{v}^n}{d^2} + \rho C_{w1} f_w \frac{1}{d^2} \right] \Omega^e \quad (11.108)$$

where

$$\tilde{S} = S + \frac{\tilde{v}}{\kappa^2 d^2} f_{v2} \quad (11.109)$$

and

$$\frac{\partial \tilde{S}}{\partial \tilde{v}} = \left[ \frac{f_{v2}}{\kappa^2 d^2} + \frac{\tilde{v}}{\kappa^2 d^2} \frac{\partial f_{v2}}{\partial \tilde{v}} \right] \quad (11.110)$$

where

$$f_{v1} = \frac{\chi^3}{\chi^3 + C_{v1}^3} \quad (11.111)$$

$$f_{v2} = 1 - \frac{\chi}{1 + \chi f_{v1}} \quad (11.112)$$

Substituting in Eq. (11.102), collecting terms, and rearranging yields

$$\begin{aligned} [M^n - \theta \Delta t K^n + \theta \Delta t (\bar{D}^n - \bar{P}^n)] \tilde{v}^{n+1} = \\ [M^n + (1 - \theta) \Delta t K^n] \tilde{v}^n - \Delta t A(\rho, \mathbf{v}) \tilde{v}^n \\ - \Delta t (D^n - P^n) \tilde{v}^n + \theta \Delta t (\bar{D}^n - \bar{P}^n) \tilde{v}^n \end{aligned} \quad (11.113)$$

where

$$(\bar{D}^n - \bar{P}^n) = pos\{D^n - P^n\} + pos\left\{\frac{\partial D}{\partial \tilde{v}} - \frac{\partial P}{\partial \tilde{v}}\right\} \tilde{v} \quad (11.114)$$

The calculation of the linearized terms used in Eq. (11.113) proceeds as follows.

1. 
$$\chi = \frac{\tilde{v}}{\nu} = \frac{\tilde{v}\rho}{\mu} \quad (11.115)$$

2. 
$$\left(\frac{1}{\kappa^2 d^2}\right) = \left(\frac{1}{\kappa^2 d^2 + \epsilon_{dbl}}\right) \quad (11.116)$$

3. 
$$S_r = \sqrt{2R_{ij}R_{ij}} \quad (11.117)$$

4. 
$$f_{v1} = \frac{\chi^3}{\chi^3 + C_{v1}^3} \quad (11.118)$$

5. 
$$f_{v2} = 1 - \frac{\chi}{1 + \chi f_{v1}} \quad (11.119)$$

6. 
$$S_a = S_r + \tilde{v} f_{v2} \left(\frac{1}{\kappa^2 d^2}\right) \quad (11.120)$$

7. 
$$r = \frac{\tilde{v}}{S_a} \left(\frac{1}{\kappa^2 d^2}\right); \quad if(r > 10) \quad r = 10 \quad (11.121)$$

8. 
$$g = r(1 - C_{w2}) + C_{w2} r^6 \quad (11.122)$$

9. 
$$f_w = g \left[ \frac{1 + C_{w3}^6}{g^6 + C_{w3}^6} \right]^{\frac{1}{6}} \quad (11.123)$$

10. 
$$\frac{\partial f_{v2}}{\partial \tilde{v}} = \frac{-\chi^6 + 3C_{v1}^3 \chi^4 - 2C_{v1}^3 \chi^3 - C_{v1}^6}{\nu(\chi^4 + \chi^3 + C_{v1}^3)^2} \quad (11.124)$$

11. 
$$\frac{\partial S_a}{\partial \tilde{v}} = \left(\frac{1}{\kappa^2 d^2}\right) \left(f_{v2} + \tilde{v} \frac{\partial f_{v2}}{\partial \tilde{v}}\right) \quad (11.125)$$

$$12. \quad \frac{\partial r}{\partial \tilde{v}} = \frac{r}{\tilde{v}} \left( 1 - \frac{\tilde{v}}{S_a} \frac{\partial S_a}{\partial \tilde{v}} \right) \quad (11.126)$$

$$13. \quad \frac{\partial g}{\partial \tilde{v}} = \frac{\partial r}{\partial \tilde{v}} [1 + C_{w2}(6r^5 - 1)] \quad (11.127)$$

$$14. \quad \frac{\partial f_w}{\partial \tilde{v}} = \frac{f_w}{g} \frac{\partial g}{\partial \tilde{v}} \left( \frac{C_{w3}^6}{C_{w3}^6 + g^6} \right) \quad (11.128)$$

$$15. \quad P = \rho C_{b1} S_a \Omega^e \quad (11.129)$$

$$16. \quad D = \rho C_{w1} f_w \tilde{v} \Omega^e \frac{1}{d^2} \quad (11.130)$$

$$17. \quad \frac{\partial P}{\partial \tilde{v}} = \rho C_{b1} \frac{\partial S_a}{\partial \tilde{v}} \Omega^e \quad (11.131)$$

$$18. \quad \frac{\partial D}{\partial \tilde{v}} = \rho \Omega^e \frac{1}{d^2} \left( C_{w1} \tilde{v} \frac{\partial f_w}{\partial \tilde{v}} + C_{w1} f_w \right) \quad (11.132)$$

$$19. \quad \{D - P\} = D - P \quad (11.133)$$

$$20. \quad \{\bar{D} - \bar{P}\} = pos(D - P) + pos\left(\frac{\partial D}{\partial \tilde{v}} - \frac{\partial P}{\partial \tilde{v}}\right) \tilde{v} \quad (11.134)$$

### *The Smagorinsky Model*

The formulation of the Smagorinsky model is described in §6.4. The turbulent viscosity is computed as

$$v_T = \mu_{sgs} / \rho = (C_s \Delta)^2 \bar{S} \quad \text{with} \quad \bar{S} = \sqrt{2 \bar{S}_{ij} \bar{S}_{ij}} \quad (11.135)$$

In Eq. (11.135)  $\Delta = V^{1/3}$  where  $V$  is the cell volume, while  $\bar{S}_{ij}$  is the symmetric part of the filtered velocity gradient tensor:

$$\bar{S}_{ij} = \frac{1}{2} \left( \frac{\partial \bar{v}_i}{\partial x_j} + \frac{\partial \bar{v}_j}{\partial x_i} \right) \quad (11.136)$$

The inner product of  $\bar{S}_{ij}$  computes the shear rate,  $S$ .



### The WALE Model

The formulation of the wall-adapted large-eddy (WALE) model is described in §6.4. The turbulent viscosity is computed based on both the filtered-scale shear,  $\bar{S}_{ij}$ , and the square of the filtered-scale velocity gradient tensors,  $\bar{g}_{ij}$ ,

$$\nu_T = (C_W \Delta)^2 \frac{(\mathcal{S}_{ij}^d \mathcal{S}_{ij}^d)^{3/2}}{(\bar{S}_{ij} \bar{S}_{ij})^{5/2} + (\mathcal{S}_{ij}^d \mathcal{S}_{ij}^d)^{5/4}} \quad (11.137)$$

where  $\Delta = V^{1/3}$  with  $V$  the cell volume and

$$\mathcal{S}_{ij}^d = \frac{1}{2} (\bar{g}_{ij}^2 + \bar{g}_{ji}^2) - \frac{1}{3} \bar{g}_{kk}^2 \delta_{ij} \quad \text{with} \quad \bar{g}_{ij} = \frac{\partial \bar{v}_i}{\partial x_j} \quad (11.138)$$

$$\bar{S}_{ij} = \frac{1}{2} \left( \frac{\partial \bar{v}_i}{\partial x_j} + \frac{\partial \bar{v}_j}{\partial x_i} \right) \quad (11.139)$$

In the following the over-bars are dropped for convenience. For every cell the following operations are performed to compute the cell turbulent viscosity:

1. Compute the symmetric part of the velocity gradient tensor:  $S_{ij}$

$$S_{ij} = \frac{1}{2} \left( \frac{\partial v_i}{\partial x_j} + \frac{\partial v_j}{\partial x_i} \right) = \frac{1}{2} (g_{ij} + g_{ji}) \quad (11.140)$$

2. Compute the square of the velocity gradient tensor:  $g_{ij}^2$

$$g_{ij}^2 = g_{ik} g_{kj} \quad (11.141)$$

3. Compute the symmetric deviator of the square of the velocity gradient:  $\mathcal{S}_{ij}^d$

$$\mathcal{S}_{ij}^d = \frac{1}{2} (g_{ij}^2 + g_{ji}^2) - \frac{1}{3} \delta_{ij} g_{kk}^2 \quad (11.142)$$

4. Compute the enumerator of  $\mu_T$ : OP1

$$\text{OP1} = (\mathcal{S}_{ij}^d \mathcal{S}_{ij}^d)^{3/2} \quad (11.143)$$

5. Compute the denominator of  $\mu_T$ : OP2

$$\text{OP2} = (S_{ij} S_{ij})^{5/2} + (\mathcal{S}_{ij}^d \mathcal{S}_{ij}^d)^{5/4} \quad (11.144)$$

6. Compute the cell turbulent viscosity:  $\mu_T = \rho \nu_T$

$$\mu_T = \rho (C_W \Delta)^2 \frac{\text{OP1}}{\text{OP2}} \quad (11.145)$$



## 12 Arbitrary Lagrangian-Eulerian Formulation

This chapter outlines the arbitrary Lagrangian-Eulerian formulation for the incompressible flow solver in the Hydra Toolkit.

### Second-order Incremental Projection Method

Since a simplified DG/FVM formulation is used for the incompressible flow solver, a natural starting point is the master balance equation for linear momentum, Eq.(5.66), which is repeated here for convenience.

$$\frac{d}{dt} \int_{\Omega_x} \rho \mathbf{v} + \oint_{\Gamma_x} \rho \mathbf{v} (\mathbf{v} - \mathbf{v}_m) \cdot \mathbf{n}_x = - \int_{\Omega_x} \nabla p + \oint_{\Gamma_x} \boldsymbol{\tau} \cdot \mathbf{n}_x + \int_{\Omega_x} \mathbf{f} \quad (12.1)$$

Using rationale similar to Förster, et al. [C. Förster and Ramm, 2007], it is assumed that  $\mathbf{x}^n, \mathbf{x}^{n+1}$  are known at time levels  $t$  and  $t + \Delta t$ . The reference configuration is the domain at “ $t$ ”,  $\Omega_t$ . The current configuration is  $\Omega_{t+\Delta t}$ . The relevant variables for the two configurations are outlined in Table 12.1.

Reference	Current
$X$	$x$
$\Omega_X = \Omega_t; \Gamma_t; \mathbf{n}_t$	$\Omega_x = \Omega_{t+\Delta t}; \Gamma_{t+\Delta t}; \mathbf{n}_{t+\Delta t}$
$\mathbf{x}^n; \Gamma_X; \mathbf{n}_X$	$\mathbf{x}^{n+1}; \Gamma_x; \mathbf{n}_x$
$\mathbf{v}^n$	$\mathbf{v}^{n+1}$
$\nabla_X$	$\nabla_x$

Table 12.1: Variable definitions for reference and current configurations.

For this discussion, and the initial implementation, we treat the advection explicitly for now, and apply the usual forward-Euler/backward-Euler  $\theta$ -weighting. With this assumption, we approximate the rate-term as

$$\frac{d}{dt} \int_{\Omega_x} \rho \mathbf{v} \approx \frac{\rho \mathbf{v}^{n+1} \Omega^{n+1} - \rho \mathbf{v}^n \Omega^n}{\Delta t} \quad (12.2)$$

Proceeding as in §11.2, we form the balance equations using a forward-Euler time-integrator, then backward-Euler, and take the weighted sum.

The forward-Euler discretization yields

$$\begin{aligned} \frac{\rho \mathbf{v}^{n+1} \Omega^{n+1} - \rho \mathbf{v}^n \Omega^n}{\Delta t} + \oint_{\Gamma_t^e} \rho \mathbf{v}^n (v_f - v_{m_f})|_{\Gamma_t^e} = \\ - \int_{\Omega_t^e} \nabla_X p^n + \oint_{\Gamma_t^e} \mu \nabla_X \mathbf{v}^n \cdot \mathbf{n}_t + \int_{\Omega_t^e} \mathbf{f}^n \end{aligned} \quad (12.3)$$

and the backward-Euler method yields

$$\begin{aligned} \frac{\rho \mathbf{v}^{n+1} \Omega^{n+1} - \rho \mathbf{v}^n \Omega^n}{\Delta t} + \oint_{\Gamma_t^e} \rho \mathbf{v}^n (v_f - v_{m_f})|_{\Gamma_t^e} = \\ - \int_{\Omega_{t+\Delta t}^e} \nabla_x p^{n+1} + \oint_{\Gamma_{t+\Delta t}^e} \mu \nabla_x \mathbf{v}^{n+1} \cdot \mathbf{n}_{t+\Delta t} + \int_{\Omega_{t+\Delta t}^e} \mathbf{f}^{n+1} \end{aligned} \quad (12.4)$$

Weighting the forward-Euler equation by  $(1 - \theta)$  and the backward-Euler equation by  $\theta$ , summing and collecting terms yields

$$\begin{aligned} \rho \mathbf{v}^{n+1} \Omega^{n+1} - \theta \Delta t \oint_{\Gamma_x^e} \mu \nabla_x \mathbf{v}^{n+1} \cdot \mathbf{n}_x = \rho \mathbf{v}^n \Omega^n - \Delta t \oint_{\Gamma_x^e} \rho \mathbf{v}^n (v_f - v_{m_f})|_{\Gamma_x^e} \\ + (1 - \theta) \Delta t \oint_{\Gamma_x^e} \mu \nabla_x \mathbf{v}^n \cdot \mathbf{n}_x - \\ \Delta t \int_{\Omega_x^e} \nabla_X p^n + \theta \Delta t \int_{\Omega_x^e} \nabla_X p^n - \theta \Delta t \int_{\Omega_x^e} \nabla_x p^{n+1} + \\ \Delta t (1 - \theta) \int_{\Omega_x^e} \mathbf{f}^n + \Delta t \theta \int_{\Omega_x^e} \mathbf{f}^{n+1} \end{aligned} \quad (12.5)$$

Introducing the divergence constraint in the current configuration,

$$\nabla_x \cdot \mathbf{v}^{n+1} = 0 \quad (12.6)$$

and the velocity decomposition,

$$\rho \mathbf{v}^* = \rho \mathbf{v}^{n+1} + \nabla_x \lambda \quad (12.7)$$

we obtain the PPE in the current configuration,  $\Omega_x$ , which we will solve for  $\lambda$

$$\nabla_x \cdot \frac{1}{\rho} \nabla_x \lambda = \nabla_x \cdot \mathbf{v}^* \quad (12.8)$$

In the pure-Eulerian frame, our formulation leads to,

$$\theta \Delta t \int_{\Omega^e} \nabla p^n - \theta \Delta t \int_{\Omega^e} \nabla p^{n+1} = - \int_{\Omega^e} \nabla \lambda \quad (12.9)$$

which permits the definition of the Lagrange multiplier,  $\lambda = \theta \Delta t (p^{n+1} - p^n)$  and corresponding pressure update  $p^{n+1} = p^n + \frac{\lambda}{\theta \Delta t}$ .

For the ALE formulation, we have the following relationship from Eq. (12.5)

$$\theta \Delta t \int_{\Omega_x^e} \nabla_X p^n - \theta \Delta t \int_{\Omega_x^e} \nabla_x p^{n+1} \quad (12.10)$$

In order to preserve the computational simplicity of the projection method in the Eulerian frame, we wish to develop a strategy to solve the PPE in the current configuration, and maintain the simple definition of the Lagrange multiplier and pressure update.

Using a push-forward from  $\Omega_X$  to  $\Omega_x$ , where

$$\begin{aligned} d\Omega_x &= Jd\Omega_X \\ \nabla_x(\cdot) &= \nabla_X(\cdot)\mathbf{F}^{-1} \end{aligned} \quad (12.11)$$

we want the  $\nabla p$ 's in  $\Omega_x$  in order to define  $\lambda$ , so the integral pressure-force difference becomes

$$\theta\Delta t \left\{ \int_{\Omega_x^e} \nabla_X p^n - \int_{\Omega_x^e} \nabla_x p^{n+1} \right\} = \theta\Delta t \left\{ \int_{\Omega_X^e} \nabla_X p^n \mathbf{F}^{-1} J d\Omega_X - \int_{\Omega_x^e} \nabla p^{n+1} \right\} \quad (12.12)$$

The pressure gradient in the reference configuration,  $\Omega_X$  is

$$\nabla_X p = \left\{ \frac{\partial p}{\partial X}, \frac{\partial p}{\partial Y}, \frac{\partial p}{\partial Z} \right\}^T \quad (12.13)$$

Pushing forward yields

$$\begin{aligned} \nabla_x p \mathbf{F}^{-1} &= \begin{pmatrix} \frac{\partial p}{\partial X} & \frac{\partial p}{\partial Y} & \frac{\partial p}{\partial Z} \end{pmatrix} \begin{bmatrix} \frac{\partial X}{\partial x} & \frac{\partial X}{\partial y} & \frac{\partial X}{\partial z} \\ \frac{\partial Y}{\partial x} & \frac{\partial Y}{\partial y} & \frac{\partial Y}{\partial z} \\ \frac{\partial Z}{\partial x} & \frac{\partial Z}{\partial y} & \frac{\partial Z}{\partial z} \end{bmatrix} = \\ &= \begin{pmatrix} \frac{\partial p}{\partial X} \frac{\partial X}{\partial x} + \frac{\partial p}{\partial Y} \frac{\partial Y}{\partial x} + \frac{\partial p}{\partial Z} \frac{\partial Z}{\partial x} \\ \frac{\partial p}{\partial X} \frac{\partial X}{\partial y} + \frac{\partial p}{\partial Y} \frac{\partial Y}{\partial y} + \frac{\partial p}{\partial Z} \frac{\partial Z}{\partial y} \\ \frac{\partial p}{\partial X} \frac{\partial X}{\partial z} + \frac{\partial p}{\partial Y} \frac{\partial Y}{\partial z} + \frac{\partial p}{\partial Z} \frac{\partial Z}{\partial z} \end{pmatrix}^T = \nabla_x p \end{aligned} \quad (12.14)$$

This permits simplification of the integral pressure difference using

$$\int_{\Omega_x^e} \nabla_X(\cdot)\mathbf{F}^{-1}J = \int_{\Omega_x^e} \nabla_x(\cdot) \quad (12.15)$$

so that

$$\theta\Delta t \left\{ \int_{\Omega_x^e} \nabla_X p^n - \int_{\Omega_x^e} \nabla_x p^{n+1} \right\} = \theta\Delta t \int_{\Omega_x^e} \nabla(p^n - p^{n+1}) \quad (12.16)$$

which permits  $\lambda = \theta\Delta t(p^{n+1} - p^n)$ .

*Revised P2  $\lambda$ -Construction*

A more rigorous approach to the derivation of the incremental projection method is outlined here. Starting with Eq. (12.5), we add and subtract  $\theta\Delta t \int_{\Omega_x} \nabla_x p^n$ . This yields

$$\begin{aligned} \rho \mathbf{v}^{n+1} \Omega^{n+1} - \theta \Delta t \oint_{\Gamma_x^e} \mu \nabla_x \mathbf{v}^{n+1} \cdot \mathbf{n}_x &= \rho \mathbf{v}^n \Omega^n - \Delta t \oint_{\Gamma_x^e} \rho \mathbf{v}^n (v_f - v_{m_f})|_{\Gamma_x^e} + \\ &\quad (1 - \theta) \Delta t \oint_{\Gamma_x^e} \mu \nabla_x \mathbf{v}^n \cdot \mathbf{n}_x - \\ (1 - \theta) \Delta t \int_{\Omega_x^e} \nabla_x p^n - \theta \Delta t \int_{\Omega_x^e} \nabla_x p^n + \theta \Delta t \int_{\Omega_x^e} \nabla_x (p^n - p^{n+1}) + \\ &\quad \Delta t (1 - \theta) \int_{\Omega_x^e} \mathbf{f}^n + \Delta t \theta \int_{\Omega_x^e} \mathbf{f}^{n+1} \end{aligned} \quad (12.17)$$

Now, as before, we define  $\lambda = \theta \Delta t (p^{n+1} - p^n)$  such that the pressure update is written as

$$p^{n+1} = p^n + \frac{\lambda}{\theta \Delta t} \quad (12.18)$$

Now, pull back  $\int_{\Omega_x^e} \nabla_x p^n$  to  $X$  using  $d\Omega_x = J d\Omega_X$ , and  $\nabla_x p^n = \nabla_X p^n \mathbf{F}^{-1}$ . So, the level “ $n$ ” pressure gradient terms become

$$\begin{aligned} I &= -(1 - \theta) \Delta t \int_{\Omega_x^e} \nabla_x p^n - \theta \Delta t \int_{\Omega_x^e} \nabla_x p^n \mathbf{F}^{-1} J d\Omega_X \\ &= -\Delta t \int_{\Omega_x^e} \{(1 - \theta) \nabla_x p^n + \theta \nabla_x p^n \mathbf{F}^{-1} J\} d\Omega_X \end{aligned} \quad (12.19)$$

Thus, for  $\theta = 0$ , i.e., forward-Euler

$$I = -\Delta t \int_{\Omega_X} \nabla_X p^n d\Omega_X \quad (12.20)$$

In the limit when  $\mathbf{x} = \mathbf{X}$ , i.e., at start-up,  $\mathbf{F} = \mathbf{I}$ , and  $J = 1$ , so

$$I = -\Delta t \int_{\Omega_X} \nabla_X p^n d\Omega_X \quad (12.21)$$

Using this result in the the momentum equation where

$$\frac{d}{dt} \int_{\Omega_{x(t)}} \rho \mathbf{v} = \int_{\Omega_x} \rho \mathbf{v}^{n+1} - \int_{\Omega_X} \rho \mathbf{v}^n \quad (12.22)$$

yields

$$\begin{aligned}
\int_{\Omega_x^e} \rho \mathbf{v}^{n+1} - \theta \Delta t \oint_{\Gamma_x^e} \mu \nabla_x \mathbf{v}^{n+1} \cdot \mathbf{n}_x &= \Delta t \left\{ (1 - \theta) \int_{\Omega_x^e} \mathbf{f}^n + \theta \int_{\Omega_x^e} \mathbf{f}^{n+1} \right\} \\
&\quad - \Delta t \oint_{\Gamma_x^e} \rho \mathbf{v}^n (v_f - v_{m_f}) \Big|_{\Gamma_x^e} \\
&\quad + \int_{\Omega_x^e} \rho \mathbf{v}^n + (1 - \theta) \Delta t \oint_{\Gamma_x^e} \mu \nabla_X \mathbf{v}^n \cdot \mathbf{n}_X \\
&\quad - \Delta t \int_{\Omega_x^e} \left\{ (1 - \theta) \nabla_X p^n + \theta \nabla_X p^n \mathbf{F}^{-1} J \right\} \\
&\quad - \theta \Delta t \int_{\Omega_x^e} \nabla_x (p^{n+1} - p^n)
\end{aligned} \tag{12.23}$$

Now, use Helmholtz decomposition

$$\rho \mathbf{v}^* = \rho \mathbf{v}^{n+1} + \nabla_x \lambda \tag{12.24}$$

with the objective that  $\nabla \cdot \mathbf{v}^{n+1} = 0$ , thus

$$\int_{\Omega_x} \rho \mathbf{v}^{n+1} = \int_{\Omega_x} (\rho \mathbf{v}^* - \nabla_x \lambda) \tag{12.25}$$

Using Eq. (12.25) in Eq. (12.23) and letting  $\lambda = \theta \Delta t (p^{n+1} - p^n)$ , we make the intermediate step

$$\begin{aligned}
\int_{\Omega_x^e} \rho \mathbf{v}^* - \int_{\Omega_x^e} \nabla_x \lambda - \{\dots\} &= \{\dots\} \\
&\quad - \theta \Delta t \int_{\Omega_x^e} \nabla_x (p^{n+1} - p^n) \\
\int_{\Omega_x^e} \rho \mathbf{v}^* - \theta \Delta t \int_{\Omega_x^e} \nabla_x (p^{n+1} - p^n) - \{\dots\} &= \{\dots\} \\
&\quad - \theta \Delta t \int_{\Omega_x^e} \nabla_x (p^{n+1} - p^n)
\end{aligned} \tag{12.26}$$

Letting,

$$\oint_{\Gamma_x^e} \mu \nabla_x \mathbf{v}^{n+1} \cdot \mathbf{n}_x \approx \oint_{\Gamma_x^e} \mu \nabla_x \mathbf{v}^* \cdot \mathbf{n}_x \tag{12.27}$$

which simplifies to  $\int_{\Omega_x} \nabla_x \cdot \nabla_x (\nabla_x \lambda) = 0$ , which only holds in  $\Omega_x$ . Strictly speaking this is a statement of commutativity of the divergence operator and the Laplacian which is true in the interior of  $\Omega_x$ .

Therefore, the momentum equation in integral form becomes

$$\begin{aligned}
\int_{\Omega_x^e} \rho \mathbf{v}^* - \theta \Delta t \oint_{\Gamma_x^e} \mu \nabla_x \mathbf{v}^* \cdot \mathbf{n}_x &= \int_{\Omega_x^e} \rho \mathbf{v}^n - \Delta t \oint_{\Gamma_x^e} \rho \mathbf{v}^n (v_f - v_{m_f}) \Big|_{\Gamma_x^e} + \\
&\quad (1 - \theta) \Delta t \oint_{\Gamma_x^e} \mu \nabla_X \mathbf{v}^n \cdot \mathbf{n}_X - \\
&\quad \Delta t \int_{\Omega_x^e} \nabla_X p^n \left[ (1 - \theta) \mathbf{I} + \theta \mathbf{F}^{-1} J \right] + \\
&\quad \Delta t (1 - \theta) \int_{\Omega_x^e} \mathbf{f}^n + \Delta t \theta \int_{\Omega_x^e} \mathbf{f}^{n+1}
\end{aligned} \tag{12.28}$$

### Geometric Conservation Law

Now, we check that geometric conservation law (GCL) is still satisfied. This requires that a constant solution be reproduced exactly and independent of domain/mesh motion.

We assume that

$$\begin{aligned}\nabla \cdot \mathbf{v}^n &= \nabla \cdot \mathbf{v}^{n+1} = 0 \\ \mathbf{f} &= 0 \\ \mathbf{v} &= \text{const} \\ \nabla p &= \text{const} \\ p^n &= p^{n+1}\end{aligned}\tag{12.29}$$

Using Eq.(12.5) for  $\mathbf{v}^n = \mathbf{v}^{n+1} = \text{const}$ , gradient vanish, so

$$\begin{aligned}\rho \mathbf{v}^{n+1} \Omega^{n+1} &= \rho \mathbf{v}^n \Omega^n - \Delta t \oint_{\Gamma_X^e} \rho \mathbf{v}^n (v_f - v_{m_f})|_{\Gamma_X^e} \\ &\quad - \Delta t(1 - \theta) \int_{\Omega_X^e} \nabla_X p^n - \Delta t \theta \int_{\Omega_X^e} \nabla_x p^{n+1}\end{aligned}\tag{12.30}$$

From the earlier analysis,

$$\int_{\Omega_X^e} \nabla_X p^n - \int_{\Omega_X^e} \nabla_x p^{n+1} = \int_{\Omega_X^e} \nabla_x (p^n - p^{n+1}) = 0\tag{12.31}$$

since  $p^n = p\theta$ . Now, for  $\theta = 1/2$  all pressure-gradient terms vanish. As an aside, for the incompressible solver, the default is  $\theta = 1/2$ .

This leaves

$$\rho \mathbf{v}^{n+1} \Omega^{n+1} = \rho \mathbf{v}^n \Omega^n - \Delta t \sum_f \rho \mathbf{v}^n (v_f - v_{m_f}) \Gamma_{X_f}^e\tag{12.32}$$

However,

$$\Delta t (v_f - v_{m_f}) \Gamma_{X_f}^e = \Delta \Omega^n,\tag{12.33}$$

where  $\Omega^{n+1} = \Omega^n + \Delta \Omega^n$ , so  $\rho \mathbf{v}^{n+1} \Omega^{n+1} = \rho \mathbf{v}^n (\Omega^n + \Delta \Omega^n)$ , thus  $\mathbf{v}^{n+1} = \mathbf{v}^n$  for all time. This concludes the exercise to show the GCL is preserved with this formulation.

### ALE Formulation Comparison

As a point of reference, we compare our formulation to that proposed by Förster, Wall and Ramm [C. Förster and Ramm, 2007].

We begin by stating the time-integrator proposed by Förster, Wall and Ramm.

$$\begin{aligned}\mathbf{u}^{n+1} J^{n+1} + \theta \Delta t J^{n+1} [(\mathbf{u}^{n+1} - \mathbf{u}_G^{n+1}) \cdot \nabla u - 2\nu \nabla \cdot \mathbf{ffl} + \nabla p^{n+1}] = \\ J^{n+1} [\theta \Delta t \mathbf{F}^{n+1} + (1 - \theta) \Delta t \dot{\mathbf{u}}^n + \mathbf{u}^n]\end{aligned}\tag{12.34}$$



where  $\mathbf{u}$  is the velocity,  $\mathbf{ffl}$  is the strain-rate, and

$$J = \frac{\Omega_x}{\Omega_X} \quad (12.35)$$

in our nomenclature.

Rearranging so to obtain a linear combination of forward and backward-Euler time integrators yields.

$$\begin{aligned} & \theta \left\{ \frac{\mathbf{u}^{n+1} - \mathbf{u}^n}{\Delta t} + (\mathbf{u}^{n+1} - \mathbf{u}_G^{n+1}) \cdot \nabla \mathbf{u}^{n+1} - 2\nu \nabla \cdot \mathbf{ffl}^{n+1} + \nabla p^{n+1} \right\} + \\ (1 - \theta) & \left\{ \frac{\mathbf{u}^{n+1} - \mathbf{u}^n}{\Delta t} + (\mathbf{u}^n - \mathbf{u}_G^n) \cdot \nabla \mathbf{u}^n - 2\nu \nabla \cdot \mathbf{ffl}^n + \nabla p^n \right\} = 0 \end{aligned} \quad (12.36)$$

This is simply a time-discrete version of Eq.(5.67) where  $\mathbf{u} = \mathbf{v}$ , and Förster, et al. have implied the reference frame by the time-index, i.e.,  $n$  and  $n + 1$ .

### Start-up procedure

The start-up procedure remains the same with one exception. An initial mesh velocity may be present, and to account for it, the partial acceleration becomes

$$\rho \Omega \tilde{\mathbf{a}} = \mathbf{f} \Omega + \oint_{\Gamma_e} \{ \mu (\nabla \mathbf{v}^o + \nabla \mathbf{v}^{oT}) \} \cdot \mathbf{n} - \oint_{\Gamma_e} \rho \mathbf{v}^o (v_f^o - v_{m_f}^o) \quad (12.37)$$

Thus the partial acceleration calculation needs to account for any initial mesh velocity, but otherwise the initial pressure computation is not changed. The remainder of start-up remains the same.

### Time Integration

Returning to Eq. (12.28), we want to solve for  $\mathbf{v}^*$  keeping only the pressure-gradient terms at  $t^{n+1}$

$$\begin{aligned} \left[ \rho \Omega^{n+1} - \theta \Delta t \oint_{\Gamma_x^e} \mu \nabla_x(\cdot) \cdot \mathbf{n}_x \right] \mathbf{v}^* &= \left[ \rho \Omega^n + (1 - \theta) \Delta t \oint_{\Gamma_X^e} \mu \nabla_X(\cdot) \cdot \mathbf{n}_X \right] \mathbf{v}^n \\ &\quad - \Delta t \oint_{\Gamma_X^e} \rho \mathbf{v}^n (v_f - v_{m_f}) |_{\Gamma_X^e} \\ &\quad - \Delta t \int_{\Omega_X^e} \nabla_x p^n [(1 - \theta) \mathbf{I} + \theta \mathbf{F}^{-1}] \\ &\quad \Delta t \left[ (1 - \theta) \int_{\Omega_X^e} \mathbf{f}^n + \theta \int_{\Omega_x^e} \mathbf{f}^{n+1} \right] \end{aligned} \quad (12.38)$$

Before proceeding, we define the operators used in both the reference and current configurations as shown in Table 12.2.

Level-n: $X$	Level-n + 1: $x$
$M^n = \rho\Omega^n$	$M^{n+1} = \rho\Omega^{n+1}$
$K^n = - \oint_{\Gamma_x^e} \mu \nabla_X(\cdot) \cdot \mathbf{n}_X$	$K^{n+1} = - \oint_{\Gamma_x^e} \mu \nabla_x(\cdot) \cdot \mathbf{n}_x$
$\mathbf{F}^n = \mathbf{f}^n \Omega^n$	$\mathbf{F}^{n+1} = \mathbf{f}^{n+1} \Omega^{n+1}$
$\mathbf{B}^n \equiv$ FEM B-Matrix	$K_{\lambda_e}^{n+1} = \int_{\Omega_x^e} \nabla_x N_I \frac{1}{\rho} \nabla_x N_T$

Table 12.2: Operators definition

### Pressure gradient

In order to provide a convenient and efficient switch between Eulerian and ALE, we write the pressure-gradient contribution to Eq. (12.38) as

$$\begin{aligned}
 - \Delta t \int_{\Omega_x^e} \nabla_x p^n [(1 - \theta)\mathbf{I} + \theta\mathbf{F}^{-1}J] = \\
 - \Delta t \int_{\Omega_x} \nabla_X p^n + \theta \Delta t \int_{\Omega_x} \nabla_X p^n (\mathbf{I} - \mathbf{F}^{-1}J) \quad (12.39)
 \end{aligned}$$

The deformation gradient in indicial form is

$$F_{ij} = \frac{\partial x_i}{\partial X_j} \quad (12.40)$$

which is computed using the B-matrix as

$$F_{ij} = \begin{bmatrix} \frac{\partial x}{\partial X} = \sum_{k=1}^{Nnpe} B_{X_k} x_k & \frac{\partial x}{\partial Y} = \sum_{k=1}^{Nnpe} B_{Y_k} x_k & \frac{\partial x}{\partial Z} = \sum_{k=1}^{Nnpe} B_{Z_k} x_k \\ \frac{\partial y}{\partial X} = \sum_{k=1}^{Nnpe} B_{X_k} y_k & \frac{\partial y}{\partial Y} = \sum_{k=1}^{Nnpe} B_{Y_k} y_k & \frac{\partial y}{\partial Z} = \sum_{k=1}^{Nnpe} B_{Z_k} y_k \\ \frac{\partial z}{\partial X} = \sum_{k=1}^{Nnpe} B_{X_k} z_k & \frac{\partial z}{\partial Y} = \sum_{k=1}^{Nnpe} B_{Y_k} z_k & \frac{\partial z}{\partial Z} = \sum_{k=1}^{Nnpe} B_{Z_k} z_k \end{bmatrix} \quad (12.41)$$

The Jacobian,  $J = \det(\mathbf{F})$ , is

$$J = \frac{\partial x}{\partial X} \left( \frac{\partial y}{\partial Z} \frac{\partial z}{\partial Z} - \frac{\partial y}{\partial Z} \frac{\partial z}{\partial Y} \right) + \frac{\partial x}{\partial Y} \left( \frac{\partial y}{\partial X} \frac{\partial z}{\partial Z} - \frac{\partial y}{\partial Z} \frac{\partial z}{\partial X} \right) + \frac{\partial x}{\partial Z} \left( \frac{\partial y}{\partial X} \frac{\partial z}{\partial Y} - \frac{\partial y}{\partial Y} \frac{\partial z}{\partial X} \right) \quad (12.42)$$

The inverse deformation gradient is

$$F_{ij}^{-1} = \begin{bmatrix} \frac{\partial X}{\partial x} & \frac{\partial X}{\partial y} & \frac{\partial X}{\partial z} \\ \frac{\partial Y}{\partial x} & \frac{\partial Y}{\partial y} & \frac{\partial Y}{\partial z} \\ \frac{\partial Z}{\partial x} & \frac{\partial Z}{\partial y} & \frac{\partial Z}{\partial z} \end{bmatrix} \quad (12.43)$$

We use Cramer's rule to compute the inverse. Given a  $3 \times 3$  matrix  $A$

$$A = \begin{bmatrix} a_{11} & a_{12} & a_{13} \\ a_{21} & a_{22} & a_{23} \\ a_{31} & a_{32} & a_{33} \end{bmatrix} \quad (12.44)$$

The cofactors of  $A$  are written as

$$B_{ij} = (-1)^{i+j} \begin{bmatrix} \cdot & \cdot \\ \cdot & \cdot \end{bmatrix} \quad (12.45)$$

$$\begin{aligned} B_{11} &= (-1)^{1+1} \begin{bmatrix} a_{22} & a_{23} \\ a_{32} & a_{33} \end{bmatrix} & B_{12} &= (-1)^{1+2} \begin{bmatrix} a_{21} & a_{23} \\ a_{31} & a_{33} \end{bmatrix} \\ B_{13} &= (-1)^{1+3} \begin{bmatrix} a_{21} & a_{22} \\ a_{31} & a_{32} \end{bmatrix} & B_{21} &= (-1)^{2+1} \begin{bmatrix} a_{12} & a_{13} \\ a_{32} & a_{33} \end{bmatrix} \\ B_{22} &= (-1)^{2+2} \begin{bmatrix} a_{11} & a_{13} \\ a_{31} & a_{33} \end{bmatrix} & B_{23} &= (-1)^{2+3} \begin{bmatrix} a_{11} & a_{12} \\ a_{31} & a_{32} \end{bmatrix} \\ B_{31} &= (-1)^{3+1} \begin{bmatrix} a_{12} & a_{13} \\ a_{22} & a_{23} \end{bmatrix} & B_{32} &= (-1)^{3+2} \begin{bmatrix} a_{11} & a_{13} \\ a_{21} & a_{23} \end{bmatrix} \\ B_{33} &= (-1)^{3+3} \begin{bmatrix} a_{11} & a_{12} \\ a_{21} & a_{22} \end{bmatrix} \end{aligned} \quad (12.46)$$

The inverse of  $A$  is

$$A^{-1} = \frac{1}{\det(A)} \begin{bmatrix} B_{11} & B_{21} & B_{31} \\ B_{12} & B_{22} & B_{32} \\ B_{13} & B_{23} & B_{33} \end{bmatrix} \quad (12.47)$$

or alternatively for the inverse deformation gradient,

$$\mathbf{F}^{-1} = \frac{1}{\det(\mathbf{F})} \begin{bmatrix} B_{11} & B_{21} & B_{31} \\ B_{12} & B_{22} & B_{32} \\ B_{13} & B_{23} & B_{33} \end{bmatrix} \quad (12.48)$$

Now, we need to compute

$$I - \mathbf{F}^{-1}J = \begin{bmatrix} 1 & 0 & 0 \\ 0 & 1 & 0 \\ 0 & 0 & 1 \end{bmatrix} - \frac{1}{\det(\mathbf{F})} \begin{bmatrix} B_{11} & B_{21} & B_{31} \\ B_{12} & B_{22} & B_{32} \\ B_{13} & B_{23} & B_{33} \end{bmatrix} \det(\mathbf{F}) \quad (12.49)$$

which, after simplifying, is

$$I - \mathbf{F}^{-1}J = \begin{bmatrix} (1 - B_{11}) & -B_{21} & -B_{31} \\ -B_{12} & (1 - B_{22}) & -B_{32} \\ -B_{13} & -B_{23} & (1 - B_{33}) \end{bmatrix} \quad (12.50)$$

Let  $\mathbf{G} = \mathbf{I} - \mathbf{F}^{-1}\mathbf{J}$  so that the right-hand-side pressure gradient terms in the momentum equation are implemented as

$$\mathbf{F}_{\nabla p} = -\Delta t \{ \mathbf{B}_X p^n \Omega^n \} + \theta \Delta t \{ \mathbf{B}_X p^n \Omega^n \} \mathbf{G} \quad (12.51)$$

### *Time-Integration Algorithm*

#### **Algorithm 2** *ALE P2 Algorithm*

The ALE algorithm relies on the reference configuration  $X$  at  $t$  ( $n$ ), and the current configuration  $x$  at  $t + \Delta t$  ( $n+1$ ). The data associated with each configuration is shown in the table below. The P2 algorithm proceeds as follows.

1. Given the interface displacements, deform the mesh to the  $x$ -configuration. Here,  $\delta \mathbf{u}^n, \delta \mathbf{u}^{n+1}$  are the total displacement with respect to  $X^0$ .

The current configuration is

$$\mathbf{x}^{n+1} = \mathbf{x}^0 + \delta \mathbf{u}^{n+1} \quad (12.52)$$

The average velocity is estimated as

$$\bar{\mathbf{v}}_m = \frac{\mathbf{x}^{n+1} - \mathbf{x}^n}{\Delta t} = \frac{\delta \underline{\mathbf{u}}^{n+1} - \delta \underline{\mathbf{u}}}{\Delta t} \quad (12.53)$$

The dual-edge mesh velocity is computed as

$$v_{m_f} = \sum_k \mathcal{N}_k|_f \bar{\mathbf{v}}_{m_k} \cdot \mathbf{n}_f. \quad (12.54)$$

The total dual-edge velocity is

$$v_f = (v_f^n - \bar{v}_{m_f}) \quad (12.55)$$

and accounts for specified velocity boundary conditions as well as the moving interface velocity conditions. The mesh-deformation step also computes the volume  $\Omega^{n+1}$ .

2. Compute all RHS terms for all equations in  $X$  configuration, update to  $\mathbf{x}^{n+1}$ , then solve the equations.

This is similar to work by Förster, et al. [C. Forster and Ramm, 2007], in which they compute  $\dot{\mathbf{v}}^n$  and uses this in the updated configuration. This approach

- Permits all objects (except  $\Omega^{n+1}, \mathbf{x}^{n+1}$ ) to be updated once per time increment.
- Seems most reasonable in terms of CPU and memory
- Requires storing time-derivatives or RHS for all equations being solved.

3. Given  $\mathbf{v}^n$  and  $v_f^n$ , and  $\bar{v}_{m_f}$ , solve for  $\mathbf{v}^*$ .

$$[M^{n+1} + \theta \Delta t K^{n+1}] \mathbf{v}^* = [M^n - (1 - \theta) \Delta t K^n] \mathbf{v}^n - \Delta t \oint_{\Gamma_f^i} \rho \mathbf{v}^n (v_f^n - \bar{v}_{m_f}) - \Delta t \mathbf{B}^n p^n \Omega^n [(1 - \theta) \mathbf{I} - \theta \mathbf{F}^{-1}] + \Delta t [(1 - \theta) \tilde{F}^n + \theta \tilde{F}^{n+1}] \quad (12.56)$$

4. Project the velocity to a div-free subspace.

- (a) Form the PPE  $K^{n+1}$  in  $\mathbf{x}^{n+1}$  configuration.
- (b) Form the PPE Rhs in  $\mathbf{x}^n$  configuration, uses  $\mathbf{v}^n$ ,  $u_f^n$ , in  $\mathbf{x}^n$  configuration.
- (c) CalcEdgeVel  $\tilde{v}_f^{n+1}$  in  $\mathbf{x}^{n+1}$ .
- (d) calcDiv()  $\rightarrow \sum_f \tilde{v}_f^{n+1} \Gamma^{n+1}$ .  
rmsDiv().
- (e) formPPERhs in  $\mathbf{x}^{n+1}$  use  $\mathbf{v}^{n+1}$ ,  $\tilde{v}_f^{n+1}$ ,  $rhsc- = rhsn$ .
- (f) Apply pressure incremental BC's.
- (g) Solve  $K^{n+1} \lambda^{n+1} = \delta(\nabla \cdot \mathbf{u})$ .
- (h) Compute  $\nabla_x \lambda^{n+1}$ ,  $(\nabla_x \lambda^{n+1})_f$ .
- (i)  $v_f^{n+1} = \tilde{v}_f^{n+1} - \frac{1}{\rho} (\nabla_x \lambda^{n+1})_f$ .
- (j)  $\mathbf{v}^{n+1} = \tilde{\mathbf{v}}^{n+1} - \frac{1}{\rho} \nabla_x \lambda^{n+1}$ .

5. Update the pressure.

**Remark 7** An alternative to the algorithm above was considered where the viscous terms are pulled-back. Consider Eq. (12.38), and assume  $\mathbf{x}^{n+1}$ ,  $\Omega^{n+1}$  are available. The only term requiring updated dual-edge data is  $K^{n+1}$ , so we pull back to the  $\mathbf{x}^n$  configuration as

$$K^{n+1} \mathbf{v}^{n+1} = - \oint_{\Gamma_x^e} \mu \nabla_x \mathbf{v}^{n+1} \cdot \mathbf{n}_x \quad (12.57)$$

Using Nanson's formula Eq.(5.11)

$$\nabla_x \mathbf{v} = \nabla_X \mathbf{v} \mathbf{F}^{-1} \quad (12.58)$$

$$K^{n+1} \mathbf{v}^{n+1} = - \oint_{\Gamma_x^e} \mu \nabla_X \mathbf{v}^{n+1} \mathbf{F}^{-1} \mathbf{J} \mathbf{F}^T \mathbf{n}_X d\Gamma_X^e \quad (12.59)$$

Now, the LHS/RHS K-operators are formed in  $X$  or reference configuration. This avoids having storage for dual-edge velocities at  $n$ ,  $n + 1$ . However,  $\mathbf{J}$ ,  $\mathbf{F}^{-1}$  requires  $10 \cdot N_{el}$  words of storage, which is as much as all the dual-edge geometry data stored in flow solver. This memory usage was considered prohibitive.

This approach also requires  $\mathbf{B}$ ,  $K_\lambda$  be updated during the momentum solve and projection. So, updates due to configuration aren't in a single place in code. This was considered untenable from a software maintenance perspective.

### Temperature dependent viscosity

If the viscosity depends on the temperature, Eq. (12.59) is the function of the temperature at time  $n + 1$ :

$$K^{n+1}\mathbf{v}^{n+1} = - \oint_{\Gamma_x^e} \mu(T^{n+1}) \nabla_X \mathbf{v}^{n+1} \mathbf{F}^{-1} J \mathbf{F}^T \mathbf{n}_X d\Gamma_X^e \quad (12.60)$$

For the RHS K-operator,  $K^n$  is the function of the temperature at time  $n$ :

$$K^n \mathbf{v}^n = - \oint_{\Gamma_x^e} \mu(T^n) \nabla_x \mathbf{v}^n \cdot \mathbf{n}_x \quad (12.61)$$

### Energy Equation

Using the master balance equation, Eq. (5.43), for the scalar case, the energy equation (see Eq. (5.55)), written in terms of temperature, with a time-weighting similar to the momentum equation is

$$\begin{aligned} (1 - \theta) \left\{ \frac{\rho C_p \Omega^{n+1} T^{n+1} - \rho C_p \Omega^n T^n}{\Delta t} = - \oint_{\Gamma_x^e} \rho C_p T^n (v_f - v_{m_f}) \Big|_{\Gamma_x^e} \right. \\ \left. + \oint_{\Gamma_x^e} \kappa \nabla_X T^n \cdot \mathbf{n}_X + \int_{\Omega_x^e} q'''^n \right\} \\ + \theta \left\{ \frac{\rho C_p \Omega^{n+1} T^{n+1} - \rho C_p \Omega^n T^n}{\Delta t} = - \oint_{\Gamma_x^e} \rho C_p T^n (v_f - v_{m_f}) \Big|_{\Gamma_x^e} \right. \\ \left. + \oint_{\Gamma_x^e} \kappa \nabla_x T^{n+1} \cdot \mathbf{n}_x + \int_{\Omega_x^e} q'''^{n+1} \right\} \end{aligned} \quad (12.62)$$

After rearranging,

$$\begin{aligned} \frac{\rho C_p \Omega^{n+1} T^{n+1} - \rho C_p \Omega^n T^n}{\Delta t} = (1 - \theta) \int_{\Omega_x^e} q'''^n + \theta \int_{\Omega_x^e} q'''^{n+1} \\ + (1 - \theta) \oint_{\Gamma_x^e} \kappa \nabla_X T^n \cdot \mathbf{n}_X + \theta \oint_{\Gamma_x^e} \kappa \nabla_x T^{n+1} \cdot \mathbf{n}_x \\ - \oint_{\Gamma_x^e} \rho C_p T^n (v_f - v_{m_f}) \Big|_{\Gamma_x^e} \end{aligned} \quad (12.63)$$

Let

$$C^n = \rho C_p \Omega^n, \quad C^{n+1} = \rho C_p \Omega^{n+1}$$

$$K_T^n = - \oint_{\Gamma_x^e} \kappa \nabla_X (\cdot) \cdot \mathbf{n}_X, \quad K_T^{n+1} = - \oint_{\Gamma_x^e} \kappa \nabla_x (\cdot) \cdot \mathbf{n}_x \quad (12.64)$$

$$Q^n = \int_{\Omega_x^e} q'''^n = q'''^n \Omega^n, \quad Q^{n+1} = \int_{\Omega_x^e} q'''^{n+1} = q'''^{n+1} \Omega^{n+1}$$

The fully-discrete energy equation is

$$\begin{aligned}
 [C^{n+1} + \theta \Delta t K_T^{n+1}] T^{n+1} &= [C^n - (1 - \theta) \Delta t K_T^n] T^n - \\
 &\quad \oint_{\Gamma_x^e} \rho C_p T^n (v_f - v_{m_f})|_{\Gamma_x^e} + \Delta t [(1 - \theta) Q^n + \theta Q^{n+1}]
 \end{aligned}
 \tag{12.65}$$

*Temperature dependent specific heat and conductivity*

If the specific heat and conductivity depend on the temperature, Eq. (12.65) needs to be modified according to the linearization:

$$\begin{aligned}
 [\tilde{C}^{n+1} + \theta \Delta t \tilde{K}_T^{n+1}] T^{n+1} &= [\tilde{C}^n - (1 - \theta) \Delta t K_T^n - \theta \Delta t \tilde{K}_T^n] T^n - \\
 &\quad \oint_{\Gamma_x^e} \rho C_p(T^n) T^n (v_f - v_{m_f})|_{\Gamma_x^e} + \Delta t [(1 - \theta) Q^n + \theta Q^{n+1}]
 \end{aligned}
 \tag{12.66}$$

where

$$\begin{aligned}
 \tilde{C}^{n+1} &= \rho [C_p(T^n) + \frac{\partial C_p(T^n)}{\partial T} T^n] \Omega^{n+1} \\
 \tilde{C}^n &= \rho [C_p(T^n) \Omega^n + \frac{\partial C_p(T^n)}{\partial T} T^n \Omega^{n+1}] \\
 \tilde{K}_T^{n+1} &= - \oint_{\Gamma_x^e} [\kappa(T^n) + \frac{\partial \kappa(T^n)}{\partial T} T^n] \nabla_x(\cdot) \cdot \mathbf{n}_x \\
 \tilde{K}_T^n &= - \oint_{\Gamma_x^e} \frac{\partial \kappa(T^n)}{\partial T} T^n \nabla_x(\cdot) \cdot \mathbf{n}_x
 \end{aligned}
 \tag{12.67}$$

*Enthalpy equation with constant density and specific heat*

The fully-discrete enthalpy equation with constant density and specific heat is

$$\begin{aligned}
 \frac{\rho \Omega^{n+1} h^{n+1} - \rho \Omega^n h^n}{\Delta t} &= (1 - \theta) \int_{\Omega_x^e} q'''^n + \theta \int_{\Omega_x^e} q'''^{n+1} \\
 &\quad + (1 - \theta) \oint_{\Gamma_x^e} \kappa \nabla_x T(h)^n \cdot \mathbf{n}_x + \theta \oint_{\Gamma_x^e} \kappa \nabla_x T(h)^{n+1} \cdot \mathbf{n}_x \\
 &\quad - \oint_{\Gamma_x^e} \rho h^n (v_f - v_{m_f})|_{\Gamma_x^e}
 \end{aligned}
 \tag{12.68}$$

The temperatures are evaluated by inverting a  $h(T)$  thermodynamic relationship.

### Spalart-Allmaras Model

Using the scalar master balance equation, Eq. (5.43), the Spalart-Allmaras (SA) model is written as

$$\begin{aligned} \frac{d}{dt} \int_{\Omega_x} \rho \tilde{v} d\Omega_x + \oint_{\Gamma_x} \rho \tilde{v} (\mathbf{v} - \mathbf{v}_m) \cdot \mathbf{n}_x d\Omega_x &= + \oint_{\Gamma_x} \rho \left( \frac{1 + C_{b2}}{\sigma} \right) (v + \tilde{v})|_{\Gamma_x} \nabla \tilde{v} \cdot \tilde{\mathbf{n}}_x d\Gamma_x \\ &- \oint_{\Gamma_x} \rho \frac{C_{b2}}{\sigma} (v + \tilde{v})|_{\Omega_x} \nabla \tilde{v} \cdot \tilde{\mathbf{n}}_x d\Gamma_x \\ &+ \int_{\Omega_x} \rho C_{b1} \tilde{S} \tilde{v} d\Omega_x - \int_{\Omega_x} \rho C_{w1} f_w \left( \frac{\tilde{v}}{d} \right)^2 d\Omega_x \end{aligned} \quad (12.69)$$

Considering the  $\mathbf{x}^n(\mathbf{X})$  and  $\mathbf{x}^{n+1}$  configurations,

$$P = \rho C_b \tilde{S} \quad \text{and} \quad D = \rho C_w f_w \frac{\tilde{v}}{d^2} \quad (12.70)$$

In the  $\mathbf{X}$  configuration,

$$\begin{aligned} M^n &= \int_{\Omega_X^e} \rho d\Omega_X \\ A^n(\rho, \tilde{v}, v_m) &= \oint_{\Gamma_X^e} \rho(\cdot) (v_f - v_{mf}) d\Gamma_X \\ K^n &= - \oint_{\Gamma_X^e} \left( \frac{1 + C_{b2}}{\sigma} \right) (v^n + \tilde{v}^n)|_{\Gamma_X^e} \nabla_X(\cdot) \cdot \mathbf{n}_X d\Gamma_X \\ &+ \oint_{\Gamma_X^e} \frac{C_{b2}}{\sigma} (v^n + \tilde{v}^n)|_{\Omega_X^e} \nabla_X(\cdot) \cdot \mathbf{n}_X d\Gamma_X \end{aligned} \quad (12.71)$$

In the  $\mathbf{x}$  configuration,

$$\begin{aligned} M^{n+1} &= \int_{\Omega_x} \rho d\Omega_x \\ K^{n+1} &= - \oint_{\Gamma_x^e} \frac{1 + C_{b2}}{\sigma} (v^n + \tilde{v}^n)|_{\Gamma_x^e} \nabla_x(\cdot) \cdot \mathbf{n}_x d\Gamma_x \\ &+ \oint_{\Gamma_x^e} \frac{C_{b2}}{\sigma} (v^n + \tilde{v}^n)|_{\Omega_x^e} \nabla_x(\cdot) \cdot \mathbf{n}_x d\Gamma_x \end{aligned} \quad (12.72)$$

We leave the source-terms "as is" for later linearization and use the  $\theta$ -weighting approach

$$\begin{aligned} (1 - \theta) \left\{ \frac{M^{n+1} \tilde{v}^{n+1} - M^n \tilde{v}^n}{\Delta t} + A^n(\rho, \mathbf{v}^n, v_m) \tilde{v}^n \right. \\ \left. + K^n \tilde{v}^n - \int_{\Omega_X^e} [P^n(\tilde{v}^n) - D^n(\tilde{v}^n)] \tilde{v}^n d\Omega_X \right\} &= 0 \\ + \theta \left\{ \frac{M^{n+1} \tilde{v}^{n+1} - M^n \tilde{v}^n}{\Delta t} + A^n(\rho, \mathbf{v}^n, v_m) \tilde{v}^n \right. \\ \left. + K^{n+1} \tilde{v}^{n+1} - \int_{\Omega_x^e} ([P^{n+1}(\tilde{v}^{n+1}) - D^{n+1}(\tilde{v}^{n+1})] \tilde{v}^{n+1} d\Omega_x) \right\} &= 0 \end{aligned} \quad (12.73)$$



After some rearrangement, we obtain

$$\begin{aligned} \frac{M^{n+1}\tilde{v}^{n+1} - M^n\tilde{v}^n}{\Delta t} + \theta K^{n+1}\tilde{v}^{n+1} + (1-\theta)K^n\tilde{v}^n + A(\rho, \mathbf{v}^n, v_m)\tilde{v}^n \\ + \theta \int_{\Omega_x^e} (D^{n+1} - P^{n+1})\tilde{v}^{n+1} d\Omega_x + (1-\theta) \int_{\Omega_x^e} (D^n - P^n)\tilde{v}^n d\Omega_x = 0 \end{aligned} \quad (12.74)$$

Now, we setup the positivity-preserving linearization following [Spalart and Allmaras, January 1992] in our current formulation. Let

$$I = \theta \int_{\Omega_x^e} (D^{n+1} - P^{n+1})\tilde{v}^{n+1} d\Omega_x + (1-\theta) \int_{\Omega_x^e} (D^n - P^n)\tilde{v}^n d\Omega_x \quad (12.75)$$

Assume that linearization takes place with respect to  $X$  and ignore the dependence of  $\mathcal{S}$  on  $R^{n+1}$  in the SA model (note: accounting for the effects of  $F$  on  $R$  in the  $n+1$  frame is complex, and ignored for now. This is consistent with the selective use of lagged variables in the original work by Spalart and Allmaras [Spalart and Allmaras, January 1992]).

Using  $d\Omega_x = Jd\Omega_X$ , and expanding about “ $n$ ”, and using  $\tilde{v}^{n+1} - \tilde{v}^n = \Delta\tilde{v}$ , we get

$$\begin{aligned} I = \theta \int_{\Omega_x^e} \left\{ \left[ D^n\tilde{v}^n + \frac{\partial D^n}{\partial \tilde{v}} \Delta\tilde{v}\tilde{v}^n + D^n\Delta\tilde{v}^n \right] \right. \\ \left. - \left[ P^n\tilde{v}^n + \frac{\partial P^n}{\partial \tilde{v}} \Delta\tilde{v}\tilde{v}^n + P^n\Delta\tilde{v} \right] \right\} J d\Omega_X \\ + (1-\theta) \int_{\Omega_x^e} (D^n\tilde{v}^n - P^n\tilde{v}^n) d\Omega_x \end{aligned} \quad (12.76)$$

Collecting terms

$$\begin{aligned} I = \theta \int_{\Omega_x^e} (D^n - P^n)\tilde{v}^n J d\Omega_X \\ + (1-\theta) \int_{\Omega_x^e} (D^n - P^n)\tilde{v}^n d\Omega_x \\ + \theta \int_{\Omega_x^e} \left\{ (D^n - P^n)(\tilde{v}^{n+1} - \tilde{v}^n) + \left( \frac{\partial D^n}{\partial \tilde{v}} - \frac{\partial P^n}{\partial \tilde{v}} \right) \tilde{v}^n (\tilde{v}^{n+1} - \tilde{v}^n) \right\} J d\Omega_X \end{aligned} \quad (12.77)$$

$$\begin{aligned} I = \int_{\Omega_x^e} [\theta J + (1-\theta)](D^n - P^n)\tilde{v}^n d\Omega_X \\ + \theta \int_{\Omega_x^e} \left\{ \underbrace{(D^n - P^n)}_{\text{}} \tilde{v}^{n+1} + \underbrace{\left( \frac{\partial D^n}{\partial \tilde{v}} - \frac{\partial P^n}{\partial \tilde{v}} \right)}_{\text{}} \tilde{v}^n \tilde{v}^{n+1} \right\} J d\Omega_X \\ - \theta \int_{\Omega_x^e} \left\{ \underbrace{(D^n - P^n)}_{\text{}} \tilde{v}^n + \underbrace{\left( \frac{\partial D^n}{\partial \tilde{v}} - \frac{\partial P^n}{\partial \tilde{v}} \right)}_{\text{}} \tilde{v}^n \tilde{v}^n \right\} J d\Omega_X \end{aligned} \quad (12.78)$$

Since  $Jd\Omega_X = d\Omega_x$ , we can map the last two integrals back to configuration  $x$ , so that the semi-discrete form of the Eq.(12.74) is given by:

$$\begin{aligned} & \left\{ M^{n+1} + \theta\Delta t K^{n+1} + \theta\Delta t \int_{\Omega_x^e} \left[ (D^n - P^n) \right. \right. \\ & \quad \left. \left. + \left( \frac{\partial D^n}{\partial \tilde{v}} - \frac{\partial P^n}{\partial \tilde{v}} \right) \tilde{v}^n \right] d\Omega_x \right\} \tilde{v}^{n+1} = \\ & [M^n - (1 - \theta)\Delta t K^n] \tilde{v}^n - \Delta t \int_{\Omega_x^e} [\theta J + (1 - \theta)] (D^n - P^n) \tilde{v}^n d\Omega_X \\ & - \Delta t A^n \tilde{v}^n + \theta\Delta t \int_{\Omega_x^e} \left[ (D^n - P^n) + \left( \frac{\partial D^n}{\partial \tilde{v}} - \frac{\partial P^n}{\partial \tilde{v}} \right) \tilde{v}^n \right] \tilde{v}^n d\Omega_x \end{aligned} \quad (12.79)$$

In the L.H.S. of the above equation,  $\tilde{v}^{n+1}$  has been pulled out of the integral assuming it to be piecewise constant across each element. A similar procedure is carried out for the last term of the R.H.S.

Let us define

$$(\bar{D}^n - \bar{P}^n) = \int_{\Omega_x^e} \left[ (D^n - P^n) + \left( \frac{\partial D^n}{\partial \tilde{v}} - \frac{\partial P^n}{\partial \tilde{v}} \right) \tilde{v}^n \right] d\Omega_x \quad (12.80)$$

Therefore,

$$\begin{aligned} [M^{n+1} + \theta\Delta t K^{n+1} + \theta\Delta t (\bar{D}^n - \bar{P}^n)] \tilde{v}^{n+1} = \\ [M^n - (1 - \theta)\Delta t K^n] \tilde{v}^n - \Delta t A^n (\rho, \mathbf{v}^n, v_m) \tilde{v}^n \\ - \Delta t \int_{\Omega_x^e} [\theta J + (1 - \theta)] (D^n - P^n) \tilde{v}^n d\Omega_X \\ + \theta\Delta t (\bar{D}^n - \bar{P}^n) \tilde{v}^n \end{aligned} \quad (12.81)$$

*Note:* In the limit of  $\mathbf{x} \rightarrow \mathbf{X}$ ,  $F = I$ ,  $J = 1$ , it can be noted that the base Eulerian SA model is recovered.

The integral term (third term) on the R.H.S of Eq.(12.81) can be rewritten in the current  $x$  configuration as follows

$$\begin{aligned} \int_{\Omega_x^e} [\theta J + (1 - \theta)] (D^n - P^n) \tilde{v}^n d\Omega_X = \\ \int_{\Omega_x^e} [\theta J + (1 - \theta)] (D^n - P^n) \tilde{v}^n \frac{d\Omega_x}{J} \\ = \int_{\Omega_x^e} \left[ \theta + \frac{(1 - \theta)}{J} \right] (D^n - P^n) \tilde{v}^n d\Omega_x \end{aligned} \quad (12.82)$$

Since  $J = \frac{d\Omega_x}{d\Omega_X} = \frac{\Omega^{n+1}}{\Omega^n}$ , Eq.(12.82), can be discretized as follows

$$\int_{\Omega_x^e} [\theta J + (1 - \theta)] (D^n - P^n) \tilde{v}^n d\Omega_X = \left[ \theta + (1 - \theta) \frac{\Omega^n}{\Omega^{n+1}} \right] (D^n - P^n) \tilde{v}^n \Omega^{n+1} \quad (12.83)$$

Equations (12.81) and (12.83) can be combined to give the following equation

$$\begin{aligned} \left[ M^{n+1} + \theta \Delta t K^{n+1} + \theta \Delta t (\bar{D}^n - \bar{P}^n) \right] \tilde{v}^{n+1} = \\ [M^n - (1 - \theta) \Delta t K^n] \tilde{v}^n - \Delta t \left[ \theta + (1 - \theta) \frac{\Omega^n}{\Omega^{n+1}} \right] (D^n - P^n) \tilde{v}^n \Omega^{n+1} \\ - \Delta t A^n \tilde{v}^n + \theta \Delta t (\bar{D}^n - \bar{P}^n) \tilde{v}^n \end{aligned} \quad (12.84)$$

For a positivity-preserving scheme which ensures that the turbulent viscosity stays positive through out the simulation, the following modification is enforced in Eq.(12.84) following [Spalart and Allmaras, January 1992].

$$(\bar{D}^n - \bar{P}^n) = \int_{\Omega_x^e} \left[ \text{Pos}(D^n - P^n) + \text{Pos} \left( \frac{\partial D^n}{\partial \tilde{v}} - \frac{\partial P^n}{\partial \tilde{v}} \right) \tilde{v}^n \right] \quad (12.85)$$

where the operator  $\text{Pos}(\cdot)$  ( $\cdot$  being any scalar) is defined as

$$\text{Pos}(\cdot) = \max(\cdot, 0) \quad (12.86)$$

### *Positivity-Preserving Discretization*

For any transient scalar transport equation involving advection, diffusion, and source terms, Eqs.(12.84) and (12.85) can be generalized. Let  $\phi$  be any generic scalar for which a positivity-preserving scheme is desired. Then, the  $\theta$ -form of the discretized scalar master balance equation for  $\phi$  can be written in its general form as

$$\begin{aligned} \left[ M^{n+1} + \theta \Delta t K^{n+1} + \theta \Delta t (\bar{D}^n - \bar{P}^n) \right] \phi^{n+1} = \\ [M^n - (1 - \theta) \Delta t K^n] \phi^n - \Delta t \left[ \theta + (1 - \theta) \frac{\Omega^n}{\Omega^{n+1}} \right] (D^n - P^n) \phi^n \Omega^{n+1} \\ - \Delta t A^n \phi^n + \theta \Delta t (\bar{D}^n - \bar{P}^n) \phi^n \end{aligned} \quad (12.87)$$

together with

$$(\bar{D}^n - \bar{P}^n) = \int_{\Omega_x^e} \left[ \text{Pos}(D^n - P^n) + \text{Pos} \left( \frac{\partial D^n}{\partial \phi} - \frac{\partial P^n}{\partial \phi} \right) \phi^n \right] \quad (12.88)$$

Here, the forms of the source term operators  $D$  and  $P$  depend on the model transport equation governing the transport of  $\phi$ .

### RNG $k - \varepsilon$ Model

The mathematical structure for the RNG  $k - \varepsilon$  model involves two transport equations, but the general approach to the discretization in space-time is very similar to that used for Spalart-Allmaras model. Consequently, some steps involved in the ALE discretization procedure are omitted here since they have already been discussed in the earlier presentation of the ALE formulation for the Spalart-Allmaras model.

The scalar master balance equation (5.43) is used to write the two-equation  $k - \varepsilon$  model in a semi-discrete form

$$\begin{aligned} \frac{\partial}{\partial t} \int_{\Omega_{\mathbf{x}}} \rho k d\Omega_{\mathbf{x}} + \oint_{\Gamma_{\mathbf{x}}} \rho k (\mathbf{v} - \mathbf{v}_m) \cdot \mathbf{n} d\Gamma_{\mathbf{x}} &= \oint_{\Gamma_{\mathbf{x}}} \left( \mu + \frac{\mu_t}{\sigma_k} \right) \nabla k \cdot \mathbf{n} d\Gamma_{\mathbf{x}} \\ &+ \int_{\Omega_{\mathbf{x}}} \underbrace{2\mu_t S_{ij} S_{ij}}_{\text{Prod}(k)} d\Omega_{\mathbf{x}} - \int_{\Omega_{\mathbf{x}}} \underbrace{\rho \varepsilon}_{\text{Diss}(k)} d\Omega_{\mathbf{x}} \end{aligned} \quad (12.89)$$

$$\begin{aligned} \frac{\partial}{\partial t} \int_{\Omega_{\mathbf{x}}} \rho \varepsilon d\Omega_{\mathbf{x}} + \oint_{\Gamma_{\mathbf{x}}} \rho \varepsilon (\mathbf{v} - \mathbf{v}_m) \cdot \mathbf{n} d\Gamma_{\mathbf{x}} &= \oint_{\Gamma_{\mathbf{x}}} \left( \mu + \frac{\mu_t}{\sigma_\varepsilon} \right) \nabla \varepsilon \cdot \mathbf{n} d\Gamma_{\mathbf{x}} \\ &+ \int_{\Omega_{\mathbf{x}}} \underbrace{C_{\varepsilon 1} \frac{\varepsilon}{k} 2\mu_t S_{ij} S_{ij}}_{\text{Prod}(\varepsilon)} d\Omega_{\mathbf{x}} - \int_{\Omega_{\mathbf{x}}} \underbrace{C_{\varepsilon 2} \frac{\rho \varepsilon^2}{k}}_{\text{Diss}(\varepsilon)} d\Omega_{\mathbf{x}} \end{aligned} \quad (12.90)$$

where, the turbulent viscosity is defined as

$$\mu_t = C_\mu \rho \frac{k^2}{\varepsilon} \quad (12.91)$$

Here,  $C_{\varepsilon 1}$ ,  $C_{\varepsilon 2}$ ,  $C_\mu$ ,  $\sigma_k$ , and  $\sigma_\varepsilon$  are the RNG model coefficients given in Table 6.3 in §6.3.

In highly strained flows, the  $k - \varepsilon$  model is known to suffer from an over-production of the turbulent kinetic energy in stagnation flows. This mechanism is generally known as the “stagnation point anomaly”, however, it can also occur for flows with high local strain rates. In order to limit the turbulent intensity, we adopt the approach proposed by Durbin [Durbin, 2009]. Here, the time-scale limiter is based on the fact that the stress intensity ratio has been experimentally observed to be about 0.3 in shear layers and cannot exceed this amount. A detailed derivation of the time-scale limiter is provided in Durbin [Durbin, 2009].

The time-scale limiter is

$$T_{\text{Lim}} = \min \left[ \frac{k}{\varepsilon}, \frac{\alpha_{\text{lim}}}{C_\mu \sqrt{S_{ij} S_{ij}}} \right], \quad (12.92)$$

where  $T_{Lim}$  is the limited time-scale,  $\alpha_{lim}$  is a constant,  $\alpha_{lim} = 0.6/\sqrt{6}$  [Durbin, 2009]. This time-scale is further used to limit the eddy viscosity,  $\mu_t$ , by recasting it in terms of  $T_{Lim}$  as follows:

$$\begin{aligned}\mu_t &= \rho C_\mu T_{Lim} k \\ &= \rho C_\mu \min \left[ \frac{k}{\varepsilon}, \frac{\alpha_{lim}}{C_\mu \sqrt{S_{ij} S_{ij}}} \right] k.\end{aligned}\quad (12.93)$$

For implementing the positivity-preserving scheme, the production and dissipation terms for the  $k$ -equation are

$$\begin{aligned}\text{Prod}(k) &= 2\mu_t S_{ij} S_{ij}, \\ \text{Diss}(k) &= \rho \varepsilon.\end{aligned}\quad (12.94)$$

Alternatively, these terms may be written as

$$\begin{aligned}\text{Prod}(k) &= P(k)k, \\ \text{Diss}(k) &= D(k)k\end{aligned}\quad (12.95)$$

where

$$\begin{aligned}P(k) &= 2\mu_t S_{ij} S_{ij} \frac{1}{k}, \\ D(k) &= \frac{\rho \varepsilon}{k}.\end{aligned}\quad (12.96)$$

Similarly, for the  $\varepsilon$  equation, the production/dissipation terms are

$$\begin{aligned}\text{Prod}(\varepsilon) &= P(\varepsilon)\varepsilon, \\ \text{Diss}(\varepsilon) &= D(\varepsilon)\varepsilon\end{aligned}\quad (12.97)$$

where

$$\begin{aligned}P(\varepsilon) &= \frac{2\rho C_\mu k C_{\varepsilon_1} S_{ij} S_{ij}}{\varepsilon}, \\ D(\varepsilon) &= C_{\varepsilon_2} \frac{\rho k}{\varepsilon}.\end{aligned}\quad (12.98)$$

### Discretized Equations

Using Eqs.(12.87) and (12.88) as a template for the positivity-preserving discretization, the  $\theta$ -weighted discretized form of the RNG  $k - \varepsilon$  equations for the scalars  $k$  and  $\varepsilon$  are

$$\begin{aligned}[M^{n+1} - \Delta t \theta \{K^{n+1} - (\overline{D}^n(k) - \overline{P}^n(k))\}]k^{n+1} &= \\ [M^n - \Delta t \{A^n - (1 - \theta)K^n\}]k^n & \\ - \Delta t \left( \theta + \frac{\Omega^n}{\Omega^{n+1}} (1 - \theta) \right) (D^n(k) - P^n(k))k^n \Omega^{n+1} & \\ + \Delta t \theta (\overline{D}^n(k) - \overline{P}^n(k))k^n &\end{aligned}\quad (12.99)$$

$$\begin{aligned}
[M^{n+1} - \Delta t \theta \{K^{n+1} - (\bar{D}^n(\varepsilon) - \bar{P}^n(\varepsilon))\}] \varepsilon^{n+1} = \\
[M^n - \Delta t \{A^n - (1 - \theta)K^n\}] \varepsilon^n \\
- \Delta t \left( \theta + \frac{\Omega^n}{\Omega^{n+1}} (1 - \theta) \right) (D^n(\varepsilon) - P^n(\varepsilon)) \varepsilon^n \Omega^{n+1} \\
+ \Delta t \theta (\bar{D}^n(\varepsilon) - \bar{P}^n(\varepsilon)) \varepsilon^n
\end{aligned} \tag{12.100}$$

Here, the element-level operators are

$$M^{n+1} = \int_{\Omega_{\mathbf{X}}} \rho d\Omega_{\mathbf{X}}, \quad M^n = \int_{\Omega_{\mathbf{X}}} \rho d\Omega_{\mathbf{X}} \tag{12.101}$$

$$A^n(\rho, \cdot, \mathbf{v}_m) = \oint_{\Gamma_{\mathbf{X}}} \rho(\cdot) (\mathbf{v} - \mathbf{v}_m) \cdot \mathbf{n} d\Gamma_{\mathbf{X}} \tag{12.102}$$

$$K^n = \oint_{\Gamma_{\mathbf{X}}} \left( \mu + \frac{\mu_t}{\sigma_{k,\varepsilon}} \right) \Big|_{\Gamma_{\mathbf{X}}} \nabla_{\mathbf{X}}(\cdot) \cdot \mathbf{n} d\Gamma_{\mathbf{X}} \tag{12.103}$$

$$K^{n+1} = \oint_{\Gamma_{\mathbf{X}}} \left( \mu + \frac{\mu_t}{\sigma_{k,\varepsilon}} \right) \Big|_{\Gamma_{\mathbf{X}}} \nabla_{\mathbf{X}}(\cdot) \cdot \mathbf{n} d\Gamma_{\mathbf{X}} \tag{12.104}$$

where the superscript  $^e$  has been dropped to simplify the notation.

In Eq.(12.99)  $\bar{P}(k)$  and  $\bar{D}(k)$  are the Jacobians for Prod( $k$ ) and Diss( $k$ ) and are given by

$$\begin{aligned}
\bar{P}(k) &= \frac{\partial}{\partial k} (P(k)k) = P(k) + \frac{\partial P(k)}{\partial k} k, \\
\bar{D}(k) &= \frac{\partial}{\partial k} (D(k)k) = D(k) + \frac{\partial D(k)}{\partial k} k
\end{aligned} \tag{12.105}$$

For the second-order incremental projection algorithm, the turbulent eddy viscosity is frozen at  $t^n$ , so that

$$\begin{aligned}
\frac{\partial P(k)}{\partial k} &= -\frac{2\mu_t S_{ij} S_{ij}}{k^2}, \\
\frac{\partial D(k)}{\partial k} &= -\frac{\rho \varepsilon}{k^2}
\end{aligned} \tag{12.106}$$

Similarly, for the  $\varepsilon$  equation,

$$\begin{aligned}
\bar{P}(\varepsilon) &= \frac{\partial}{\partial \varepsilon} (P(\varepsilon)\varepsilon) = P(\varepsilon) + \frac{\partial P(\varepsilon)}{\partial \varepsilon} \varepsilon, \\
\bar{D}(\varepsilon) &= \frac{\partial}{\partial \varepsilon} (D(\varepsilon)\varepsilon) = D(\varepsilon) + \frac{\partial D(\varepsilon)}{\partial \varepsilon} \varepsilon
\end{aligned} \tag{12.107}$$

The derivatives of Prod( $\varepsilon$ ) and Diss( $\varepsilon$ ) become

$$\begin{aligned}
\frac{\partial P}{\partial \varepsilon} &= -C_{\varepsilon 1} \frac{2\rho C_{\mu} k}{\varepsilon^2} S_{ij} S_{ij} \\
\frac{\partial D}{\partial \varepsilon} &= \frac{\partial}{\partial \varepsilon} \left[ C_{\varepsilon 2}(\varepsilon) \frac{\rho \varepsilon}{k} \right]
\end{aligned} \tag{12.108}$$

Substituting Eqs.(6.32) and (6.33) for  $C_{\varepsilon 2}$ ,  $\frac{\partial D}{\partial \varepsilon}$  can be expanded as

$$\frac{\partial D}{\partial \varepsilon} = -\frac{\rho S_{\eta} k}{\varepsilon^2} \left[ -\frac{\tilde{C}_{\varepsilon 2} S_{\eta}}{\eta^2} + C_{\mu} S_{\eta} \eta \left\{ \frac{2 - 3\eta/\eta_0}{1 + \beta\eta^3} - \frac{3\beta\eta^3(1 - \eta/\eta_0)}{(1 + \beta\eta^3)^2} \right\} \right] \quad (12.109)$$

where,  $S_{\eta} = \sqrt{2 S_{ij} S_{ij}}$ .

### Positivity-Preserving Discretization

For the positivity-preserving algorithm, using Eq.(12.88), the source terms are implemented with both implicit (RHS) and explicit (LHS) contributions in Eqs.(12.99) and (12.100) as

$$\bar{D}^n(k) - \bar{P}^n(k) = \text{Pos}(D^n(k) - P^n(k)) + \text{Pos}\left\{ \frac{\partial D}{\partial k} - \frac{\partial P}{\partial k} \right\} \quad (12.110)$$

$$\bar{D}^n(\varepsilon) - \bar{P}^n(\varepsilon) = \text{Pos}(D^n(\varepsilon) - P^n(\varepsilon)) + \text{Pos}\left\{ \frac{\partial D}{\partial \varepsilon} - \frac{\partial P}{\partial \varepsilon} \right\} \quad (12.111)$$

The implementation of the  $k$ - $\varepsilon$  model is based on a two-layer formulation. For all interior elements, omitting any that are attached to no-slip/no-penetration walls, the source terms are implemented as follows.

#### **k – equation:**

1. Compute:  $\|S\|^2 = S_{ij} S_{ij}$
2. Compute:  $P = 2\mu_t \|S\|^2 / k$ ,
3. Compute:  $\frac{\partial P}{\partial k} = P' = -\frac{P}{k}$
4. Compute:  $D = \rho\varepsilon/k$
5. Compute:  $\frac{\partial D}{\partial k} = D' = -\frac{D}{k}$
6. Compute:  $\{D - P\} = D - P$
7. Compute:  $\{\bar{D} - \bar{P}\} = \text{Pos}(D - P) + \text{Pos}(D' - P')k$

The source terms for the  $\varepsilon$ -equation are implemented using the same positivity-preserving treatment as follows.

#### **$\varepsilon$ – equation:**

1. Compute:  $\|S\|^2 = S_{ij} S_{ij}$
2. Compute:  $S_{\eta} = \sqrt{2S_{ij} S_{ij}}$
3. Compute:  $\eta = S_{\eta} k / \varepsilon$

4. Compute:  $P = C_{\varepsilon 1} 2\mu_t \|S\|^2 / k$
5. Compute:  $\frac{\partial P}{\partial \varepsilon} = P' = 0$
6. Compute:  $\frac{\partial D}{\partial \varepsilon} = D' = \rho(C_{2\varepsilon} + C_{\mu}\eta^3(1 - \eta/\eta_0)/(1 + \beta\eta^3))k$
7. Compute:  $D = \frac{\partial D}{\partial \varepsilon} \varepsilon$
8. Compute:  $\{D - P\} = D - P$
9. Compute:  $\{\bar{D} - \bar{P}\} = \text{Pos}(D - P) + \text{Pos}(D' - P')\varepsilon$

### *y\**-Insensitive Wall Functions

The RNG  $k$ - $\varepsilon$  model is implemented using a two-layer approach with wall functions. Wall functions bridge the viscosity-dominated thin near-wall boundary layer region with that of the fully turbulent region. Wall function methods allow simulations using a moderate number of mesh cells making large industrial problems computationally tractable. However, it must be noted that grid-sensitivity is one of the most troublesome aspects of using wall functions (Albets-Chico et al. [Albets-Chico et al., 2008]) with turbulence models.

The basis for most wall-function models traces back to the modified law-of-the-wall approach used by Launder and Spalding [Launder and Spalding, 1974] (also, see the discussions Section 6.3). This type of wall modeling approach is designed for use with meshes where the first near-wall cell is placed in the logarithmic layer (inertial sublayer). From an industrial point of view, for complex geometries, ensuring that all the near wall cells are outside the viscous sublayer is problematic. Also, the precise location of the logarithmic region is solution dependent and may vary during the solution process. In order to accommodate a more flexible meshing technique/mesh, we follow a  $y^*$ -insensitive wall function (also called “scalable wall function”) approach as outlined in Grotjans et al. [Grotjans and Menter, 1998].

For the  $k$ - $\varepsilon$  model, we use a two-layer approach that is common in many industrial CFD codes. In this approach, the  $k$ -equation is solved in the entire flow domain, while the  $\varepsilon$  equation is solved only up to the wall-attached elements. In the wall region,  $\varepsilon$  is prescribed based on the near-wall flow behavior, i.e., using the law of the wall. This approach works very well with both the “scalable” and hybrid wall function modeling approach.

The scalable wall function approach is based on limiting the minimum value of the scaled wall coordinate (commonly denoted by  $y^+$ ,  $y^*$ ) such that the value of the velocity gradient at the first cell will be



the same as if it was on the edge of the viscous sublayer. This constrains the lowest grid point to lie above the physical wall. Thus, this approach neglects the true fluid dynamics within the viscous sublayer, but this is also the case for the standard wall function approach where the formulation breaks down for mesh points within the viscous sublayer.

To begin the discussion of the wall-function implementation, a representative near wall element is shown in Fig. 12.1 along with the various wall normal distances. The wall element centroid distance (denoted by  $y_p$  in Fig. 12.1) is scaled using

$$y_p^* = \frac{C_\mu^{1/4} \rho \sqrt{k} y_p}{\mu}, \quad (12.112)$$

where,  $k$  is the turbulent kinetic energy,  $\rho$  is the fluid density, and  $\mu$  is the molecular viscosity. The edge of the viscous sublayer is taken to be at a distance  $y_v$  from the wall (see Fig. 12.1) and the corresponding scaled viscous sublayer distance is given by

$$y_v^* = \frac{C_\mu^{1/4} \rho \sqrt{k} y_v}{\mu} = 11.225. \quad (12.113)$$

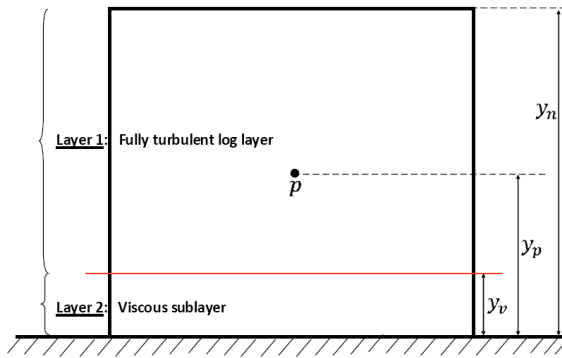


Figure 12.1: Schematic of the two-layer model of a near-wall element used in the wall treatment. Here,  $p$  is the centroid of the element, while  $y_v$  and  $y_p$  represent the normal distances of the viscous sublayer and the element centroid from the wall, respectively, and  $y_n$  refers to the maximum of the normal distances of all the vertices of the given wall element.

**Remark 8** In the Hydra implementation,  $y_v^*$  is referred by  $y_{p11}$ .

Following the procedure outlined in Craft et al. [Craft et al., 2002] and Albets-Chico et al. [Albets-Chico et al., 2008], a two-layer model as shown in Fig. 12.1 is used to evaluate an average production of  $k$  to be used in Eq.(12.89) for wall-attached elements.

The individual production rates of  $k$  in the log layer (Layer 1) and

viscous sublayer (Layer 2) are given by

$$\text{Prod}(k) = \begin{cases} 0 & \text{for } y_p^* < y_v^* \text{ (Layer 2)} \\ \frac{\tau_{wall}^2}{\kappa C_\mu^{1/4} \rho k^{3/2} y} & \text{for } y_p^* \geq y_v^* \text{ (Layer 1)} \end{cases} \quad (12.114)$$

where,

$$\tau_{wall} = \frac{\kappa C_\mu^{1/4} \rho V_p \sqrt{k}}{\ln(E y_p^*)}. \quad (12.115)$$

Here,  $\kappa = 0.41$  is the von Karman constant,  $E = 9.8$ , and  $V_p$  is the wall-tangent velocity evaluated at the wall-element centroid  $p$  which is evaluated as

$$V_p = \| \mathbf{v}_p \| \quad (12.116)$$

where

$$\mathbf{v}_p = (\mathbf{v} - \mathbf{v}_{wall}) - [(\mathbf{v} - \mathbf{v}_{wall}) \cdot \mathbf{n}] \mathbf{n} \quad (12.117)$$

and  $\mathbf{n}$  is the wall normal.

For the  $y^*$ -insensitive wall functions,  $y_p^*$  is replaced by applying the following limiter

$$y_{p_{lim}}^* = \max(y_p^*, y_v^*). \quad (12.118)$$

which ensures that  $y_p^*$  is always above or at the edge of the viscous sublayer. The value of  $y_p$  and  $y_n$  are then calculated from the modified  $y_{p_{lim}}^*$  using Eqs.(12.112) and (12.118) and is given by:

$$y_{p_{lim}} = \frac{y_{p_{lim}}^* \mu}{C_\mu^{1/4} \rho \sqrt{k}}. \quad (12.119)$$

**Remark 9** The definition of  $y^*$  in our formulation (Eqs.(12.112) and (12.113)) differs from Craft et al. [Craft et al., 2002] in that,

$$y_{Craft}^* = \frac{\sqrt{k} \rho y}{\mu}, \quad (12.120)$$

and hence does not explicitly include the factor  $C_\mu^{1/4}$  in their definition. Considering this,  $y_{v_{Craft}}^* = 20$  for their formulation.

Since  $\text{Prod}(k)$  is not a constant over the wall element but varies as given in (12.114), an average value of  $\text{Prod}(k)$  denoted by  $\text{Prod}(k)|_{Av}$  is used in the  $k$ -transport equation, Eq. (12.89). In our implementation, a depth-averaged integration (i.e. integration along the wall normal distance,  $y$ ) is performed to obtain  $\text{Prod}(k)|_{Av}$  with the averaging limits for  $y$  taken to be 0 and  $y_n$  (see, Fig. 12.1). Here,  $y_n$  is the maximum of the wall normal distances of all the vertices in a given wall element.

In the present formulation,  $y_n$  is approximated to be twice the value of  $y_p$  for all element types (strictly equal only for Cartesian grids):

$$y_n \approx 2y_p. \quad (12.121)$$

The two-layer averaged production is then given as,

$$\begin{aligned} \text{Prod}(k)|_{Av.} &= \frac{1}{y_n} \int_0^{y_n} \text{Prod}(k) dy \\ &= \underbrace{\frac{1}{y_n} \int_0^{y_v} \text{Prod}(k) dy}_{\text{Viscous sublayer}} + \underbrace{\frac{1}{y_n} \int_{y_v}^{y_n} \text{Prod}(k) dy}_{\text{Turbulent loglayer}} \end{aligned} \quad (12.122)$$

Using Eq.(12.114) in Eq.(12.122),  $\text{Prod}(k)|_{Av.}$  is simplified to

$$\text{Prod}(k)|_{Av.} = \frac{\tau_{wall}^2}{\kappa C_\mu^{1/4} \rho k^{1/2} y_n} \ln\left(\frac{y_n}{y_v}\right) \quad (12.123)$$

where  $\text{Prod}(k)|_{Av.}$  is used in place of  $\text{Prod}(k)$  in Eq.(12.89) for elements along no-slip/no-penetration boundaries.

Similar to  $\text{Prod}(k)|_{Av.}$ , an average dissipation rate of  $k$  denoted by  $\text{Diss}(k)|_{Av.}$  is evaluated using a two-layer variation of  $\varepsilon$  as prescribed in [Craft et al., 2002] and [Albets-Chico et al., 2008]. This average is then used in Eq.(12.90). The assumed variation is shown in Fig. 12.2 and is expressed as

$$\varepsilon = \begin{cases} \frac{2\nu k}{y_v^2} & \text{for } y_p^* \leq y_v^* \\ \frac{C_\mu^{3/4} k^{3/2}}{\kappa y} & \text{for } y_p^* > y_v^* \end{cases} \quad (12.124)$$

where  $\nu = \mu/\rho$ . This implies that

$$\text{Diss}(k) = \rho\varepsilon = \begin{cases} \frac{2\mu k}{y_v^2} & \text{for } y_p^* \leq y_v^* \\ \rho \frac{C_\mu^{3/4} k^{3/2}}{\kappa y} & \text{for } y_p^* > y_v^* \end{cases} \quad (12.125)$$

Similar to  $\text{Prod}(k)|_{Av.}$ ,  $\text{Diss}(k)|_{Av.}$  is obtained using a depth-averaged two-layer integration and is given by:

$$\begin{aligned} \text{Diss}(k)|_{Av.} &= \frac{1}{y_n} \int_0^{y_n} \text{Diss}(k) dy \\ &= \underbrace{\frac{1}{y_n} \int_0^{y_v} \text{Diss}(k) dy}_{\text{Viscous sublayer}} + \underbrace{\frac{1}{y_n} \int_{y_v}^{y_n} \text{Diss}(k) dy}_{\text{Turbulent log-layer}} \end{aligned} \quad (12.126)$$

Using Eq. (12.125) in Eq. (12.126), we then obtain

$$\text{Diss}(k)|_{Av.} = \frac{2\mu k}{y_n y_v} + \frac{\rho C_\mu^{3/4} k^{3/2}}{\kappa y_n} \ln\left(\frac{y_n}{y_v}\right). \quad (12.127)$$

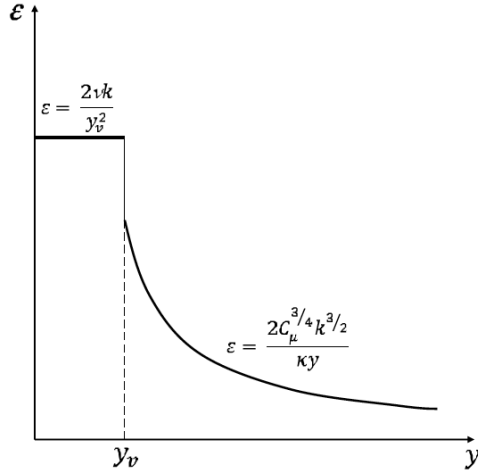


Figure 12.2: Schematic of the assumed two-layer variation of  $\varepsilon$  in the wall layer elements. See Fig. 12.1 for the definitions of the length scales.

### Positivity-Preserving Discretization

For the positivity-preserving discretization, the production and dissipation terms are written as

$$\begin{aligned} \text{Prod}(k)|_{Av} &= P(k)k, \\ \text{Diss}(k)|_{Av} &= D(k)k. \end{aligned} \quad (12.128)$$

Using Eqs.(12.123), (12.127), and (12.128), the following expressions are obtained for  $P(k)$  and  $D(k)$

$$P(k) = \frac{\tau_{wall}^2}{\kappa C_\mu^{1/4} \rho y_n} \ln\left(\frac{y_n}{y_v}\right) \frac{1}{k^{3/2}}. \quad (12.129)$$

$$D(k) = \frac{2\mu}{y_n y_v} + \frac{\rho C_\mu^{3/4}}{\kappa y_n} \ln\left(\frac{y_n}{y_v}\right) k^{1/2}. \quad (12.130)$$

The Jacobians for  $\text{Prod}(k)|_{Av}$  and  $\text{Diss}(k)|_{Av}$  are evaluated using the same procedure as given in Eq.(12.105). However,  $\tau_{wall}$  as given by Eq.(12.115) is held constant during the Jacobian evaluation. With this assumption and using Eqs.(12.129),(12.130), the following partial derivatives are obtained

$$\frac{\partial P(k)}{\partial k} = -\frac{3}{2} \frac{P(k)}{k}. \quad (12.131)$$

$$\frac{\partial D(k)}{\partial k} = \frac{1}{2} \frac{\rho C_\mu^{3/4}}{\kappa y_n} \ln\left(\frac{y_n}{y_v}\right) \frac{1}{k^{1/2}} \quad (12.132)$$

The following implementation is used for computing the implicit and explicit terms in Eqs.(12.99) and (12.100) for the wall-attached elements:

**k – equation:**

1. Compute:  $y_p = \| (\mathbf{r}_{\text{edge}} - \mathbf{r}_{\text{centroid}}) \cdot \mathbf{n} \|$
2. Compute:  $y_p^* = \frac{C_\mu^{1/4} \rho \sqrt{k} y_p}{\mu}$
3. Compute: Limited  $y_p^* = \max(y_p^*, y_{p11})$
4. Compute: Limited  $y_p = \frac{y_p^* \mu}{C_\mu^{1/4} \rho \sqrt{k}}$
5. Compute:  $y_n = 2y_p$
6. Compute:  $y_v = \frac{y_{p11} \mu}{C_\mu^{1/4} \rho \sqrt{k}}$
7. Compute:  $\mathbf{v}_p = (\mathbf{v} - \mathbf{v}_{\text{wall}}) - \left[ (\mathbf{v} - \mathbf{v}_{\text{wall}}) \cdot \mathbf{n} \right] \mathbf{n}$
8. Compute:  $V_p = \| \mathbf{v}_p \|$
9. Compute:  $\tau_{\text{wall}} = \frac{\kappa C_\mu^{1/4} \rho V_p \sqrt{k}}{\ln(E y_p^*)}$
10. Compute:  $P = \frac{\tau_{\text{wall}}^2 \ln(\frac{y_n}{y_v})}{\kappa C_\mu^{1/4} \rho y_n k^{3/2}}$
11. Compute:  $\frac{\partial P}{\partial k} = -\frac{3}{2} \frac{P}{k}$
12. Compute:  $D = \frac{2\mu}{y_n y_v} + \frac{\rho C_\mu^{3/4} \sqrt{k}}{\kappa y_n} \ln\left(\frac{y_n}{y_v}\right)$
13. Compute:  $\frac{\partial D}{\partial k} = \frac{C_\mu^{3/4} \rho \ln(\frac{y_n}{y_v})}{2\kappa y_n \sqrt{k}}$
14. Compute:  $\{D - P\} = D - P$
15. Compute:  $\bar{D} - \bar{P} = \text{Pos}(D - P) + \text{Pos}\left(\frac{\partial D}{\partial k} - \frac{\partial P}{\partial k}\right)k$

In the two-layer model, the  $\varepsilon$ -equation, Eq.(12.90), is not solved in the wall-attached elements. Instead,  $\varepsilon$  is prescribed at the centroid  $p$  of the wall element as using Eq.(12.124) (se also, see Fig. 12.2). Similar to the  $k$ -equation, the limited values of  $y_p^*$  and  $y_p$  are calculated from Eqs.(12.119) and (12.118). Then, the value of  $\varepsilon$  at the wall-element centroid is directly specified using

$$\varepsilon = \frac{C_\mu^{3/4} k^{3/2}}{\kappa y_p}. \quad (12.133)$$

$\varepsilon$  – equation:

1. Compute:  $y_p = \| (\mathbf{r}_{\text{edge}} - \mathbf{r}_{\text{centroid}}) \cdot \mathbf{n} \|$
2. Compute:  $y_p^* = \frac{C_\mu^{1/4} \rho \sqrt{k} y_p}{\mu}$
3. Compute: Limited  $y_p^* = \max(y_p^*, y_{p11})$
4. Compute: Limited  $y_p = \frac{y_p^* \mu}{C_\mu^{1/4} \rho \sqrt{k}}$
5. Compute:  $\varepsilon = \frac{C_\mu^{3/4} k^{3/2}}{\kappa y_p}$

Modification of the momentum equation for the wall elements:

Very large velocity gradients occur close to the wall in a turbulent boundary layer. With a wall-function-based model, the mesh needs to be relatively coarse (due to the imposed lower limit on  $y^*$  as explained earlier) that results in a significant error in the prediction of such gradients. Calculation of wall shear stress or the viscous flux of momentum based on the molecular viscosity  $\mu$  and the numerically estimated velocity gradient would thus be largely in error. Hence, proper modifications to the momentum equations need to be introduced to account for the poorly resolved wall friction. The necessary modifications can be either made through an added source term for the wall elements in the momentum equation or through a modified viscosity  $\mu_{\text{eff}}$  for the wall elements that corrects for the erroneous estimate of the velocity gradient [Bredberg, 2000]. The latter is implemented in our methodology and the modified viscosity for the wall elements is given by

$$\mu_{\text{eff}} = \begin{cases} \mu & \text{for } y_p^* \leq y_v^* \\ \frac{\rho C_\mu^{1/4} k^{1/2} \kappa y_p}{\ln(E y_p^*)} & \text{for } y_p^* > y_v^*. \end{cases} \quad (12.134)$$

Modification of the turbulent viscosity:

The turbulent viscosity, as mentioned earlier, is limited to avoid spurious overproduction of the turbulent kinetic energy. The turbulent viscosity is limited using the following equation

$$\mu_t = \rho C_\mu \min \left[ \frac{k}{\varepsilon}, \frac{\alpha_{lim}}{C_\mu \sqrt{S_{ij} S_{ij}}} \right] k. \quad (12.135)$$

*Note that the time-scale limiter is not used by default, and must be enabled through keyword input.*

Modification of the thermal conductivity:

For the turbulent model, the thermal conductivity,  $\kappa$ , for the wall elements is modified as follows:

$$\kappa_{\text{eff}} = \kappa + \frac{\mu_t C_p}{p_r} \quad (12.136)$$

The derivative of the thermal conductivity is given by

$$\frac{\partial \kappa_{\text{eff}}}{\partial T} = \frac{\partial \kappa(T^n)}{\partial T} + \frac{\mu_t}{p_r} \frac{\partial C_p(T^n)}{\partial T} \quad (12.137)$$

For the  $k$ - $\varepsilon$  model, the thermal conductivity  $\kappa$  for the wall elements is given by

$$\kappa_{\text{eff}} = \frac{\mu C_p y^*}{t^*} \quad (12.138)$$

The derivative is

$$\frac{\partial \kappa_{\text{eff}}}{\partial T} = \left( \mu \frac{\partial C_p(T^n)}{\partial T} + C_p \frac{\partial \mu(T^n)}{\partial T} \right) \frac{y^*}{t^*} + \mu C_p \frac{\partial (\frac{y^*}{t^*})}{\partial T} \quad (12.139)$$

where the last term is ignored in the current implementation.

### *Modeling Guidelines*

The main advantage of wall-functions is the relaxed requirement on mesh resolution at walls. However, the main disadvantage of these wall-functions is a strong dependence on the location of the mesh point closest to a wall where the wall-functions are applied. Wall functions based on the modified law-of-the-wall approach usually work the best for wall elements whose centers lie in the fully turbulent layer (inertial or log layer) which effectively imposes a lower limit on the value of  $y^*$ . Some of the recommendations for a proper model setup as outlined in Casey and Wintergerste [Casey and Wintergerste, 2000] are provided below.

1. The usual recommendation for the lower limit of  $y^*$  is typically between  $20 \leq y^* \leq 30$ .
2. For moderate Reynolds number flows, the boundary layer extends to  $300 \leq y^* \leq 500$ . Hence, a suggested upper limit for  $y^*$  is  $\approx 100$ .
3. A good resolution of the boundary layer is usually preferred for flows in which the boundary layer effects are important. This has to be done with the above imposed restrictions on choosing the values of  $y^*$ . Recommended boundary layer resolution requires at least 8–10 points in the region  $20 \leq y^* \leq 300$ .





## 13 *Fluid-Solid Interaction*

This chapter presents a survey of current literature on the algorithmic aspects of fluid-structure interaction (FSI), and the implementation currently available in the Hydra Toolkit for FSI.

### *FSI Literature Survey*

The global “elliptic” nature of the pressure in incompressible flows introduces additional difficulties for coupling algorithms that are realized as instabilities with exponential growth in the pressure. Unlike the staggered algorithms used for compressible FSI, incompressible FSI exhibits this behavior for near unity fluid-solid density ratios with flexible structures. The development of stable, staggered, time-accurate, incompressible FSI algorithms continues to be an active area of research today. Here, we briefly review some of the relevant work in this area.

The search for stable and accurate staggered fluid-structure interaction algorithms can be traced back to work on staggered methods in the late 1970’s and early 1980’s. Examples of this include the work by Park, et al. [Park et al., 1977], Hughes and Liu [Hughes and Liu, 1978a,b], Felippa and Park [Felippa and Park, 1980, Park, 1980, Park and Felippa, 1980]. The bulk of this work focused on various partitioning strategies that included implicit-explicit, explicit-implicit, and implicit-implicit time-integrators. Although not directly relevant, this work suggests the “partitioning-of-operators” strategy that has been used for FSI in the Hydra Toolkit.

### *Partitioned/Staggered Algorithms*

The work by Slone, et al. [Slone et al., 2002] coupled an unstructured-grid finite volume incompressible solver to a finite element structural code using the three-field formulation of Farhat, et al. [Farhat et al., 1998]. In effect, this work used an iterative, staggered approach, albeit implemented in a single code.

Gerbeau, et al. [Gerbeau et al., 2003], use a first-order approxi-

mation of the mesh velocity in an apparently single-step algorithm with a Jacobian-Free Newton-Krylov (JFNK) solution strategy for the structure. Here, a potential-flow problem is introduced with the JFNK iteration to achieve a more accurate estimate for the pressure. This approach neglects the velocity-pressure coupling in the fluid during the JFNK iteration

In 2005, Fernandez, et al. [Fernández et al., 2005] introduced a method based on a semi-implicit projection for the FSI coupling. A second-order extrapolation is used for the structural displacements, followed by advection-diffusion for the fluid velocity. The projection used to obtain a div-free velocity field is integrated with the structural solution. An iterative approach is used to achieve a stable algorithm, accurate interface pressures, and a final div-free velocity field.

### *Monolithic Algorithms*

The work by Noble, et al. [Noble et al., 2003] is one example of a fully-coupled, monolithic Galerkin FEM approach to fluid-structure interaction using level-sets to represent the structural interface. Although the authors claim success for this approach, they also note that the method performs best when the fluid and solid mesh size matches at the interface. When the mesh sizes are not matched, they cite severe ill-conditioning partly due to the use of Lagrange multipliers for the kinematic constraints.

Michler, et al. [Michler et al., 2004] compare partitioned and monolithic solution strategies for FSI and demonstrate the importance of predictors for both approaches. In the case of monolithic algorithms, the predictor helps to reduce the overall solution cost. For partitioned schemes, the predictors improve the stability and accuracy of the method. They demonstrate that second-order temporal accuracy can be achieved using partitioned schemes with predictors.

Ahn and Kallinderis [Ahn and Kallinderis, 2006] present a geometrically conservative finite-volume ALE method for general meshes. Here, they demonstrate that a predictor-corrector method exhibits superior stability and accuracy relative to segregated solution schemes.

The work by Hron and Turek [Hron and Turek, 2006] presents a monolithic FEM ALE formulation for fluid-structure interaction problems. The displacement, velocity and pressure degrees-of-freedom are solved using preconditioned Krylov methods in a monolithic system of equations. This effort provides a good baseline for comparison with prototypical benchmark FSI problems.

It is anticipated that the presence of flexible structural (shell) elements, sliding contact, and normal constraints in the structural models will produce linear systems that are extremely difficult to solve

with iterative solution techniques. For example, it is well known that commercial solid/structural codes such as Abaqus/Standard have difficulties using iterative solvers under these conditions. This suggests the possibility that fully-coupled monolithic solution schemes may not be tractable.

### *Load Transfers and Conservation*

Michler, et al. [Michler et al., 2003] investigate the impact of conservation at the fluid-structure interface on stability and accuracy. The results indicate that preserving conservation at the interface has a significant impact on stability and accuracy. Related to this work is the work by Farhat, et al. [Farhat et al., 1998] on load/motion transfer in aeroelastic applications.

In 2006, Jaiman, et al. [Jaiman et al., 2006] considered the conservative transfer of load information at fluid-solid interfaces with non-matching meshes. They considered the accuracy of point-to-element projections and common-refinement methods for a curved interface. They show that conservative transfers associated with common-refinement preserve the stability of the coupled FSI system while maintaining energy conservation. In contrast, the point-to-element methods exhibited spurious numerical oscillations that were related to the degree of grid mismatch at the interface, and increased with surface curvature.

### *Formulation Issues*

Hansbo [Hansbo, 2004] presents Nitsche's method as a generalized framework for treating coupled physics problems where an interface is involved. This approach does not rely on Lagrange multipliers to enforce interface constraints and permits generality in treating arbitrary meshes at the interface.

Causin, et al. [Causin et al., 2005] attempt to explain the influence of added-mass in the observed numerical instabilities associated with incompressible fluid-structure problems. They demonstrate that for an explicit partitioned algorithm, the method is unconditionally unstable when

$$\frac{\rho_s h_s}{\rho_f \mu_{max}} < 1 \quad (13.1)$$

where  $\rho_s$  is the solid density,  $h_s$  is the mesh size of the structure at the interface,  $\rho_f$  is the fluid density,  $\mu_{max}$  is the maximal eigenvalue for the added-mass operator. They also note that for problem parameters where the explicit algorithm is unstable, fully-coupled monolithic methods will require additional computational effort as well.

The work by Förster, Wall and Ramm also considers the instabilities due to added-mass effects in staggered solution methods. They

demonstrate the behavior of staggered and fully-coupled algorithms on a driven-cavity with a flexible bottom. They conclude that the destabilizing effects of the added-mass is a consequence of the segregated solution method, and increasing accuracy of the scheme won't necessarily cure the instability.

The use of Robin transmission conditions for segregated FSI problems is considered in a series of papers by Badia, et al. [Badia et al., 2008b,a, 2009]. The approach used here is applied in the context of hemodynamics with thin membranes for simplified blood-vessel models. Here, a fully-coupled system is apparently solved using a custom preconditioner based on the Robin-Robin boundary conditions.

Guidoboni [Guidoboni et al., 2009], Glowinski, Cavillini and Canic, claim the development of a stable, loosely-coupled FSI algorithm that requires no iterations between the fluid and structure. They use the added-mass to stabilize the algorithm with the kinematic conditions at the interface. The kinematically-coupled method uses a novel splitting approach that segregates the structure and fluid-loading from the fluid-only problem. They claim an energy-preserving scheme that provides a single-step algorithm.

The recent work by Burman and Fernández [Burman and Fernández, 2007, 2009] and Fernández, et al. [Fernández et al., 2005, 2006] use Nitsche's method as a framework for developing their solution strategies. We have borrowed directly from this work to develop the stabilized solution method used in the Hydra Toolkit for FSI.

As an aside, we note here that the work by Roe, et al. [Roe et al., 2007] considers the stability of fluid-thermal problems, i.e., conjugate heat-transfer.

### *Stablized FSI Formulation*

The momentum equation for the structure is given by

$$\rho_s \mathbf{a} = \nabla \cdot \boldsymbol{\sigma}_s + \mathbf{f}_s \quad \text{in } \Omega_s \quad (13.2)$$

where,  $\boldsymbol{\sigma}_s$  is the stress tensor corresponding to the displacement field  $\mathbf{u}$ ;  $\mathbf{v} = \dot{\mathbf{u}}$  (or  $v_i = \dot{u}_i$ ) and  $\mathbf{a} = \dot{\mathbf{v}}$  (or  $a_i = \dot{v}_i$ ) are the velocity and acceleration, respectively;  $\mathbf{f}_s$  is the body force and  $\rho_s$  is the density of the structure. The initial value problem consists of finding the displacement  $\mathbf{u}$  which satisfy Eq. (13.2) together with the initial conditions, natural boundary conditions and kinematic boundary conditions. The initial conditions are given by

$$u_i(\mathbf{x}, 0) = u_{i0}(\mathbf{x}) \quad \text{in } \Omega \quad (13.3)$$

$$v_i(\mathbf{x}, 0) = v_{i0}(\mathbf{x}) \quad \text{in } \Omega \quad (13.4)$$

the natural boundary conditions are given by

$$\sigma_{ij}n_j = \bar{t}_i \quad \text{on } \Gamma_t \quad (13.5)$$

and the kinematic boundary conditions can be specified in terms of displacement, velocity, or acceleration. Whichever quantity is given, the other two can be determined as

$$u_i = \bar{u}_i \quad \text{or} \quad v_i = \bar{v}_i \quad \text{or} \quad a_i = \bar{a}_i \quad \text{on } \Gamma_{ui} \quad (13.6)$$

where the superposed bar denotes prescribed boundary values;  $u_{i0}(\mathbf{x}, 0)$  and  $v_{i0}(\mathbf{x}, 0)$  are the initial displacement and velocity respectively;  $\mathbf{n}$  is the unit normal to the domain  $\Omega$ .

The momentum equation for the fluid is given by Eq.(1.5) which can be written as

$$\rho \frac{\partial \mathbf{v}_f}{\partial t} + (\mathbf{v}_f - \mathbf{v}_m) \cdot \nabla \mathbf{v}_f = \nabla \cdot \boldsymbol{\alpha}_f + \mathbf{f} \quad \text{in } \Omega_f \quad (13.7)$$

here,  $\boldsymbol{\alpha}_f$  is given by Eq.(3.5), and  $\mathbf{v}_m$  is the mesh velocity.

On the fluid-structure interface  $\Gamma_l$ , the following coupling conditions must be satisfied

$$\mathbf{u}_s = \mathbf{u}_f \quad \text{and} \quad \mathbf{v}_s = \mathbf{v}_f \quad \text{on } \Gamma_l \quad (13.8a)$$

$$\boldsymbol{\alpha}_s \cdot \mathbf{n} = \boldsymbol{\alpha}_f \cdot \mathbf{n} \quad \text{on } \Gamma_l \quad (13.8b)$$

where  $\mathbf{u}_s$  and  $\mathbf{u}_f$  are the displacements of fluid and structure, respectively.

The momentum equation for the structure is solved using the finite element method (FEM) with the choice of time integrator either explicit or implicit. The semi-discrete momentum equation for the structure is given by

$$\mathbf{M}_s \mathbf{a}_s^{n+1} + \mathbf{K}_s \mathbf{u}_s^{n+1} = \mathbf{f}_s^{n+1} + \mathbf{f}_l^{n+1} \quad \text{in } \Omega_f \quad (13.9)$$

where  $\mathbf{M}_s$  is the mass matrix,  $\mathbf{K}_s$  is the stiffness matrix,  $\mathbf{f}_s^{n+1}$  is the external force, and  $\mathbf{f}_l^{n+1}$  is the coupling force due to the interaction between fluid and structure. The superscript is used to denote the time, e.g.,  $\mathbf{u}_s^n = \mathbf{u}_s(n\Delta t)$ , and  $\Delta t$  is the time step.

The explicit or loosely coupled fluid-structure algorithm is currently implemented as follows

1. Given  $\mathbf{u}_f^n$ ,  $\mathbf{v}_f^n$ ,  $\mathbf{v}_m^n$ , and  $p^n$ , calculate the interface force  $\mathbf{f}_l^n$ , and send to solid/structural mechanics solver.
2. Given  $\mathbf{u}_s^n$ ,  $\mathbf{v}_s^n$ ,  $\mathbf{a}_s^n$ , and receive the interface force  $\mathbf{f}_l^n$ , solve Eq.(13.9) for  $\mathbf{u}_s^{n+1}$ ,  $\mathbf{v}_s^{n+1}$ , and  $\mathbf{a}_s^{n+1}$ , then send  $\mathbf{u}_s^{n+1}$  and  $\mathbf{v}_s^{n+1}$  to CFD.

3. CFD receives  $\mathbf{u}_s^{n+1}$  and  $\mathbf{v}_s^{n+1}$ , solve Eq.(12.56) for  $\mathbf{u}_f^{n+1}$  by enforcing the interface condition Eq.(13.8).
4. Solve Eq.(11.29) for  $\lambda$ .
5. Update the pressure by using Eq.(11.30).

The above algorithm is known in the literature as a conventional staggered algorithm [Burman and Fernández, 2009]. However, this algorithm for incompressible FSI exhibits the instability for near unity fluid-solid density ratio. In order to overcome this instability, the stabilization term  $\frac{a}{\theta\Delta t}$  is added in Eq.(11.29) as follows

$$\left(\mathbf{K}_p + \frac{a}{\theta\Delta t}\right)\lambda = D \quad (13.10)$$

where  $a$  is the penalty parameter and is given by  $a = \min(h/p, \text{diagArea})W\theta\Delta t$  and  $W$  is a parameter.

The stabilization term added in the PPE equation has the following form [Burman and Fernández, 2009]

$$\oint_{\Gamma} a(p^{n+1} - p^n)d\Gamma \quad (13.11)$$

where

$$a = \min(h/\rho, \text{diagArea})W \times \theta\Delta t \quad (13.12)$$

$$W = \text{penalty\_factor} \times A_{\text{edge}} \quad (13.13)$$

$$\text{penalty\_factor} = 4\beta S \quad (13.14)$$

$S$  is a user defined scale factor with default value of 1.

$$\beta = \begin{cases} 1, & \text{if velocity in edge normal direction} > 0 \\ 0, & \text{otherwise} \end{cases} \quad (13.15)$$

$A_{\text{edge}}$ =area of edge (facet).

$$h = \frac{1}{V_{\min}^{1/3}} \quad (13.16)$$

$V_{\min}$  = minimum of element volume.

$$\text{diagArea} = \frac{\text{diagMin}}{\text{areaMax}}$$

$\text{diagMin}$  = minimum value of the diagonal term in PPE matrix

areaMax = maximum of A\_edge

$\rho$  is the fluid density.

The role of the stabilization term is to provide a slight damping at the fluid-solid interface that effectively slows the rate of change of the pressure over a time-step. The damping introduced is localized at the fluid-solid interface and vanishes in the limit at  $h \rightarrow 0$ .





## **Part III**

# **Appendix A**



## 14 Vector Notation

The dot product of two vectors,  $\mathbf{a} = \{a_x, a_y, a_z\}^T$  and  $\mathbf{b} = \{b_x, b_y, b_z\}^T$  defined in  $\mathbb{R}^3$ , is defined as

$$\mathbf{a} \cdot \mathbf{b} = a_x b_x + a_y b_y + a_z b_z \quad (14.1)$$

The dyadic product [Chadwick, 1976] between two vectors<sup>1</sup> in  $\mathbb{R}^3$  is denoted as

$$\mathbf{ab} = \mathbf{a} \otimes \mathbf{b} = \begin{bmatrix} a_x b_x & a_x b_y & a_x b_z \\ a_y b_x & a_y b_y & a_y b_z \\ a_z b_x & a_z b_y & a_z b_z \end{bmatrix} \quad (14.2)$$

<sup>1</sup> In general the vectors must have the same dimensions.

Spatial derivatives are represented in vector notation using the  $\nabla$ , which is defined as

$$\nabla = \left\{ \frac{\partial}{\partial x}, \frac{\partial}{\partial y}, \frac{\partial}{\partial z} \right\}^T \quad (14.3)$$

thus, the gradient of an arbitrary scalar  $\phi$  can be written as

$$\nabla \phi = \left\{ \frac{\partial \phi}{\partial x}, \frac{\partial \phi}{\partial y}, \frac{\partial \phi}{\partial z} \right\}^T \quad (14.4)$$

The additional relations relevant to the ensuing discussion are

$$\nabla \cdot \nabla \phi = \nabla^2 \phi = \Delta \phi = \frac{\partial^2 \phi}{\partial x^2} + \frac{\partial^2 \phi}{\partial y^2} + \frac{\partial^2 \phi}{\partial z^2} \quad (14.5)$$

$$\mathbf{a} \cdot \nabla \phi = a_x \frac{\partial \phi}{\partial x} + a_y \frac{\partial \phi}{\partial y} + a_z \frac{\partial \phi}{\partial z} \quad (14.6)$$

$$\nabla \cdot \mathbf{a} = \frac{\partial a_x}{\partial x} + \frac{\partial a_y}{\partial y} + \frac{\partial a_z}{\partial z} \quad (14.7)$$

$$\nabla \mathbf{a} = \begin{bmatrix} \frac{\partial a_x}{\partial x} & \frac{\partial a_x}{\partial y} & \frac{\partial a_x}{\partial z} \\ \frac{\partial a_y}{\partial x} & \frac{\partial a_y}{\partial y} & \frac{\partial a_y}{\partial z} \\ \frac{\partial a_z}{\partial x} & \frac{\partial a_z}{\partial y} & \frac{\partial a_z}{\partial z} \end{bmatrix} \quad (14.8)$$

$$\nabla \mathbf{a}^T = \begin{bmatrix} \frac{\partial a_x}{\partial x} & \frac{\partial a_y}{\partial x} & \frac{\partial a_z}{\partial x} \\ \frac{\partial a_x}{\partial y} & \frac{\partial a_y}{\partial y} & \frac{\partial a_z}{\partial y} \\ \frac{\partial a_x}{\partial z} & \frac{\partial a_y}{\partial z} & \frac{\partial a_z}{\partial z} \end{bmatrix} \quad (14.9)$$

$$\mathbf{a} \cdot \nabla \mathbf{b} = \begin{Bmatrix} a_x \cdot \nabla b_x \\ a_y \cdot \nabla b_y \\ a_z \cdot \nabla b_z \end{Bmatrix} = \begin{Bmatrix} a_x \frac{\partial b_x}{\partial x} + a_y \frac{\partial b_x}{\partial y} + a_z \frac{\partial b_x}{\partial z} \\ a_x \frac{\partial b_y}{\partial x} + a_y \frac{\partial b_y}{\partial y} + a_z \frac{\partial b_y}{\partial z} \\ a_x \frac{\partial b_z}{\partial x} + a_y \frac{\partial b_z}{\partial y} + a_z \frac{\partial b_z}{\partial z} \end{Bmatrix} \quad (14.10)$$

$$\nabla \cdot (\mathbf{a}\mathbf{b}) = \nabla \cdot (\mathbf{a} \otimes \mathbf{b}) = \begin{Bmatrix} \frac{\partial}{\partial x}(a_x b_x) + \frac{\partial}{\partial y}(a_x b_y) + \frac{\partial}{\partial z}(a_x b_z) \\ \frac{\partial}{\partial x}(a_y b_x) + \frac{\partial}{\partial y}(a_y b_y) + \frac{\partial}{\partial z}(a_y b_z) \\ \frac{\partial}{\partial x}(a_z b_x) + \frac{\partial}{\partial y}(a_z b_y) + \frac{\partial}{\partial z}(a_z b_z) \end{Bmatrix} \quad (14.11)$$

## 15 Low Reynolds Number Functions used in the $k - \varepsilon$ Model

In general, the  $k - \varepsilon$  model performs poorly on wall-bounded flows, where the model equation for  $\varepsilon$  cannot be integrated all the way to the wall due to the singularities that develop in the  $\varepsilon$  equation. These singularities are related to low-Re number effects. For the simplest wall-bounded cases (channel flows and boundary layers with zero pressure gradients) corrections to the original model have been presented that improve the accuracy of the predictions. These low-Re corrections usually consist of damping functions that bound the source terms in the  $\varepsilon$  equation and reduce the amount of turbulence viscosity in the near wall region, enhancing the accuracy of the model in wall-bounded flows.

$$\begin{aligned} \frac{\partial \tilde{\rho} \tilde{\varepsilon}}{\partial t} + \frac{\partial}{\partial x_j} (\tilde{\rho} \tilde{u}_j \tilde{\varepsilon}) &= \frac{\partial}{\partial x_j} \left( \tilde{\rho} (\bar{v} + \nu_t / \sigma_\varepsilon) \frac{\partial \tilde{\varepsilon}}{\partial x_j} \right) - c_{\varepsilon 1} f_1 \frac{\tilde{\varepsilon}}{k} \bar{\tau} (u_i, u_j) \frac{\partial \tilde{u}_i}{\partial x_j} \\ &\quad - c_{\varepsilon 2} \tilde{\rho} f_2 \frac{\tilde{\varepsilon}^2}{k} - \frac{2}{3} (2 - c_{\varepsilon 1}) \tilde{\rho} \tilde{\varepsilon} \frac{\partial \tilde{u}_j}{\partial x_j} + \tilde{\rho} E \end{aligned} \quad (15.1)$$

$$\varepsilon = \varepsilon_{\Gamma_{D_{\text{wall}}}} + \tilde{\varepsilon} \quad (15.2)$$

The turbulent viscosity is controlled using damping functions

$$\nu_t = c_\mu f_\mu \frac{k^2}{\tilde{\varepsilon}} \quad (15.3)$$

In general the wall-functions depend on the following parameters

$$Re_T = \frac{k^2}{\tilde{\varepsilon} \nu}, \quad R_y = \frac{k^{1/2} y}{\nu}, \quad y^+ = \frac{u_\tau y}{\nu} \quad (15.4)$$

However the selection of the previous parameters is absolutely empirical, therefore the selection of the wall-function is purely determined by their performance predicting turbulent flows.

Different low-Re corrections have been proposed to handle the wall-boundary conditions, here some of the most relevant are summarized [Wilcox, 1998].

- Jones-Launder Model [Launder and Spalding, 1974]:

$$f_\mu = e^{-2.5/(1+Re_T/50)} \quad (15.5a)$$

$$f_1 = 1 \quad (15.5b)$$

$$f_2 = 1 - 0.3e^{-Re_T^2} \quad (15.5c)$$

$$\varepsilon_{\Gamma_{Dwall}} = 2\nu \left( \frac{\partial \sqrt{k}}{\partial y} \right)^2 \quad (15.5d)$$

$$E = -2\nu\nu_T \left( \frac{\partial^2 U}{\partial y^2} \right)^2 \quad (15.5e)$$

$$c_{\varepsilon 1} = 1.44, \quad c_{\varepsilon 2} = 1.92, \quad c_\mu = 0.09, \quad \sigma_k = 1.0, \quad \sigma_\varepsilon = 1.3 \quad (15.6)$$

Note, the coefficients reported for the high Re version of  $k - \varepsilon$  in the original reference [Jones and Launder, 1972] depart slightly from the standard coefficients. However, the differences observed between these two sets of coefficients is negligible, because the effect of the different coefficients is on the production and dissipation of  $\varepsilon$ , which in the end cancels out, see Launder and Spalding [Launder and Spalding, 1974].

- Launder-Sharma Model [Launder and Sharma, 1974]

$$f_\mu = e^{-3.4/(1+Re_T/50)^2} \quad (15.7a)$$

$$f_1 = 1 \quad (15.7b)$$

$$f_2 = 1 - 0.3e^{-Re_T^2} \quad (15.7c)$$

$$\varepsilon_{\Gamma_{Dwall}} = 2\nu \left( \frac{\partial \sqrt{k}}{\partial y} \right)^2 \quad (15.7d)$$

$$E = 2\nu\nu_T \left( \frac{\partial^2 U}{\partial y^2} \right)^2 \quad (15.7e)$$

$$c_{\varepsilon 1} = 1.44, \quad c_{\varepsilon 2} = 1.92, \quad c_\mu = 0.09, \quad \sigma_k = 1.0, \quad \sigma_\varepsilon = 1.3 \quad (15.8)$$

- Lam-Bremhorst Model [Lam and Bremhorst, 1981]

$$f_\mu = (1 - e^{-0.0165Re_T})^2 (1 + 20.5/Re_T) \quad (15.9a)$$

$$f_1 = 1 + (0.05/f_\mu)^3 \quad (15.9b)$$

$$f_2 = 1 - e^{-Re_T^2} \quad (15.9c)$$

$$\varepsilon_{\Gamma_{Dwall}} = 0 \quad (15.9d)$$

$$E = 0 \quad (15.9e)$$

$$c_{\varepsilon 1} = 1.44, \quad c_{\varepsilon 2} = 1.92, \quad c_{\mu} = 0.09, \quad \sigma_k = 1.0, \quad \sigma_{\varepsilon} = 1.3 \quad (15.10)$$

- Chien Model [Chien, 1982]

$$f_{\mu} = 1 - e^{-0.0115y^+} \quad (15.11a)$$

$$f_1 = 1 \quad (15.11b)$$

$$f_2 = 1 - 0.22e^{-(Re_T/6)^2} \quad (15.11c)$$

$$\varepsilon_{\Gamma_{Dwall}} = 2\nu \frac{k}{y^2} \quad (15.11d)$$

$$E = -2\nu \frac{\tilde{\varepsilon}}{y^2} e^{-y^+/2} \quad (15.11e)$$

$$c_{\varepsilon 1} = 1.35, \quad c_{\varepsilon 2} = 1.80, \quad c_{\mu} = 0.09, \quad \sigma_k = 1.0, \quad \sigma_{\varepsilon} = 1.3 \quad (15.12)$$

For the Jones-Launder, Launder-Sharma and Chien models the wall-function reproduces the correct asymptotic behavior for  $\varepsilon$  in the most simple wall-bounded flows. Therefore, the following conditions at the wall can be specified for these models:

$$k_{\Gamma_{Dwall}} = 0 \quad \text{and} \quad \varepsilon_{\Gamma_{Dwall}} = 0 \quad (15.13)$$

For the Lam-Bremhorst model the boundary conditions are applied directly on  $\varepsilon$ .

$$\varepsilon_{\Gamma_{Dwall}} = \nu \frac{\partial^2 k}{\partial y^2} \quad \text{or} \quad \varepsilon_{\Gamma_{Nwall}} = \frac{\partial \varepsilon}{\partial x_j} \hat{n}_j = 0 \quad (15.14)$$

We note here that the original paper of Jones and Launder [Jones and Launder, 1972] suggested the use of  $\varepsilon = 0$  at the wall. For free-stream boundary conditions the following relations are usually implemented

$$k_{\Gamma_{Din}} = \frac{3}{2} \left[ U_{\infty} \left( \frac{u'}{U_{\infty}} \right) \right]^2 \quad (15.15a)$$

$$\varepsilon_{\Gamma_{Din}} = c_{\mu}^{3/4} \frac{k^{3/2}}{l} \quad (15.15b)$$

$$\varepsilon_{\Gamma_{Din}} = c_{\mu} \rho \frac{k_{\infty}^2}{\mu} \left( \frac{\mu_T}{\mu} \right) \quad (15.15c)$$

Here,  $u'$  is the intensity of the velocity fluctuations,  $l$  is the turbulent integral scale and  $\mu_T$  is the turbulent viscosity.

The turbulent transport terms require gradients of the flow and turbulent variables, the flow and turbulent variables and, the distance from the wall.





## 16 Bibliography

- Jayantha Pasdunkorale A. and Ian W. Turner. A second-order control-volume finite-element least-squares strategy for simulating diffusion in strongly anisotropic media. *Journal of Computational Mathematics*, 23:1–16, 2005.
- Hyung Taek Ahn and Yannis Kallinderis. Strongly coupled flow/structure interaction with a geometrically conservative ALE scheme on general hybrid meshes. *Journal of Computational Physics*, 219:671–696, 2006.
- B. Alazmi and K. Vafai. Analysis of fluid flow and heat transfer interfacial conditions between a porous medium and a fluid layer. *Int. J. Heat Mass Transf.*, 44(9):1735–1749, 2001.
- X. Albets-Chico, C.D. Perez-Segarra, A. Oliva, and J. Bredberg. Analysis of wall-function approaches using two-equation turbulence models. *International Journal of Heat and Mass Transfer*, 51(19-20):4940–4957, 2008.
- A. S. Almgren, J. B. Bell, P. Colella, L. H. Howell, and M. L. Welcome. A conservative adaptive projection method for the variable density incompressible navier-stokes equal-order. *Journal of Computational Mechanics*, 142:1–46, 1998.
- Ann S. Almgren, John B. Bell, Phillip Colella, and Louis H Howell. An adaptive projection method for the incompressible euler equations. In *Eleventh AIAA Computational Fluid Dynamics Conference*, pages 530–539. AIAA, 1993.
- Ann S. Almgren, John B. Bell, and William G. Szymczyk. A numerical method for the incompressible navier-stokes equations based on an approximate projection. *SIAM Journal for Scientific Computing*, 17(2): 358–369, March 1996.
- Ann S. Almgren, John B. Bell, and William Y. Crutchfield. Approximate projection methods: Part i. inviscid analysis. *SIAM Journal on Scientific Computing*, 22(4):1139–1159, 2000.

- W. Kyle Anderson and Daryl L. Bonhaus. An implicit upwind algorithm for computing turbulent flows on unstructured grids. *Computers and Fluids*, 23(1):1–21, 1994.
- Nikolai Andrianov. *Analytical and numerical investigation of two-phase flows*. PhD thesis, University Magdeburg, 2003.
- T.R. Auton, J.C.R. Hunt, and M. Prud’Homme. The force exerted on a body in inviscid unsteady non-uniform rotational flow. *Journal of Fluid Mechanics*, 197:241–257, 12 1988. ISSN 1469-7645. DOI: 10.1017/S0022112088003246. URL [http://journals.cambridge.org/article\\_S0022112088003246](http://journals.cambridge.org/article_S0022112088003246).
- AVL Swift version 3.3. AVL, 2004.
- S. Badia, A. Quaini, and A. Quarteroni. Splitting methods based on algebraic factorization for fluid-structure interaction. *SIAM Journal on Scientific Computing*, 30:1778–1805, 2008a.
- Santiago Badia, Fabio Nobile, and Christian Vergara. Fluid-structure partitioned procedures based on robin transmission conditions. *Journal of Computational Physics*, 227:7027–7051, 2008b.
- Santiago Badia, Fabio NObile, and Christian Vergara. Robin-Robin preconditioned Krylov methods for fluid-structure interaction problems. *Computer Methods in Applied Mechanics and Engineering*, 198: 2768–2784, 2009.
- J. S. Baggett. On the feasibility of merging LES with RANS for the near wall region of attached turbulent flows. In *Annual Research Briefs*, pages 267–277. Center for Turbulence Research, 1998.
- S. Balachandar and A. Properetti. Report on a symposium on "computational approaches to disperse multiphase flow". *International Journal of Multiphase Flow*, 21:1337–1341, 2005.
- Antonio M. Baptista, E. Eric Adams, and Philip Gresho. Benchmarks for the transport equation: the convection-diffusion equation and beyond. *Quantitative Skill Assessment for Coastal Ocean Models*, 47: 241–268, 1995.
- Timothy Barth. Numerical methods for conservation laws on structured and unstructured meshes, vki march 2003 lecture series.
- Timothy Barth and Mario Ohlberger. *Encyclopedia of Computational Mechanics*, chapter Finite Volume Methods: Foundation and Analysis, page Chapter 15. John Wiley & Sons, 2004.

- Timothy J. Barth. Recent developments in high order k-exact reconstruction on unstructured meshes. In *AIAA-93-0668*, Reno, Nevada, January 1993. AIAA 31st Aerospace Sciences Meeting & Exhibit.
- Timothy J. Barth and Paul O. Frederickson. Higher order solution of the Euler equations on unstructured grids using quadratic reconstruction. In *AISS-90-0013*, Reno, Nevada, January 1990. AIAA 28th Aerospace Sciences Meeting.
- Timothy J. Barth and Dennis C. Jespersen. The design and application of upwind schemes on unstructured meshes. In *AIAA-89-0366*, Reno, Nevada, January 1989. AIAA 27th Aerospace Sciences Meeting.
- G. K. Batchelor. *The Theory of Homogeneous Turbulence*. Cambridge University Press, 1953.
- G. K. Batchelor. *An Introduction to Fluid Dynamics*. Cambridge University Press, 1967.
- P. Batten, U. Goldberg, and S. Chakravarthy. Interfacing statistical turbulence closures with large-eddy simulation. *AIAA J.*, 42(3):485–492, 2004.
- R. A. Baurle, C. J. Tam, J. R. Edwards, and H. A. Hassan. Hybrid simulation approach for cavity flows: Blending, algorithm, and boundary treatment issues. *AIAA J.*, 41(8):1463–1480, 2003.
- M. Behnia and S. Parneix. Prediction of heat transfer in an axisymmetric turbulent jet impinging on a flat plate. *Int. J. Heat Mass Transf.*, 41(12):1845–1855, 1998.
- M. Behnia, S. Parneix, Y. Shabany, and P. A. Durbin. Numerical study of turbulent heat transfer in confined and unconfined impinging jets. *Int. J. Heat Fluid Flow*, 20:1–9, 1999.
- J. B. Bell and D. L. Marcus. A second-order projection for variable density flows. *Journal of Computational Physics*, 101:334–348, 2002.
- John B. Bell, Philip Colella, and Harland M. Glaz. A second-order projection method for the incompressible navier-stokes equations. *Journal of Computational Physics*, 85:257–283, 1989.
- R. A. Berry. Some specific casl requirements for advanced multiphase flow simulation of light water reactors. Technical report, Idaho National Laboratory, 2010.
- D. C. Besnard and F. H. Harlow. Turbulence in multiphase flow". *International Journal of Multiphase Flow*, 6:679–699, 1988.

- D. Bestion. The physical closure laws in the CATHARE code. *Nuclear Engineering and Design*, 124:229–245, 1990.
- D> Bestion, H. Anglart, D. Caraghiaur, P. Péturaud, B. Smith, M. Andreani, B. Niceno, E. Krepper, D. Lucas, F. Moretti, M. C. Galassi, J. Macek, L. Vyskocil, B. Koncar, and G. Hazi. Review of available data for validation of Nuresim two-phase CFD software applied to CHF investigations. *Science and Technology of Nuclear Installations*, pages 1–14, 2009.
- L. Betchen, A. G. Straatman, and B. E. Thompson. A nonequilibrium finite-volume model for conjugate fluid/porous/solid domains. *Numerical Heat Transfer, Part A: Applications*, 49(6):543–565, 2006.
- Lee J. Betchen and Anthony G. Straatman. An accurate gradient and hessian reconstruction method for cell-centered finite volume discretizations on general unstructured grids. *International Journal for Numerical Methods in Fluids*, 62:945–962, 2010.
- G. Bozzano and M. Dente. Shape and terminal velocity of single bubble motion: a novel approach. *Computers and Chemical Engineering*, 25(4–6):571–576, 2001. ISSN 0098-1354. DOI: [http://dx.doi.org/10.1016/S0098-1354\(01\)00636-6](http://dx.doi.org/10.1016/S0098-1354(01)00636-6). URL <http://www.sciencedirect.com/science/article/pii/S0098135401006366>.
- J. Bredberg. On the Wall Boundary Condition for Turbulence Models. Technical Report 00/4, Chalmers University of Technology, 2000.
- H. C. Brinkman. A calculation of the viscous force exerted by a flowing fluid on a dense swarm of particles. *Applied Scientific Research*, 1(1): 27–34, 1949.
- David L. Brown and Michael L. Minion. Performance of under-resolved two-dimensional incompressible flow simulations. *Journal of Computational Physics*, 122:165–183, 1995.
- Erik Burman and Miguel A. Fernández. Stabilized explicit coupling for fluid-structure interaction using nitsche’s method. *C. R. Acad. Sci. Paris, Ser. I*, 345:467–472, 2007.
- Erik Burman and Miguel A. Fernández. Stabilization of explicit coupling in fluid-structure interaction involving fluid incompressibility. *Computer Methods in Applied Mechanics and Engineering*, 198:766–784, 2009.
- W. A. Wall C. Forster and E. Ramm. Artificial added mass instabilities in sequential staggered coupling of nonlinear structures and incompressible viscous flow. *Computer Methods in Applied Mechanics and Engineering*, 196:1278–1293, 2007.

- C. Calgari, E. Creusé, and T. Gordon. An hybrid finite volume-finite element method for variable density incompressible flows. *Journal of Computational Physics*, 227:4671–4696, 2008.
- M. Casey and T. Wintergerste. *ERCOTAC Special Interest Group on "Quality and Trust in Industrial CFD"*. European Research Community on Flow, Turbulence and Combustion (ERCOTAC), 2000.
- P. Causin, J. F. Gerbeau, and F. Nobile. Added-mass effect in the design of partitioned algorithms for fluid-structure problems. *Computer Methods in Applied Mechanics and Engineering*, 194:4506–4527, 2005.
- G. Černe, S. Petelin, and I. Tiselj. Coupling of the interface tracking and the two-fluid models for the simulation of incompressible two-phase flow. *Journal of Computational Physics*, 171:776–804, 2001.
- P. Chadwick. *Continuum Mechanics*. Dover, 1976.
- C.-H. Chang and M.-S. Liou. A robust and accurate approach to computing compressible multiphase flow: Stratified flow model and AUSM<sup>+</sup>-up scheme. *Journal of Computational Physics*, 225:840–873, 2007.
- Lina Chang and Guanwei Yuan. Cell-centered finite volume methods with flexible stencils for diffusion equations on general nonconforming meshes. *Computer Methods in Applied Mechanics and Engineering*, 198:1638–1646, 2009.
- S. Chapman and T. G. Cowling. *The Mathematical Theory of Non-Uniform Gases*. Cambridge University Press., 1952.
- P. Chassaing. *Variable density fluid turbulence*. Fluid mechanics and its applications. Kluwer Academic Publishers, 2002. ISBN 9781402006715. URL <http://books.google.com/books?id=mwTq3yDRp9IC>.
- X. Chen, P. Yu, S. H. Winoto, and H. T. Low. A numerical method for forced convection in porous and homogeneous fluid domains coupled at interface by stress jump. *Int. J. Numer. Methods Fluids*, 56(9):1705–1729, 2008.
- S. K. M. Chenoweth, J. Soria, and A. Ooi. A singularity-avoiding moving least squares scheme for two dimensional unstructured meshes. In *16th Australasian Fluid Mechanics Conference*, 2007.
- K-Y Chien. Predictions of channel and boundary-layer flows with a low-reynolds-number turbulence model. *AIAA J.*, 20(1):33–38, 1982.

- Alexandre Joel Chorin. Numerical solution of the Navier-Stokes equations. *Mathematics of Computations*, 22:745–762, 1968.
- M. A. Christon. QACINA V<sub>3</sub> a multiphysics toolkit for 2D/3D unstructured grid simulation. Technical Report in preparation, Los Alamos National Laboratories, 2007.
- M. A. Christon and R. S. Patil. A finite element projection method for low-Mach number reacting flows. In K. J. Bathe, editor, *Third MIT Conference on Computational Fluid and Solid Mechanics*, pages 617–622, New York, June 2005. Elsevier.
- M. A. Christon, D. I. Ketcheson, and A. C. Robinson. An assessment of semi-discrete central schemes for hyperbolic conservation laws. SAND2003-3238, Sandia National Laboratories, Albuquerque, New Mexico, May 2003.
- M. A. Christon, M. J. Martinez, and T. E. Voth. Generalized Fourier analysis of the advection-diffusion equation – part I: One-dimensional domains. *International Journal for Numerical Methods in Fluids*, 45:839–887, 2004.
- Mark A. Christon and Thomas E. Spelce. Visualization of high resolution three-dimensional nonlinear finite element analyses. In *Visualization '92*, pages 324–331, Boston, MA, 1992. IEEE. (LLNL UCRL-JC-110110).
- T.J. Craft, A.V. Gerasimov, H. Iacovides, and B.E. Launder. Progress in the generalization of wall-function treatments. *International Journal of Heat and Fluid Flow*, 23(2):148–160, 2002.
- R. Danchin. Density-dependent incompressible viscous fluids in critical spaces. *Proceedings of the Royal Society of Edinburgh*, 133A:1311–1334, 2003.
- L. Davidson and M. Billson. Hybrid LES-RANS using synthesized turbulent fluctuations for forcing in the interface region. *Int. J. Heat Fluid Flow*, 27:1028–1042, 2006.
- L. Davidson and S. Dahlström. Hybrid LES-RANS: an approach to make LES applicable at high Reynolds number. *Int. J. Comput. Fluid Dyn.*, 19(6):415–427, 2005.
- N. Deck, P. Duveau, P. dEspiney, and P. Guillen. Development and application of spalart-allmaras one equation turbulence model to three-dimensional supersonic complex configurations. *Aerosp. Sci. Technol.*, 6:171–183, 2002.

- C. Delanghe, B. Merci, and E. Dick. Hybrid RANS/LES modelling with an approximate renormalization group. I: Model development. *J. Turbul.*, 6(13), 2005.
- Jean Donea. *Computational methods for transient analysis*, chapter Arbitrary Lagrangian-Eulerian Finite Element Methods, pages 474–516. North-Holland, 1983.
- D. A. Drew and S. L. Passman. *Theory of multicomponent fluids*. Springer-Verlag, 1998.
- D. S. Drumheller. *Introduction to Wave Propagation in Nonlinear Fluids and Solids*. Cambridge University Press, New York, New York, 1998.
- P. A. Durbin. Near-wall turbulence closure modeling without ‘damping functions’. *Theor. Comput. Fluid Dyn.*, 3:1–13, 1991.
- P. A. Durbin. Limiters and wall treatments in applied turbulence modeling. *Fluid Dynamics Research*, (41):012203, 2009.
- P.A. Durbin. Separated flow computations with the  $k - \epsilon - v^2$  model. *AIAA J.*, 33(4):659–664, 1995.
- C-C. Fan, X. Xiao, J. R. Edwards, H. A. Hassan, and R. A. Baurle. Hybrid Large-Eddy/Reynolds-Averaged Navier-Stokes simulations of shock-separated flows. *J. Spacecr. Rockets*, 41(6):897–906, 2004.
- E. Fares and W. Schroder. A differential equation for approximate wall distance. *Int. J. Numer. Methods Fluids*, 39:743–762, 2002.
- C. Farhat, M. Lesoinne, and P. LeTallec. Load and motion transfer algorithms for fluid/structure interaction problems with non-matching discrete interfaces: momentum and energy conservation, optimal discretization and application to aeroelasticity. *Computer Methods in Applied Mechanics and Engineering*, 157:95–114, 1998.
- C. A. Felippa and K. C. Park. Staggered transient analysis procedures for coupled mechanical systems: formulation. *Computer Methods in Applied Mechanics and Engineering*, 24:61–111, 1980.
- Miguel A. Fernández, J. F. Gerbeau, and C. Grandmont. A projection semi-implicit scheme for the coupling of an elastic structure with an incompressible fluid. Technical Report 5700, INRIA, 2005.
- Miguel A. Fernández, J. F. Gerbeau, and C. Grandmont. A projection algorithm for fluid-structure interaction with strong added-mass effect. *C. R. Acad. Sci., Paris, Ser. I*, 342:279–284, 2006.
- J. H. Ferziger. Interfacial transfer in tryggvason’s method. *International Journal for Numerical Methods in Fluids*, 41:551–560, 2003.

- Y. Fraigneau, J.-L. Guermond, and L. Quartapelle. Approximation of variable density incompressible flows by means of finite element and finite volumes. *Communications in Numerical Methods in Engineering*, 17:893–902, 2001.
- N. J. Georgiadis, J. I. D. Alexander, and E. Reshotko. Hybrid Reynolds-Averaged Navier-Stokes/Large-Eddy simulations of supersonic turbulent mixing. *AIAA J.*, 41(2):218–229, 2003.
- J.-F. Gerbeau, M. Vidrascu, and P. Frey. Fluid-structure interaction in blood flows on geometries coming from medical imaging. Technical Report 5052, INRIA, 2003.
- M. Germano. Turbulence: The filtering approach. *J. Fluid Mech.*, 238:325–336, 1992.
- M. Germano. Properties of the hybrid RANS/LES filter. *Theor. Comput. Fluid Dyn.*, 17:225–231, 2004.
- S. S. Girimaji. Partially-Averaged Navier-Stokes model for turbulence: A Reynolds-Averaged Navier-Stokes to Direct Numerical Simulation bridging method. *J. Appl. Mech.-Trans. ASME*, 73:413–421, 2006.
- P. M. Gresho and R. L. Sani. *Incompressible flow and the finite element method, Advection-diffusion and isothermal laminar flow*. John Wiley & Sons, Chichester, England, 1998.
- Philip M. Gresho. On the theory of semi-implicit projection methods for viscous incompressible flow and its implementation via a finite element method that also introduces a nearly consistent mass matrix. part 1: Theory. *International Journal for Numerical Methods in Fluids*, 11:587–620, 1990.
- Philip M. Gresho and Stevens T. Chan. On the theory of semi-implicit projection methods for viscous incompressible flow and its implementation via a finite element method that also introduces a nearly consistent mass matrix. part 2: Implementation. *International Journal for Numerical Methods in Fluids*, 11:621–659, 1990.
- Philip M. Gresho and Stevens T. Chan. Projection 2 goes turbulent – and fully implicit. *preprint International Journal for Computational Fluid Dynamics*, March 1996. (LLNL UCRL-JC-123727).
- Philip M. Gresho and Robert L. Sani. On pressure boundary conditions for the incompressible Navier-Stokes equations. *International Journal for Numerical Methods in Fluids*, 7:1111–1145, 1987.
- Philip M. Gresho, Stevens T. Chan, Mark A. Christon, and Allen C. Hindmarsh. A little more on stabilized  $q_1q_1$  for transient viscous



- incompressible flow. *International Journal for Numerical Methods in Fluids*, 21:837–856, 1995.
- F.F. Grinstein, L.G. Margolin, and W. Rider. *Implicit large eddy simulation: computing turbulent fluid dynamics*. Cambridge University Press, 2007. ISBN 9780521869829. URL <http://books.google.com/books?id=Xk-eb9kPgXsC>.
- H. Grotjans and F.R. Menter. Wall functions for general application CFD codes. In *ECCOMAS 98 Proceedings of the Fourth European Computational Fluid Dynamics Conference*, pages 1112–1117. John Wiley and Sons, 1998.
- A. Guelfi, D. Bestion, M. Boucker, P. Boudier, P. Fillion, M. Grandotto, J.-M. Hérard, E. Hervieu, and P. Péturaud. NEPTUNE: A new software platform for advanced nuclear thermal hydraulics. *Nuclear Science and Engineering*, 156:281–324, 2007.
- J.-L. Guermond and L. Quartapelle. Calculation of incompressible viscous flow by an unconditionally stable projection fem. *Journal of Computational Physics*, 132:12–23, 1997.
- J.-L. Guermond and L. Quartapelle. A projection FEM for variable density incompressible flows. *Journal of Computational Physics*, 165:167–188, 2000.
- Jean-Luc Guermond. Some implementations of projection methods for Navier-Stokes equations. *Mathematical Modelling and Numerical Analysis*, 30(5):637–667, 1996.
- Jean-Luc Guermond. A convergence result for the approximation of the Navier-Stokes equations by an incremental projection method. *C. R. Acad. Sci. Paris*, 325:1329–1332, 1997.
- Jean-Luc Guermond and L. Quartapelle. On the approximation of the unsteady Navier-Stokes equations by finite element projection methods. *Numerische Mathematik*, 80:207–238, 1998a.
- Jean-Luc Guermond and L. Quartapelle. On stability and convergence of projection methods based on pressure Poisson equation. *International Journal for Numerical Methods in Fluids*, 26:1039–1053, 1998b.
- Giovanna Guidoboni, Roland Glowinski, Nicola Cavallini, and Sunčica Canic. Stable loosely-coupled-type algorithm for fluid-structure interaction in blood flow. *Journal of Computational Physics*, 228:6916–6937, 2009.
- Morton E. Gurtin. *An Introduction to Continuum Mechanics*. Academic Press, 2003.

- F. Hamba. A hybrid RANS/LES simulation of turbulent channel flow. *Theor. Comput. Fluid Dyn.*, 16:387–403, 2003.
- F. Hamba. A hybrid RANS/LES simulation of high-Reynolds-number channel flow using additional filtering at the interface. *Theor. Comput. Fluid Dyn.*, 20(2):89–101, 2006.
- K. Hanjalic, M. Popovac, and M. Hadziabdic. A robust near-wall elliptic-relaxation eddy-viscosity turbulent model for cfd. *Int. J. Heat Fluid Flow*, 25:1047–1051, 2004.
- Peter Hansbo. Nitsche’s method for interface problems in computational mechanics. *GAMM-Mitt*, 28(2):183–206, 2004.
- Jaroslav Hron and Stefan Turek. A monolithic FEM solver for an ALE formulation of fluid-structure interaction with configuration for numerical benchmarking. In P. Wesseling, E. O nate, and J. Périaux, editors, *European Conference on Computational Fluid Dynamics*, 2006.
- T. J. R. Hughes and W. K. Liu. Implicit-explicit finite elements in transient analysis: stability theory. *Journal of Applied Mechanics*, 45:371–374, 1978a.
- T. J. R. Hughes and W. K. Liu. Implicit-explicit finite elements in transient analysis: Implementation and numerical examples. *Journal of Applied Mechanics*, 45:375–378, 1978b.
- A. G. Hutton and R. M. Ashworth. The challenge of turbulence modeling in modern aeronautical design. *Int. J. Numer. Methods Fluids*, 47:721–737, 2005.
- LLC InterPhase Dynamics. Nphase-cmfd example manual. Technical report, InterPhase Dynamics, LLC, 2008a.
- LLC InterPhase Dynamics. Nphase-cmfd program manual. Technical report, InterPhase Dynamics, LLC, 2008b.
- LLC InterPhase Dynamics. Nphase-cmfd user manual. Technical report, InterPhase Dynamics, LLC, 2010.
- Mamoru Ishii and Novak Zuber. Drag coefficient and relative velocity in bubbly, droplet or particulate flows. *AIChE Journal*, 25(5):843–855, 1979. ISSN 1547-5905. DOI: 10.1002/aic.690250513. URL <http://dx.doi.org/10.1002/aic.690250513>.
- R. K. Jaiman, X. Jiao, P. H. Geubelle, and E. Loth. Conservative load transfer along curved fluid-solid interface with non-matching meshes. *Journal of Computational Physics*, 218:372–397, 2006.

- W. P. Jones and B. E. Launder. The prediction of laminarization with with a two-equation model of turbulence. *Int. J. Heat Mass Transf.*, 15:301–314, 1972.
- G. Kalitzin, G. Medic, G. Iaccarino, and P. Durbin. Near-wall behaviour of rans turbulence models and implications for wall functions. *J. Comput. Phys.*, 204:265–291, 2005.
- J. Van Kan. A second-order accurate pressure-correction scheme for viscous incompressible flow. *SIAM Journal for Scientific and Statistical Computing*, 7:870–891, 1986.
- B. Kashiwa and R. M. Rauenzahn. A multimaterial formalism. Technical report, Los Alamos National Laboratory, 1994.
- B. A. Kashiwa, N. T. Padial, R. M. Rauenzahn, and W. B. VanderHeyden. A cell-centered ICE method for multiphase flow simulations. Technical report, Los Alamos National Laboratory, 1993.
- S. Kawai and K. Fujii. Analysis and prediction of thin-airfoil stall phenomena with hybrid turbulence methodology. *AIAA J.*, 43(5):953–961, 2005.
- A. R. A. Khaled and K. Vafai. The role of porous media in modeling flow and heat transfer in biological tissues. *Int. J. Heat Mass Transf.*, 46(26):4989–5003, 2003.
- W. W. Kim and S. Menon. An unsteady incompressible navier-stokes solver for Large Eddy simulation of turbulence flows. *Int. J. Numer. Methods Fluids*, 31:983–1017, 1999.
- L. Klinger, J. B. Vos, and K. Appert. A simplified gradient evaluation on non-orthogonal meshes; application to plasma torch simulation. *Computers & Fluids*, 33:643–654, 2004.
- Omar M. Knio, Habib N. Najm, and Peter S. Wyckoff. A semi-implicit numerical scheme for reacting flow. ii. stiff operator-split formulation. *pre-print submitted to Journal of Computational Physics*, 154(2): 428–467, 1999.
- A. N. Kolmogorov. The local structure of turbulence in incompressible viscous fluid for very large Reynolds numbers. *Proceedings of the Royal Society of London Series A*, 434:9–13, 1991.
- D. B. Kothe, M. Bussmann, R. C. Ferrell, J. Durachta, J. Guo, and C. Beckermann. Exploiting weighted and constrained least squares techniques for function reconstruction of abruptly-varying discrete data. *Submitted to International Journal for Numerical Methods in Fluids*, 2002.

- Yuri Kuznetsov, Konstantin Lipnikov, and Mikhail Shashkov. Mimetic finite difference method on polygonal meshes for diffusion-type problems. *Computers & Geosciences*, 8(4):301–324, 2004.
- C. K. G. Lam and K. A. Bremhorst. Modified form of  $k - \varepsilon$  model for predicting wall turbulence. *J. Fluids Eng.-Trans. ASME*, 103:456–460, 1981.
- B. E. Launder and B. I. Sharma. Application of the energy-dissipation model of turbulence to the calculation of flow near a spinning disc. *Lett. in Heat Mass Transf.*, 1:131–138, 1974.
- B. E. Launder and D. B. Spalding. The numerical computation of turbulent flows. *Comput. Meth. Appl. Mech. Eng.*, 3:269–289, 1974.
- T. Lehnhaäuser and M. Schäfer. Improved linear interpolation practice for finite-volume schemes on complex grids. *International Journal for Numerical Methods in Fluids*, 38:625–645, 2002.
- M. J. Li and M. Abdou. A variable-density projection method for interfacial flows. *Numerical Heat Transfer, Part B*, 44:553–574, 2003.
- F.S. Lien and G. Kalitzin. Computations of transonic flow with the  $v^2 - f$  turbulence model. *Int. J. Heat Fluid Flow*, 22:53–61, 2001.
- Konstantin Lipnikov, Mikhail Shashkov, D. Svyatskiy, and Yu Vasilevski. Monotone finite volume schemes for diffusion equations on unstructured triangular and shape-regular polygonal meshes. *Journal of Computational Physics*, 227:492–512, 2007.
- C. Liu and N. J. Walkington. Convergence of numerical approximations of the incompressible navier-stokes equations with variable density and viscosity. *SIAM Journal on Numerical Analysis*, 45:1287–1304, 2007.
- G. R. Liu and George X. Xu. A gradient smoothing method (GSM) for fluid dynamics problems. *International Journal for Numerical Methods in Fluids*, 58:1101–1133, 2008.
- N. S. Liu and T. H. Shih. Turbulence modeling for very Large-Eddy simulation. *AIAA J.*, 44(4):687–697, 2006.
- D. Livescu, J. R. Ristorcelli, R. A. Gore, S. H. Dean, W. H. Cabot, and A. W. Cook. High-Reynolds number Rayleigh-Taylor turbulence. *J. Turbul.*, 10(13), 2009.
- C. E. Lynch and M. J. Smith. Hybrid rans-les turbulence models on unstructured grids. *AIAA paper 08-3854*, 23-26 June, Seattle Washington 2008.

- Dimitri J. Mavriplis. Revisiting the least-squares procedure for gradient reconstruction on unstructured meshes. In *AIAA 2003-3986*, Orlando, Florida, June 2003. AIAA 16th Computational Fluid Dynamics Conference.
- Dimitri J. Mavriplis. Unstructured mesh discretizations and solvers for computational aerodynamics. In *18th AIAA Computational Fluid Dynamics Conference*. AIAA, June 2007.
- S. Menon and N. Patel. Subgrid modeling for simulation of spray combustion in Large-Scale combustors. *AIAA J.*, 44(4):709–723, 2006.
- F. R. Menter. Influence of freestream values on  $k - \omega$  turbulence model prediction. *AIAA J.*, 30(6):1657–1659, 1992.
- F. R. Menter. Two-equation eddy-viscosity turbulence models for engineering applications. *AIAA J.*, 32(8):1598–1605, 1994.
- C. Michler, E. H. van Brummelen, S. J. Hulshoff, and R. de Borst. The relevance of conservation for stability and accuracy of numerical methods for fluid-structure interaction. *Computer Methods in Applied Mechanics and Engineering*, 192:4195–4215, 2003.
- C. Michler, S. J. Hulshoff, E. H. van Brummelen, and R. de Borst. A monolithic approach to fluid-structure interaction. *Computers & Fluids*, 33:839–848, 2004.
- Michael L. Minion. A projection method for locally refined grids. *Journal of Computational Physics*, 127:158–178, 1996.
- Michael L. Minion and David L. Brown. Performance of under-resolved two-dimensional incompressible flow simulations, II. *Journal of Computational Physics*, 138:734–765, 1997.
- P. Moin and K. Mahesh. Direct numerical simulation: A tool in turbulence research. *Annu. Rev. Fluid Mech.*, 30:539–78, 1998.
- A. S. Monin and A. M. Yaglom. *Statistical Fluid Mechanics*. MIT Press, 1979.
- F. Nicoud and F. Ducros. Subgrid-scale stress modelling based on the square of the velocity gradient tensor. *Flow, Turbulence and Combustion*, 62:183–200, 1999. ISSN 1386-6184. URL <http://dx.doi.org/10.1023/A:1009995426001>. 10.1023/A:1009995426001.
- P. Nithiarasu, K. S. Sujatha, K. Ravindran, T. Sundararajan, and K. N. Seetharamu. Non-Darcy natural convection in a hydrodynamically and thermally anisotropic porous medium. *Comput. Meth. Appl. Mech. Eng.*, 188(1-3):413–430, 2000.

- Bojan Ničeno. A three dimensional, finite volume method for incompressible Navier-Stokes on unstructured, staggered grids. In *European Conference on Computational Fluid Dynamics*. ECCOMAS, 2006.
- D. R. Noble, P. R. Schunk, E. D. Wildes, T. A. Baer, R. R. Rao, and P. K. Notz. Large deformation solid-fluid interaction via a level set approach. Technical Report SAND2003-4649, Sandia National Laboratories, December 2003.
- J. A. Ochoa-Tapia and S. Whitaker. Momentum transfer at the boundary between a porous medium and a homogeneous fluid—I. theoretical development. *Int. J. Heat Mass Transf.*, 38(14):2635–2646, 1995a.
- J. A. Ochoa-Tapia and S. Whitaker. Momentum transfer at the boundary between a porous medium and a homogeneous fluid—ii. comparison with experiment. *Int. J. Heat Mass Transf.*, 38(14):2647–2655, 1995b.
- J. A. Ochoa-Tapia and S. Whitaker. Momentum jump condition at the boundary between a porous medium and a homogeneous fluid: inertial effects. *Journal of Porous Media*, 1:201–218, 1998.
- Carl Ollivier-Gooch and Michal Van Altena. A high-order-accurate unstructured mesh finite-volume scheme for the advection-diffusion equation. *Journal of Computational Physics*, 181:729–752, 2002.
- K. C. Park. Partitioned transient analysis procedures for coupled field problems: stability analysis. *Transactions of the ASME*, 47:370–376, 1980.
- K. C. Park and C. A. Felippa. Partitioned transient analysis procedures for coupled-field problems: accuracy analysis. *Journal of Applied Mechanics*, 47:919–926, 1980.
- K. C. Park, C. A. Felippa, and J. A. DeRuntz. Stabilization of staggered solution procedures for fluid-structure interaction analysis. In T. Belytschko and T. L. Geers, editors, *Computational Methods for Fluid-Structure Interaction Problems*, volume AMD-Vol. 26, Atlanta, Georgia, 1977.
- S. Parneix, P.A. Durbin, and M. Behnia. Computation of 3-d turbulent boundary layers using the v2f model. *Flow Turbul. Combust.*, 60:19–46, 1998.
- U. Piomelli and E. Balaras. Wall-layer models for large-eddy simulations. *Annu. Rev. Fluid Mech.*, 34:349–74, 2002.
- M. Z. Podowski. On the consistency of mechanistic multidimensional modeling of gas/liquid two-phase flows. *Nuclear Engineering and Design*, 239:933–940, 2009.

- S. B. Pope. Ten questions concerning the large-eddy simulation of turbulent flows. *New J. Phys.*, 6(35):1–24, 2004.
- Stephen. B Pope. *Turbulent Flows*. Cambridge University Press, 2000.
- Elbridge G. Puckett, Ann S. Almgren, John B. Bell, Daniel L. Marcus, and William J. Rider. A high-order projection method for tracking fluid interfaces in variable density incompressible flows. *Journal of Computational Physics*, 130:269–282, 1997.
- G. Puigt, V. Auffray, and J. D. Müller. Discretisation of diffusive fluxes on hybrid grids. *Journal of Computational Physics*, 229:1425–1447, 2010.
- J.-H. Pyo and J. Shen. Guage-uzawa methods for incompressible flows with variable density. *Journal of Computational Physics*, 221:181–197, 2007.
- Jr. R. T. Lahey. On the computationl of multiphase flow. *Nuclear Technology*, 167:29–45, 2009.
- Jr. R. T. Lahey and D. A. Drew. The analysis of two-phase flow and heat transfer using a multidimensional, four field, two-fluid model. *Nuclear Engineering and Design*, 204:29–44, 2001.
- L. F. Richardson. *Weather Prediction by Numerical Process*. Cambridge Univ. Press, 1922.
- W. J. Rider, D. B. Kothe, S. J. Mosso, J. H. Cerutti, and J. I. Hochstein. Accurate solution algorithms for incompressible multiphase flows. Technical Report AIAA-95-0699, AIAA, Reno, Nevada, January 1995.
- William J. Rider. The robust formulation of approximate projection methods for incompressible flows. Technical Report LA-UR-3015, Los Alamos National Laboratory, 1994a.
- William J. Rider. Filtering nonsolenoidal modes in numerical solutions of incompressible flows. Technical Report LA-UR-3014, Los Alamos National Laboratory, Los Alamos, New Mexico, September 1994b.
- William J. Rider. Approximate projection methods for incompressible flow: implementation, variants and robustness. Technical Report LA-UR-2000, Los Alamos National Laboratory, Los Alamos, New Mexico, July 1995.
- William J. Rider and Douglas B. Kothe. Constrained minimization for monotonic reconstruction. *Preprint*, 2002.
- B. Roe, A. Haselbacher, and P. H Geubelle. Stability of fluid-structure thermal simulations on moving grids. *International Journal for Numerical Methods in Fluids*, 54:1097–1117, 2007.

- M. Rudman. A volume-tracking method for incompressible multifluid flows with large density variations. *International Journal for Numerical Methods in Fluids*, 28:357–378, 1998.
- P. Sagaut. *Large Eddy Simulation for incompressible flows, An introduction*. Springer, third edition, 2005.
- M. Sánchez-Rocha and S. Menon. The compressible hybrid RANS/LES formulation using an additive operator. *J. Comput. Phys.*, 228:2037–2062, 2009.
- M. Sánchez-Rocha, M. Kirtas, and S. Menon. Zonal hybrid RANS-LES method for static and oscillating airfoils and wings. *AIAA paper 06-1256*, 9-12 January 2006.
- J. U. Schluter, H. Pitsch, and P. Moin. Large Eddy simulation inflow conditions for coupling with Reynolds-average flow solvers. *AIAA J.*, 42(3):478–484, 2004.
- S. P. Schofield, M. A. Christon, V. Dyadechko, R. V. Garimella, R. B. Lowrie, and B. K. Swartz. Multi-material incompressible flow simulation using the moment-of-fluid method. *International Journal for Numerical Methods in Fluids*, 63:931–952, 2010. DOI: 10.1002/fld.2108. (Los Alamos National Laboratory LA-UR-09-00733).
- Samuel P. Schofield and Mark A. Christon. Effects of element order and interface reconstruction in FEM/volume-of-fluid incompressible flow simulation. *International Journal for Numerical Methods in Fluids*, 68:1422–1437, 2010. (Los Alamos National Laboratory LA-UR-10-00004).
- A. Scotti, C. Meneveau, and M. Fatica. Dynamic smagorinsky model on anisotropic grids. *Phys. Fluids A.*, 9(6):1856–1858, 1997.
- Guglielmo Scovazzi and Thomas J. R. Hughes. Lecture notes on continuum mechanics on arbitrary moving domains. Technical Report SAND2007-6312P, Sandia National Laboratories, 2007.
- L. A. Segel. *Mathematics applied to continuum mechanics*. Dover, 1965.
- J. A. Sethian. Fast marching methods. *SIAM Rev.*, 41(2):199–235, 1999.
- D. R. Shaver, S. P. Antal, and M. Z. Podowski. Validation of NPHASE-CMFD against the experimental data of Wang, et al. May have been published in NURETH-14.
- D. R. Shaver, S. P. Antal, and M. Z. Podowski. Multidimensional modeling of interfacial boiling and condensation. In *ANS Winter Meeting*, Washington, D. C., October 2011.



- W. T. Shaw and S. L. Soo. On the effect of  $\rho\nabla\alpha$  term in multiphase mechanics. *International Journal of Multiphase Flow*, 5:153–158, 1979.
- F. Simon, S. Deck, and P. Guillen. Renolds-Averaged Navier-Stokes/Large-Eddy simulations of supersonic base flow. *AIAA J.*, 44(11):2578–2590, 2006.
- A. K. Slone, K. Pericleous, C. Bailey, and M. Cross. Dynamic fluid-structure interaction using finite volume unstructured mesh procedures. *Computers and Structures*, 80:371–390, 2002.
- J. Smagorinsky. General circulation experiments with the primitive equations: I. the basic equations. *Monthly Weather Rev*, 91, 1963.
- T. M. Smith, M. F. Barone, R. B. Bond, A. A. Lorber, and D. G. Baur. Comparison of reconstruction techniques for unstructured mesh vertex centered finite volume schemes. In *18th AIAA Computational Fluid Dynamics Conference*, June 2007.
- J. H. Song. A remedy for the ill-posedness of the one-dimensional two-fluid model. *Nuclear Engineering and Design*, 222:40–53, 2003.
- J. H. Song and M. Ishii. The well-posedness of incompressible one-dimensional two-fluid model. *International Journal of Heat and Mass Transfer*, 43:2221–2231, 2000.
- P. R. Spalart. Strategies for turbulence modelling and simulations. *Int. J. Heat Fluid Flow*, 21:252–263, 2000.
- P. R. Spalart. Detached-eddy simulation. *Annu. Rev. Fluid Mech.*, 41:181–202, 2009.
- P. R. Spalart. Trends in turbulence treatments. *AIAA Paper 2000-2306*, June 2000.
- P. R. Spalart and S. R. Allmaras. A one-equation turbulence model for aerodynamic flows. *AIAA Paper 1992-0439*, January 1992.
- P. R. Spalart, S. Deck, M. L. Shur, K. D. Squires, M. Kh. Strelets, and A. Travin. A new version of detached-eddy simulation, resistant to ambiguous grid densities. *Theor. Comput. Fluid Dyn.*, 20:181–195, 2006.
- P.R Spalart and S. R. Allmaras. A one-equation turbulence model for aerodynamic flows. *La Recherche Aerospatiale*, 1:5–21, 1994.
- P.R Spalart, W.H. Jou, M. Strelets, and S. R. Allmaras. Comments on the feasibility of LES for wings and on a hybrid RANS/LES approach. In *First AFOSR International Conference on DNS/LES*, Ruston Louisiana, 4-8 Aug 1997. Greyden Press.

- C. G. Speziale. Turbulence modeling for time dependent RANS and VLES: A review. *AIAA J.*, 36(2):173–184, 1998.
- E. F. Spina, A. J. Smits, and S. K. Robinson. The physics of supersonic turbulent boundary layers. *Annu. Rev. Fluid Mech.*, 26:287–319, 1994.
- H. Staedtke, G. Franchello, B. Worth, U. Graf, P. Romstedt, A. Kumbaro, J. García-Cascales, H. Pallére, H. Deconinck, M. Ricchiuto, B. Smith, F. DeCachard, E. F. Toro, E. Romenski, and S. Mimouni. Advanced three-dimensional two-phase flow simulation tools for application to reactor safety (ASTAR). *Nuclear Engineering and Design*, 235:379–400, 2005.
- H. B. Stewart and B. Wendroff. Two-phase flow: Models and methods. *Journal of Computational Physics*, 56:363–409, 1984.
- L. Štrubelj and I. Tiselj. Two-fluid model with interface sharpening. *International Journal for Numerical Methods in Engineering*, 87:575–590, 2011.
- Mark Sussman, Ann S. Almgren, John B. Bell, Phillip Colella, Louis H. Howell, and Michael L. Welcome. An adaptive level set approach for two-phase flows. *Journal of Computational Physics*, 148:81–124, 1999.
- Magnus Svärd and Jan Nordström. Stability of finite volume approximations for the Laplacian operator on quadrilateral and triangular grids. *Applied Numerical Mathematics*, 51:101–125, 2004.
- H. Tan and K. M. Pillai. Finite element implementation of stress-jump and stress-continuity conditions at porous-medium, clear-fluid interface. *Comput. Fluids*, 38(6):1118–1131, 2009.
- L. Temmerman, M. Hadziabdic, M. A. Leschziner, and K. Hanjalic. A hybrid two-layer URANS-LES approach for large eddy simulation at high Reynolds number. *Int. J. Heat Fluid Flow*, 26:173–190, 2005.
- Tennekes and Lumley. *A First Course in Turbulence*. The MIT Press, 1997.
- The Truchas Team. Truchas physics and algorithms. Technical Report LA-UR-03-0166, Los Alamos National Laboratory, 2003.
- I. Tiselj and S. Petelin. Modelling of two-phase flow with second-order accurate scheme. *Journal of Computational Physics*, 136:503–521, 1997.
- Akio TOMIYAMA, Isao KATAOKA, Iztok ZUN, and Tadashi SAKAGUCHI. Drag coefficients of single bubbles under normal and micro gravity conditions. *JSME International Journal Series B*, 41(2): 472–479, 1998.

- I. Toumi, A. Bergeron, D. Gallo, E. Royer, and D. Caruge. FLICA-4: a three-dimensional two-phase flow computer code with advanced numerical methods for nuclear applications. *Nuclear Engineering and Design*, 200:139–155, 2000.
- Shuangzhang Tu and Shahrouz Aliabadi. Development of a hybrid finite volume/element solver for incompressible flows. *International Journal for Numerical Methods in Fluids*, 20:177–203, 2007.
- Shuangzhang Tu, Shahrouz Aliabadi, Reena Patel, and Marvin Watts. An implementation of the spalart-allmaras des model in an implicit unstructured hybrid finite volume/element solver for incompressible turbulent flow. *International Journal for Numerical Methods in Fluids*, 30:1051–1062, 2009.
- P. Tucker and L. Davidson. Zonal  $k - l$  based large eddy simulation. *Comput. Fluids*, 33(2):267–287, 2004.
- P. G. Tucker. Differential equation-based wall distance computation for DES and RANS. *J. Comput. Phys.*, 190:229–248, 2003.
- P. G. Tucker. Computations of wall distances based on differential equations. *AIAA J.*, 43(3):539–549, 2005.
- P. G. Tucker. Turbulence modelling of problem aerospace flows. *Int. J. Numer. Methods Fluids*, 51:261–283, 2006.
- P. G. Tucker. Turbulence modeling for flows around convex features giving rapid eddy distortion. *Int. J. Heat Fluid Flow*, 28:1073–1091, 2007.
- K. Vafai and C. L. Tien. Boundary and inertia effects on flow and heat transfer in porous media. *Int. J. Heat Mass Transf.*, 24(2):195–203, 1981.
- D. Vigneron, J. M. Vaassen, and J. A. Essers. An implicit high order cell-centered finite volume scheme for the solution of three-dimensional Navier-Stokes on unstructured grids. *Computational Fluid and Solid Mechanics*, pages 923–927, 2005.
- W. G. Vincenti and C. H. Kruger. *Introduction to Physical Gas Dynamics*. Krieger Publishing, 1965.
- T. E. Voth, M. J. Martinez, and M. A. Christon. Generalized Fourier analysis of the advection-diffusion equation – part II: Two-dimensional domains. *International Journal for Numerical Methods in Fluids*, 45:889–920, 2004.

- Tian Wan, Shahrouz Aliabadi, and Christopher Bigler. A hybrid scheme based on finite element/volume methods for two immiscible fluid flows. *International Journal for Numerical Methods in Fluids*, 61:930–944, 2009.
- Z. J. Wang. Improved formulation for geometric properties of arbitrary polyhedra. *AIAA Journal*, 37, No. 10:1326–1327, 1999.
- Brian B. Wetton. Error analysis of pressure increment schemes. *submitted to SINUM*, 38(1):160–169, April 1998.
- S. Whitaker. *The Method of Volume Averaging*. Kluwer Academic Publishers, 1999.
- F. M. White. *Viscous Fluid Flow*. McGraw Hill, 1991.
- D. C. Wilcox. Reassessment of the scale-determining equation for advanced turbulence models. *AIAA J.*, 26(11):1299–1310, 1988.
- D. C. Wilcox. *Turbulence Modeling for CFD*. CDW Industries 2nd ed., 1998.
- X. Xiao, J. R. Edwards, H. A. Hassan, and R. A. Baurle. Inflow boundary conditions for hybrid Large Eddy/Reynolds Averaged Navier-Stokes simulations. *AIAA J.*, 41(8):1481–1489, 2003.
- X. Xiao, J. R. Edwards, and H. A. Hassan. Blending functions in hybrid Large-Eddy/Reynolds-Averaged Navier-Stokes simulations. *AIAA J.*, 42(12):2508–2515, 2004.
- G. Yadigaroglu. Letter to the editor, “CMFD (a brand name) and other acronyms. *International Journal of Multiphase Flow*, 29:719–720, 2003.
- V. Yakhot, S. A. Orszag, S. Thangam, T. B. Gatski, and C. G. Speziale. Development of turbulence models for shear flows by a double expansion technique. *Phys. Fluids*, 4(7):1510–1520, 1992.
- G.H. Yeoh and J. Tu. *Computational Techniques for Multiphase Flows*. Elsevier Science, 2009. ISBN 9780080914893.
- P. Yu, T. S. Lee, Y. Zeng, S. A. Meguid, and H. T. Low. A numerical technique for laminar swirling flow at the interface between porous and homogenous fluid domains. *Int. J. Numer. Methods Fluids*, 60(3): 337–353, 2009.
- P. Yu, Y. Zeng, T. S. Lee, H. X. Bai, and H. T. Low. Wake structure for flow past and through a porous square cylinder. *Int. J. Heat Fluid Flow*, 31(2):141–153, 2010.
- B. Zhong and P. G. Tucker.  $k-l$  based hybrid LES/RANS approach and its applications to heat transfer simulation. *Int. J. Numer. Methods Fluids*, 46:983–1005, 2004.

# 17 Index

- Appendix
  - low Reynolds number functions, 213
  - vector notation, 211
- Appendix A, 211
- Conservation Equations
  - Incompressible Flows
    - boundary conditions, 33, 35
    - energy conservation, 32, 35
    - governing equations in vector notation, 31, 34
    - incompressible equations, 31
    - initial conditions, 33, 35
    - mass conservation, 31, 34
    - momentum conservation, 32, 35
  - Multicomponent Flows, 39
  - Multifluid Flows, 42
  - Multiphase Flows, 43
  - Multispecies Flows, 39
- Copyright, 2
- General Conservation Equations
  - ALE, 51
  - Arbitrary Lagrangian-Eulerian Formulation, 51
    - basics, 51
    - continuity equation, 58
    - deformation gradient, 53, 55
    - displacement, 53, 54
    - energy equation, 58
    - generic forms, 56
    - inverse mapping, 54
    - invertible map, 51
    - Jacobian of the map, 51
    - kinematics, 52
    - Lagrangian-to-Eulerian map, 52
    - Lagrangian-to-referential map (ALE), 54
    - master balance equation, 56
    - material velocity, 53
    - momentum equation, 59
    - Nanson's formula, 52
    - Navier-Stokes equations, 58
    - Reynolds Transport Theorem, 56
    - time derivative, 53, 55
    - time derivative of the Jacobian, 54, 55
    - vector form, 57
    - velocity, 55
    - volume relations, 52
- Compressible Flows
  - equation of state, 27
  - ideal gas, 28
- Governing Equations, 19
  - boundary conditions, 22
  - Carreau-Yasuda model, 24
  - constitutive relations, 23
  - Cross model, 25
  - Ellis-Meter model, 25
  - heat transfer, 26
  - Herschel-Bulkey model, 25
  - initial conditions, 23
  - Navier-Stokes equations, 19
  - Navier-Stokes equations in vector form, 21
  - Newtonian fluid, 23
  - non-Newtonian fluid, 24
  - Powell-Eyring model, 26
  - power law model, 26
- Low-Mach Flows, 29
  - governing equations, 29
- Turbulence Modeling, 61
  - $k - \omega$  SST model, 74
  - $k - \varepsilon$  model, 71
  - $k - \varepsilon - \zeta - f$  model, 78
  - $k - \varepsilon - v^2 - f$  model, 77
  - anisotropic stress tensor, 103
  - compressible hybrid RANS/LES Navier-Stokes equations, 87
  - derived statistics, 99
  - detached eddy simulation, 98
  - direct numerical simulation approach, 65
  - higher order statistics, 102
  - hybrid RANS/LES approach, 84
  - hybrid RANS/LES operators, 84
  - incompressible hybrid Navier-Stokes equations, 93
  - large eddy simulation approach, 80
  - LES governing equations, 81
  - localized dynamic  $k_{sgs}$ -equation model, 83
  - mean and fluctuating decomposition, 101
  - RANS-SST/LES-LDKM hybrid model, 95
  - Reynolds-averaged Navier-Stokes approach, 66
  - Reynolds-averaged statistics, 99
  - Smagorinsky model, 82
  - Spalart-Allmaras model, 69
  - time-dependent hybrid RANS/LES formulation, 93
  - turbulence basics, 62
  - Wall-Adapted Large Eddy model, 83
- Incompressible Flow Solver
  - Arbitrary Lagrangian-Eulerian Formulation
    - RNG  $k - \varepsilon$  equations, 188
  - Arbitrary Lagrangian-Eulerian Formulation, 171
  - energy equation, 182
  - enthalpy, 183

- geometric conservation law , 176
- pressure gradient, 178
- revised P2  $\lambda$ -construction, 174
- second-order incremental projection method, 171
- Spalart-Allmaras equation, 184
- specific heat, 183
- start-up procedure, 177
- time integration, 177
- viscosity, 182
- Eulerian Formulation, 147
  - advection, 155
  - div-free projection, 157
  - divergence, 154
  - dual-edge velocities, 154, 156
  - edge interpolation, 153
  - initial pressure, 159
  - P2 algorithm, 150
  - Porous Media model, 160
  - pressure gradient, 153
  - projection method, 147
  - projection properties, 149
  - RMS divergence, 156
- semi-implicit projection method, 150
- Smagorinsky model, 168
- Spalart-Allmaras model, 164
- stable time-step, 155
- start-up procedure, 155
- WALE model, 169
- FSI, 201
  - background, 201
  - Stabilized FSI Formulation, 204
- Numerical Methods
  - Discontinuous Galerkin/FVM, 111
    - convergence studies, 119
    - element-centered gradient, 113
    - flux functions, 113
    - formulation, 111
    - Green-Gauss gradient, 114
    - least-squares gradient, 114
    - mixed quad/tri meshes, 125
    - phase-speed and artificial diffusivity, 118
    - quadrilateral elements, 124
  - quadrilateral elements – rotated grid, 124
  - scalar conservation law, 111
  - triangular elements – rotated grid, 123
  - uniform triangular elements, 121
  - weighted least-squares gradient, 117
- Finite Volume Method, 111
- Gradient Approximation, 133
  - background, 133
  - diffusive fluxes, 138
  - edge-centered, 136
  - element-centered, 113, 136
  - full least-squares, 136
  - Green-Gauss, 114
  - least-squares, 114, 136
  - weighted least-squares, 117
- Unstructured Grid Topology, 107
  - dual, 107
- Wall-Normal Distance Calculation, 141
  - Numerical Examples, 142